



TECHNISCHE
UNIVERSITÄT
WIEN

Vienna University of Technology

Competing Pair-Breaking Effects in Thin Superconducting Films and Bulk Superconductivity

DISSERTATION

ausgeführt zum Zwecke der Erlangung des akademischen Grades eines Doktors der
Technischen Wissenschaften unter der Leitung von

a.o. Univ. Prof. Dr.techn. Herwig Michor

E138

Institut für Festkörperphysik

eingereicht an der Technischen Universität Wien

Fakultät für Physik

von

Dipl.-Ing. Sherryl Manalo

Matr.-Nr. 9325152

Halbgasse 25/8

1070 Wien

Wien, am 04. November 2011

Kurzfassung

Der Fulde-Ferrell-Larkin-Ovchinnikov (FFLO) Zustand ist ein räumlich inhomogener supraleitender Zustand bei dem vermutet wird, daß er in reinen Supraleitern mit rein paramagnetischer Paarbrechung auftritt. Wir vergleichen die Berechnungen des oberen kritischen Feldes mit experimentellen Ergebnissen des quasi-zwei-dimensionalen organischen Supraleiters κ -(BEDT-TTF)₂Cu(NCS)₂, die vermuten lassen, daß der FFLO Zustand in diesem Material existiert. Die Übereinstimmung zwischen Experiment und existierenden Theorien wurden erfolgreich sowohl in Bezug auf die Winkelabhängigkeit und das Temperaturverhalten des oberen kritischen Feldes untersucht.

Danach veralgemeinern wir das gängige Modell der rein paramagnetischen Paarbrechung für einen Supraleiter endlicher Dicke in einem Magnetfeld, der in beliebigem Winkel zur stromführenden Ebene steht. Wir formulieren das Modell im Rahmen der quasiklassischen Eilenberger Gleichungen und leiten thermodynamische Eigenschaften her. Diese neue Theorie der konkurrierenden spin und orbitaler Paarbrechungsmechanismen in reinen supraleitenden Filmen oder Schichten werden mit Hilfe von experimentellen Ergebnissen an YBa₂Cu₃O₇ und möglichen orbitalen paarbrechenden Einflüssen bei einem Magnetfeld in plan-paralleler Konfiguration diskutiert. Wir berücksichtigen auch den Einfluß von Verunreinigungen und vergleichen die Ergebnisse von Tunnelmessungen an einem dünnen Al Film mit den numerischen Berechnungen der oberen und unteren Stabilitätsgrenze eines Systems mit endlicher Dicke. Bei Temperaturen unterhalb der trikritischen Temperatur existieren zwei Phasengrenzen, deren Verhalten den experimentellen Ergebnissen näherkommen.

Diese Arbeit wird mit Untersuchungen an den konventionellen *s*-Wellen Supraleiter RbOs₂O₆ und La₃Ni₂B₂N_{3- δ} abgeschlossen. Wir untersuchen das obere kritische Feld $H_{c2}(T)$ des β -Pyrochlore Supraleiters RbOs₂O₆ im Rahmen der *s*-Wellen Eliashberg Theorie unter Berücksichtigung von Anisotropie und Streuzentren. Der Vergleich zwischen dem Experiment und den theoretischen Berechnungen der thermodynamischen Eigenschaften bestätigt, daß RbOs₂O₆ ein konventioneller *s*-Wellen Supraleiter ist. Neue Messungen an La₃Ni₂B₂N_{3- δ} zeigen eine Reduktion der kritischen Temperatur mit steigenden Stickstoff-Fehlstellen im Gitter. Diese Fehlstellen können als Streuzentren dienen, die die Anisotropie der Elektron-Phonon Kopplung verschmieren. Wir untersuchen den Zusammenhang zwischen der Reduktion der kritischen Temperatur T_c einerseits mit Hilfe von Streuung durch Verunreinigungen. Andererseits verwenden wir ein Einstein-Spektrum als Elektron-Phonon Kopplungsspektrum, mit dem wir die experimentelle kritische Temperatur durch Verschiebung des Mittelpunktes reproduzieren. Unsere Ergebnisse zeigen, dass der Effekt von Verunreinigungen zu schwach ist, um die T_c -Reduktion zu erklären. Die Verschiebung der Elektron-Phonon Kopplungsfrequenz liefert jedoch den ausschlaggebenden Beitrag zu diesem Phänomen.

Abstract

The Fulde-Ferrell-Larkin-Ovchinnikov (FFLO) state is a spatially inhomogeneous superconducting state predicted to occur in clean superconductors with purely paramagnetic limiting. We calculated the upper critical field and compared the results with measurements in the quasi-two-dimensional organic superconductor κ -(BEDT-TTF)₂Cu(NCS)₂, which strongly suggest that a state of the FFLO type exists in this material. Agreement between experiment and existing theories has been successfully checked both in view of the angle-dependence and the temperature dependence of the upper critical field.

We then generalized the usual model of purely paramagnetic pair breaking for a superconducting film of finite thickness in a magnetic field with an arbitrary angle to the conducting plane, taking into account the influence of a finite orbital pair breaking component on the FFLO state. The model was formulated using the framework of the quasiclassical Eilenberger equations, and thermodynamic properties were derived. This new theory of competing spin and orbital pair breaking in clean superconducting films or layers was discussed with the help of experimental results on YBa₂Cu₃O₇ and possible orbital pair breaking contributions in the plane-parallel field configuration. We also included impurity scattering in our equations and compared the tunneling measurements on a thin Al film with the numerical results on the upper and lower stability limit of a system with finite thickness. At temperatures below a tricritical temperature, the behaviour of the two boundary solutions for the critical field improved to meet the characteristics of the experimental data.

This work was concluded with investigations on conventional *s*-wave superconductors RbOs₂O₆ and La₃Ni₂B₂N_{3- δ} . We analyzed the upper critical field $H_{c2}(T)$ of the β -pyrochlore superconductor RbOs₂O₆ within the framework of *s*-wave Eliashberg theory including anisotropy and scattering effects. Comparison between experiment and theory of thermodynamic properties such as the specific-heat difference between superconducting and normal states $C_s - C_n$, and the thermodynamic critical field $H_c(T)$ confirms, that RbOs₂O₆ is a conventional *s*-wave superconductor. Results from our previous work already showed, that La₃Ni₂B₂N_{3- δ} is a conventional *s*-wave superconductor, which properties can be very well described with Eliashberg theory. Measurements on La₃Ni₂B₂N_{3- δ} show a decrease in the critical temperature with increasing vacancy on the nitrogen site. The nitrogen vacancies may act as scattering centers, which smear out the electron-phonon coupling anisotropy. We investigated the vacancy related T_c -depression both with respect to impurity scattering and with a model Einstein spectrum, by shifting the center of the δ -peak to reproduce the experimental T_c -values. Our results show, that the effect of additional scattering centers on anisotropy is too weak to explain the decrease in T_c . However, a shift of the electron-phonon pairing frequency yields the important contribution to this phenomenon.

Acknowledgement

Foremost, I want to express my appreciation and sincere gratitude to my supervisor Herwig Michor, who has supported me not only in the time of my Ph.D.-studies, but has accompanied my whole scientific history since the beginning of the second term. I thank him for his interest, time, effort and contributions to my thesis, as well as help in all the phases of my studies.

I also want to express my deepest gratitude towards Gerfried Hilscher, who encouraged me to take the last leap and finish my dissertation. He supported me over all these years since my first project work as a student and for gave the inspirational spark to my interest in magnetism and superconductivity. I also thank him for the valuable discussions, contributions to session talks and publications.

The supervision of Ulf Klein made it possible to work on the theoretical part of my dissertation in the first two chapters. His great knowledge on the theory of superconductivity gave essential contributions to these chapters. I want to express my gratitude for his patience, fairness, valuable guidance and discussions.

Ewald Schachinger has inspired me to look into the theory of superconductivity while I was working on my diploma. Until now, the fascination for this field of physics has not weakened. His support, guidance and contributions refined several important aspects of my work, for which I am very grateful.

I also thank Raimund Podloucky for evaluating my thesis, and other special people who made important contributions and various valuable discussions that enabled me to finish my work. Our joint publication on RbOs_2O_6 was done in cooperation with Markus Brühwiler and Bertram Batlogg. Without the thesis and experimental data of Tahir Ali, it would not have been possible to analyze the T_c -depression in $\text{La}_3\text{Ni}_2\text{B}_2\text{N}_x$. Transport studies on $\text{La}_3\text{Ni}_2\text{B}_2\text{N}_{3-\delta}$ were made possible by Ernst Bauer and his team. Support during my experimental work on preparing boronitride materials was given by Herbert Sassik and Peter Hundegger on occasion.

My current employer Microsoft has sharpened my competencies beyond the scientific range in the past 4 years. Being in the company would not have been this exciting, challenging and fun if not for the people who I work with. I want to thank them for their support, friendship and for encouraging me to develop my strengths and taking on challenges.

Best comes last, I thank my beloved husband Markus Brehmer for the past seven years of our time together. He has strengthened my emotional foundation on which I can take on all the things I have done and still want to do. Let us discover more of this world!

Contents

| | |
|--|-----------|
| Introduction | 13 |
| 1 Upper critical field H_{c2} of a 2d superconductor | 17 |
| 1.1 Derivation of the linearized gap-equation | 19 |
| 1.2 Calculation of the H_{c2} -equations for different pairing symmetries | 21 |
| 1.2.1 s -wave symmetry | 22 |
| 1.2.2 d -wave symmetry | 24 |
| 1.3 Phase diagrams | 29 |
| 1.3.1 s -wave | 30 |
| 1.3.2 d -wave | 31 |
| 1.4 Comparison with experiment | 40 |
| 2 Layered superconductors with finite thickness d | 47 |
| 2.1 Derivation of the Gap-equation | 48 |
| 2.1.1 Eigenfunctions $f_{\mathbf{k},\mathbf{p}}(\mathbf{r})$ | 49 |
| 2.1.2 Calculation of the Green's function $f_{(+)}(\mathbf{r})$ | 50 |
| 2.1.3 Equivalence to the z -independent formalism | 52 |
| 2.1.4 Green's function $f_{(-)}(\mathbf{r})$ | 53 |
| 2.1.5 Averaged functions | 54 |
| 2.1.6 Gap-equation | 54 |
| 2.1.7 Gap equation for s -wave symmetry | 55 |
| 2.1.8 Gap equation for d -wave symmetry | 57 |
| 2.2 Phase boundaries for s -wave symmetry | 59 |
| 2.2.1 Limit of a plane-parallel magnetic field | 65 |
| 2.2.2 h_{c2} in the limit $\vartheta \rightarrow 0$: FFLO critical field | 71 |
| 2.3 Thermodynamic properties | 76 |
| 2.3.1 Quasiclassical equations in the limit $d \rightarrow 0$ or the BCS state | 77 |
| 2.3.2 Equations in the d -wave case | 79 |
| 2.3.3 Phase boundary diagrams | 80 |
| 2.3.4 Finite thickness equations | 86 |
| 2.3.5 Phase boundary analysis and numerical results for $d > 0$ | 89 |

| | | |
|----------|--|------------|
| 2.3.6 | Discussion on pair-breaking effects in $\text{YBa}_2\text{Cu}_3\text{O}_7$ | 97 |
| 2.4 | System with impurities | 98 |
| 2.4.1 | Gap equation | 100 |
| 2.4.2 | Stability limits | 101 |
| 2.4.3 | Comparison of numerical results with Al experimental data | 102 |
| 3 | Bulk superconductivity | 109 |
| 3.1 | Eliashberg Theory | 109 |
| 3.1.1 | Thermodynamic properties | 110 |
| 3.1.2 | Upper critical field | 110 |
| 3.1.3 | Impurity scattering | 113 |
| 3.1.4 | Optimal spectrum | 113 |
| 3.2 | Thermodynamic properties of RbOs_2O_6 analyzed within Eliashberg theory | 115 |
| 3.2.1 | Introduction | 115 |
| 3.2.2 | Spectral function | 116 |
| 3.2.3 | Results | 118 |
| 3.3 | Analysis of the T_c reduction in $\text{La}_3\text{Ni}_2\text{B}_2\text{N}_{3-\delta}$ | 124 |
| 3.3.1 | Do N site vacancies act as scattering centers? | 125 |
| 3.3.2 | Shift in phonon modes: Analysis with an Einstein spectrum | 127 |
| 3.3.3 | Conclusion | 131 |
| A | Units and summary of equations | 141 |
| A.1 | Equations in units used in the numerical calculations | 141 |
| A.1.1 | Upper critical field at $d = 0$ | 142 |
| A.1.2 | Upper critical field at $d > 0$ | 142 |
| A.2 | Equations in Eilenberger units | 144 |
| A.2.1 | Upper critical field at $d = 0$ | 145 |
| A.2.2 | Upper critical field at $d > 0$ | 146 |
| B | Detailed calculations to chapter 2 | 149 |
| B.1 | A different way to calculate $f_{(+)}(\mathbf{r})$ | 149 |
| B.2 | Periodicity in the p_z -direction | 151 |
| B.3 | Critical field for $\kappa_\perp \rightarrow 0$ | 152 |
| C | Notes on the equations in Chapter 3 | 155 |
| C.1 | Ad 2.3.1, Derivation of the gap-equation for $d = 0$ | 155 |
| C.2 | Ad 2.3.1, The free-energy equation for $d = 0$ | 156 |
| C.3 | Ad 2.3.4, gap equation for $d \geq 0$ | 156 |
| C.4 | Ad 2.3.4, free energy difference for $d \geq 0$ | 157 |
| D | Eigenfunctions of the Hamiltonian | 159 |

| | | |
|-------|---|-----|
| D.1 | Landau gauge | 159 |
| D.1.1 | Quasi-periodic solutions | 161 |
| D.2 | Symmetric gauge | 163 |
| D.2.1 | Orbit center representation | 164 |
| D.2.2 | Angular momentum representation | 164 |

Introduction

In the wake of classical papers by Clogston [1] and Chandrasekhar [2], where only spin pair breaking was considered and the orbital component was assumed to be negligibly small, most theoretical studies neglected paramagnetic pair breaking in superconductors. A notable exception is the dirty limit theory developed by Maki [3], Fulde [4] and others. In several experiments, on the other hand, both pair breaking components are present and the neglect of the orbital contribution is not really justified. In the past years, ultra-thin films became available and several new classes of layered superconducting compounds have been discovered. For applied field parallel to the films [5] or conducting planes [6], Pauli paramagnetism can be the dominating pair breaking effect, provided the conducting layers are sufficiently separated from each other or the thickness of the films is sufficiently small. In many of these compounds, including high- T_c cuprates and organic superconductors, impurity scattering and spin-orbit coupling is small and orbital pair breaking is - for an applied field parallel to the planes - the most important second order effect, next to the spin effect, to be taken into account.

The focus of Chapter 1 is the Fulde-Ferrell-Larkin-Ovchinnikov (FFLO) state [7, 8], which is a spatially inhomogeneous superconducting state, predicted to occur in clean superconductors with purely paramagnetic limiting. Critical field measurements in the quasi-two-dimensional organic superconductor κ -(BEDT-TTF)₂Cu(NCS)₂ strongly suggest that a state of the FFLO type exists in this material; agreement between experiment [9] and existing theories has been successfully checked [10] both in view of the angle-dependence [11] and the temperature dependence [12] of the upper critical field [13]. Apparently, this is the first time since the original predictions in 1964 [7, 8] that quantitative agreement between theory and experiment with regard to the FFLO phase boundary has been established.

Strong paramagnetic effects can also be expected for the high- T_c cuprate superconductors at low temperatures, when the conducting planes in adjacent unit cells are well separated from each other. A measurement [6, 14] at $T = 1.6$ K in YBa₂Cu₃O₇ indicates rather clearly that the superconducting state is paramagnetically limited but, on the other hand, the observed transition is too broad to allow a decision between the FFLO state and the homogeneous superconducting state. A measure of the relative strength of orbital and paramagnetic pair

breaking is the ratio of the paramagnetic critical field H_p divided by the orbital upper critical field H_{c2} of a type II superconductor. In a thin superconducting layer of thickness $d < \xi_0$, where ξ_0 is the coherence length of BCS theory, the orbital critical field $H_c(d)$ is increased by a factor of ξ_0/d and the corresponding ratio is given by [15]

$$\frac{H_p}{H_c(d)} \sim \frac{d}{k_F^{-1}}$$

A small transverse dimension $d \ll \xi_0$ of the film suppresses the orbital effect and enlarges the spin effect drastically. However, this equation also shows, that the critical thickness which separates the spin pair-breaking and orbital pair-breaking dominated regimes is still of the order of an atomic distance. Thus, the above estimate, which is confirmed by more quantitative calculations to be presented in this work, indicates that a nearly perfect two-dimensional situation is required in order to justify the neglect of orbital pair breaking contribution in clean superconductors. The situation in dirty superconductors is much more favorable for the spin effect. The FFLO state, however, is suppressed by impurities.

In Chapter 2, we investigate a superconducting film of *finite thickness* in a magnetic field parallel and with arbitrary angles ϑ to the conducting plane. Thus, the usual model of purely paramagnetic pair breaking is generalized in a different way, taking into account the influence of a finite orbital pair breaking component on the FFLO state. The model is formulated in the first part of this Chapter, using the framework of the quasiclassical Eilenberger equations, and thermodynamic properties are derived. This new theory of competing spin and orbital pair breaking in clean superconducting films or layers is discussed with the help of experimental results on $\text{YBa}_2\text{Cu}_3\text{O}_7$ and possible orbital pair breaking contributions in the plane-parallel field configuration [15]. To conclude this Chapter, we included impurity scattering in our equations and compared the tunneling measurements of Ref. [5] on a thin Al film with the numerical results on the upper and lower stability limit of a system with finite thickness. At temperatures below a tricritical temperature, the behaviour of the two boundary solutions for the critical field improves to meet the characteristics of the experimental data.

For a bulk superconductor in the clean limit, on the other hand, the ratio of the paramagnetic critical field H_p divided by the orbital upper critical field H_{c2} can be written as

$$\frac{H_p}{H_{c2}} \sim \frac{\xi_0}{k_F^{-1}}$$

in terms of the Fermi wavelength k_F . This relation implies that orbital pair breaking will always be the dominating mechanism in bulk superconductors, no matter how large the Ginzburg-Landau (GL) parameter κ is. This holds in the framework of conventional BCS and related theories. Conventional superconductors are well described by Eliashberg theory [16] which treats superconductivity as a boson-exchange phenomenon. The dominant feature of this theory is the electron-phonon interaction spectral function $\alpha^2F(\omega)$ which can

be determined from tunneling experiments [17] or theoretically from band structure calculations. Using such an $\alpha^2 F(\omega)$ within Eliashberg theory allows to reproduce the superconducting properties of a conventional superconductor within experimental accuracy and this established the phonons as the exchange boson between the two charge carriers building the Cooper pair in conventional superconductors. In Chapter 3, the upper critical field $H_{c2}(T)$ of the β -pyrochlore superconductor RbOs_2O_6 is analyzed within the framework of s -wave Eliashberg theory including anisotropy and scattering effects. Experimental data on thermodynamic properties such as the specific-heat difference between superconducting and normal states $C_s - C_n$, and the thermodynamic critical field $H_c(T)$ align with the results from the upper critical field analysis [18, 19].

We already concluded from previous work, that $\text{La}_3\text{Ni}_2\text{B}_2\text{N}_{3-\delta}$ is a conventional s -wave superconductor, which properties can be very well described with Eliashberg theory [20, 21]. Measurements on $\text{La}_3\text{Ni}_2\text{B}_2\text{N}_{3-\delta}$ show a decrease in the critical temperature with increasing vacancy on the nitrogen site [22]. The nitrogen vacancies may act as scattering centers, which reduce the effect of the electron-phonon coupling anisotropy. We investigated the vacancy related T_c -depression both with respect to impurity scattering and with a model Einstein spectrum, by shifting the center of the δ -peak. The consistency of our calculations were then checked with the ability of the theory to describe the experimental data on the upper critical field $H_{c2}(T)$, which is very sensitive to changes in anisotropy and impurity scattering. Our results show, that the effect of the additional scattering centers on anisotropy is too weak to explain the decrease in T_c . However, a shift of the electron-phonon pairing frequency may give the important contribution to this phenomenon. We achieved an excellent agreement between theoretical predictions and experiment over the whole temperature range for $H_{c2}(T)$ and for all investigated samples of $\text{La}_3\text{Ni}_2\text{B}_2\text{N}_x$ with varying x .

Chapter 1

Upper critical field H_{c2} of a 2d superconductor

Superfluid phases with unequal numbers of particles forming Cooper pairs have been the focus of interest for many years [23]. Of particular interest was the prediction of Fulde and Ferrell [7] and by Larkin and Ovchinnikov [8] in 1964 (the FFLO state) that at low temperatures, superfluid states with spontaneously broken translational symmetry should form. These FFLO states have been under theoretical investigation including metals [24, 25], ultra-cold atoms [26], nuclear matter and dense quark systems [27, 28].

Due to the formation of Cooper pairs the susceptibility of the superconductor is reduced compared to the normal state. For high differences in the chemical potentials the polarized normal state has a lower energy than the superconducting phase. Qualitatively, the transition from the paired superconducting to the polarized normal phase will occur when the polarization energy equals the condensation energy of the Cooper pairs. This condition defines the limiting chemical potential mismatch $\delta\mu_c(T)$ beyond which homogeneous superconductivity will not exist. The low-temperature limit $\delta\mu_c(0)$ for a conventional superconductor was first given by Chandrasekhar [2] and Clogston [1] and the $\delta\mu$ vs. T phase diagram for homogeneous superconductors was studied in detail by Sarma [29]. In addition to the normal phase and the homogeneous superconductor, he considered a compromise state which embodies ‘phase separation in momentum space’. The breached-pair (BP) states [30] are characterized by the coexistence of paired superfluid and normal polarized components which reside in different regions of momentum space. Unfortunately, these gapless states turn out to be unstable in the ‘classical’ situation of a superconductor in an external magnetic field acting on the spins of the electrons. The interest in BP states, however, has been recently rekindled since they could be realized in dense quark systems or ultra-cold atoms. FFLO predicted a spatially inhomogeneous partially gapped compromise state with both paired superfluid and normal polarized regions to be the stable ground state in a (narrow) range above the Chandrasekhar-Clogston

limit.

The idea of forming a textured state with paired and normal regions closely parallels the concept of the vortex phase which appears in type-II superconductors below the upper critical field. This phase gains its stability from the fact that it allows magnetic flux to penetrate into the superconductor. Like the FFLO state, it was predicted theoretically by Abrikosov [31]. Shortly afterwards, it was confirmed by numerous experiments employing a variety of techniques. Although the existence of inhomogeneous compromise states in imbalanced superfluids seems plausible, despite intensive search, these states have not yet been identified unambiguously. There are, however, indications that they are realized in some highly anisotropic materials.

There are several reasons for the difficulties in the experimental observation. First, the FFLO state requires very stringent conditions which strongly restrict the appropriate classes of superconducting materials. Soon after the FFLO phases were predicted, it became clear that impurities act as pair breakers suppressing the corresponding transition temperatures [32]. A necessary criterion for the realization of the FFLO state is a long mean-free path exceeding the superconducting coherence length. An additional technical difficulty encountered in metals is related to the fact that electrons are charged particles. An external magnetic field required to create the imbalance in the conduction electron system will inevitably act on their orbits and suppress superconductivity. To observe imbalance-induced high-field phases the orbital pair-breaking must be strongly reduced as pointed out by Maki [32]. The early search for the FFLO phases concentrated on thin superconducting films in parallel magnetic fields [4]. Although polarization effects were clearly seen, it was not possible to stabilize the FFLO state. Promising candidates are recently discovered heavy-fermion compounds and layered organic superconductors as we will discuss in this work. Second, there are no simple criteria which could help to identify the phases. The order parameter as such is a quantum mechanical object and hence cannot be observed directly. The generally accepted procedure in this situation is to calculate observable properties which depend on the order parameter and hence reflect its structure. It turns out, however, that the properties of FFLO states are non-universal depending sensitively on the normal state, i.e. the dispersion of quasiparticles and their interactions. The latter strongly affect the transition line separating the normal and superfluid phases as well as the order of phase transitions. In addition, the anisotropy of the order parameter in the homogeneously balanced phase which is related to the presence or absence of low-energy excitations plays an important role.

Favourable conditions for observing the FFLO state are found in clean superconductors with orbital critical fields much larger than the Pauli limiting field H_p . In practice, it seems always necessary to reduce the orbital pair-breaking effect by using layered superconductors with nearly decoupled planes or extremely thin films (quasi-two-dimensional superconductors) and

applying the magnetic field in a direction parallel to the conducting planes. Several classes of superconducting materials with favourable conditions for observing the FFLO state do exist. These include the classical intercalated transition metal dichalcogenides as well as more exotic materials like high- T_c compounds and organic superconductors. Experimental data of the organic d -wave superconductor κ -(BEDT-TTF) $_2$ Cu(NCS) $_2$ with almost 2d electronic structure show good agreement with the numerical results for the upper critical field H_{c2} of a two dimensional superconductor, derived from the linearized gap equation of Eilenberger's theory [33], as was done by Bulaevskii [34], Shimahara and Rainer [11]. This confirms the previous assumptions, that this material could indeed be a FFLO superconductor [10]. For TaS $_2$ -pyridine, which has s -wave pairing symmetry, the results of the theory for the upper critical field as function of the off-plane field angle align well with the experimental data.

In the next section, the s - and d -wave linearized gap equations are derived from Eilenberger's [33] quasiclassical equations of superconductivity to calculate the upper critical field H_{c2} in Section 1.2. Phase diagrams are shown in Section 1.3 and are compared to experimental results in Section 1.4.

1.1 Derivation of the linearized gap-equation

The microscopic theory of superconductivity by Bardeen, Cooper, and Schrieffer (BCS) is established as one of the most popular theories in condensed matter physics. Even though it is based on a simplified model and is used to describe weakly coupled homogeneous superconductors in the clean limit, it gives surprisingly good description of many properties of superconductors. With the formulation in terms of the Green functions by Gorkov, the BCS model grew into a highly powerful theory of superconductivity. Eilenberger [33] generalized the model by describing a weakly coupled superconductor in a spatially inhomogeneous state, with a pairing potential $\Delta(\mathbf{r})$. As Anderson's Theorem of negligible scattering effects is only valid in the homogeneous state, Eilenberger also introduced a non-zero impurity potential $V(\mathbf{r})$ to account for effects due to impurity scattering.

To calculate the equations for the upper critical field, we must first derive the linearized gap equation from the quasiclassical equations of superconductivity. We consider the isotropic, weak-coupling and time-independent version of Eilenberger's theory [33] without the 'impurity potentials', consisting of three differential equations for the components $f_{(+)}$, $f_{(-)}$ and $g_{(+)}$ of the matrix Green's function \hat{g}

$$\begin{aligned} \left[2(\omega_l - i\mu H) + \hbar \mathbf{v}_{\mathbf{F}} \partial_{\mathbf{r}}\right] f_{(+)} &= 2\Delta g_{(+)} \\ \left[2(\omega_l - i\mu H) - \hbar \mathbf{v}_{\mathbf{F}} \partial_{\mathbf{r}}^*\right] f_{(-)}^+ &= 2\Delta^* g_{(+)} \\ g_{(+)} &= \sqrt{1 - f_{(+)} f_{(-)}^+}, \end{aligned} \quad (1.1)$$

with the order parameter Δ , the Fermi velocity $\mathbf{v}_{\mathbf{F}}$, the electron magnetic moment $\mu =$

$g_L\mu_B/2$ (g_L is Lande's factor and $\mu_B = \hbar|e|/(2mc)$ Bohr's magneton), and the magnetic field strength $H = |\mathbf{H}|$. Vectors are denoted in bold font. The differential operator $\partial_{\mathbf{r}}$ is given by

$$\partial_{\mathbf{r}} = \nabla_{\mathbf{r}} - i\frac{2e}{\hbar c}\mathbf{A} \quad (1.2)$$

with the vector potential \mathbf{A} . The Green's functions $f_{(+)}$, $f_{(-)}$ and $g_{(+)}$ and the order parameter Δ are functions of the spatial coordinate \mathbf{r} , the unit vector \hat{k} in the direction of the particle momentum and the Matsubara frequency ω_l

$$\omega_l = (2l + 1)\pi k_B T \quad l = 0, \pm 1, \pm 2, \dots \quad (1.3)$$

The Fermi surface is assumed to be cylindrical and to lie in xy -plane. In this case the Fermi velocity $\mathbf{v}_{\mathbf{F}}$ is given by

$$\mathbf{v}_{\mathbf{F}} = v_F \begin{pmatrix} \cos \varphi \\ \sin \varphi \\ 0 \end{pmatrix}. \quad (1.4)$$

The gap equation is linearized by giving the Green's function $g_{(+)}$ its normal-state solution

$$g_{(+)} = \text{sgn}\omega_l,$$

instead of taking the full normalization condition in eq. (1.1). In order to calculate the gap function $\Delta(\mathbf{r}, \hat{k})$, the operator Q is introduced

$$Qf_{(+)}(\mathbf{r}, \hat{k}, l) = 2\Delta(\mathbf{r}, \hat{k})\text{sgn}\omega_l. \quad (1.5)$$

It follows from equation (1.1)

$$\begin{aligned} Q &= 2(\omega_l - i\mu H) + \hbar\mathbf{v}_{\mathbf{F}}\partial_{\mathbf{r}} \\ &= \text{sgn}\omega_l \left[2(|\omega_l| - i\mu H\text{sgn}\omega_l) + \text{sgn}\omega_l\hbar\mathbf{v}_{\mathbf{F}}\partial_{\mathbf{r}} \right], \end{aligned} \quad (1.6)$$

and because no eigenvalues of Q are null, Q^{-1} exists

$$Q^{-1} = \frac{1}{\text{sgn}\omega_l} \left[2(|\omega_l| - i\mu H\text{sgn}\omega_l) + \text{sgn}\omega_l\hbar\mathbf{v}_{\mathbf{F}}\partial_{\mathbf{r}} \right]^{-1}. \quad (1.7)$$

Therefore, with the application of Q^{-1} to eq. 1.5 we can write

$$\begin{aligned} f_{(+)}(\mathbf{r}, \hat{k}, l) &= 2 \int_0^\infty dx \exp(-x[2(|\omega_l| - i\mu H\text{sgn}\omega_l) + \text{sgn}\omega_l\hbar\mathbf{v}_{\mathbf{F}}\partial_{\mathbf{r}}]) \Delta(\mathbf{r}, \hat{k}) \\ f_{(-)}(\mathbf{r}, \hat{k}, l) &= 2 \int_0^\infty dx \exp(-x[2(|\omega_l| + i\mu H\text{sgn}\omega_l) - \text{sgn}\omega_l\hbar\mathbf{v}_{\mathbf{F}}\partial_{\mathbf{r}}]) \Delta(\mathbf{r}, \hat{k}) \end{aligned} \quad (1.8)$$

as integration over an inverse energy spectrum for the formal solutions for the Green's functions $f_{(+)}$ and $f_{(-)}$, and the gap-function is given by

$$\Delta = \pi\lambda N(E_F)k_B T \sum_{l=0}^N \int_0^{2\pi} \frac{d\varphi'}{2\pi} (f_{(+)} + f_{(-)}). \quad (1.9)$$

with N , the cutoff-index corresponding to the highest or Debye-frequency $\omega_D = \pi k_B T(2N+1)$ of the excitations and the coupling factor λ . Eq. (1.8) and (1.9) yield the self-consistency relation for the order parameter

$$\Delta(\mathbf{r}, \hat{k}) = 2\pi\lambda N(E_F)k_B T \sum_{l=0}^N \int_0^{2\pi} \frac{d\varphi'}{2\pi} \int_0^\infty dx e^{-2x\omega_l} V(\hat{k}, \hat{k}') \times \\ \left(\exp(2ix\mu H - x\hbar\mathbf{v}_{\mathbf{F}}'\partial_{\mathbf{r}}) + \exp(-2ix\mu H + x\hbar\mathbf{v}_{\mathbf{F}}'\partial_{\mathbf{r}}) \right) \Delta(\mathbf{r}, \hat{k}') \quad (1.10)$$

which can be transformed further by using the sum of the geometric series

$$\sum_{k=0}^n z^k = \frac{z^{n+1} - 1}{z - 1} \quad (1.11)$$

and approximating $\pi k_B T(2N+2) \simeq \pi k_B T(2N+1) = \omega_D$ for large values of N . With the substitutions $s = 2x$, $h = \mu H$ and by replacing $\partial_{\mathbf{r}}$ with the canonical momentum $\Pi = \hbar\partial_{\mathbf{r}}/i$ the linearized gap-equation is obtained

$$\Delta(\mathbf{r}, \hat{k}) = \pi\lambda N(E_F)k_B T \int_0^{2\pi} \frac{d\varphi'}{2\pi} V(\hat{k}, \hat{k}') \int_0^\infty ds \frac{1 - e^{-s\omega_D}}{\sinh(\pi k_B T s)} \times \\ \cos\left[s\left(h - \frac{\mathbf{v}_{\mathbf{F}}\Pi}{2}\right)\right] \Delta(\mathbf{r}, \hat{k}'). \quad (1.12)$$

1.2 Calculation of the H_{c2} -equations for different pairing symmetries

The magnetic field H is assumed to lie in the yz -plane

$$\mathbf{H} = \begin{pmatrix} 0 \\ H_{\parallel} \\ H_{\perp} \end{pmatrix} = H \begin{pmatrix} 0 \\ \cos\vartheta \\ \sin\vartheta \end{pmatrix}, \quad (1.13)$$

and the vector potential is given by

$$\mathbf{A} = \begin{pmatrix} H_{\parallel}z - H_{\perp}y \\ 0 \\ 0 \end{pmatrix} \quad (1.14)$$

with an appropriate gauge. The components of the canonical momentum $\Pi = \hbar\partial_{\mathbf{r}}/i$ are

$$\Pi_x = \frac{\hbar}{i} \frac{\partial}{\partial x} - \kappa_{\perp}y \quad \text{and} \quad \Pi_y = \frac{\hbar}{i} \frac{\partial}{\partial y}, \quad (1.15)$$

with $\kappa_{\perp} = 2|e|H_{\perp}/c$ and $\kappa_{\parallel} = 2|e|H_{\parallel}/c$. Because of the commutation relation $[\Pi_x, \Pi_y] = \hbar\kappa_{\perp}/i$ we are able to introduce annihilation and creation operators η and η^+

$$\eta = \frac{1}{\sqrt{2\hbar\kappa_{\perp}}}(\Pi_x - i\Pi_y) \quad \eta^+ = \frac{1}{\sqrt{2\hbar\kappa_{\perp}}}(\Pi_x + i\Pi_y), \quad (1.16)$$

which satisfy the relation $[\eta, \eta^+] = 1$. The components of the canonical momentum expressed with these operators are

$$\Pi_x = \sqrt{\frac{\kappa_\perp \hbar}{2}}(\eta + \eta^+) \quad \Pi_y = i\sqrt{\frac{\kappa_\perp \hbar}{2}}(\eta - \eta^+) \quad (1.17)$$

and the operator $\eta^+ \eta$ is given by

$$\eta^+ \eta = \frac{1}{2\hbar\kappa_\perp}(\Pi_x^2 + \Pi_y^2) - \frac{1}{2}. \quad (1.18)$$

The hamiltonian $H_0 = \Pi^2/2m = \Pi^2/4m_e$ is constructed out of $\eta^+ \eta$

$$H_0 = \hbar\omega\left(\eta^+ \eta + \frac{1}{2}\right) \quad \text{with} \quad \omega = \frac{1}{2\hbar\kappa_\perp}, \quad (1.19)$$

which is equivalent to the hamilton operator of the harmonic oscillator. Therefore, the eigenfunctions of the hamiltonian Φ_n are obtained from the eigenfunction Φ_0 by applying the creation operator n -times on the ground state

$$|\Phi_n\rangle = \frac{1}{\sqrt{n!}}(\eta^+)^n |\Phi_0\rangle, \quad (1.20)$$

while Φ_0 is calculated from the differential equation $\eta|\Phi_0\rangle = 0$. As in the case of the harmonic oscillator the application of the operators η and η^+ on Φ_n yield

$$\eta^+ |\Phi_n\rangle = \sqrt{n+1} |\Phi_{n+1}\rangle \quad \text{and} \quad \eta |\Phi_n\rangle = \sqrt{n} |\Phi_{n-1}\rangle. \quad (1.21)$$

The derivation of the eigenfunctions is given in Appendix D.1. To further simplify the linearized gap-equation (1.12) the pairing interaction $V(\hat{k}, \hat{k}')$ is approximated by $V(\hat{k}, \hat{k}') = -\gamma_\alpha(\hat{k})\gamma_\alpha(\hat{k}')$. The gap-function is also assumed to be separable $\Delta(\mathbf{r}, \hat{k}) = \Delta_\alpha(\mathbf{r})\gamma_\alpha(\hat{k})$ and we obtain with eq. (1.17) the linearized gap-equation

$$\begin{aligned} -\ln\left(\frac{T}{T_c^{(0)}}\right)\Delta_\alpha(\mathbf{r}) &= \pi k_B T \int_0^\infty ds \frac{1}{\sinh(\pi k_B T s)} \int_0^{2\pi} \frac{d\varphi'}{2\pi} \gamma_\alpha(\hat{k}')^2 \times \left[1 - \right. \\ &\quad \left. \cos\left(hs - \frac{1}{2}sv_F \sqrt{\frac{\hbar\kappa_\perp}{2}}(e^{i\varphi'}\eta + e^{-i\varphi'}\eta^+)\right)\right] \Delta_\alpha(\mathbf{r}), \end{aligned} \quad (1.22)$$

where $k_B T_c^{(0)} = 2e^\gamma \pi^{-1} \hbar \omega_D e^{-1/\lambda N(E_F)}$ is the zero-field transition temperature with Euler's constant $\gamma \simeq 0.57721$.

1.2.1 s -wave symmetry

The symmetry function $\gamma_s(\hat{k}')^2$ is 1 for s -wave superconductors. With the relation

$$\cos(A \pm B) = \cos(A)\cos(B) \mp \sin(A)\sin(B) \quad (1.23)$$

the cosine-term in eq.(1.22) translates to

$$\begin{aligned} \cos\left(hs - \frac{1}{2}sv_F\sqrt{\frac{\hbar\kappa_\perp}{2}}(e^{i\varphi'}\eta + e^{-i\varphi'}\eta^+)\right) = \\ \cos(hs)\cos(v e^{i\varphi'}\eta + v e^{-i\varphi'}\eta^+) - \sin(hs)\sin(v e^{i\varphi'}\eta + v e^{-i\varphi'}\eta^+), \end{aligned} \quad (1.24)$$

and $v = v_F s \sqrt{\hbar\kappa_\perp/2}/2$. The sine-term on the right hand side of eq.(1.24) vanishes after the φ' -integration. Now the cosine of the creation and annihilation operators η and η^+ is transformed into exponential functions

$$\cos(v e^{i\varphi'}\eta + v e^{-i\varphi'}\eta^+) = \frac{1}{2}\left(e^{iv(e^{i\varphi'}\eta + e^{-i\varphi'}\eta^+)} + e^{-iv(e^{i\varphi'}\eta + e^{-i\varphi'}\eta^+)}\right) \quad (1.25)$$

and the Hausdorff-formula

$$e^{(\alpha+\beta)} = e^\alpha e^\beta e^{[\alpha,\beta]/2} \quad (1.26)$$

is applied with the substitutions $\alpha = v i e^{i\varphi'}\eta$ and $\beta = v i e^{-i\varphi'}\eta^+$. The commutation relation $[\alpha, \beta]$ with $[\eta, \eta^+] = 1$ results in

$$[\alpha, \beta] = -\frac{v^2}{2} \quad (1.27)$$

and the integration over the cosine term can be written as

$$\begin{aligned} \int_0^{2\pi} \frac{d\varphi'}{2\pi} \cos((\alpha + \beta)/i) &= e^{-\frac{v^2}{2}} \sum_{m=0}^{\infty} \sum_{l=0}^{\infty} \int_0^{2\pi} \frac{d\varphi'}{2\pi} \frac{1}{2} \left(\frac{\alpha^l \beta^m}{l!m!} + \frac{(-\alpha)^l (-\beta)^m}{l!m!} \right) \\ &= e^{-\frac{v^2}{2}} \sum_{m=0}^{\infty} \sum_{l=0}^{\infty} \int_0^{2\pi} \frac{d\varphi'}{2\pi} \frac{1}{2} (i^{l+m} + (-i)^{l+m}) \frac{1}{l!m!} v^{l+m} \\ &\quad \times \eta^{+l} \eta^m e^{i\varphi'(m-l)} \end{aligned} \quad (1.28)$$

after applying the sum-rule for the exponential functions. It can be clearly shown that

$$\int_0^{2\pi} \frac{d\varphi'}{2\pi} e^{i\varphi'(m-l)} = \delta_{l,m} = \begin{cases} 1 & l = m \\ 0 & l \neq m \end{cases} \quad (1.29)$$

with the Kronecker- δ , which is 1 for $l = m$ and null otherwise. Therefore, eq.(1.28) reduces to

$$\sum_{l=0}^{\infty} \frac{(-1)^l}{l!^2} v^{2l} \eta^{+l} \eta^l e^{-\frac{v^2}{2}}, \quad (1.30)$$

because all terms with unequal powers in η and η^+ were eliminated by the φ' -integration. The linearized gap-equation (1.22) becomes

$$-\ln\left(\frac{T}{T_c^{(0)}}\right)\Delta_s(\mathbf{r}) = \pi k_B T \int_0^\infty ds \frac{1}{\sinh(\pi k_B T s)} \left\{ 1 - \cos(hs) e^{-s^2 v_F^2 \hbar \kappa_\perp / 16} \right.$$

$$\times \sum_{l=0}^{\infty} \frac{(-1)^l}{l!^2} \left(\frac{s^2 v_F^2 \hbar \kappa_{\perp}}{8} \right)^{2l} \eta^{+l} \eta^l \} \Delta_s(\mathbf{r}). \quad (1.31)$$

For s-wave pairing the gap function $\Delta_s(\mathbf{r})$ has to be proportional to one of the eigenfunctions $\Phi_n(\mathbf{r})$. The annihilation operators η^l applied to $|\Phi_n\rangle$ give

$$\begin{aligned} \eta^l |\Phi_n\rangle &= \sqrt{\frac{n!}{(n-l)!}} |\Phi_{n-l}\rangle \\ \eta^n |\Phi_n\rangle &= \sqrt{n!} |\Phi_0\rangle \\ \eta |\Phi_0\rangle &= 0 \end{aligned} \quad (1.32)$$

resulting in

$$\langle \Phi_{n'} | \eta^{+l} \eta^l | \Phi_n \rangle = \sqrt{\frac{n!n!}{(n-l)!(n'-l)!}} \delta_{n,n'}. \quad (1.33)$$

The eigenfunctions $\langle \Phi_{n'} |$ and $|\Phi_n\rangle$ applied to the left and to the right of eq.(1.31) finally results in the equation for the upper critical field

$$\begin{aligned} -\ln\left(\frac{T}{T_c^{(0)}}\right) &= \pi k_B T \int_0^{\infty} ds \frac{1}{\sinh(\pi k_B T s)} \left(1 - \cos(hs) e^{-s^2 v_F^2 \hbar \kappa_{\perp} / 16} \right. \\ &\quad \times \left. \sum_{l=0}^n \frac{(-1)^l n!}{l!^2 (n-l)!} \left(\frac{s^2 v_F^2 \hbar \kappa_{\perp}}{8} \right)^l \right). \end{aligned} \quad (1.34)$$

For fixed temperatures T and angles ϑ_H , the upper critical field is the largest H given by eq.(1.34) for a certain quantum number n . The corresponding equation in Eilenberger units can be found in Appendix A, equation (A.29).

1.2.2 d-wave symmetry

Because of $\gamma_d(\hat{k}') = \sqrt{2}(\hat{k}_x'^2 - \hat{k}_y'^2)$, with $k'_x = \cos(\varphi')$ and $k'_y = \sin(\varphi')$, the symmetry function $\gamma_d(\hat{k}')^2$ is given by $1 + \cos(4\varphi')$ for d-wave superconductors. The linearized gap-equation (1.22) can be split into two parts, one containing the φ' -dependence of the symmetry function $\gamma_d(\hat{k}')^2$

$$\begin{aligned} &\pi k_B T \int_0^{\infty} ds \frac{1}{\sinh(\pi k_B T s)} \times \\ &\int_0^{2\pi} \frac{d\varphi'}{2\pi} \cos(4\varphi') \left[1 - \cos\left(hs - \frac{1}{2} s v_F \sqrt{\frac{\hbar \kappa_{\perp}}{2}} (e^{i\varphi'} \eta + e^{-i\varphi'} \eta^+) \right) \right] \end{aligned} \quad (1.35)$$

and the other part is the same as in the s-wave case

$$\pi k_B T \int_0^{\infty} ds \frac{1}{\sinh(\pi k_B T s)} \times$$

$$\int_0^{2\pi} \frac{d\varphi'}{2\pi} \left[1 - \cos \left(hs - \frac{1}{2} s v_F \sqrt{\frac{\hbar \kappa_{\perp}}{2}} (e^{i\varphi'} \eta + e^{-i\varphi'} \eta^+) \right) \right], \quad (1.36)$$

which solution is a diagonal matrix in the quantum number n . This part will be denoted as $D_{n,n}$ in the following calculations. The φ' -integration in eq. (1.35) contains the following contributions if the cosine-rule (1.23) is applied to it:

$$\int_0^{2\pi} \frac{d\varphi'}{2\pi} \cos(4\varphi') \sin(hs) \sin \left(\frac{1}{2} s v_F \sqrt{\frac{\hbar \kappa_{\perp}}{2}} (e^{i\varphi'} \eta + e^{-i\varphi'} \eta^+) \right) \quad (1.37)$$

and

$$\int_0^{2\pi} \frac{d\varphi'}{2\pi} \cos(4\varphi') \left[1 - \cos(hs) \cos \left(\frac{1}{2} s v_F \sqrt{\frac{\hbar \kappa_{\perp}}{2}} (e^{i\varphi'} \eta + e^{-i\varphi'} \eta^+) \right) \right]. \quad (1.38)$$

Eq. (1.37) contains an integration over even and odd functions of φ' . Therefore, the only remaining contribution to be determined is

$$\int_0^{2\pi} \frac{d\varphi'}{2\pi} \cos(4\varphi') \cos \left(\frac{1}{2} t v_F \sqrt{\frac{\hbar \kappa_{\perp}}{2}} (e^{i\varphi'} \eta + e^{-i\varphi'} \eta^+) \right), \quad (1.39)$$

because of

$$\int_0^{2\pi} \frac{d\varphi'}{2\pi} \cos(4\varphi') = 0. \quad (1.40)$$

As in the case of s -wave symmetry the cosine-term containing the annihilation and creation operators are substituted by exponential functions (see eqs. (1.25-1.28))

$$\begin{aligned} \int_0^{2\pi} \frac{d\varphi'}{2\pi} \cos(4\varphi') \cos((\alpha + \beta)/i) &= e^{-\frac{v^2}{2}} \sum_{m=0}^{\infty} \sum_{l=0}^{\infty} \int_0^{2\pi} \frac{d\varphi'}{2\pi} \frac{1}{2} \left(\frac{\alpha^l \beta^m}{l!m!} + \frac{(-\alpha)^l (-\beta)^m}{l!m!} \right) \\ &= e^{-\frac{v^2}{2}} \sum_{m=0}^{\infty} \sum_{l=0}^{\infty} \int_0^{2\pi} \frac{d\varphi'}{2\pi} \frac{1}{2} (i^{l+m} + (-i)^{l+m}) \frac{1}{l!m!} \times \\ &\quad v^{l+m} \eta^{+l} \eta^m \cos(4\varphi') e^{i\varphi'(m-l)}. \end{aligned} \quad (1.41)$$

With the integration over φ'

$$\int_0^{2\pi} \frac{d\varphi'}{2\pi} \cos(4\varphi') e^{i\varphi'(m-l)} = \frac{1}{2} (\delta_{m,l+4} + \delta_{l,m+4}) \quad (1.42)$$

eq. (1.39) becomes

$$\sum_{l=0}^{\infty} \frac{1}{2} \frac{(-1)^l}{l!(l+4)!} v^{2l+4} \left(\eta^{+l+4} \eta^l + \eta^{+l} \eta^{l+4} \right) e^{-\frac{v^2}{2}}, \quad (1.43)$$

and we obtain for the linearized gap-equation

$$\begin{aligned}
 -\ln\left(\frac{T}{T_c^{(0)}}\right)\Delta_d(\mathbf{r}) &= [\text{eq. (1.36)}]\Delta_d(\mathbf{r}) - \frac{1}{2}\pi k_B T \int_0^\infty ds \frac{1}{\sinh(\pi k_B T s)} \cos(hs) \times \\
 &\quad \sum_{l=0}^\infty \frac{(-1)^l}{l!(l+4)!} v^{2l+4} \left(\eta^{+l+4} \eta^l + \eta^{+l} \eta^{l+4} \right) e^{-\frac{v^2}{2}} \Delta_d(\mathbf{r})
 \end{aligned} \tag{1.44}$$

with $v = \frac{1}{2}sv_F\sqrt{\frac{\hbar\kappa_\perp}{2}}$. For d -wave pairing symmetry the gap-function $\Delta_d(\mathbf{r})$ is expanded in terms of the eigenfunctions $\Phi_n(\mathbf{r})$

$$\Delta_d(\mathbf{r}) = \sum_{n=0}^\infty \Delta_n \Phi_n(\mathbf{r}). \tag{1.45}$$

Therefore, the operators $\eta^{+l}\eta^{l+4}$ and $\eta^{+l+4}\eta^l$ are applied to the eigenfunctions $\Phi_n(\mathbf{r})$, which results in

$$\langle \Phi_{n'} | \eta^{+l+4} \eta^l | \Phi_n \rangle = \sqrt{\frac{n'!n!}{(n'-l-4)!(n-l)!}} \delta_{n',n+4} \tag{1.46}$$

and

$$\langle \Phi_{n'} | \eta^{+l} \eta^{l+4} | \Phi_n \rangle = \sqrt{\frac{n'!n!}{(n-l-4)!(n'-l)!}} \delta_{n,n'+4}. \tag{1.47}$$

The matrix equation for H_{c2} in case of d -wave symmetry is therefore

$$-\ln\left(\frac{T}{T_c^{(0)}}\right)\Delta_n = \sum_{n'=0}^\infty D_{n,n'} \Delta_{n'} \tag{1.48}$$

with

$$D_{n,n'} = \delta_{n,n'} D_{n,n} + (\delta_{n,n'+4} + \delta_{n+4,n'}) D_{n,n'}^{(4)} \tag{1.49}$$

and the matrices

$$\begin{aligned}
 D_{n,n} &= \pi k_B T \int_0^\infty ds \frac{1}{\sinh(\pi k_B T s)} \left\{ 1 - \cos(hs) \times \right. \\
 &\quad \left. e^{-s^2 v_F^2 \hbar \kappa_\perp / 16} \sum_{l=0}^n \frac{(-1)^l n!}{l!^2 (n-l)!} \left(\frac{s^2 v_F^2 \hbar \kappa_\perp}{8} \right)^l \right\}
 \end{aligned} \tag{1.50}$$

$$\begin{aligned}
 D_{n,n'}^{(4)} &= -\frac{1}{2}\pi k_B T \int_0^\infty ds \frac{1}{\sinh(\pi k_B T s)} \cos(hs) \times \\
 &\quad e^{-s^2 v_F^2 \hbar \kappa_\perp / 16} \sum_{l=0}^{\min(n,n')} \frac{(-1)^l \sqrt{n!n'}}{l!(l+4)!(\min(n,n')-l)!} \left(\frac{s^2 v_F^2 \hbar \kappa_\perp}{8} \right)^{l+2}.
 \end{aligned} \tag{1.51}$$

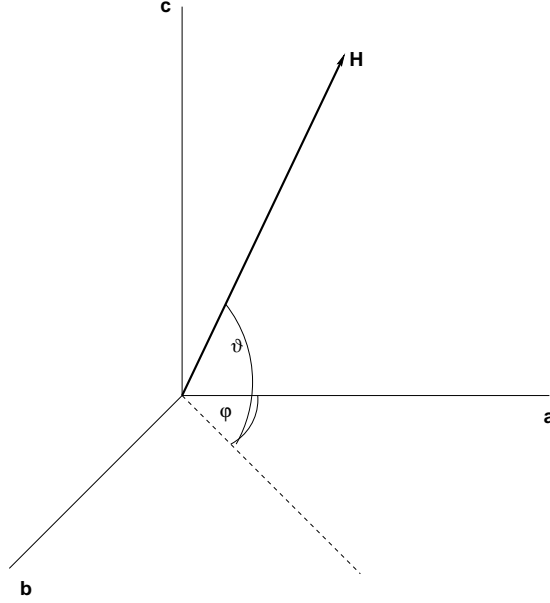


FIGURE 1.1: Direction of the magnetic field and angles ϑ between H and the a - b plane and φ between H and a .

One can see from eq. (1.49) that the coefficients Δ_n are mixed with $\Delta_{n\pm 4}$ in eq. (1.45) for any n . Thus, the coefficients Δ_n with $n = n_0, n_0 + 4, n_0 + 8 \dots$ are all mixed, with $n_0 = 0, 1, 2$ and 3. Inserting eq. (1.49) into (1.48) results in

$$-\ln\left(\frac{T}{T_c^{(0)}}\right)\Delta_n = D_{n,n}\Delta_n + D_{n,n+4}^{(4)}\Delta_{n+4} + D_{n,n-4}^{(4)}\Delta_{n-4} \quad (1.52)$$

The corresponding equations in Eilenberger units can be found in Appendix A, equations (A.30-A.33).

Rotation of the magnetic field in the a - b plane

We have derived equations for the upper critical field H_{c2} considering the angle ϑ_H between the magnetic field H and the c -axis or the a - b plane. In this section, a rotation of the fermi velocity \mathbf{v}_F by an angle φ with respect to the coordinate system (\hat{k}'_x, \hat{k}'_y) is considered to be equivalent to a rotation of H by φ with respect to the a - b plane and equations for the φ -dependence of H_{c2} are derived (see Fig. 1.1).

The transformation matrix

$$T = \begin{pmatrix} \cos(\varphi) & \sin(\varphi) & 0 \\ -\sin(\varphi) & \cos(\varphi) & 0 \\ 0 & 0 & 1 \end{pmatrix} \quad (1.53)$$

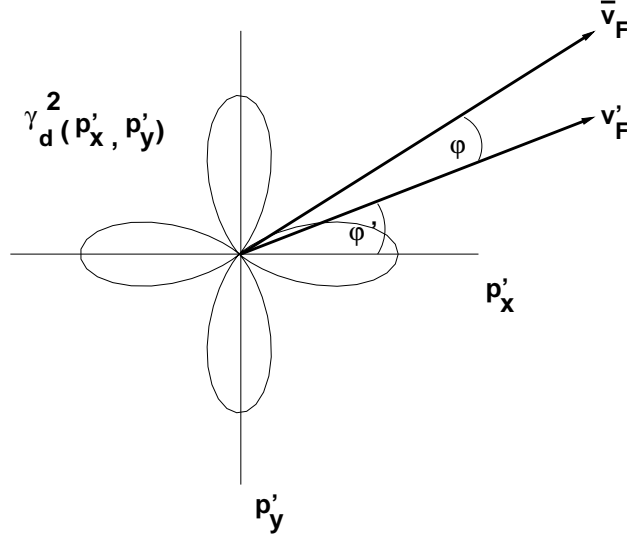


FIGURE 1.2: Symmetry function $\gamma_d(\hat{k})^2$ and transformation of the Fermi velocity \mathbf{v}'_F to $\bar{\mathbf{v}}_F$.

rotates the Fermi velocity \mathbf{v}'_F by φ

$$\bar{\mathbf{v}}_F = T \mathbf{v}'_F = T v_F \begin{pmatrix} \cos(\varphi') \\ \sin(\varphi') \\ 0 \end{pmatrix} = v_F \begin{pmatrix} \cos(\varphi' - \varphi) \\ \sin(\varphi' - \varphi) \\ 0 \end{pmatrix} \quad (1.54)$$

Therefore the linearized gap-equation (1.22) is modified by replacing φ' with $\varphi' - \varphi$ in the exponential functions without altering the other φ' -dependencies. The calculation of the equations for H_{c2} is completely analogous to those of the previous d -wave case and the results are the same except for the matrix

$$D_{n,n'} = \delta_{n,n'} D_{n,n} + (\delta_{n,n'+4} e^{-i4\varphi} + \delta_{n+4,n'} e^{i4\varphi}) D_{n,n'}^{(4)}. \quad (1.55)$$

Because of

$$e^{\pm i4\varphi} = \cos(4\varphi) \pm i \sin(4\varphi) \quad (1.56)$$

the matrix $D_{n,n'}$ is complex and can be split into its real and imaginary parts

$$\begin{aligned} D_{n,n'} = D_{n,n'}^r + i D_{n,n'}^i &= \delta_{n,n'} D_{n,n} + (\delta_{n,n'+4} + \delta_{n+4,n'}) D_{n,n'}^{(4)} \cos(4\varphi) + \\ &\quad i(\delta_{n+4,n'} - \delta_{n,n'+4}) D_{n,n'}^{(4)} \sin(4\varphi). \end{aligned} \quad (1.57)$$

The same can be done with the gap-coefficients Δ_n

$$\Delta_n = \Delta_n^r + i \Delta_n^i \quad (1.58)$$

and the results for H_{c2} consist of two coupled equations

$$-\ln\left(\frac{T}{T_c^{(0)}}\right) \Delta_n^r = \sum_{n'=0}^{\infty} \left(\Delta_n^r D_{n,n'}^r - \Delta_n^i D_{n,n'}^i \right)$$

$$-\ln\left(\frac{T}{T_c^{(0)}}\right)\Delta_n^i = \sum_{n'=0}^{\infty} \left(\Delta_n^i D_{n,n'}^r + \Delta_n^r D_{n,n'}^i\right) \quad (1.59)$$

giving

$$\begin{aligned} -\ln\left(\frac{T}{T_c^{(0)}}\right)\Delta_n^r &= D_{n,n}\Delta_n^r + (D_{n,n+4}^{(4)}\Delta_{n+4}^r + D_{n,n-4}^{(4)}\Delta_{n-4}^r) \cos(4\varphi) - \\ &\quad (D_{n,n+4}^{(4)}\Delta_{n+4}^i - D_{n,n-4}^{(4)}\Delta_{n-4}^i) \sin(4\varphi) \\ -\ln\left(\frac{T}{T_c^{(0)}}\right)\Delta_n^i &= D_{n,n}\Delta_n^i + (D_{n,n+4}^{(4)}\Delta_{n+4}^i + D_{n,n-4}^{(4)}\Delta_{n-4}^i) \cos(4\varphi) + \\ &\quad (D_{n,n+4}^{(4)}\Delta_{n+4}^r - D_{n,n-4}^{(4)}\Delta_{n-4}^r) \sin(4\varphi). \end{aligned} \quad (1.60)$$

1.3 Phase diagrams

In the previous section equations for the upper critical field, which is determined by the first appearance of a high- n vortex state for magnetic fields not strictly parallel to the conducting plane, were derived. In this section, the phase diagrams in the $H - T$ plane for the s - and d -wave cases and for various tilt angles of the magnetic field are examined.

Below the stability limit of the normal-conducting state, a series of different inhomogeneous superconducting states, depending on ϑ , appear. For s -wave superconductors each one of these states relates to a particular value of Landau quantum number n , which takes integer values $n = 0, 1, 2, \dots$. These states are (for the s -wave) the following:

- The vortex state for ϑ near $\pi/2$ relating to $n = 0$.
- A series of inhomogeneous states for ϑ near 0, each one characterized by a single value of $n > 0$, with n increasing with decreasing ϑ .
- The FFLO state for $\vartheta = 0$, which may be characterized by $n \rightarrow \infty$.

The structure of the higher Landau level states, for $n > 0$, has been calculated for s -wave superconductors by minimizing the quasiclassical free energy [35]. For d -wave superconductors [11] a state below $H_{c2}(\vartheta, T)$ is characterized no longer by a single value of n but rather by an infinite subset $\{n_0, n_0 \pm 4, n_0 \pm 8, \dots\}$. However, the dominant contribution may still be characterized by a single number n , which increases again with decreasing ϑ and approaches infinity in the FFLO limit. Thus, basically the above classification scheme remains valid for d -wave symmetry. The phase boundary of the pure FFLO state for d -wave superconductors (the curve $H_{c2}(0, T)$) has been calculated by Maki and Won [12].

Prior to showing the numerical results, reduced units are introduced, such as the parameter r_m , which characterizes the strength of the orbital magnetic effect relative to that of the spin

| r_m | $\sin \vartheta$ | ϑ (deg) |
|-------------------|------------------|-------------------|
| 0.5 ^s | 0.15 | 8.63 |
| 0.2 | 0.06 | 3.44 |
| 0.1 | 0.03 | 1.72 |
| 0.08 ^d | 0.24 | 1.38 |
| 0.05 | 0.015 | 0.86 |
| 0.025 | 0.0075 | 0.43 |

Table 1.1: Parameter r_m and corresponding tilt angles of the magnetic field

magnetic effect

$$r_m = \frac{H_{\perp}}{z_m H} \quad (1.61)$$

with

$$z_m = \frac{\frac{|h|}{2\pi k_B T_c^{(0)}}}{\frac{2|e|\hbar}{c} \left(\frac{v_F}{2\pi k_B T_c^{(0)}} \right)^2 H} = \frac{\pi g_L}{4} \frac{k_B T_c^{(0)}}{m v_F^2}. \quad (1.62)$$

The parameter z_m can be expressed in terms of the effective mass $m^* = p_F/v_F$ and the BCS coherence length $\xi_0 = \hbar v_F/\pi \Delta_0$ as

$$z_m = \frac{g_L}{4} \frac{k_B T_c^{(0)}}{\Delta_0} \frac{m^*}{m} \frac{\hbar}{p_F \xi_0}, \quad (1.63)$$

where $k_B T_c^{(0)}/\Delta_0 = e^{\gamma}/\pi$ in the present weak-coupling theory and Δ_0 is the zero-field gap. The equations for *s*- and *d*-wave symmetry in these units can be found in Appendix A, (A.8-A.12). For high- T_c superconductors, if we assume $\xi_0 \sim 20 \text{ \AA}$, a lattice constant $a \sim 10 \text{ \AA}$, an effective mass $m^* \sim 2m$, and $g_L \sim 2$, $\pi p_F/(4\pi^2/a^2) \sim 0.5$ for nearly half filling, as an example, then z_m is estimated to be $z_m \sim 0.3$. With this value, the tilt angles ϑ obtained from the equation $\sin \vartheta = r_m z_m$ are shown in the following table for certain values of r_m used in the numerical calculations. The superscripts ^{s,d} indicate that these values were only used in the given symmetry. The phase diagrams are shown as h_{c2}/Δ_0 vs. T/T_{c0} plots.

1.3.1 *s*-wave

The tilt angle dependence of the critical field in the ground state of the *s*-wave case was already obtained by Bulaevskii [34] and the temperature dependence of the critical field for various values of $r_m \geq 0.05$ was shown by Shimahara and Rainer [11]. The results obtained for the *s*-wave case for $r_m \geq 0.05$ are the same as in Ref. [11], additionally the temperature dependence of the critical field for $r_m = 0.025$ is shown in this work.

Figure 1.3 depicts the results for $r_m = 0.5$. At each temperature the line with the highest critical field corresponds to the upper critical field. One can see clearly that at high temper-

atures, the vortex state with $n = 0$ occurs and at low temperatures, the vortex state with $n = 1$ is favoured in accordance with eq. (4.3) of Ref. [11]. The resulting critical field is larger than the thermodynamic critical field of the BCS-state for $r_m = 0$.

The phase diagrams for $r_m = 0.2$ is also shown in Fig. 1.3. With $r_m = 0.2$, vortex states with higher n occur, and the critical field of the FFLO (Fulde Ferell Larkin Ovchinnikov, Refs. [7] and [8]) state for magnetic fields parallel to the conducting planes is approached. As discussed above, the optimum value of the quantum number n of the vortex state increases as the temperature decreases. The vortex state with the largest n is $n = 3$ in this case.

The temperature dependence of the upper critical field shows kinks due to the discrete changes of the optimum n for these values of r_m , which become less pronounced as r_m decreases. Fig. 1.4 shows the results for $r_m = 0.1$ and $r_m = 0.05$. The upper critical field becomes nearly smooth despite of the discrete changes of n from $n = 0$ to the highest vortex state at low temperatures with $n = 6$. For $r_m = 0.05$ the upper critical field h_{c2}/Δ_0 is almost indistinguishable from the FFLO critical field, which is drawn with points in these diagrams in order to allow a better comparison. For low temperatures, however, one can see that the linear temperature dependence of the FFLO critical field is not yet recovered for these values of r_m .

The agreement between the upper critical field h_{c2}/Δ_0 and the FFLO critical field at low temperatures improves even more with $r_m = 0.025$, which is shown in Fig. 1.5. The vortex state with the highest critical field at low temperatures is $n = 24$.

1.3.2 d-wave

In the case of d wave pairing symmetry, mixing between all n and $n + 4$ occurs in the solution linearized gap equation (1.52). The solutions are classified by n_0 , which is the smallest value of n in each solution. However, the dominant contribution may still be characterized by a single number n , which increases with decreasing temperature and angle ϑ between the field and the conducting planes and reaches infinity in the FFLO-limit. Thus, the above classification scheme remains valid for d -wave symmetry. When solving the linearized gap equation numerically a cut-off n_c has to be set, which is the automatically the dimension of the matrices $D_{n,n}$ and $D_{n,n\pm 4}^{(4)}$. The cut-off is set to $n_c = n_0 + 4l_c$ with $l_c = 5$ for $r_m > 0.025$ and $l_c = 6$ for $r_m = 0.025$, because the vortex state with $n = 24$ gave the highest critical field at low temperatures for $r_m = 0.025$.

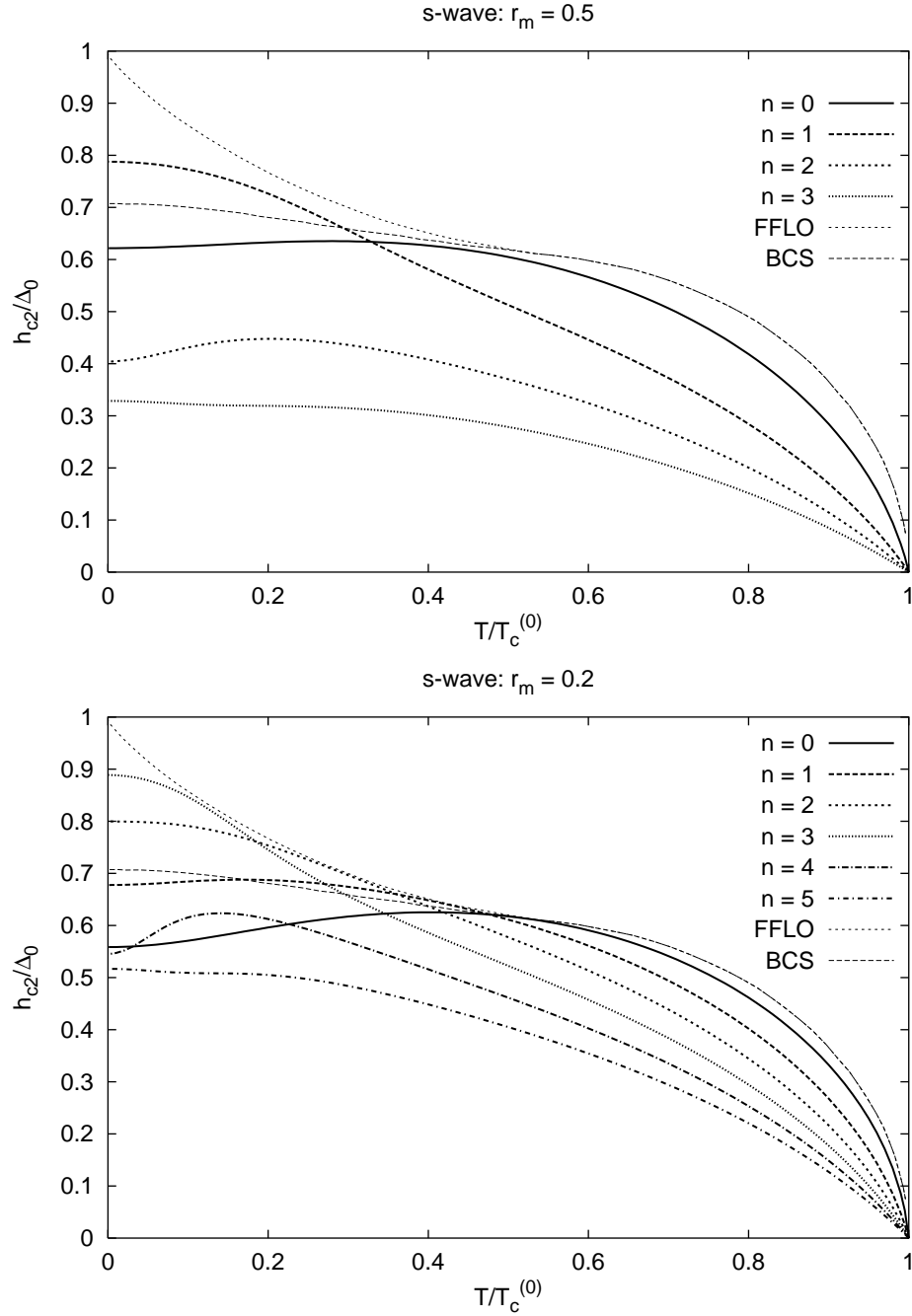


FIGURE 1.3: Temperature dependence of the upper critical field for $r_m = 0.5$ and 0.2 in the s -wave case. The thick lines are the solutions of eq. (1.34) for fixed n . The thin, broken lines show the thermodynamic critical field of the BCS-state and the critical field of the FFLO state, respectively, in the absence of the orbital effect, *i.e.*, for $r_m = 0$.

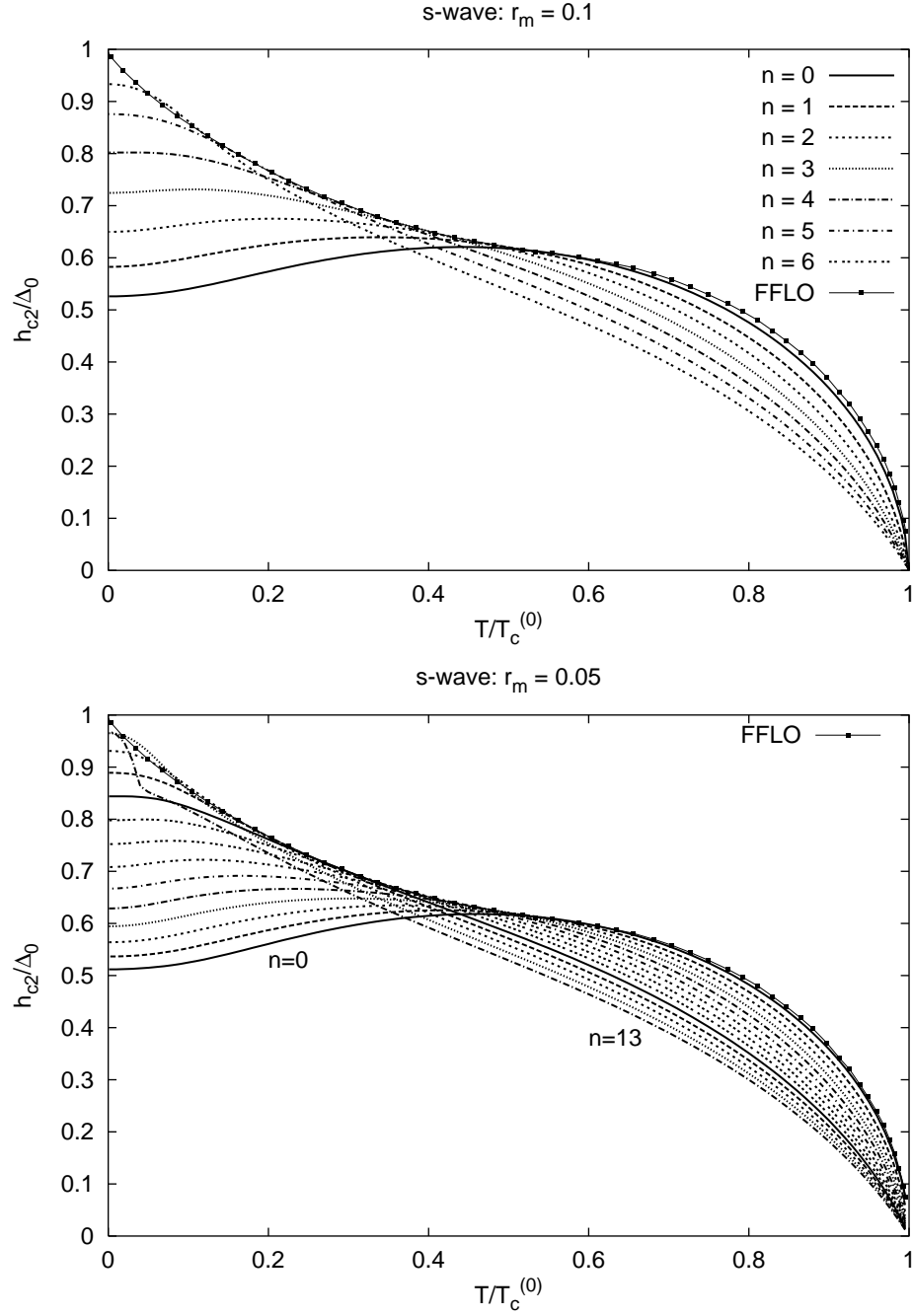


FIGURE 1.4: Temperature dependence of the upper critical field for $r_m = 0.1$ and $r_m = 0.05$ in the s -wave case. The thick lines are the solutions of eq. (1.34) for fixed n . Points were added to the thin, broken line showing the critical field of the FFLO state for clarity.

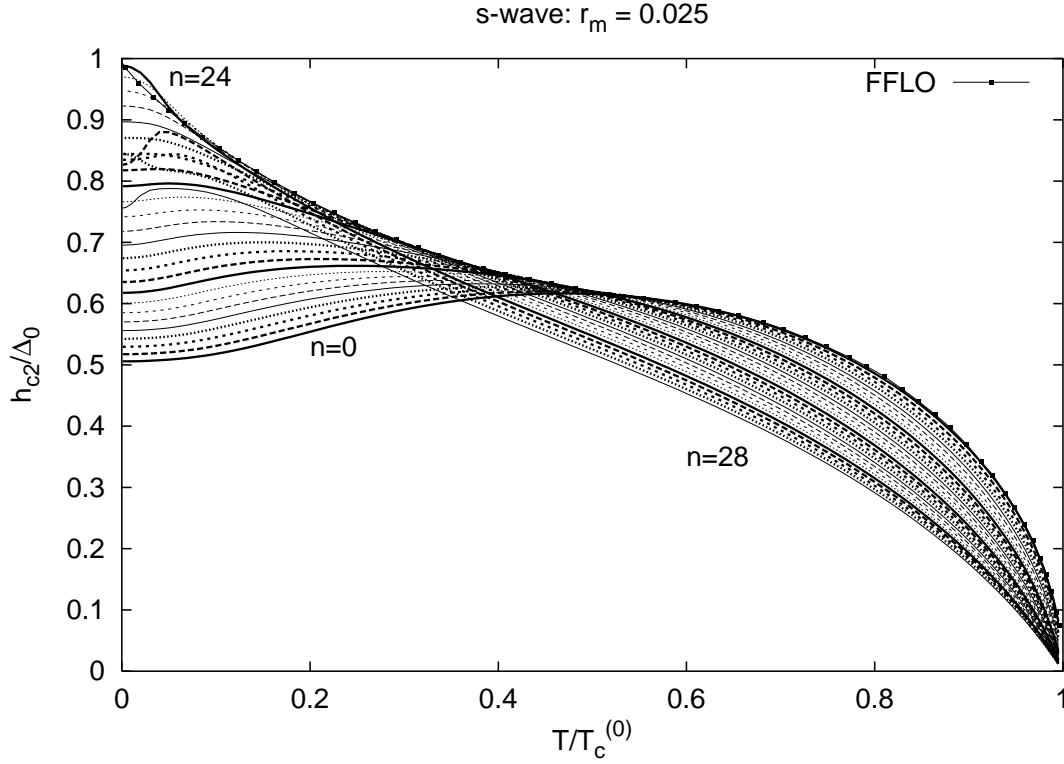


FIGURE 1.5: Temperature dependence of the upper critical field for $r_m = 0.025$ in the s -wave case. The thick lines are the solutions of eq. (1.34) for fixed n . Points were added to the thin, broken line showing the critical field of the FFLO state for clarity.

Fig. 1.6 shows the results for $r_m = 0.2$. As in the s -wave case, the critical field is already higher than the thermodynamic critical field. With this value of r_m it is not clear yet, which of the two FFLO-cases with different angles of \mathbf{q} is approached. The FFLO critical field was obtained by Won and Maki in Ref. [36]. The thick solid line shows the upper critical field in the whole temperature range, where n_0 changes from 0 at high to 3 at low temperatures. Whenever n_0 changes, kinks show up in the upper critical field as in the s -wave case. The mixing of n and $n \pm 4$ due to the anisotropy of the d -wave order parameter does not smear out the kinks in the temperature dependence of the upper critical field. The figure also shows the result for $r_m = 0.1$. Compared to the s -wave case the convergence with respect to r_m is rather slow due to the mixing of n caused by the anisotropy of the d -wave order parameter. The FFLO upper critical field with $r_m = 0$ and $\varphi_q = \pi/4$ is approached at higher temperatures, but at low temperatures the solution for $r_m = 0.1$ is still remarkably lower than the FFLO-case with $\varphi_q = 0$.

Fig. 1.7 shows the solutions for $r_m = 0.08$ and $r_m = 0.05$. The agreement between the

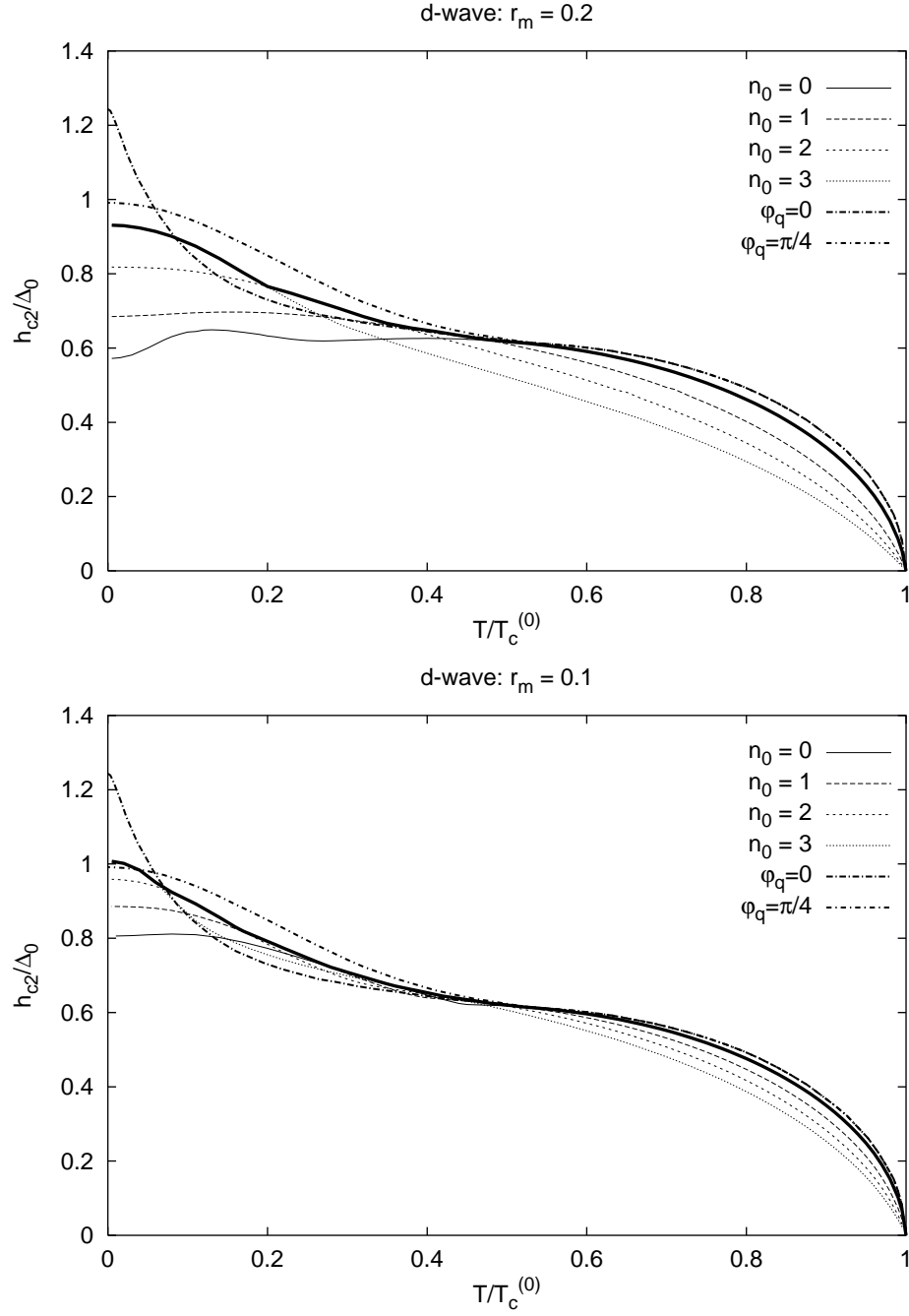


FIGURE 1.6: Temperature dependence of the upper critical field for $r_m = 0.2$ and $r_m = 0.1$ in the d -wave case. The thin lines are the solutions of eq. (1.52) for fixed n . The thick solid line is the largest h_{c2} . The critical field of the FFLO state for $\varphi_q = 0$ and $\varphi_q = \pi/4$, in the absence of the orbital effect, *i.e.*, for $r_m = 0$ are shown for comparison.

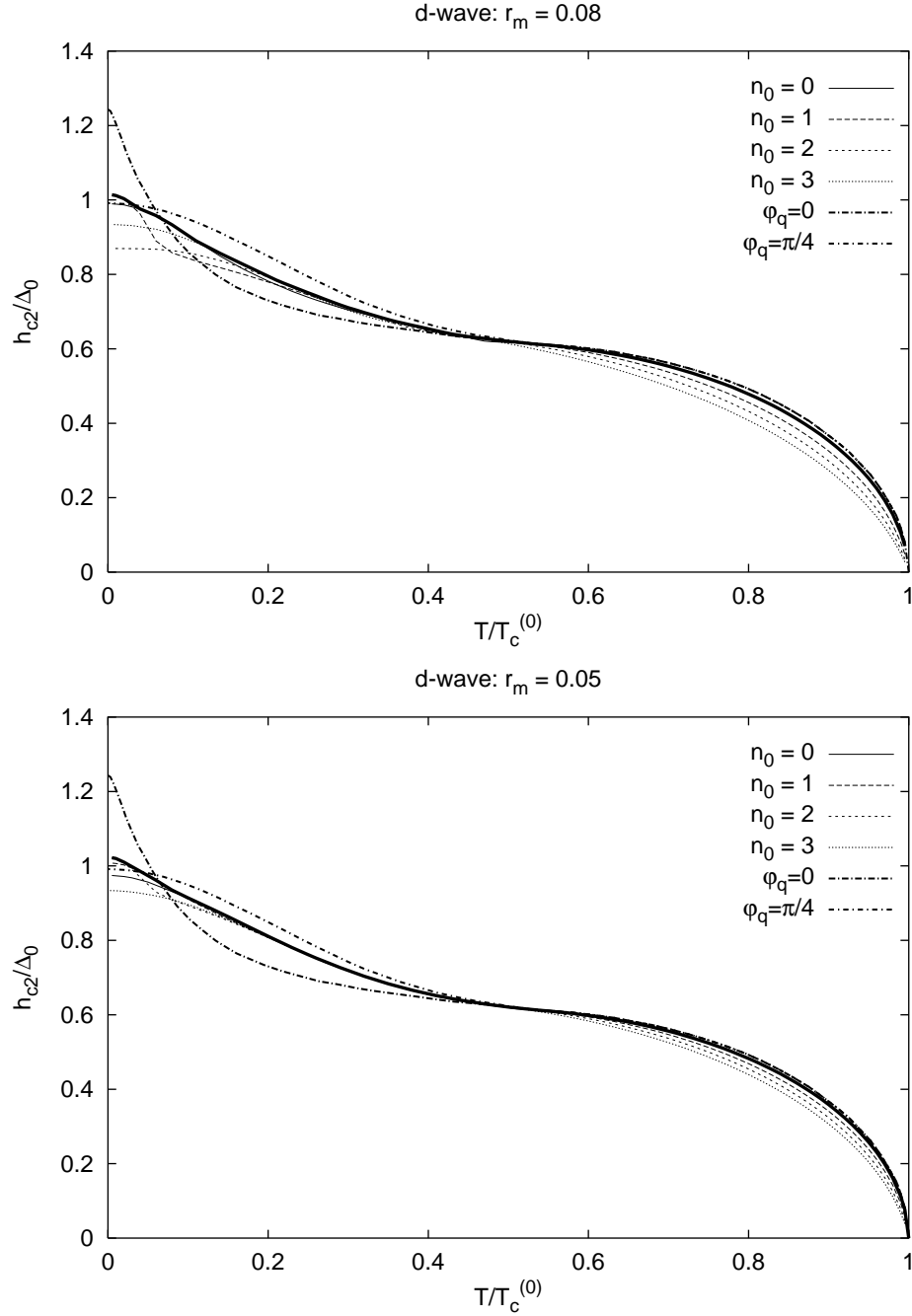


FIGURE 1.7: Temperature dependence of the upper critical field for $r_m = 0.2$ and $r_m = 0.1$ in the d -wave case. The thin lines are the solutions of eq. (1.52) for fixed n . The thick solid line is the largest h_{c2} . The critical field of the FFLO state for $\varphi_q = 0$ and $\varphi_q = \pi/4$, in the absence of the orbital effect, *i.e.*, for $r_m = 0$ are shown for comparison.

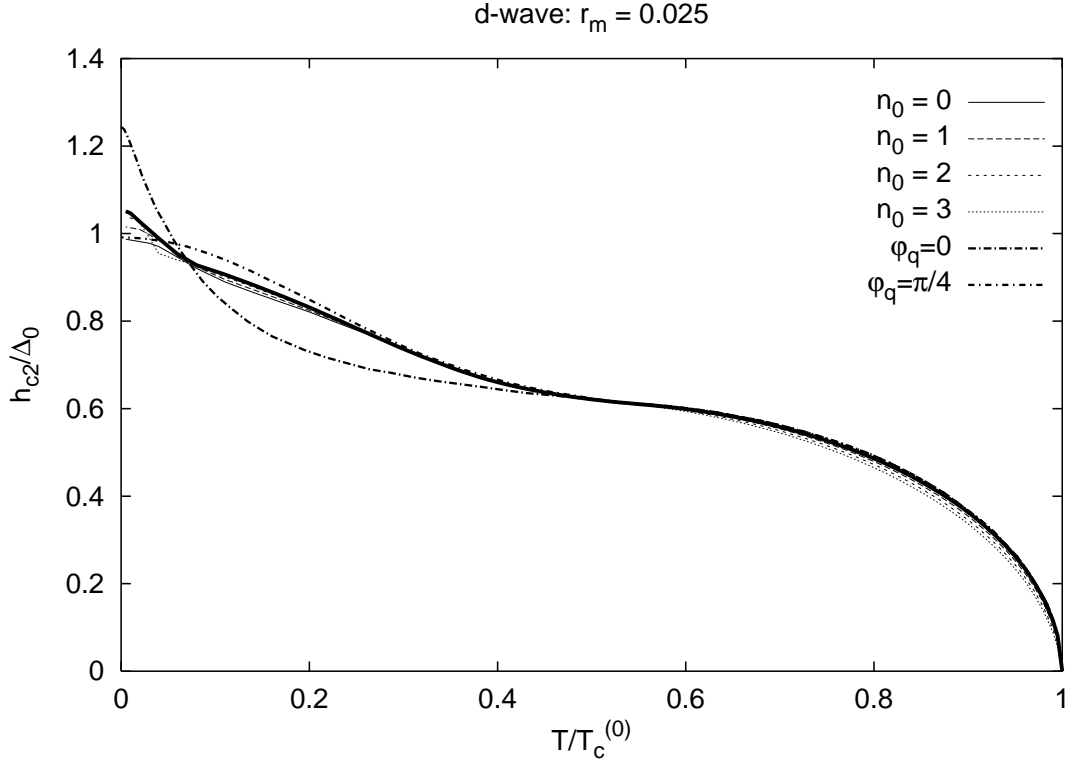


FIGURE 1.8: Temperature dependence of the upper critical field for $r_m = 0.025$ in the d -wave case. The thin lines are the solutions of eq. (1.52) for fixed n . The thick solid line is the largest h_{c2} . The critical field of the FFLO state for $\varphi_q = 0$ and $\varphi_q = \pi/4$, in the absence of the orbital effect, *i.e.*, for $r_m = 0$ are shown for comparison.

solutions and the FFLO critical field with $\varphi_q = \pi/4$ improves, and the upper critical field at low temperatures increases towards the case with $\varphi_q = 0$, but is not yet recovered at these values of r_m . The kinks in the upper critical field due to the changes in n_0 become less pronounced as r_m decreases, however, for $r_m = 0.025$ (Fig. 1.8) a remarkable kink shows up at low temperatures as h_{c2} increases towards the FFLO critical field with $\varphi_q = 0$. In the FFLO-case, the wavevector \mathbf{q} is optimized in order to obtain the upper critical field. As the direction of \mathbf{q} changes discretely from $\varphi_q = \pi/4$ to $\varphi_q = 0$, the slope of the FFLO critical field becomes very steep and there is a discontinuity in the derivative of the upper critical field at $t \simeq 0.06$. The solution for $r_m = 0.025$ shows a similar behavior. The evolution of the upper critical field with r_m is depicted in Fig. 1.9.

In-plane angle dependence of the upper critical field

The numerical solutions of eq. (1.60) with the same set of parameters as in $\varphi = 0$ show no change in the upper critical field with respect to φ . In the case $\varphi = 0$ (1.52) there are two solutions that give different values for the upper critical field, one in which the initial value

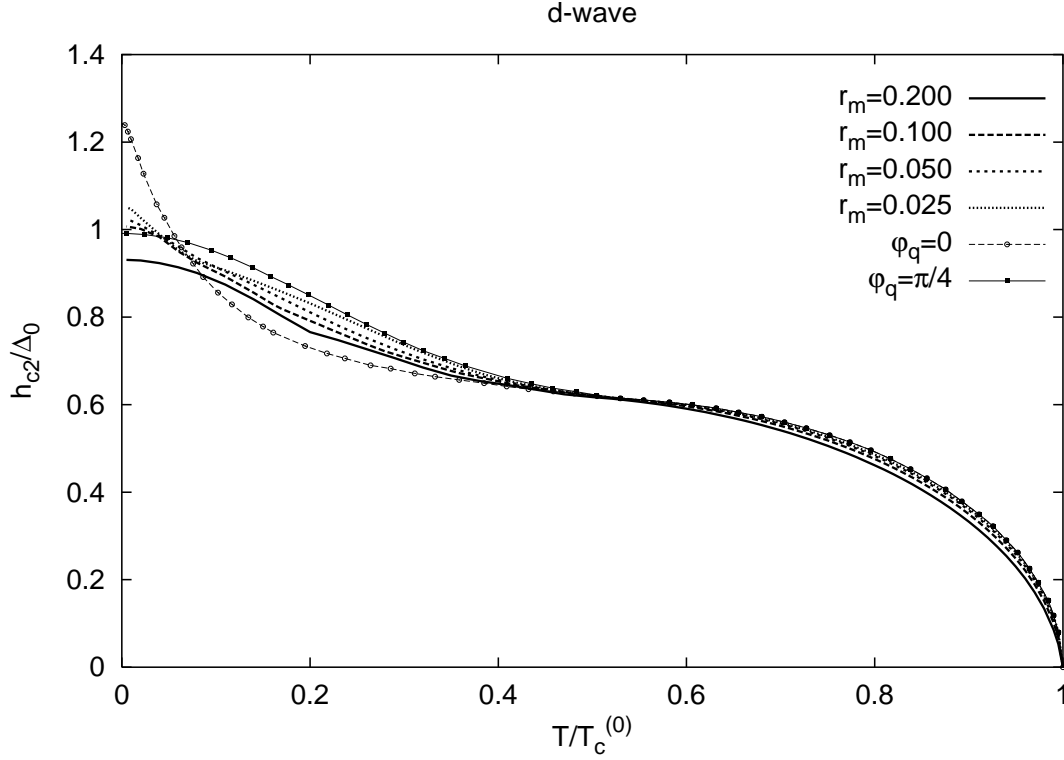


FIGURE 1.9: Behavior of the temperature-dependent upper critical field with r_m . Points were added to the FFLO critical fields for clarity.

for Δ_{n+4}/Δ_n is negative and the other with a positive initial value. The upper critical field is then given by the highest solution of the equation

$$0 = \ln\left(\frac{T}{T_c^{(0)}}\right) + D_{n,n} + D_{n,n+4}^{(4)} \frac{\Delta_{n+4}}{\Delta_n} + D_{n,n-4}^{(4)} \frac{\Delta_{n-4}}{\Delta_n} \quad (1.64)$$

which is the one with the negative initial value for Δ_{n+4}/Δ_n . The largest change in H_{c2} should be seen for $\varphi = \pi/4$, where the Fermi velocity lies in between the maximal values of the symmetry fuction $\gamma_d = 1 + \cos(4\varphi)$. The equation to be solved in this case is

$$0 = \ln\left(\frac{T}{T_c^{(0)}}\right) + D_{n,n} - D_{n,n+4}^{(4)} \frac{\Delta_{n+4}}{\Delta_n} - D_{n,n-4}^{(4)} \frac{\Delta_{n-4}}{\Delta_n} \quad (1.65)$$

because of $\cos(\pi) = -1$ and $\sin(\pi) = 0$. Again, there are two solutions for H_{c2} depending on the sign of the initial value for Δ_{n+4}/Δ_n . Only in the case of $\varphi = \pi/4$ the situation is reversed because of the negative sign in the above equation. The highest critical field is then obtained with a positive initial value for Δ_{n+4}/Δ_n .

Let us discuss another example with $\varphi = \pi/8$, where $\cos(\pi/2) = 0$ and $\sin(\pi/2) = 1$. The

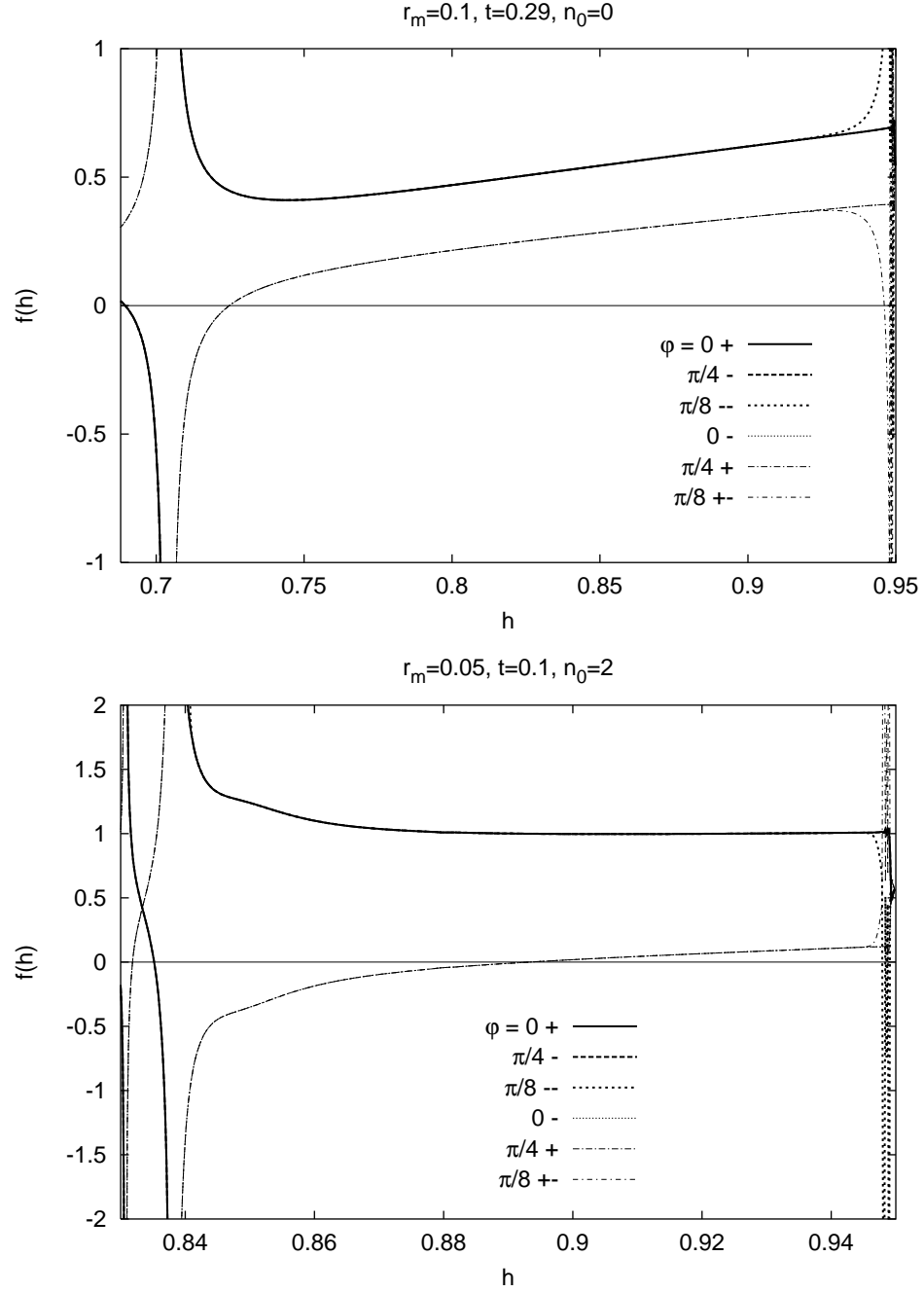


FIGURE 1.10: Numerical results of eqs. (1.64-1.66) which give the critical field from the solution of the equation $f(h) = 0$ with different signs of the initial values indicated by a + or -.

equations to be solved are given by

$$\begin{aligned} 0 &= \ln\left(\frac{T}{T_c^{(0)}}\right) + D_{n,n} - D_{n,n+4}^{(4)} \frac{\Delta_{n+4}^i}{\Delta_n^r} + D_{n,n-4}^{(4)} \frac{\Delta_{n-4}^i}{\Delta_n^r} \\ 0 &= \ln\left(\frac{T}{T_c^{(0)}}\right) + D_{n,n} + D_{n,n+4}^{(4)} \frac{\Delta_{n+4}^r}{\Delta_n^i} - D_{n,n-4}^{(4)} \frac{\Delta_{n-4}^r}{\Delta_n^i} \end{aligned} \quad (1.66)$$

which give fully equivalent solutions for the same set of parameters and initial values. There are two sets of initial values in this case because of the mixing of the real and imaginary parts Δ_n^r and Δ_n^i . If the signs of the initial values for $\Delta_{n+4}^r/\Delta_n^r$ and $\Delta_{n+4}^i/\Delta_n^i$ are the same, eq. (1.66) gives the lower numerical results of eqs. (1.64-1.65). With mixed initial values, the highest solution is obtained, which is the same upper critical field obtained in the previous cases with $\varphi = 0$ and $\pi/4$.

The numerical results of eqs. (1.64-1.66) which give the critical field from the solution of the equation $f(h) = 0$ with different signs of the initial values indicated by a + or – are shown in Fig. 1.10 for $r_m = 0.1$, $t = 0.29$, $n_0 = 0$ and $r_m = 0.05$, $t = 0.1$, $n_0 = 2$. Please note that $f(h)$ is an arbitrary choice for the name of the numerical evaluation of the eqs. (1.64-1.66) and does not indicate a physical property. The solutions giving the lower critical field are plotted with a thick line, whereas those giving the resultant upper critical field are plotted with a thin line. There is a discontinuity of $f(h)$ near the solution in both cases. The oscillations on the right end of the plots are the initial oscillations before converging to the solution given by $f(h)$ with decreasing h .

1.4 Comparison with experiment

To round up this Chapter we refer to the measurement of the upper critical field H_{c2} of the organic superconductor κ -(BEDT-TTF)₂Cu(NCS)₂ in Ref. [9]. This layered material shows strong anisotropy of the superconducting properties regarding out-of-plane directions. In addition, a number of experiments listed in reference [9] are interpreted in terms of a strong in-plane anisotropy of the gap parameter of the d -wave type. The coherence length ξ_{\perp} perpendicular to the layers of this clean material is smaller than the interlayer spacing d and one expects an extreme reduction of orbital pair breaking for plane-parallel applied field. The angular dependence of H_{c2} was measured both with respect to the angle ϑ between applied magnetic field and the direction normal to the conducting planes and with respect to the azimuthal angle φ , which denotes the direction of magnetic field lying within the plane. The results showed, as expected, a strong variation of H_{c2} with ϑ . On the other hand, no dependence on φ was observed. The maximal value of H_{c2} at the plane-parallel position $\vartheta = 0$ was of the order of, but 50% higher than, the Pauli paramagnetic limit $\mu_0 H_P = 1.83 T_c$ in Tesla. These facts led the authors of reference [9] to propose that their in-plane critical field

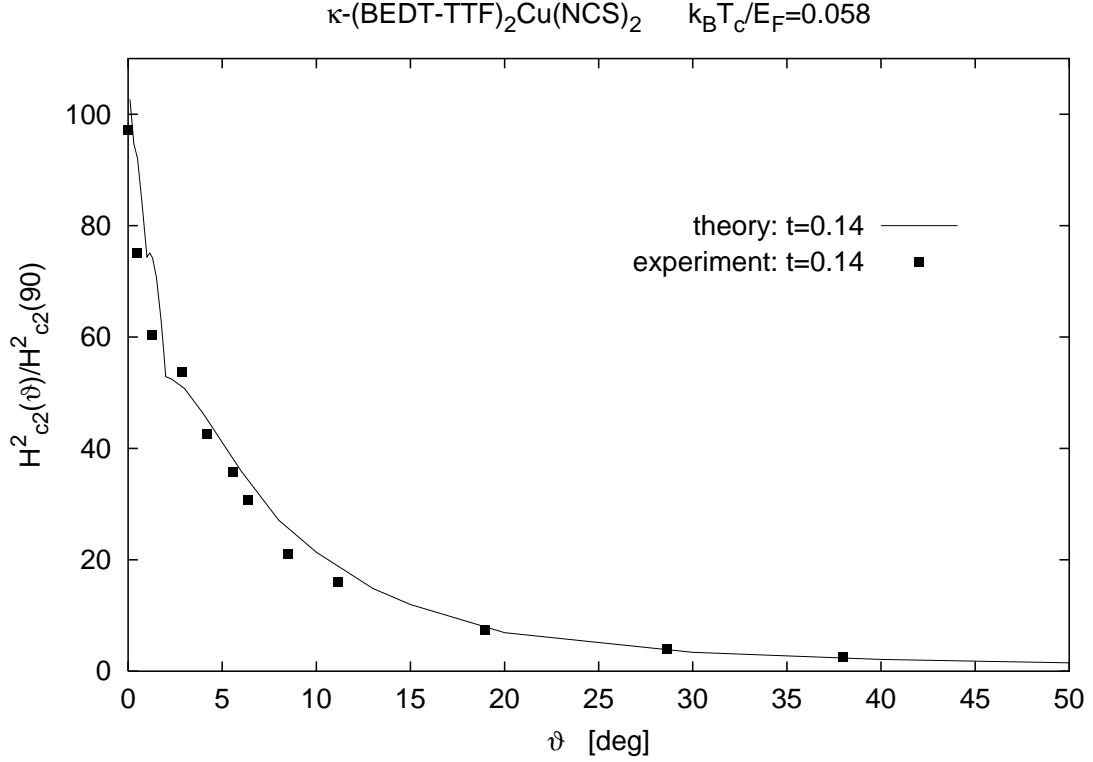


FIGURE 1.11: Square of upper critical field, normalized to its value at $\vartheta = 90^\circ$, as a function of ϑ . Full squares: data of reference [3] at $t = T/T_c = 0.14$. Full line: theoretical result for the Bulaevskii-Shimahara-Rainer phase boundary for $t = 0.14$.

is the phase boundary between the normal-conducting state and the FFLO state of a d -wave superconductor.

Assuming that the coupling between the conducting planes of κ -(BEDT-TTF)₂Cu(NCS)₂ can be neglected, the problem is effectively two-dimensional. Then, if the field has both a perpendicular and a parallel component, the superconducting state is limited by both orbital and paramagnetic pair breaking. For an exactly plane-parallel magnetic field the FFLO phase should be realized below a reduced temperature ($t = T/T_c$) of $t \approx 0.4$ (Ref. [36]). The present model requires only one single parameter $k_B T_c/E_F$ (1.62) to be fitted. In the present anisotropic model the actual ratio of spin and orbital pair-breaking depends on ϑ and may be written in the form $k_B T_c/(E_F \sin \vartheta)$ (1.61). The best fit to the ϑ -dependence of H_{c2} at $T = 1.45$ K (see Fig. 4 of Ref. [9]) has been obtained for $k_B T_c/E_F = 0.058$. This value of $k_B T_c/E_F$ is consistent with a critical temperature $T_c = 10.4$ K of the sample studied in Ref. [9], and a Fermi energy of the order of 100 K as estimated from several experiments [37]. Using this value the agreement between present model and the data of Ref. [9] is very good, as shown in Fig. 1.11. The theoretical curves in figure 1.11 have been calculated assuming

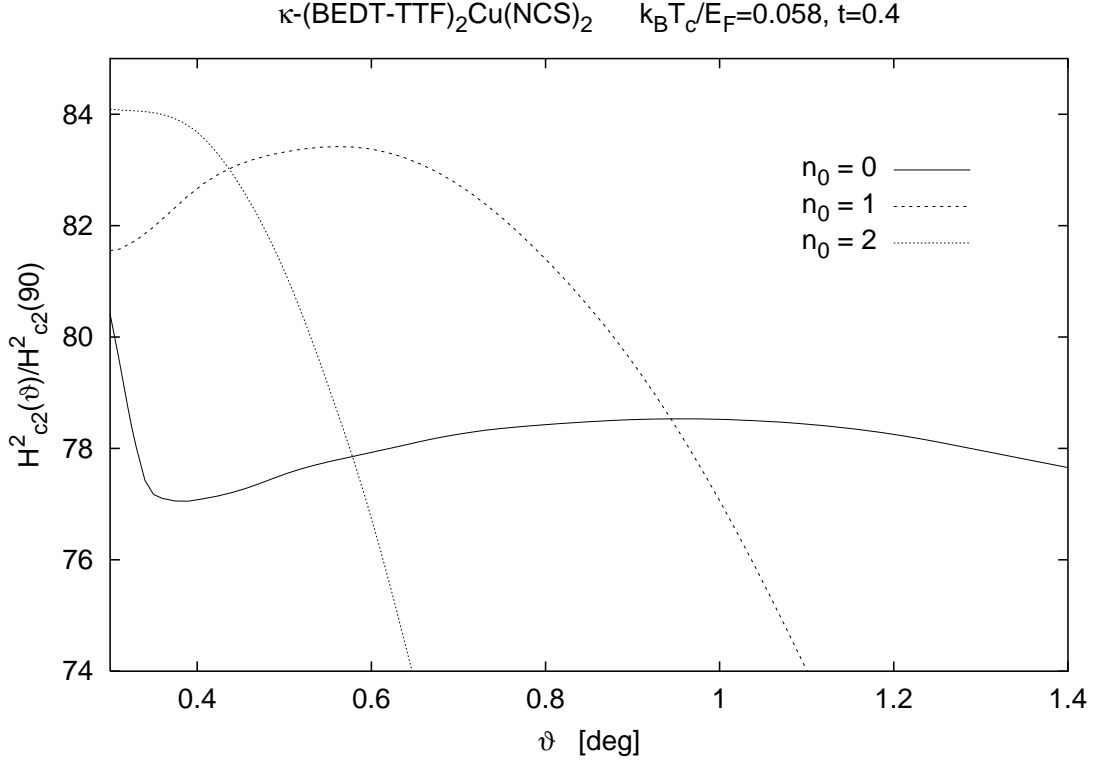


FIGURE 1.12: The branches $n_0 = 0, 1, 2$ of the upper critical field, as calculated from equation (1.52), are plotted in more detail at the temperature $t = 0.4$.

d -wave symmetry; the difference between d -wave and s -wave was found to be small except very close to $T = 0$ K and $\vartheta = 0$ deg. The H_{c2} data show a small but clearly visible kink near the plane-parallel orientation, at $\vartheta \approx 3$ deg. A similar feature is also found in the theoretical phase boundary $H_{c2}(\vartheta)$, as shown in Fig. 1.11. The square of the critical fields has been plotted in order to improve the visibility of the discontinuous change in slope. This kink indicates the transition from the vortex state, with $n = 0$, to the first of the FFLO-precursor states, with $n = 1$. Still closer to $\vartheta \approx 0$ deg equation (1) yields additional transitions corresponding to $n = 2, 3$, which are still visible in figure 1 in the theoretical curve but not in the data points. The H_{c2} -curves describing the $n = 0, 1, 2$ transitions, for the same material but higher T , are shown on a larger scale in figure 1.12. The shape of the $H_{c2}(\vartheta)$ curve depends distinctively on temperature, as shown by the plot of $H_{c2}(\vartheta)^2$ at $t = 0.8$ and $t = 0.4$ in figure 1.13. The reason for this enhancement at higher T is, of course, that paramagnetic pair breaking becomes less effective at higher temperature. Data at higher T have not been reported in Ref. [9] but would be useful in order to check the present interpretation.

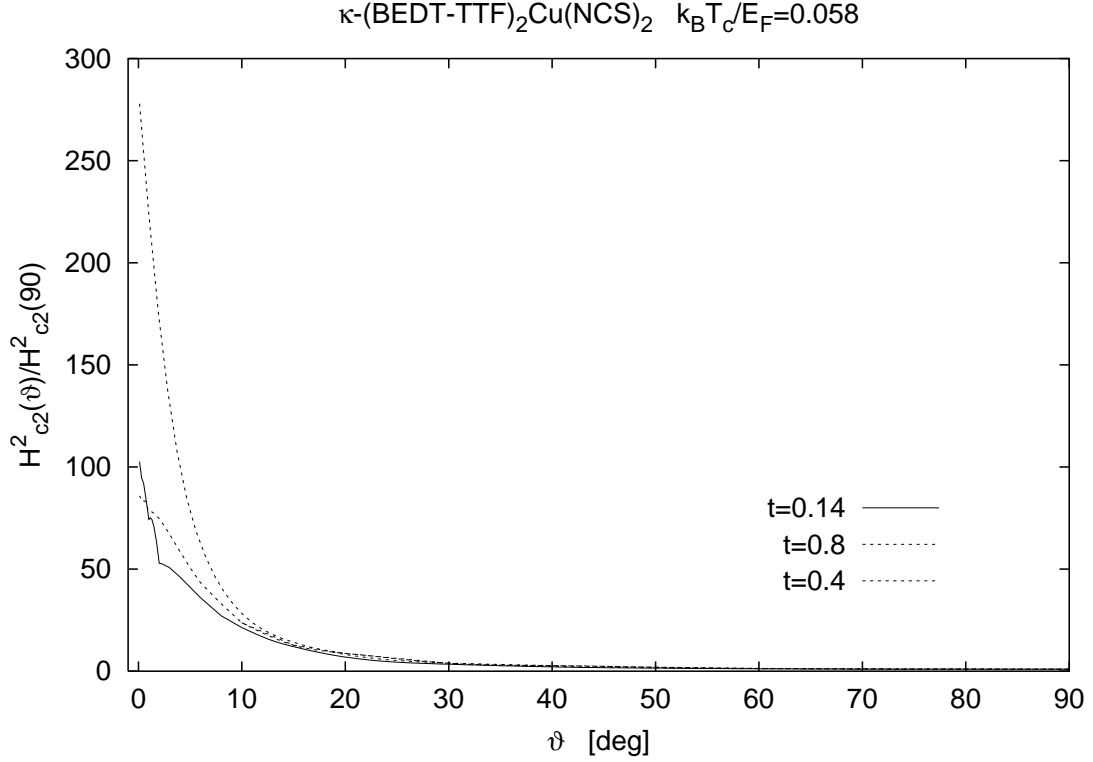


FIGURE 1.13: Square of upper critical field, normalized to its value at $\vartheta = 90$, as a function of ϑ . Full line: theoretical result for the Bulaevskii-Shimahara-Rainer phase boundary for $t = 0.14$. Dashed lines: theoretical results for the phase boundary for $t = 0.4$ and $t = 0.8$.

Finally, the measured temperature-dependence of H_{c2} for the plane-parallel field orientation (Fig. 3 of Ref. [9]) with $H_{c2}(T)$ and $\vartheta = 0$. This phase boundary has been calculated first by Won and Maki [36] and the phase boundary with $r_m = 0.025$ (Fig. 1.8) agrees with reference [36] in the limit $\vartheta \rightarrow 0$ except for the step rise of $H_{c2}(T)$ and $\vartheta = 0$ below $0.05T_c$. The comparison between theory [36] and experiment [9] depicted in figure 1.14 shows again fairly good agreement. No new parameter, except T_c , must be adjusted to obtain the absolute scale of the magnetic field in Tesla.

Similar measurements can be found in the old data by Morris and Coleman [38] for intercalated transition metal dichalcogenide $TaS_2 - (pyridine)$ samples. In this material, which represents a nearly perfect realization of two-dimensional superconductivity, an unexplained anomaly regarding the behavior of the upper critical field at different T has been reported (Fig. 10 of Ref. [38]). The agreement is excellent (Fig. 1.15) comparing the experimental data with the highest solutions of equation (1.34) for an s -wave superconductor. Again, a single parameter has been adjusted ($k_B T_c / E_F = 0.024$) to obtain both of the theoretical

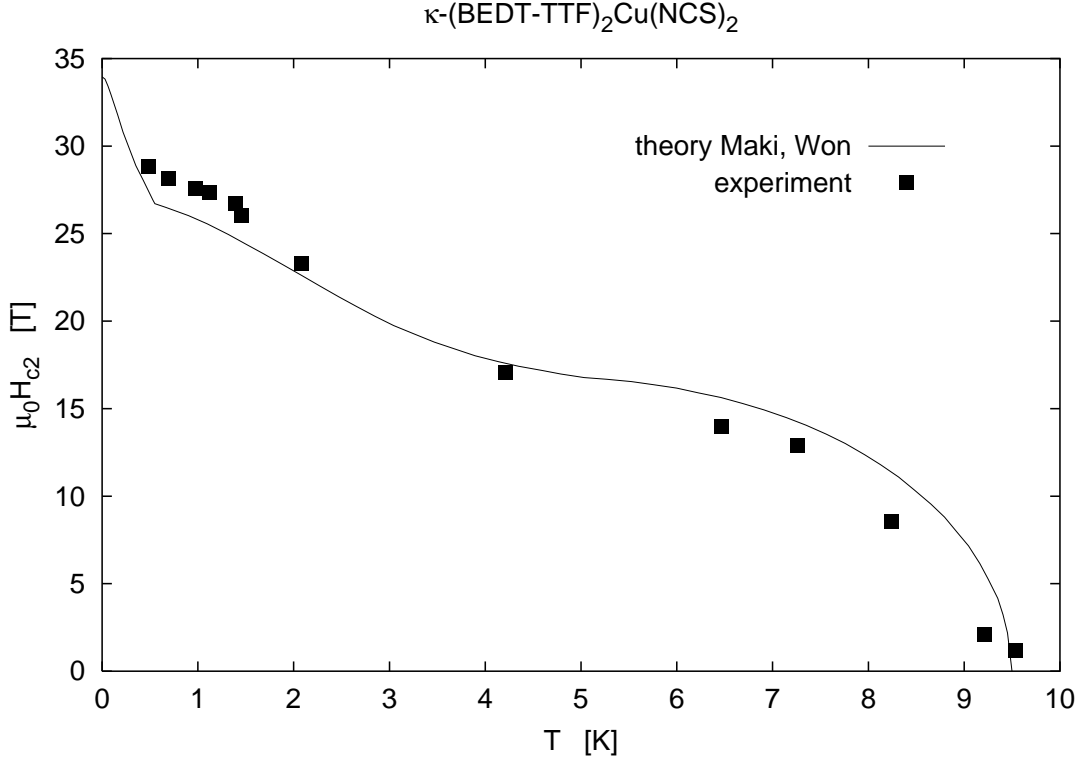


FIGURE 1.14: Comparison of the temperature dependence of the plane-parallel upper critical field reported in reference [9] with the theoretical result reported in reference [36].

curves shown in figure 1.15. The resistance data reported in reference show a non-monotonic behaviour near the plane-parallel field orientation (Fig. 3 of Ref. [38]), which may be due to transitions to the $n > 0$ states.

Summarizing, the proposal of Nam et al [9], that upper critical field data for a plane-parallel field orientation in the layered organic superconductor κ -(BEDT-TTF) $_2$ Cu(NCS) $_2$ should be interpreted in terms of a FFLO state, has been supported by our calculations. The data agree with the predictions of a model of a quasi-two-dimensional superconductor as regards both the angular and the temperature dependence of the critical field. Further confirmation of this interpretation could be obtained by means of measurements at higher temperatures, where paramagnetic pair breaking is strongly reduced. If this interpretation is correct, precursor states with interesting properties should appear for applied fields close to the plane-parallel orientation.

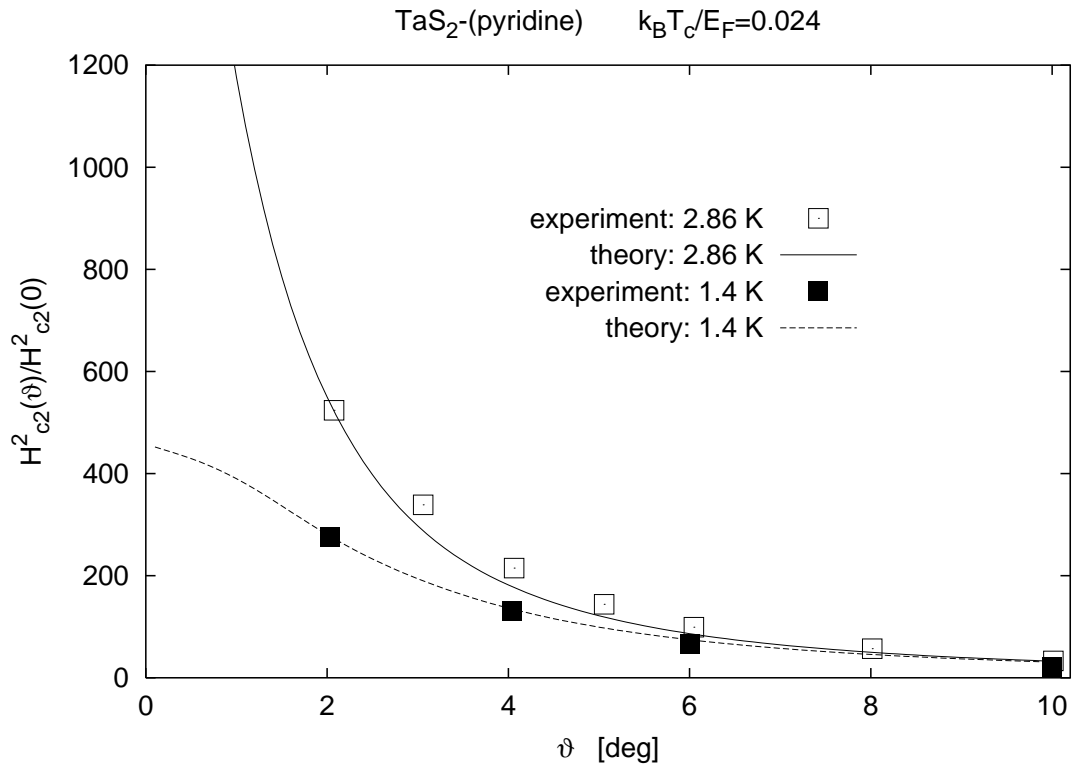


FIGURE 1.15: Comparison of the ϑ -dependence of the upper critical field of TaS_2 -(pyridine), as reported in reference [38], with the solutions of equation (1.34) for s -wave superconductivity at $t = 2.86$ and $t = 1.4$.

Chapter 2

Layered superconductors with finite thickness d

In the previous chapter we have derived the H_{c2} -equations of a 2-dimensional superconductor for a variable angle ϑ of the external magnetic field and compared the numerical results with experimental data on the organic superconductor κ -(BEDT-TTF)₂Cu(NCS)₂ and on TaS₂-*pyridine*. The Fulde-Ferrell-Larkin-Ovchinnikov (FFLO) state [7, 8], which is a spatially inhomogeneous superconducting state, is predicted to occur in clean superconductors with purely paramagnetic limiting. Agreement between experiment [9] and existing theories has been successfully checked [10] both in view of the angle-dependence [11] and the temperature dependence [12] of the upper critical field.

As these systems almost have 2-dimensional electronic properties, we obtained very good agreement with the experimental results. A small transverse dimension $d \ll \xi_0$ of the film suppresses the orbital effect and enlarges the spin effect rigorously. Strong paramagnetic effects can also be expected for the High- T_c cuprate superconductors at low temperatures, when the conducting planes in adjacent unit cells are well separated from each other. This is due to the fact that the critical thickness, which separates the spin pair-breaking and orbital pair-breaking dominated regimes, is still of the order of an atomic distance. Thus, a nearly perfect two-dimensional situation is required in order to justify the neglect of orbital pair breaking contribution in clean superconductors.

In this Chapter we investigate a superconducting film of finite thickness in a magnetic field with a certain angle ϑ to the conducting plane. Thus, the usual model of purely paramagnetic pair breaking is generalized in a different way, taking into account the influence of a finite orbital pair breaking component on the FFLO state. The model is formulated in Section 2.1, using the framework of the quasiclassical Eilenberger equations. We assume that the film thickness is smaller than the coherence length and use a cylindrical Fermi surface. This

shape of the Fermi surface allows us to study the influence of orbital pair breaking without any additional complications, like scattering of quasiparticles at the film boundaries. Such boundary effects seem less important in the present context, but may, nevertheless, be present in many materials and should be taken into account in future work. In addition, the cylindrical shape of the Fermi surface, which corresponds to a truly 2-dimensional situation, allows us to extend our investigations to superconducting layers of atomic dimension. The phase diagrams, obtained by solving numerically the relevant phase boundary and stability equations, are reported in Section 2.2. Thermodynamic properties are calculated with the help of the free energy difference between normal and superconducting states, and a discussion of possible orbital pair breaking contributions in the plane-parallel field configuration of $\text{YBa}_2\text{Cu}_3\text{O}_7$ is conducted in Section 2.3.

Results of the critical field calculations show, that at temperatures below a tricritical temperature there are two boundary solutions for the critical field: the upper stability limit, which is of first order and at which the gap is still finite, and the lower stability limit, which is a second order phase transition. Impurity scattering is accounted for in Section 2.4 and the tunneling measurements of Ref. [5] on a thin Al film is compared with the numerical results on the upper and lower stability limit of a system with finite thickness.

2.1 Derivation of the Gap-equation

With a complete set of orthogonal eigenfunctions $\Phi_n(\mathbf{r})$, the gap-function can be expressed as

$$\Delta(\mathbf{r}) = \sum_n \int d^3r_1 \Phi_n^*(\mathbf{r}_1) \Phi_n(\mathbf{r}) \Delta(\mathbf{r}_1), \quad (2.1)$$

where n is the discrete index of the eigenfunctions, which can also be degenerate and continuous. In the latter case the summation is transformed into an integration

$$\sum_n \rightarrow \int \frac{d^3p}{(2\pi)^3}. \quad (2.2)$$

The differential equation for the Green's function $f_{(+)}(\mathbf{r})$ is given by (eq. (1.1) with $g_{(+)} = \text{sgn}\omega_l$)

$$\left[(|\omega_l| - i\text{sgn}\omega_l\mu H) + \frac{1}{2}\text{sgn}\omega_l\hbar\mathbf{v}_F\partial_{\mathbf{r}} \right] f_{(+)}(\mathbf{r}) = \Delta(\mathbf{r}).$$

The operator $\partial_{\mathbf{r}}$ is given in eq. (1.2). The Fermi velocity \mathbf{v}_F can be written as $\mathbf{v}_F = v_F\hat{\mathbf{k}}$, with the unit vector $\hat{\mathbf{k}} = \mathbf{v}_F/v_F$ and

$$v_F = \sqrt{v_{F,x}^2 + v_{F,y}^2 + v_{F,z}^2}. \quad (2.3)$$

If the Fermi surface is cylindrical ($v_{F,z} = 0$ or $\hat{k}_z = 0$), \mathbf{v}_F is given by eq. (1.4), with v_F as the radius of the cylinder. In general, the z -component has to be taken into account and v_F is calculated from eq. (2.3).

In the following the complete set of orthogonal eigenfunctions of the operator $\hat{\mathbf{k}}\partial_{\mathbf{r}}$ are denoted by $f_{\hat{\mathbf{k}},\mathbf{p}}(\mathbf{r})$ with the eigenvalues $i\hat{\mathbf{k}}\mathbf{p}$:

$$\hat{\mathbf{k}}\left(\nabla_{\mathbf{r}} - i\frac{2e}{\hbar c}\mathbf{A}\right)f_{\hat{\mathbf{k}},\mathbf{p}}(\mathbf{r}) = \hat{\mathbf{k}}\partial_{\mathbf{r}}f_{\hat{\mathbf{k}},\mathbf{p}}(\mathbf{r}) = i\hat{\mathbf{k}}\mathbf{p}f_{\hat{\mathbf{k}},\mathbf{p}}(\mathbf{r}). \quad (2.4)$$

The eigenfunctions $f_{\hat{\mathbf{k}},\mathbf{p}}(\mathbf{r})$ have the property

$$F(\mathbf{r}) = \int d^3r_1 \delta(\mathbf{r} - \mathbf{r}_1)F(\mathbf{r}_1) = \int \frac{d^3p}{(2\pi)^3} \int d^3r_1 f_{\hat{\mathbf{k}},\mathbf{p}}^*(\mathbf{r}_1)f_{\hat{\mathbf{k}},\mathbf{p}}(\mathbf{r})F(\mathbf{r}_1). \quad (2.5)$$

Using the above completeness relation explicitly, and the summation over the index n in eq. (2.1) transformed into an integral (2.2), the Green's function $f_{(+)}(\mathbf{r})$ can be expressed as

$$f_{(+)}(\mathbf{r}) = \int \frac{d^3p}{(2\pi)^3} \int d^3r_1 \frac{f_{\hat{\mathbf{k}},\mathbf{p}}^*(\mathbf{r}_1)f_{\hat{\mathbf{k}},\mathbf{p}}(\mathbf{r})}{\omega_a + i\text{sgn}\omega_l\hbar\mathbf{v}_{\mathbf{F}}\mathbf{p}/2} \Delta(\mathbf{r}_1), \quad (2.6)$$

with $\omega_a = |\omega_l| - i\text{sgn}\omega_l\mu H$ and by replacing $v_F\hat{\mathbf{k}}\partial_{\mathbf{r}}$ with its eigenvalue $iv_F\hat{\mathbf{k}}\mathbf{p} = i\mathbf{v}_{\mathbf{F}}\mathbf{p}$ (2.4).

The finite thickness of the superconducting film is accounted for by restricting the integration over the spatial coordinate z to an interval $[-d/2, d/2]$

$$\int d^3r \Theta\left(\frac{d}{2} + z\right) \Theta\left(\frac{d}{2} - z\right) = \int_{-\infty}^{\infty} dx \int_{-\infty}^{\infty} dy \int_{-d/2}^{d/2} dz, \quad (2.7)$$

without imposing the disappearance of the eigenfunctions at the film boundary

$$f_{\hat{\mathbf{k}},\mathbf{p}}\left(x, y, \pm\frac{d}{2}\right) = 0. \quad (2.8)$$

Heavyside's function $\Theta(x)$ is defined to be 1 for $x > 0$ and null otherwise.

2.1.1 Eigenfunctions $f_{\hat{\mathbf{k}},\mathbf{p}}(\mathbf{r})$

One needs a complete set of eigenfunctions $f_{\hat{\mathbf{k}},\mathbf{p}}(\mathbf{r})$ of the operator $\hat{\mathbf{k}}\partial_{\mathbf{r}}$:

$$f_{\hat{\mathbf{k}},\mathbf{p}}(\mathbf{r}) = \exp\left(-\frac{i}{2}\frac{2|e|}{\hbar c}(\hat{\mathbf{k}}\mathbf{r})((\mathbf{H} \times \mathbf{r})\hat{\mathbf{k}}) + ig(\mathbf{r}) + i\mathbf{p}\mathbf{r}\right). \quad (2.9)$$

The function $g(\mathbf{r})$ is determined by solving the differential equation (2.4) for the present gauge (1.14). With the gradient of the eigenfunctions $\nabla_{\mathbf{r}}f_{\hat{\mathbf{k}},\mathbf{p}}(\mathbf{r})$ given by

$$\begin{aligned} \nabla_{\mathbf{r}}f_{\hat{\mathbf{k}},\mathbf{p}}(\mathbf{r}) = & i\left[-\frac{1}{2}\frac{2|e|}{\hbar c}\hat{\mathbf{k}}((\mathbf{H} \times \mathbf{r})\hat{\mathbf{k}}) + \right. \\ & \left. \frac{1}{2\hbar}(\hat{\mathbf{k}}\mathbf{r})\begin{pmatrix} \hat{k}_z\kappa_{\parallel} - \hat{k}_y\kappa_{\perp} \\ \kappa_{\perp}\hat{k}_x \\ -\kappa_{\parallel}\hat{k}_x \end{pmatrix} + \nabla g(\mathbf{r}) + \mathbf{p}\right]f_{\hat{\mathbf{k}},\mathbf{p}}(\mathbf{r}), \end{aligned} \quad (2.10)$$

with $\kappa_{\perp} = 2|e|H_{\perp}/c$, $\kappa_{\parallel} = 2|e|H_{\parallel}/c$, and

$$\frac{2|e|}{\hbar c}(\mathbf{H} \times \mathbf{r})\hat{\mathbf{k}} = \frac{1}{\hbar} \left[(\kappa_{\parallel}z - \kappa_{\perp}y)\hat{k}_x + \kappa_{\perp}x\hat{k}_y - \kappa_{\parallel}x\hat{k}_z \right], \quad (2.11)$$

equation (2.4) yields

$$\begin{aligned} \hat{\mathbf{k}} \left(\nabla_{\mathbf{r}} + i \frac{2|e|}{\hbar c} \mathbf{A} - i\mathbf{p} \right) &= 0 \\ &= i \left\{ -\frac{1}{2\hbar} [-\hat{k}_x(\kappa_{\parallel}z - \kappa_{\perp}y) + \hat{k}_y\kappa_{\perp}x - \hat{k}_z\kappa_{\parallel}x] + \right. \\ &\quad \hat{\mathbf{k}}\nabla_{\mathbf{r}}g(\mathbf{r}) + \frac{1}{2\hbar}(\hat{\mathbf{k}}\mathbf{r}) \left[\hat{k}_x\hat{k}_z\kappa_{\parallel} - \hat{k}_x\hat{k}_y\kappa_{\perp} + \right. \\ &\quad \left. \left. \hat{k}_x\hat{k}_y\kappa_{\perp} - \hat{k}_x\hat{k}_z\kappa_{\parallel} \right] \right\}. \end{aligned} \quad (2.12)$$

The expression in the large square brackets at the end of the equation gives $[\dots] = 0$, which results in the following differential equation for $g(\mathbf{r})$

$$(\hat{k}_x\partial_x + \hat{k}_y\partial_y + \hat{k}_z\partial_z)g(\mathbf{r}) = \frac{1}{2\hbar} \left(-\hat{k}_x(\kappa_{\parallel}z - \kappa_{\perp}y) + \hat{k}_y\kappa_{\perp}x - \hat{k}_z\kappa_{\parallel}x \right). \quad (2.13)$$

One finds for its components:

$$\begin{aligned} \partial_x g(\mathbf{r}) &= -\frac{1}{2\hbar} (\kappa_{\parallel}z - \kappa_{\perp}y) \\ \partial_y g(\mathbf{r}) &= \frac{1}{2\hbar} \kappa_{\perp}x \\ \partial_z g(\mathbf{r}) &= -\frac{1}{2\hbar} \kappa_{\parallel}x, \end{aligned} \quad (2.14)$$

which give the function

$$g(\mathbf{r}) = -\frac{1}{2\hbar} (\kappa_{\parallel}z - \kappa_{\perp}y)x. \quad (2.15)$$

Therefore, the complete set of orthogonal eigenfunctions $f_{\hat{\mathbf{k}},\mathbf{p}}(\mathbf{r})$ is obtained as

$$f_{\hat{\mathbf{k}},\mathbf{p}}(\mathbf{r}) = \exp \left(-\frac{i}{2} \left[\frac{2|e|}{\hbar c} (\hat{\mathbf{k}}\mathbf{r}) \left((\mathbf{H} \times \mathbf{r})\hat{\mathbf{k}} \right) + \frac{1}{\hbar} (\kappa_{\parallel}z - \kappa_{\perp}y)x \right] + i\mathbf{p}\mathbf{r} \right) \quad (2.16)$$

for the chosen gauge.

2.1.2 Calculation of the Green's function $f_{(+)}(\mathbf{r})$

With the help of the identity

$$\frac{1}{r} \equiv \int_0^{\infty} ds e^{-rs} \quad (2.17)$$

the Green's function $f_{(+)}(\mathbf{r})$ (2.6) can be written as

$$f_{(+)}(\mathbf{r}) = \int_0^{\infty} ds \int \frac{d^3p}{(2\pi)^3} \int d^3r_1 f_{\hat{\mathbf{k}},\mathbf{p}}^*(\mathbf{r}_1) f_{\hat{\mathbf{k}},\mathbf{p}}(\mathbf{r}) \exp \left(-s \left[\omega_a + \frac{i}{2} \text{sgn}\omega_l \hbar \mathbf{v}_{\mathbf{F}}\mathbf{p} \right] \right) \times$$

$$\begin{aligned}
& \Theta\left(\frac{d}{2} + z\right) \Theta\left(\frac{d}{2} - z\right) \Delta(\mathbf{r}_1) \\
&= \int_0^\infty ds e^{-s\omega_a} \int_{-\infty}^\infty d^2 r_1 \int_{-d/2}^{d/2} dz_1 \times \\
& \exp\left(-\frac{i}{2} \frac{2|e|}{\hbar c} \left[(\hat{\mathbf{k}}\mathbf{r}) \left((\mathbf{H} \times \mathbf{r})\hat{\mathbf{k}}\right) - (\hat{\mathbf{k}}\mathbf{r}_1) \left((\mathbf{H} \times \mathbf{r}_1)\hat{\mathbf{k}}\right)\right]\right) \times \\
& \exp\left(-\frac{i}{2\hbar} \left[(\kappa_{\parallel} z - \kappa_{\perp} y)x\right] - (\kappa_{\parallel} z_1 - \kappa_{\perp} y_1)x_1\right) \times \\
& \int \frac{d^3 p}{(2\pi)^3} \exp\left(i\mathbf{p} \left[\mathbf{r} - \mathbf{r}_1 - \hbar\mathbf{v}_F \text{sgn}\omega_l \frac{s}{2}\right]\right) \Delta(\mathbf{r}_1).
\end{aligned} \tag{2.18}$$

The integration over p results in a δ -function

$$\int \frac{d^3 p}{(2\pi)^3} \exp\left(i\mathbf{p} \left[\mathbf{r} - \mathbf{r}_1 - \hbar\mathbf{v}_F \text{sgn}\omega_l \frac{s}{2}\right]\right) = \delta\left(\mathbf{r} - \mathbf{r}_1 - \hbar\mathbf{v}_F \text{sgn}\omega_l \frac{s}{2}\right), \tag{2.19}$$

with x_1 and y_1 replaced by $x - \hbar v_F \hat{k}_x \text{sgn}\omega_l \frac{s}{2}$ and $y - \hbar v_F \hat{k}_y \text{sgn}\omega_l \frac{s}{2}$ in the integration over x_1 and y_1 in eq. (2.18), because all these coordinates are defined in the range between $-\infty$ and ∞ , respectively. For z_1 the range is restricted to $-\frac{d}{2} \leq z_1 \leq \frac{d}{2}$ which leads to the condition

$$-\frac{d}{2} \leq z - \hbar v_F \hat{k}_z \text{sgn}\omega_l \frac{s}{2} \leq \frac{d}{2}. \tag{2.20}$$

After performing the \mathbf{r}_1 -integration the following terms in the exponential function of eq. (2.18) are determined:

$$\begin{aligned}
& (\hat{\mathbf{k}}\mathbf{r}) \left\{ (\mathbf{H} \times \mathbf{r})\hat{\mathbf{k}} \right\} - \left\{ \hat{\mathbf{k}} \left(\mathbf{r} - \hbar\mathbf{v}_F \text{sgn}\omega_l \frac{s}{2} \right) \right\} \left\{ \mathbf{H} \times \left(\mathbf{r} - \hbar\mathbf{v}_F \text{sgn}\omega_l \frac{s}{2} \right) \hat{\mathbf{k}} \right\} = \\
& (\hat{\mathbf{k}}\mathbf{r}) \left\{ (\mathbf{H} \times \mathbf{r})\hat{\mathbf{k}} \right\} - (\hat{\mathbf{k}}\mathbf{r}) \left\{ \mathbf{H} \times \left(\mathbf{r} - \hbar\mathbf{v}_F \text{sgn}\omega_l \frac{s}{2} \right) \hat{\mathbf{k}} \right\} + \\
& \hbar v_F \text{sgn}\omega_l \frac{s}{2} \left\{ \mathbf{H} \times \left(\mathbf{r} - \hbar\mathbf{v}_F \text{sgn}\omega_l \frac{s}{2} \right) \hat{\mathbf{k}} \right\} = \\
& (\hat{\mathbf{k}}\mathbf{r}) \left\{ (\mathbf{H} \times \mathbf{r})\hat{\mathbf{k}} \right\} - (\hat{\mathbf{k}}\mathbf{r}) \left\{ (\mathbf{H} \times \mathbf{r})\hat{\mathbf{k}} \right\} + \text{sgn}\omega_l \frac{s}{2} (\hat{\mathbf{k}}\mathbf{r}) \left\{ (\mathbf{H} \times \hbar\mathbf{v}_F) \hat{\mathbf{k}} \right\} + \\
& \hbar v_F \text{sgn}\omega_l \frac{s}{2} \left\{ (\mathbf{H} \times \mathbf{r})\hat{\mathbf{k}} \right\} - \hbar v_F \frac{s^2}{4} \left\{ (\mathbf{H} \times \hbar\mathbf{v}_F) \hat{\mathbf{k}} \right\} = \\
& \text{sgn}\omega_l \frac{s}{2} \left\{ (\mathbf{H} \times \mathbf{r})\hbar\mathbf{v}_F \right\},
\end{aligned} \tag{2.21}$$

which results in

$$\frac{2|e|}{\hbar c} \text{sgn}\omega_l \frac{s}{2} \left\{ (\mathbf{H} \times \mathbf{r})\hbar\mathbf{v}_F \right\} = \text{sgn}\omega_l v_F \frac{s}{2} \left\{ (\kappa_{\parallel} z - \kappa_{\perp} y)\hat{k}_x + \kappa_{\perp} x\hat{k}_y - \kappa_{\parallel} x\hat{k}_z \right\}. \tag{2.22}$$

The second contribution is

$$\frac{1}{\hbar} \left[(\kappa_{\parallel} z - \kappa_{\perp} y)x - \left(\kappa_{\parallel} \left(z - \hbar v_F \text{sgn}\omega_l \hat{k}_z \frac{s}{2} \right) - \kappa_{\perp} \left(y - \hbar v_F \text{sgn}\omega_l \hat{k}_y \frac{s}{2} \right) \right) \right] \times$$

$$\begin{aligned}
& \left(x - \hbar v_F \text{sgn} \omega_l \hat{k}_x \frac{s}{2} \right) = \\
& \text{sgn} \omega_l \frac{s}{2} v_F \left(-\kappa_{\perp} x \hat{k}_y + \kappa_{\parallel} x \hat{k}_z + \kappa_{\parallel} z \hat{k}_x - \kappa_{\perp} y \hat{k}_x \right) + \\
& \frac{s^2}{4} \hbar v_F^2 \left(\kappa_{\perp} \hat{k}_y - \kappa_{\parallel} \hat{k}_z \right) \hat{k}_x.
\end{aligned} \tag{2.23}$$

Equations (2.22) and (2.23) yield

$$\text{sgn} \omega_l s v_F (\kappa_{\parallel} z - \kappa_{\perp} y) \hat{k}_x + \frac{s^2}{4} \hbar v_F^2 (\kappa_{\perp} \hat{k}_y - \kappa_{\parallel} \hat{k}_z) \hat{k}_x, \tag{2.24}$$

resulting in the the Green's function

$$\begin{aligned}
f_{(+)}(\mathbf{r}) &= \int_0^{\infty} ds e^{-s\omega_a} \exp \left(-\frac{i}{2} \left[\text{sgn} \omega_l s v_F (\kappa_{\parallel} z - \kappa_{\perp} y) \hat{k}_x + \frac{s^2}{4} v_F^2 \hbar (\kappa_{\perp} \hat{k}_y - \kappa_{\parallel} \hat{k}_z) \hat{k}_x \right] \right) \times \\
& \Theta \left(\frac{d}{2} + z - \hbar v_F \text{sgn} \omega_l \hat{k}_z \frac{s}{2} \right) \Theta \left(\frac{d}{2} - z + \hbar v_F \text{sgn} \omega_l \hat{k}_z \frac{s}{2} \right) \times \\
& \Delta \left(\mathbf{r} - \text{sgn} \omega_l \frac{s}{2} \hbar \mathbf{v}_F \right),
\end{aligned} \tag{2.25}$$

which is given only if restriction (2.20) applies, otherwise $f_{(+)}(\mathbf{r}) = 0$.

If the z_1 -integration is carried out first, the same result for the Green's function is obtained, which is shown in appendix B.1 in the case of $\hat{k}_z = 0$. The p_z -integration results in Heavyside Θ -functions corresponding to the condition (2.20). The same result for $f_{(+)}(\mathbf{r})$ also applies, if the p_z -component is taken to be periodic with a period $2\pi/d$, transforming the integration over p_z into an infinite summation over a discrete index. See appendix B.2 for details.

2.1.3 Equivalence to the z -independent formalism

The z - and k_z -independent part of eq (2.25) is denoted as $f^{(1)}(x, y)$:

$$f^{(1)}(x, y) = \int_0^{\infty} ds e^{-s\omega_a} \exp \left(\frac{i}{2} \left[\text{sgn} \omega_l s v_F \kappa_{\perp} y \hat{k}_x - \frac{s^2}{4} v_F^2 \hbar \kappa_{\perp} \hat{k}_x \hat{k}_y \right] \right) \Delta \left(\mathbf{r} - \text{sgn} \omega_l \frac{s}{2} \hbar \mathbf{v}_F \right), \tag{2.26}$$

with $\mathbf{r} = (x, y)$. As it is the same differential equation (1.1) leading to this result and to $f_{(+)}(\mathbf{r})$ of eq. (1.8) (now written as $f^{(2)}(x, y)$), the two functions are equivalent, which is shown below.

The z -independent Green's function was written as

$$\begin{aligned}
f^{(2)}(x, y) &= \int_0^{\infty} ds e^{-s\omega_a} \exp \left(-\frac{1}{2} \text{sgn} \omega_l s \hbar \mathbf{v}_F \partial_{\mathbf{r}} \right) \Delta(\mathbf{r}) \\
&= \int_0^{\infty} ds e^{-s\omega_a} \exp \left(-\frac{1}{2} \text{sgn} \omega_l s \hbar \mathbf{v}_F \left[\nabla_{\mathbf{r}} + i \frac{2|e|}{\hbar c} \mathbf{A} \right] \right) \Delta(\mathbf{r})
\end{aligned}$$

$$= \int_0^\infty ds e^{-s\omega_a} \exp \left(\frac{i}{2} \left\{ \text{sgn}\omega_l s v_F \kappa_\perp y \hat{k}_x + \frac{s^2}{4} \frac{2|e|}{c} \hbar v_F^2 \left[\hat{\mathbf{k}} \nabla_{\mathbf{r}}, \hat{\mathbf{k}} \mathbf{A} \right] \right\} \right) \times \exp \left(-\frac{s}{2} \text{sgn}\omega_l \hbar \mathbf{v}_{\mathbf{F}} \nabla_{\mathbf{r}} \right) \Delta(\mathbf{r}), \quad (2.27)$$

with the commutation relation

$$\left[\hat{\mathbf{k}} \nabla_{\mathbf{r}}, \hat{\mathbf{k}} \mathbf{A} \right] = \left[\hat{k}_x \partial_x + \hat{k}_y \partial_y + \hat{k}_z \partial_z, -H_\perp y \hat{k}_x \right] = -H_\perp \hat{k}_x \hat{k}_y. \quad (2.28)$$

Therefore $f^{(2)}(x, y)$ is given by

$$f^{(2)}(x, y) = \int_0^\infty ds e^{-s\omega_a} \exp \left(\frac{i}{2} \left[\text{sgn}\omega_l s v_F \kappa_\perp y \hat{k}_x - \frac{s^2}{4} v_F^2 \hbar \kappa_\perp \hat{k}_x \hat{k}_y \right] \right) \times \exp \left(-\frac{s}{2} \text{sgn}\omega_l \hbar \mathbf{v}_{\mathbf{F}} \nabla_{\mathbf{r}} \right) \Delta(\mathbf{r}). \quad (2.29)$$

We now develop $\Delta(\mathbf{r} - \text{sgn}\omega_l \frac{s}{2} \hbar \mathbf{v}_{\mathbf{F}})$ in eq. (2.26) into an infinite Taylor-series

$$\Delta(\mathbf{r} - \text{sgn}\omega_l \frac{s}{2} \hbar \mathbf{v}_{\mathbf{F}}) = \sum_{n=0}^\infty \frac{(-\text{sgn}\omega_l s \hbar \mathbf{v}_{\mathbf{F}})^n}{n! 2^n} \nabla_{\mathbf{r}}^n \Delta(\mathbf{r}) = \exp \left(-\frac{s}{2} \text{sgn}\omega_l \hbar \mathbf{v}_{\mathbf{F}} \nabla_{\mathbf{r}} \right) \Delta(\mathbf{r}). \quad (2.30)$$

It is obvious by comparing eqs. (2.26), (2.29), and (2.30) that

$$f^{(2)}(x, y) = f^{(1)}(x, y) \quad (2.31)$$

2.1.4 Green's function $f_{(-)}(\mathbf{r})$

As in the case of $f_{(+)}(\mathbf{r})$, the differential equation for the Green's function $f_{(-)}(\mathbf{r})$ is given by eq. (1.1) with $g_{(+)} = \text{sgn}\omega_l$. The function $f_{(-)}(\mathbf{r})$ is then determined by

$$f_{(-)}(\mathbf{r}) = \int \frac{d^3 p}{(2\pi)^3} \int d^3 r_1 \frac{f_{\mathbf{k}, \mathbf{p}}^*(\mathbf{r}_1) f_{\mathbf{k}, \mathbf{p}}(\mathbf{r})}{\omega_a - i \text{sgn}\omega_l \hbar \mathbf{v}_{\mathbf{F}} \mathbf{p} / 2} \Delta(\mathbf{r}_1). \quad (2.32)$$

After following the same steps as in the calculation of $f_{(+)}(\mathbf{r})$, one finds

$$f_{(-)}(\mathbf{r}) = \int_0^\infty ds e^{-s\omega_a^*} \exp \left(\frac{i}{2} \left[\text{sgn}\omega_l s v_F (\kappa_\parallel z - \kappa_\perp y) \hat{k}_x - \frac{s^2}{4} v_F^2 \hbar (\kappa_\perp \hat{k}_y - \kappa_\parallel \hat{k}_z) \hat{k}_x \right] \right) \times \Theta \left(\frac{d}{2} - z - \hbar v_F \text{sgn}\omega_l \hat{k}_z \frac{s}{2} \right) \Theta \left(\frac{d}{2} + z + \hbar v_F \text{sgn}\omega_l \hat{k}_z \frac{s}{2} \right) \times \Delta \left(\mathbf{r} + \text{sgn}\omega_l \frac{s}{2} \hbar \mathbf{v}_{\mathbf{F}} \right) \quad (2.33)$$

which is given for

$$-\frac{d}{2} \leq z + \hbar v_F \hat{k}_z \text{sgn}\omega_l \frac{s}{2} \leq \frac{d}{2} \quad (2.34)$$

and is zero if this inequality relation is not fulfilled. As with $f_{(+)}(\mathbf{r})$, it can be easily shown that the z and \hat{k}_z -independent part of $f_{(-)}(\mathbf{r})$ is given by

$$f_{(-)}(x, y) = \int_0^\infty ds e^{-s\omega_a^*} \exp \left(\frac{1}{2} \text{sgn}\omega_l s \hbar \mathbf{v}_{\mathbf{F}} \partial_{\mathbf{r}} \right) \Delta(\mathbf{r}), \quad (2.35)$$

with a z -independent gap function, which corresponds to $f_{(-)}(\mathbf{r})$ of eq. (1.8).

2.1.5 Averaged functions

Still, the Green's functions $f_{(\pm)}$ depend on the spatial coordinate z . To account for the thickness d of the film, the functions are averaged in the interval $[-d/2, d/2]$

$$\bar{f}_{(\pm)}(x, y) = \frac{1}{d} \int_{-d/2}^{d/2} dz f_{(\pm)}(\mathbf{r}) \quad (2.36)$$

before applying eq. (1.9) to calculate the gap-function, in order to obtain a z -independent $\Delta(\mathbf{r})$. For very thin films, such that $d \ll \xi_0$, the gap-function $\Delta(\mathbf{r})$ is assumed to be independent of z . This simple method works only for a cylindrical Fermi surface, where the momentum of the quasiparticles is always parallel to the film boundaries. Otherwise, quasi-particle scattering at the film boundaries leads, for small $d < \xi_0$, to a modification of the integral kernel which has to be calculated by solving this equation in a finite volume, with appropriate boundary conditions.

Assuming that the Fermi surface is circular ($\hat{k}_z = 0$), the average over the z -dependent part of eqs. (2.25) and (2.33) gives

$$\begin{aligned} \frac{1}{d} \int_{-d/2}^{d/2} dz \exp\left(\mp \frac{i}{2} \text{sgn} \omega_l s v_F \kappa_{\parallel} z \hat{k}_x\right) &= \frac{1}{\mp \frac{i}{2} \text{sgn} \omega_l s v_F \kappa_{\parallel} d \hat{k}_x} \left(\exp\left(\mp \frac{i}{2} \text{sgn} \omega_l s v_F \kappa_{\parallel} \frac{d}{2} \hat{k}_x\right) - \right. \\ &\quad \left. \exp\left(\pm \frac{i}{2} \text{sgn} \omega_l s v_F \kappa_{\parallel} \frac{d}{2} \hat{k}_x\right) \right) \\ &= \frac{1}{\frac{1}{4} s v_F \kappa_{\parallel} d \hat{k}_x} \sin\left(\frac{1}{4} s v_F \kappa_{\parallel} d \hat{k}_x\right). \end{aligned} \quad (2.37)$$

Because $\sin(x)$ is an odd function, $\sin(\text{sgn} \omega_l A)/(\text{sgn} \omega_l A) = \sin(A)/A$ applies. Therefore, the averaged Green's functions $\bar{f}_{(\pm)}(x, y)$ with $\hat{k}_z = 0$ are given by

$$\begin{aligned} \bar{f}_{(\pm)}(x, y) &= \int_0^{\infty} ds \exp(-s(|\omega_l| \mp i \text{sgn} \omega_l \mu H)) \times \\ &\quad \exp\left(\frac{i}{2} \left[\pm \text{sgn} \omega_l s v_F \kappa_{\perp} y \hat{k}_x - \frac{s^2}{4} v_F^2 \hbar \kappa_{\perp} \hat{k}_x \hat{k}_y \right]\right) \times \\ &\quad \frac{1}{\frac{1}{4} s v_F \kappa_{\parallel} d \hat{k}_x} \sin\left(\frac{1}{4} s v_F \kappa_{\parallel} d \hat{k}_x\right) \Delta\left(\mathbf{r} \mp \text{sgn} \omega_l \frac{s}{2} \hbar \mathbf{v}_F\right). \end{aligned} \quad (2.38)$$

2.1.6 Gap-equation

As the x, y -dependence of the Green's function $f_{(+)}(\mathbf{r})$ is the same as in the former situation with $d = 0$ (See sec. 2.1.3), the z and \hat{k}_z -independent part can be written as

$$\exp\left(\frac{i}{2} \left[\text{sgn} \omega_l s v_F \kappa_{\perp} y \hat{k}_x - \frac{s^2}{4} \hbar v_F^2 \kappa_{\perp} \hat{k}_x \hat{k}_y \right]\right) \Delta\left(\mathbf{r} - \text{sgn} \omega_l \frac{s}{2} \hbar \mathbf{v}_F\right) =$$

$$\exp\left(-\frac{1}{2}\text{sgn}\omega_l s\hbar\mathbf{v}_F\partial_{\mathbf{r}}\right)\Delta(\mathbf{r}). \quad (2.39)$$

Analogous to the derivation of the linearized gap-equation in section 1.2 the operator $\mathbf{\Pi} = \partial_{\mathbf{r}}/i$ is expressed in terms of creation and annihilation operators, and as the gap-function $\Delta(\mathbf{r})$ is assumed to be z -independent, the same relations apply for the present situation.

The same procedure applies for the derivation of the gap-equation as in eqs. (1.8-1.22), where the functions $f_{(+)}(\mathbf{r})$ and $f_{(-)}(\mathbf{r})$ are replaced by the z -averaged functions $\bar{f}_{(+)}(x, y)$ and $\bar{f}_{(-)}(x, y)$

$$\bar{f}_{(\pm)}(x, y) = \int_0^\infty ds e^{-s(|\omega_l| \mp i\text{sgn}\omega_l \mu H)} \frac{1}{\frac{1}{4}sv_F\kappa_{\parallel}d\hat{k}_x} \sin\left(\frac{1}{4}sv_F\kappa_{\parallel}d\hat{k}_x\right) e^{\mp\frac{1}{2}\text{sgn}\omega_l s\hbar\mathbf{v}_F\partial_{\mathbf{r}}} \Delta(\mathbf{r}), \quad (2.40)$$

resulting in the gap-equation

$$\begin{aligned} -\ln\left(\frac{T}{T_c^{(0)}}\right)\Delta_{\alpha}(\mathbf{r}) &= \pi k_B T \int_0^\infty ds \frac{1}{\sinh(\pi k_B T s)} \int_0^{2\pi} \frac{d\varphi'}{2\pi} \gamma_{\alpha}(\hat{p}')^2 \times \\ &\quad \left[1 - \frac{1}{\frac{1}{4}sv_F\kappa_{\parallel}d\hat{k}'_x} \sin\left(\frac{1}{4}sv_F\kappa_{\parallel}d\hat{k}'_x\right) \times \right. \\ &\quad \left. \cos\left(hs - \frac{1}{2}sv_F\sqrt{\frac{\hbar\kappa_{\perp}}{2}}(e^{i\varphi'}\eta + e^{-i\varphi'}\eta^+)\right) \right] \Delta_{\alpha}(\mathbf{r}). \end{aligned} \quad (2.41)$$

2.1.7 Gap equation for s -wave symmetry

As in the previous chapter, the cosine-term in eq. (2.41) is split into cosine and sine functions of φ' (eq. (1.24)), in which the cosine term results in eq. (1.28). Now the function

$$\frac{1}{\frac{1}{4}sv_F\kappa_{\parallel}d\hat{k}'_x} \sin\left(\frac{1}{4}sv_F\kappa_{\parallel}d\hat{k}'_x\right) = \frac{1}{A \cos \varphi'} \sin(A \cos \varphi'), \quad (2.42)$$

with $A = \frac{1}{4}sv_F\kappa_{\parallel}d$, is expanded into the series

$$\begin{aligned} &\frac{1}{A \cos \varphi'} \sum_{j=0}^{\infty} \frac{(-1)^j}{(2j+1)!} (A \cos \varphi')^{2j+1} \\ &= \sum_{j=0}^{\infty} \frac{(-1)^j}{(2j+1)!} \left(\frac{A}{2}\right)^{2j} (e^{i\varphi'} + e^{-i\varphi'})^{2j} \\ &= \sum_{j=0}^{\infty} \frac{(-1)^j}{(2j+1)!} \left(\frac{A}{2}\right)^{2j} \sum_{k=0}^{2j} \binom{2j}{k} e^{-i\varphi'k} e^{i\varphi'(2j-k)} \\ &= \sum_{j=0}^{\infty} \sum_{k=0}^{2j} \frac{(-1)^j}{k!(2j-k)!(2j+1)} \left(\frac{A}{2}\right)^{2j} e^{2i\varphi'(j-k)}, \end{aligned} \quad (2.43)$$

which leads to

$$e^{-\frac{v^2}{2}} \sum_{m=0}^{\infty} \sum_{l=0}^{\infty} \sum_{j=0}^{\infty} \sum_{k=0}^{2j} \int_0^{2\pi} \frac{d\varphi'}{2\pi} \frac{(-1)^j}{k!(2j-k)!(2j+1)} \left(\frac{A}{2}\right)^{2j} \\ \times \frac{1}{2} (i^{l+m} + (-i)^{l+m}) \frac{1}{l!m!} v^{l+m} \eta^{+m} \eta^l e^{i\varphi'(l-m+2(j-k))} \quad (2.44)$$

with the use of eq. (1.28). The φ' -integration gives

$$\int_0^{2\pi} \frac{d\varphi'}{2\pi} e^{i\varphi'(l-m+2(j-k))} = \delta_{m, l+2(j-k)} \quad (2.45)$$

resulting in

$$e^{-\frac{v^2}{2}} \sum_{l=0}^{\infty} \sum_{j=0}^{\infty} \sum_{k=0}^{2j} \frac{(-1)^{l+k}}{l!(l+2(j-k))!} v^{2(l+j-k)} \frac{1}{k!(2j-k)!(2j+1)} \left(\frac{A}{2}\right)^{2j} \eta^{+l+2(j-k)} \eta^l \quad (2.46)$$

for eq. (2.44). The condition

$$l + 2(j - k) \geq 0 \quad (2.47)$$

must be fulfilled, because $m \geq 0$. Applying the wavefunctions $\langle \Phi_{n'} |$ to the left and $|\Phi_n\rangle$ to the right side of the creation and annihilation operators in eq. (2.46) gives

$$\langle n' | \eta^{+l+2(j-k)} \eta^l | n \rangle = \sqrt{\frac{n!n!}{(n-l)!(n' - [l + 2(j-k)])!}} \delta_{n', n+2(j-k)}, \quad (2.48)$$

where the conditions $l \leq n$ and $l \leq n' - 2(j-k)$ must be fulfilled. The summation over n' and the gap-coefficients $\Delta_{n'}$ yields

$$e^{-\frac{v^2}{2}} \sum_{l=0}^n \sum_{j=0}^{\infty} \sum_{k=0}^{2j} v^{2(l+j-k)} \frac{(-1)^{l+k}}{k!(2j-k)!(2j+1)} \left(\frac{A}{2}\right)^{2j} \frac{\sqrt{n!(n+2(j-k))!}}{(n-l)!l!(l+2(j-k))!} \Delta_{n+2(j-k)}, \quad (2.49)$$

and we obtain the gap-equation for a superconductor with s -wave symmetry and finite thickness d

$$-\ln\left(\frac{T}{T_c^{(0)}}\right) = \pi k_B T \int_0^{\infty} ds \frac{1}{\sinh(\pi k_B T s)} \left(1 - \cos(hs) e^{-s^2 v_F^2 \hbar \kappa_{\perp} / 16} \times \right. \\ \left. \sum_{l=0}^n \sum_{j=0}^{\infty} \sum_{k=0}^{2j} \left(\frac{s^2 v_F^2 \hbar \kappa_{\perp}}{8}\right)^{l+j-k} \frac{(-1)^{l+k}}{k!(2j-k)!(2j+1)} \times \right. \\ \left. \left(\frac{1}{64} s^2 v_F^2 \kappa_{\parallel}^2 d^2\right)^j \frac{\sqrt{n!(n+2(j-k))!}}{(n-l)!l!(l+2(j-k))!} \frac{\Delta_{n+2(j-k)}}{\Delta_n} \right). \quad (2.50)$$

Notice that coupling between gap-coefficients of different Landau levels occur. In the limit $d \rightarrow 0$ the same solution as in $d = 0$ is obtained (1.34).

2.1.8 Gap equation for d -wave symmetry

Analogous to the previous calculation of the gap equation for $d = 0$ (Sec. 1.3.2) and following the steps outlined in the previous section, we obtain for the part with $\cos(4\varphi')$

$$e^{-\frac{v^2}{2}} \sum_{m=0}^{\infty} \sum_{l=0}^{\infty} \sum_{j=0}^{\infty} \sum_{k=0}^{2j} \int_0^{2\pi} \frac{d\varphi'}{2\pi} \frac{(-1)^j}{k!(2j-k)!(2j+1)} \left(\frac{A}{2}\right)^{2j} \times \\ \frac{1}{2} (i^{l+m} + (-i)^{l+m}) \frac{1}{l!m!} v^{l+m} \eta^{+m} \eta^l e^{i\varphi'(l-m+2(j-k))} \cos(4\varphi'). \quad (2.51)$$

The φ' -integration gives

$$\int_0^{2\pi} \frac{d\varphi'}{2\pi} e^{i\varphi'(l-m+2(j-k))} \cos(4\varphi') = \frac{1}{2} \left(\delta_{m, l+2(j-k)+4} + \delta_{m, l+2(j-k)-4} \right), \quad (2.52)$$

resulting in

$$e^{-\frac{v^2}{2}} \sum_{l=0}^{\infty} \sum_{j=0}^{\infty} \sum_{k=0}^{2j} \frac{(-1)^{l+k}}{k!(2j-k)!(2j+1)} \left(\frac{A}{2}\right)^{2j} \times \\ \frac{1}{2} \left(\frac{1}{l!(l+2(j-k)+4)!} v^{2(l+j-k+2)} \eta^{+l+2(j-k)+4} \eta^l + \right. \\ \left. \frac{1}{l!(l+2(j-k)-4)!} v^{2(l+j-k-2)} \eta^{+l+2(j-k)-4} \eta^l \right) \quad (2.53)$$

for eq. (2.51). The conditions

$$l + 2(j - k) \pm 4 \geq 0 \quad (2.54)$$

must be fulfilled, because $m \geq 0$. Application of the wavefunctions $\langle \Phi'_n |$ to the left and $|\Phi_n\rangle$ to the right side of the creation and annihilation operators in eq. (2.46) gives

$$(i) \quad \langle n' | \eta^{+l+2(j-k)+4} \eta^l | n \rangle = \sqrt{\frac{n!n'}{(n-l)!(n'-[l+2(j-k)+4])!}} \delta_{n', n+2(j-k)+4} \\ (ii) \quad \langle n' | \eta^{+l+2(j-k)-4} \eta^l | n \rangle = \sqrt{\frac{n!n'}{(n-l)!(n'-[l+2(j-k)-4])!}} \delta_{n', n+2(j-k)-4}, \quad (2.55)$$

where the conditions $l \leq n$ applies for the first (i) and for the second (ii) case. Multiplying (2.53) with the gap-coefficient Δ_n and the sum over n' yields

$$\sum_{j=0}^{\infty} \sum_{k=0}^{2j} D_{n, n+2(j-k)+4, j, k}^{(4,1)} \Delta_{n+2(j-k)+4} = e^{-\frac{v^2}{2}} \sum_{j=0}^{\infty} \sum_{k=0}^{2j} \sum_{l=0}^n \frac{(-1)^{l+k}}{k!(2j-k)!(2j+1)} \times \\ \left(\frac{A}{2}\right)^{2j} \frac{1}{2} \frac{1}{l!(l+2(j-k)+4)!} \times \\ v^{2(l+j-k+2)} \frac{\sqrt{n!(n+2(j-k)+4)!}}{(n-l)!} \times$$

$$\begin{aligned}
& \Delta_{n+2(j-k)+4} \\
& \sum_{j=0}^{\infty} \sum_{k=0}^{2j} D_{n,n+2(j-k)-4,j,k}^{(4,2)} \Delta_{n+2(j-k)-4} = e^{-\frac{v^2}{2}} \sum_{j=0}^{\infty} \sum_{k=0}^{2j} \sum_{l=0}^n \frac{(-1)^{l+k}}{k!(2j-k)!(2j+1)!} \times \\
& \left(\frac{A}{2}\right)^{2j} \frac{1}{2!l!(l+2(j-k)-4)!} \times \\
& v^{2(l+j-k-2)} \frac{\sqrt{n!(n+2(j-k)-4)!}}{(n-l)!} \times \\
& \Delta_{n+2(j-k)-4}.
\end{aligned} \tag{2.56}$$

We obtain the equation for the upper critical field in case of d -wave symmetry

$$\begin{aligned}
-\ln\left(\frac{T}{T_c}\right)\Delta_n &= D_{n,n}\Delta_n + D_{n,n+4}^{(4)}\Delta_{n+4} + D_{n,n-4}^{(4)}\Delta_{n-4} \\
&+ \sum_{j=1}^{\infty} \sum_{k=0}^{2j} D_{n,n+2(j-k),j,k} \Delta_{n+2(j-k)} \\
&+ \sum_{j=1}^{\infty} \sum_{k=0}^{2j} D_{n,n+2(j-k)+4,j,k}^{(4,1)} \Delta_{n+2(j-k)+4} \\
&+ \sum_{j=1}^{\infty} \sum_{k=0}^{2j} D_{n,n+2(j-k)-4,j,k}^{(4,2)} \Delta_{n+2(j-k)-4},
\end{aligned} \tag{2.57}$$

where the matrices $D_{n,n+2(j-k),j,k}$ and $D_{n,n',j,k}^{(4,i)}$ are functions of d and are given by

$$\begin{aligned}
D_{n,n+2(j-k),j,k} &= -\pi k_B T \sum_{l=0}^n \int_0^{\infty} ds \frac{\cos(hs)}{\sinh(\pi k_B T s)} e^{-s^2 v_F^2 \hbar \kappa_{\perp}/16} \left(\frac{s^2 v_F^2 \hbar \kappa_{\perp}}{8}\right)^{l+j-k} \\
&\times \frac{(-1)^{l+k}}{k!(2j-k)!(2j+1)!} \left(\frac{1}{64} s^2 v_F^2 \kappa_{\parallel}^2 d^2\right)^j \frac{\sqrt{n!(n+2(j-k))!}}{(n-l)!l!(l+2(j-k))!}
\end{aligned} \tag{2.58}$$

and

$$\begin{aligned}
D_{n,n+2(j-k)+4,j,k}^{(4,1)} &= -\frac{1}{2} \pi k_B T \sum_{l=0}^n \int_0^{\infty} ds \frac{\cos(hs)}{\sinh(\pi k_B T s)} e^{-s^2 v_F^2 \hbar \kappa_{\perp}/16} \\
&\times \frac{(-1)^{l+k}}{k!(2j-k)!(2j+1)!} \left(\frac{1}{64} s^2 v_F^2 \kappa_{\parallel}^2 d^2\right)^j \frac{1}{l!(l+2(j-k)+4)!} \\
&\times \left(\frac{s^2 v_F^2 \hbar \kappa_{\perp}}{8}\right)^{l+j-k+2} \frac{\sqrt{n!(n+2(j-k)+4)!}}{(n-l)!} \\
D_{n,n+2(j-k)-4,j,k}^{(4,2)} &= -\frac{1}{2} \pi k_B T \sum_{l=0}^n \int_0^{\infty} ds \frac{\cos(hs)}{\sinh(\pi k_B T s)} e^{-s^2 v_F^2 \hbar \kappa_{\perp}/16} \\
&\times \frac{(-1)^{l+k}}{k!(2j-k)!(2j+1)!} \left(\frac{1}{64} s^2 v_F^2 \kappa_{\parallel}^2 d^2\right)^j \frac{1}{l!(l+2(j-k)-4)!}
\end{aligned}$$

$$\times \left(\frac{s^2 v_F^2 \hbar \kappa_{\perp}}{8} \right)^{l+j-k-2} \frac{\sqrt{n!(n+2(j-k)-4)!}}{(n-l)!}. \quad (2.59)$$

As in the s -wave case, the condition $l+2(j-k) \geq 0$ applies for eq. (2.58).

2.2 Phase boundaries for s -wave symmetry

Equation (2.50) was solved numerically for various values of the thickness parameter s_m , which can be written as the film thickness normalized by the inverse Fermi wave vector k_F

$$s_m = \frac{mv_F d}{\hbar} = \frac{d}{k_F^{-1}}, \quad (2.60)$$

$z_m = \pi g_l k_B T_c^{(0)} / 4mv_F^2$ and tilt angles ϑ of the magnetic field with respect to the xy -plane. The critical field h_{c2}/Δ_0 for a finite thickness d of the conducting plane ($s_m > 0$) as a function of reduced temperature and vortex state n does not depend on the single parameter $r_m = H_{\perp}/z_m H = \sin \vartheta / z_m$ (eq. (1.61)) alone as in the previous case with $d = 0$, but is now calculated with fixed values of z_m , ϑ and s_m . As κ_{\parallel} appears in eq. (2.50), z_m and ϑ have to be given explicitly in the numerical calculations. In Section 1.3 the equivalence of r_m and ϑ for a fixed $z_m = 0.3$ was shown in a table for various parameters r_m . In order to allow comparison with the previous results, z_m was fixed to 0.3 and the ϑ -values in the table were used, giving the same r_m -values used in the previous calculations. The relation between s_m and Eilenberger's dimensionless parameter d^* (A.28) is given by $d^* = 4z_m s_m$, which results in

$$\frac{d}{\xi_0} \simeq 1.06 s_m \quad (z_m = 0.3), \quad (2.61)$$

if we consider $z_m = 0.3$, and with the BCS coherence length ξ_0 .

The infinite sum over j in eq. (2.50) was cut off at a certain index j_{max} , where the difference between the critical fields $h_{c2,j_{max}}/\Delta_0$ and $h_{c2,j_{max}-1}/\Delta_0$ was smaller than a given tolerance limit. As the order j of s_m^2 increases, the convergence of $h_{c2,j}$ to $h_{c2,j_{max}}$ improves over the whole temperature range, starting at temperatures near $T_c^{(0)}$. It is not sufficient to neglect higher orders other than $s_m^2 \propto d^2$, especially at low temperatures. The cut-off j_{max} does not only increase with s_m and decreasing temperature, but also with the vortex state n and decreasing r_m . A tolerance limit of 10^{-5} was employed in the calculation of the phase diagrams.

For $z_m = 0.3$ and a tilt angle $\vartheta = 8.63$, corresponding to $r_m = 0.5$, the critical field is reduced with increasing thickness d in the whole temperature range for the vortex states $n = 0$ and 1, and for the chosen values of $s_m = 0.3, 0.5, 0.8$ and 1 as can be seen in Fig. 2.1. Thus, the transition of the vortex state from $n = 0$ to $n = 1$ is shifted to lower temperatures. At higher tilt angles, where the vortex state $n = 1$ does not yet appear, the critical field is lowered at

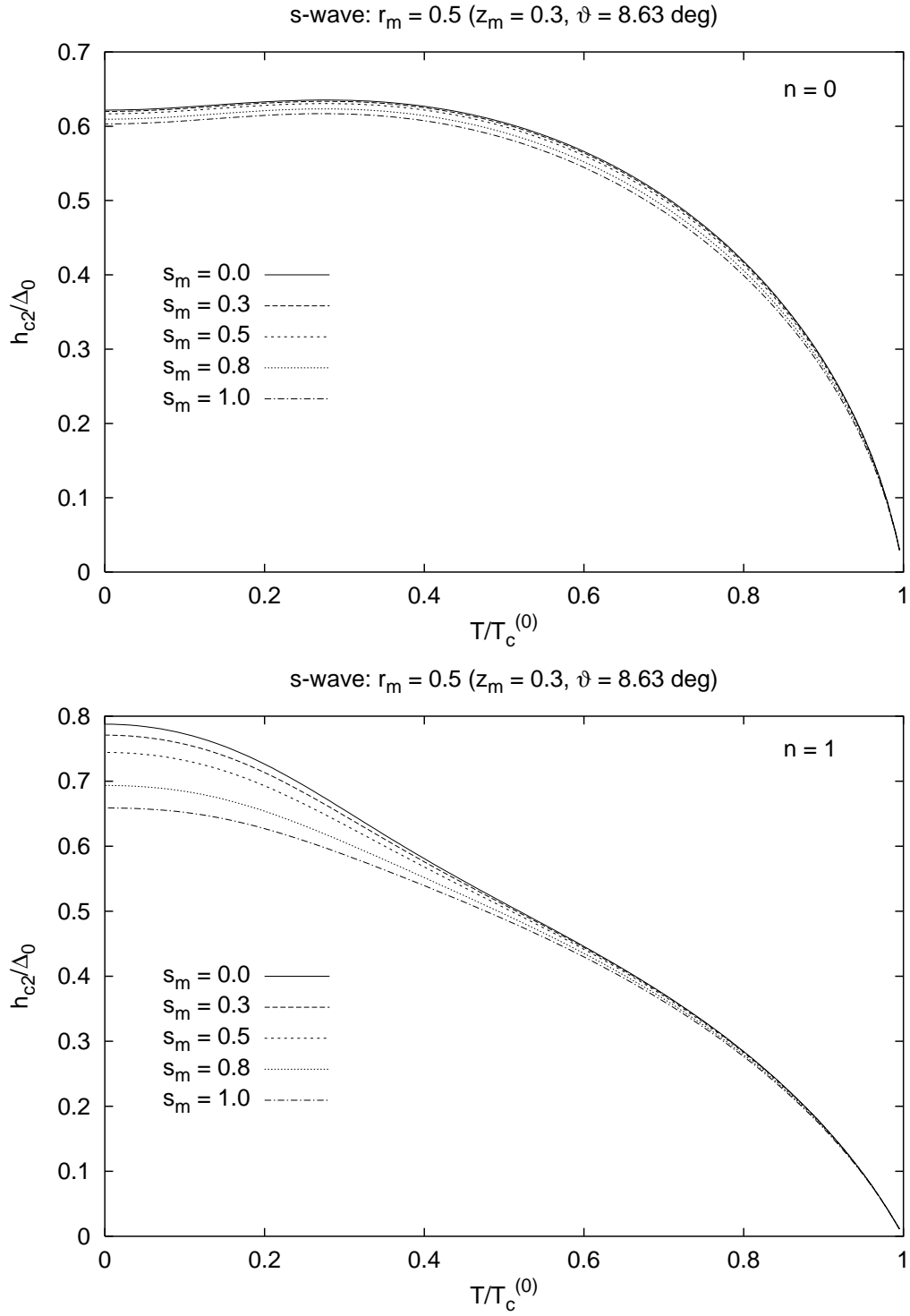


FIGURE 2.1: Critical fields as a function of reduced temperature for parameters $z_m = 0.3$, $\vartheta = 8.63$ corresponding to $r_m = 0.5$, and at vortex states $n = 0$ and 1 for various $s_m = mv_F d/\hbar = d/k_F^{-1}$.

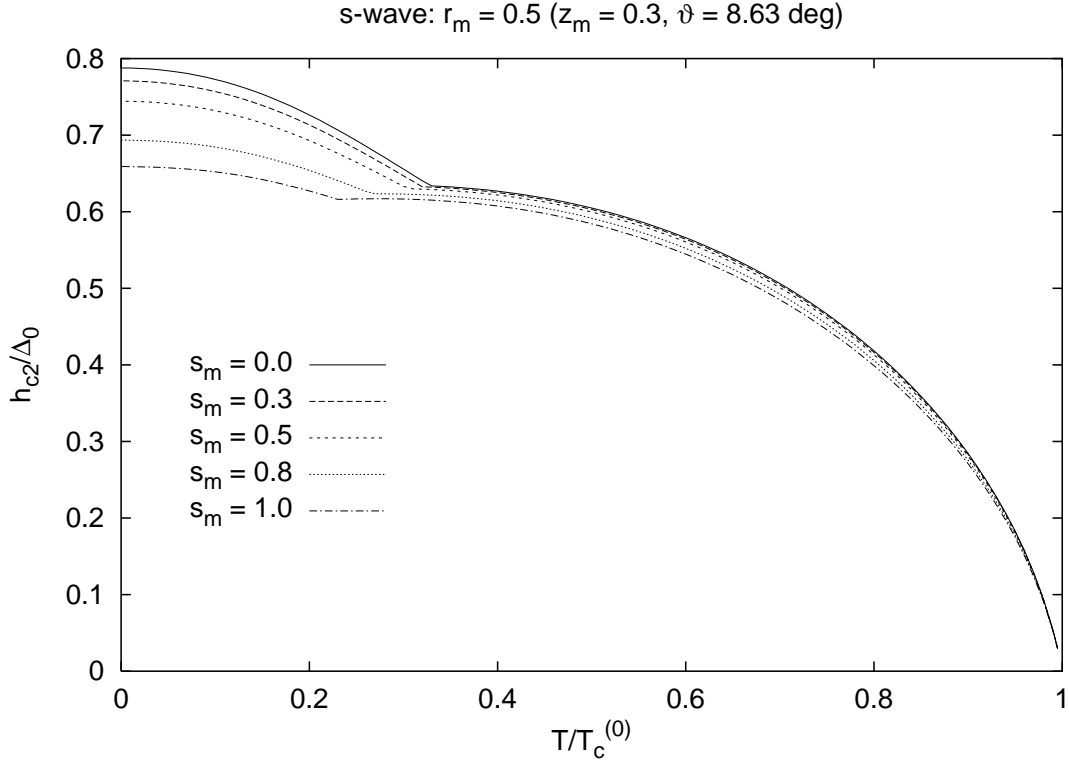


FIGURE 2.2: Upper critical field as a function of reduced temperature for various parameters s_m . Note that the vortex state $n = 1$ is shifted to lower temperatures with increasing s_m .

all temperatures, as can be seen in Fig. 2.3. The highest cut-off for this case is $j_{max} = 6$ for $s_m = 1$ and $n = 1$.

Fig. 2.4 shows the critical fields for $z_m = 0.3$ and $\vartheta = 3.44$ ($r_m = 0.2$) at the vortex states $n = 0$ and 1. Compared to the case with $r_m = 0.5$, where the critical field was reduced at all temperatures for the the vortex states $n = 0$, one can see that the critical fields are enhanced at low temperatures for this tilt angle. As the vortex state increases, h_{c2} decreases compared to the two-dimensional case, as can be seen in this figure and Fig. 2.5, where the critical fields for various s_m at the vortex states $n = 2$ and 3 are depicted. It results in the upper critical field shown in Fig. 2.6 as a function of temperature for various values of s_m . The vortex state $n = 3$ is shifted to lower temperatures with increasing s_m and has disappeared for $s_m = 0.5$. A cut-off of $j_{max} = 9$ had to be employed in the low temperature range of the case with $s_m = 1$ and $n = 1$. The s_m -dependence of the upper critical field is shown for a few reduced temperatures $t = T/T_c^{(0)}$ in Fig. 2.7. As with the dependence on r_m , the upper critical field as a function of s_m shows kinks as the transition between vortex states occur. At high temperatures, only the vortex state $n = 0$ appears (top frame), and as the temperature decreases higher vortex states show up, like $n = 1$ at $t = 0.4$, and $n = 2, 3$ at $t = 0.1$ in the

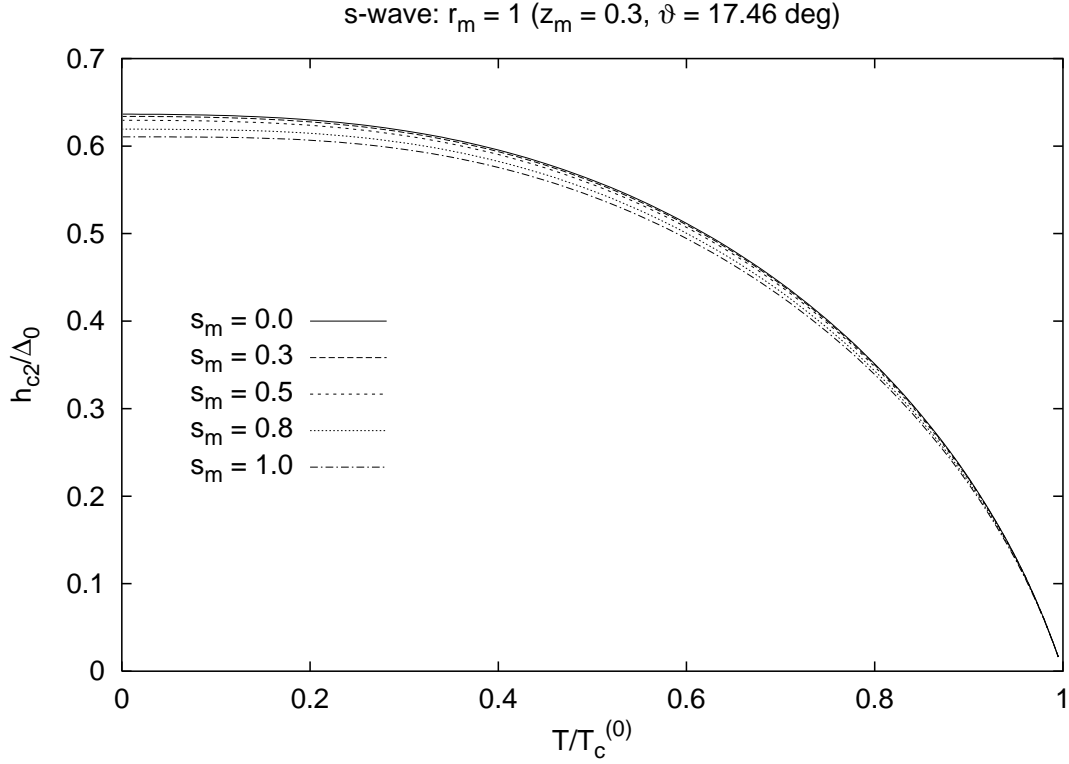


FIGURE 2.3: Upper critical field for $r_m = 1$ at $s_m = 0$ and $s_m > 0$ for $r_m = 1$ as a function of temperature.

case of $r_m = 0.2$.

For $z_m = 0.3$ and $\vartheta = 1.72$ (Fig. 2.8), corresponding to $r_m = 0.1$, the vortex state $n = 6$ has already disappeared for $s_m = 0.3$. As the slopes of the critical fields at high vortex states lessen with increasing s_m , the kinks originating from the transition between vortex states become less pronounced in the temperature dependence of h_{c2} , which appears smoother compared to the two-dimensional case. As s_m increases, the strong rise of the upper critical field at low temperatures is lessened, and h_{c2} of $s_m = 1$ becomes almost flat as a consequence. A cut-off of $j_{max} = 20$ had to be employed in the low temperature range of the case with $s_m = 1$ and $n = 4$.

Finally, the dependence of the upper critical field on the out of plane angle ϑ for a fixed $z_m = 0.3$ and for two values of s_m is depicted in Fig. 2.9. The transitions between vortex states can be observed in the significant kinks of the curves, starting from $n = 0$ at $\vartheta \gtrsim 15$ up to $n \rightarrow \infty$ for $\vartheta \rightarrow 0$.

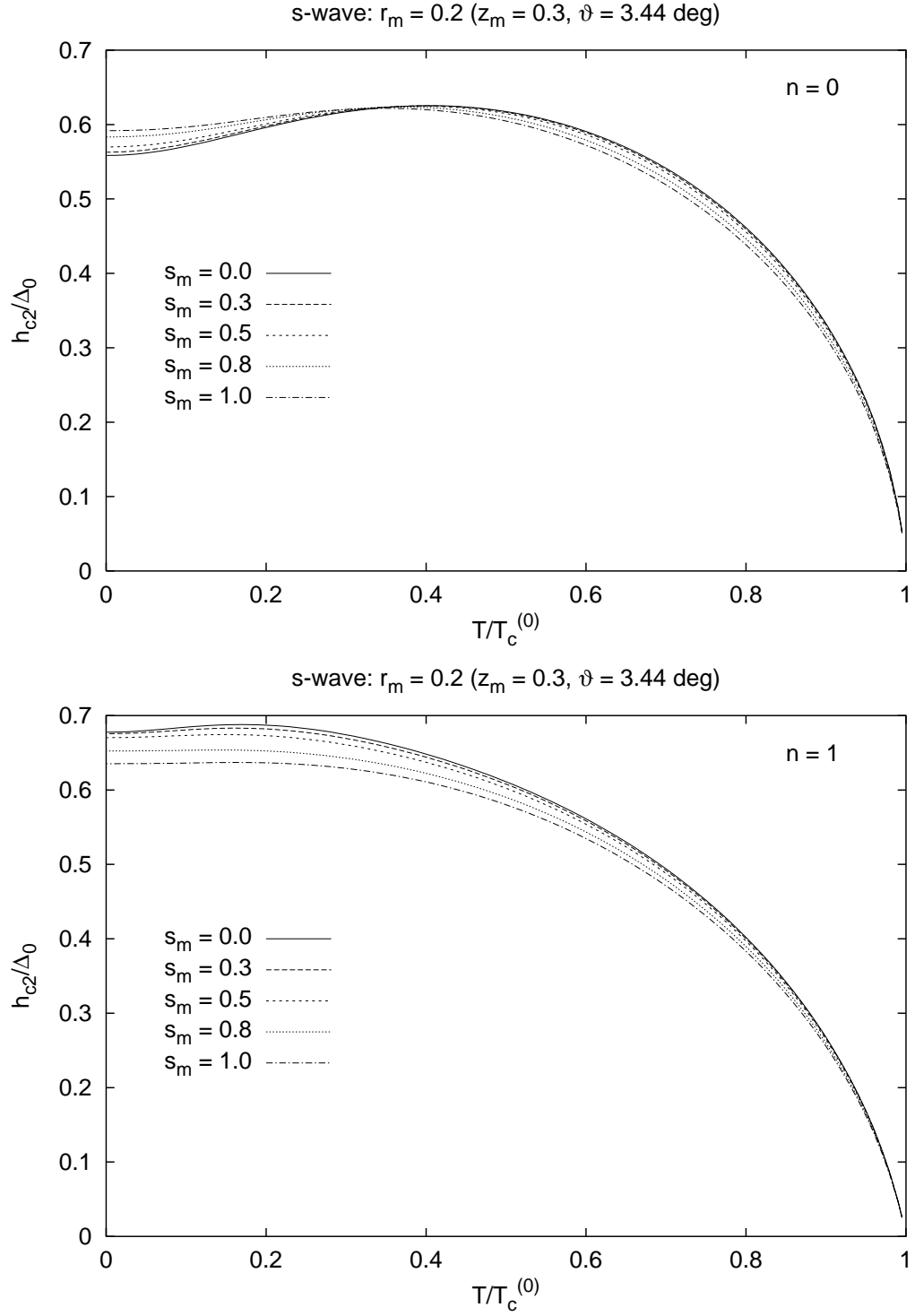


FIGURE 2.4: Critical field as a function of reduced temperature at the vortex states $n = 0$ and 1 for various $s_m = d/k_F^{-1}$.

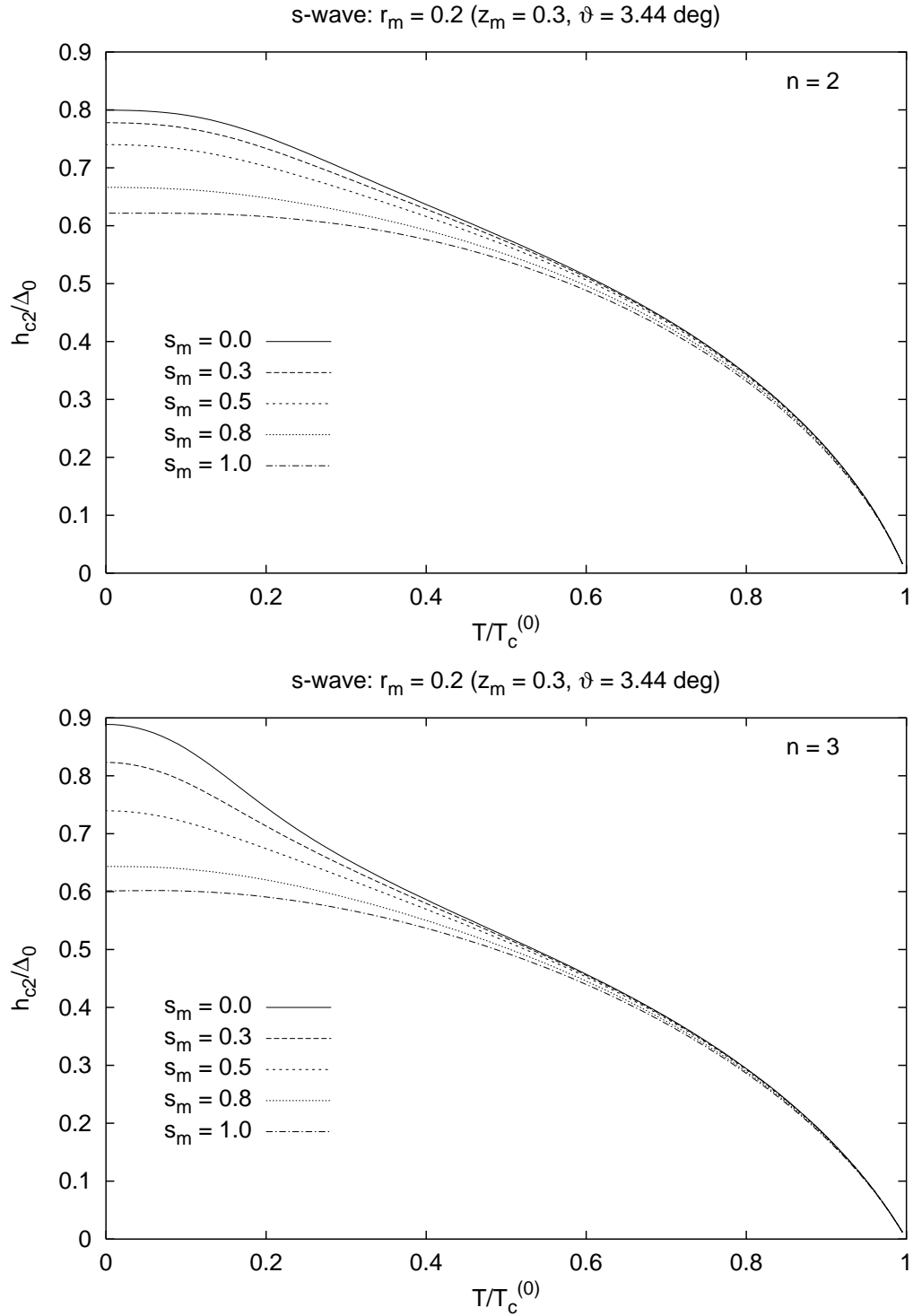


FIGURE 2.5: Critical field as a function of reduced temperature at the vortex states $n = 2$ and 3 for various $s_m = d/k_F^{-1}$.

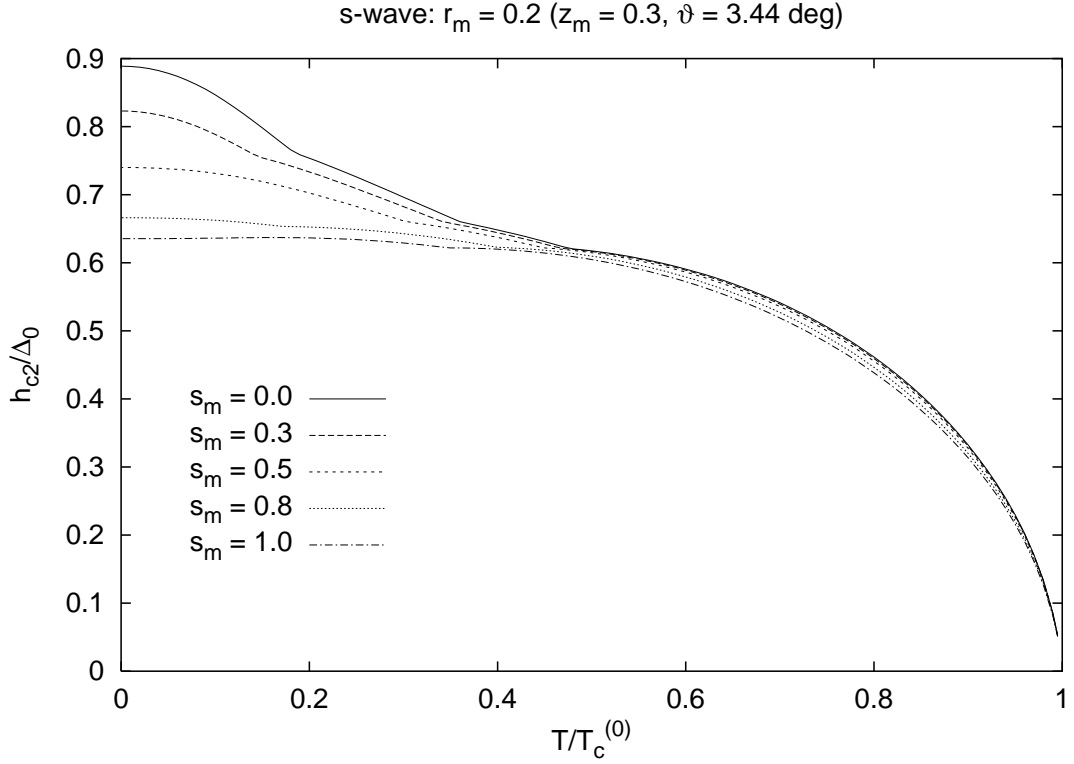


FIGURE 2.6: Upper critical field as a function of reduced temperature for $z_m = 0.3$ and $\vartheta = 3.44$, corresponding to $r_m = 0.2$ for various s_m .

2.2.1 Limit of a plane-parallel magnetic field

In the limit $\kappa_\perp \rightarrow 0$ the averaged Green's functions take the form

$$\bar{f}_{(\pm)}(x, y) = \int_0^\infty ds e^{-s(|\omega_l| \mp i \text{sgn} \omega_l \mu H)} \frac{1}{\frac{1}{4} s v_F \kappa_\parallel d \hat{k}_x} \sin\left(\frac{1}{4} s v_F \kappa_\parallel d \hat{k}_x\right) e^{\mp \frac{1}{2} \text{sgn} \omega_l s \hbar \mathbf{v}_F \nabla} \Delta(\mathbf{r}), \quad (2.62)$$

which results in the gap-equation

$$\begin{aligned} -\ln\left(\frac{T}{T_c^{(0)}}\right) \Delta_\alpha(\mathbf{r}) &= \pi k_B T \int_0^\infty ds \frac{1}{\sinh(\pi k_B T s)} \int_0^{2\pi} \frac{d\varphi'}{2\pi} \gamma_\alpha(\hat{p}')^2 \left[1 - \frac{1}{\frac{1}{4} s v_F \kappa_\parallel d \hat{k}_x'} \right. \\ &\quad \times \left. \sin\left(\frac{1}{4} s v_F \kappa_\parallel d \hat{k}_x'\right) \cos\left(s\left(h - \frac{\hbar}{2i} \mathbf{v}_F \nabla\right)\right) \right] \Delta_\alpha(\mathbf{r}). \end{aligned} \quad (2.63)$$

If the gap-function $\Delta_\alpha(\mathbf{r})$ is replaced by $e^{i\mathbf{q}\mathbf{r}}$, the equation for critical field is results in

$$-\ln\left(\frac{T}{T_c^{(0)}}\right) = \pi k_B T \int_0^\infty ds \frac{1}{\sinh(\pi k_B T s)} \int_0^{2\pi} \frac{d\varphi'}{2\pi} \gamma_\alpha(\hat{p}')^2 \left[1 - \frac{1}{\frac{1}{4} s v_F \kappa_\parallel d \hat{k}_x'} \right]$$

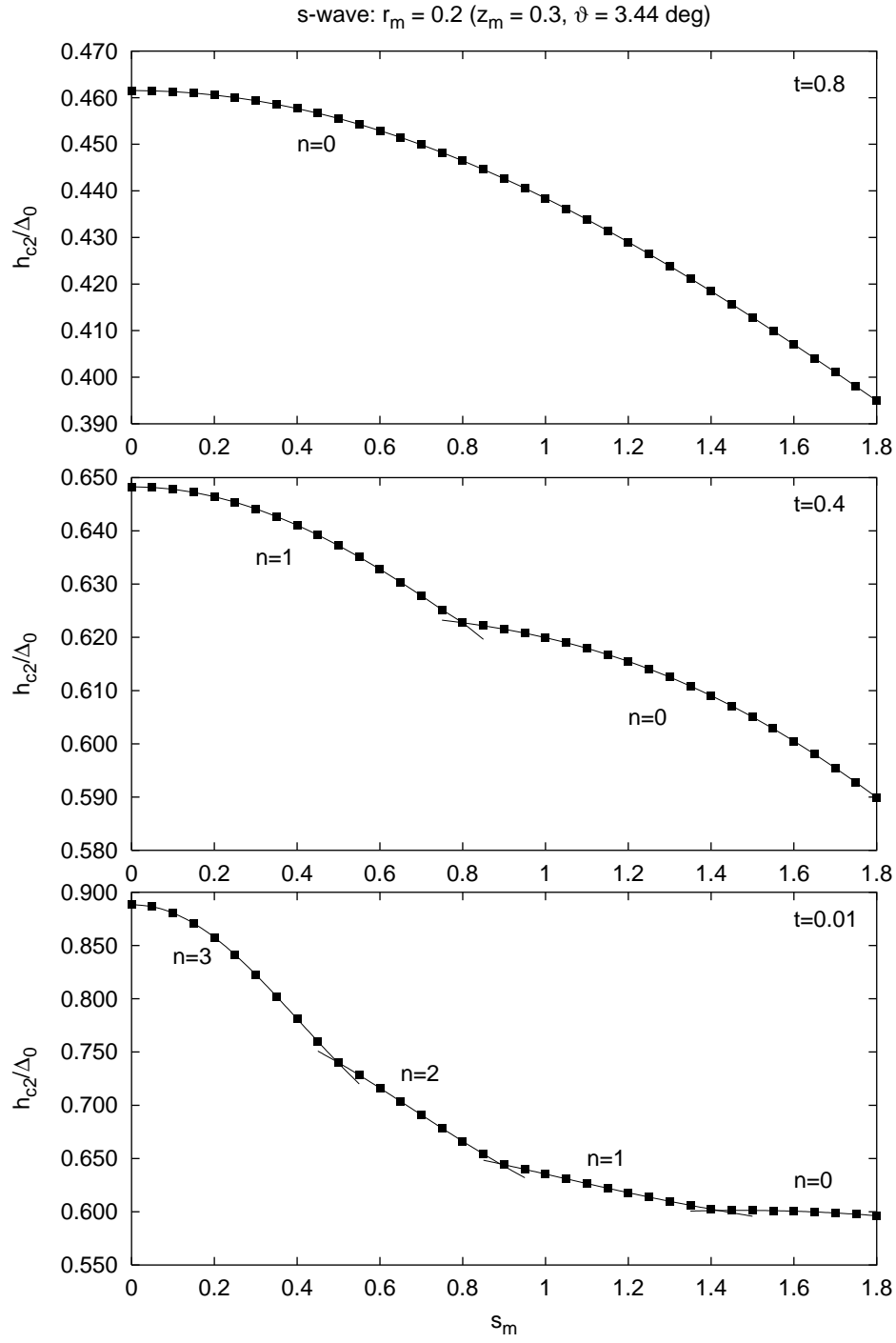


FIGURE 2.7: Dependence of the upper critical field on s_m for various reduced temperatures t .

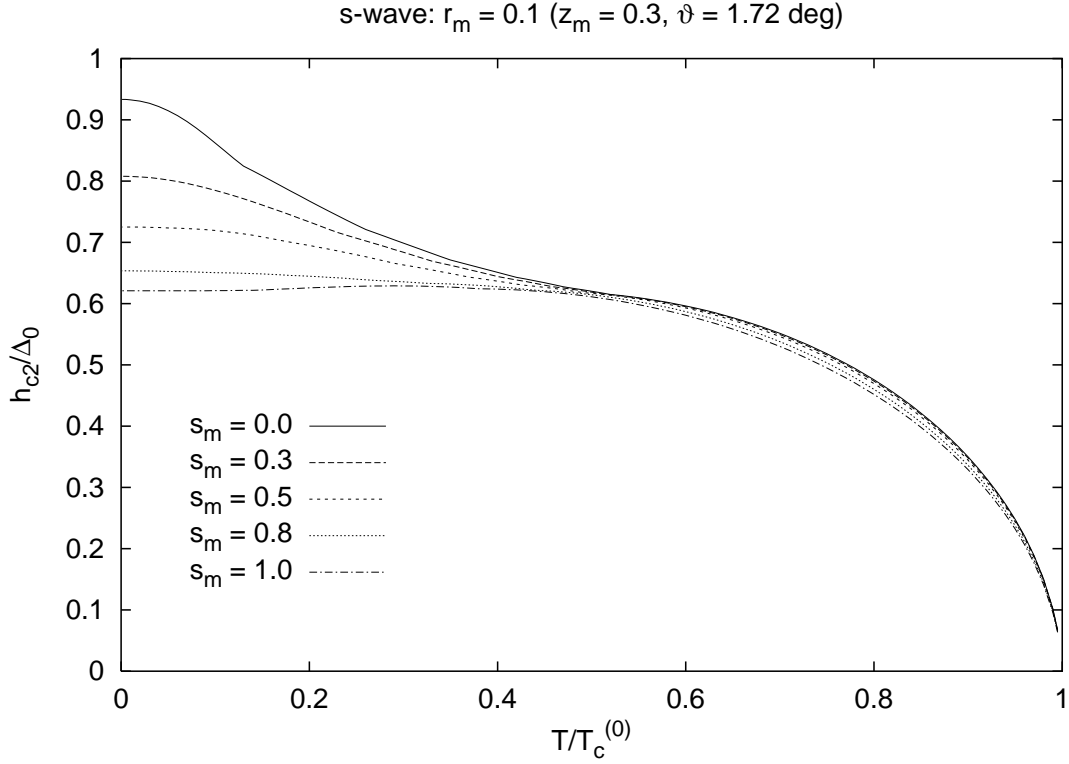


FIGURE 2.8: Upper critical field as a function of reduced temperature for $z_m = 0.3$ and $\vartheta = 1.72$, corresponding to $r_m = 0.1$ for various s_m .

$$\times \sin\left(\frac{1}{4}sv_F\kappa_{\parallel}d\hat{k}'_x\right)\cos\left(s\left(h - \frac{\hbar}{2}\mathbf{v}_F\mathbf{q}\right)\right)\Bigg], \quad (2.64)$$

which gives the FFLO critical field for $d = 0$. The vector \mathbf{q} is optimized to obtain the largest critical field. Shimahara and Rainer [11] have shown in the case of $d = 0$, that the FFLO critical field and the order parameter are recovered for s - and d -wave superconductors (eqs. (1.34) and (1.52)) in the limit of $n \rightarrow \infty$ and $\kappa_{\perp} \rightarrow 0$, with the FFLO state expressed in this limit as

$$|\mathbf{q}| = q = \lim_{\kappa_{\perp} \rightarrow 0} \sqrt{2\kappa_{\perp}n(\kappa_{\perp})}. \quad (2.65)$$

Therefore, if a solution with nonzero q is the optimum solution in the FFLO critical field equation, the optimized $n = n(\kappa_{\perp})$ diverges when $\kappa_{\perp} \rightarrow 0$.

Supposing that $\kappa_{\perp} = 0$ and that there is no Pauli limiting field, which corresponds to the limit $\mu \rightarrow 0$, we obtain for s -wave symmetry and with the substitution $s' = s\pi k_B T_c^{(0)}$,

$$-\ln\left(\frac{T}{T_c^{(0)}}\right) = \frac{T}{T_c^{(0)}} \int_0^{\infty} ds' \frac{1}{\sinh\left(s' \frac{T}{T_c^{(0)}}\right)}$$

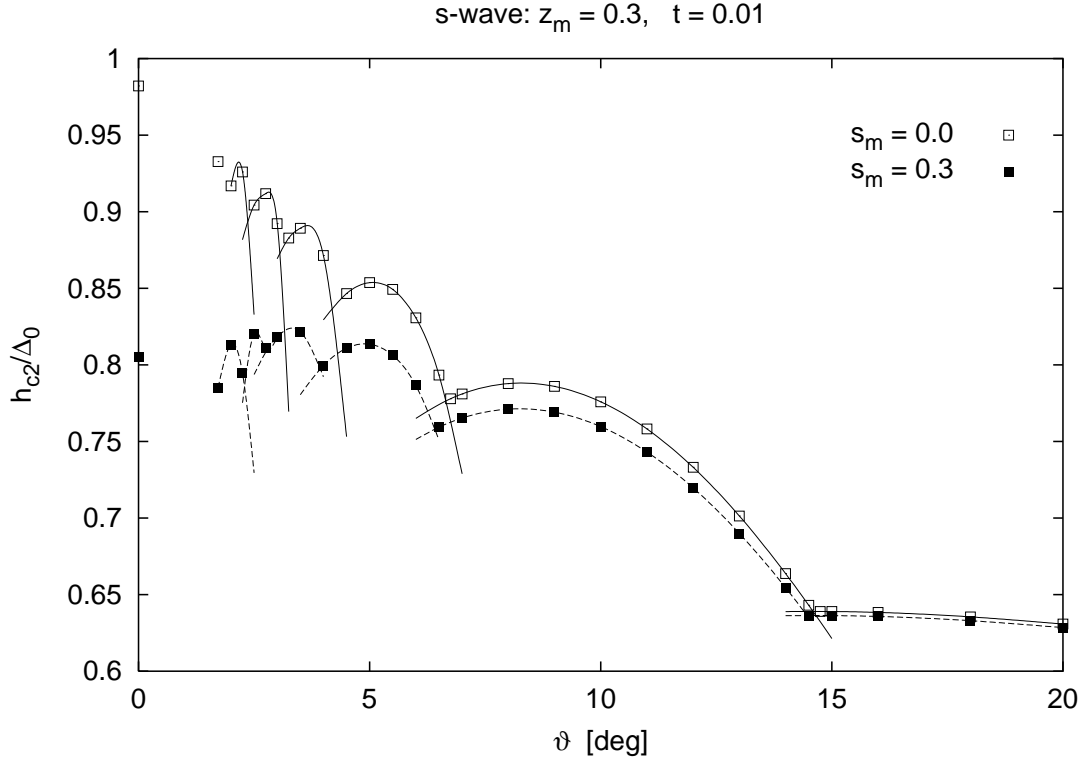


FIGURE 2.9: Upper critical field as a function of the out of plane angle ϑ for the two dimensional case and $s_m = 0.3$. The solid and dashed lines point out the transitions between vortex states and are guides to the eye.

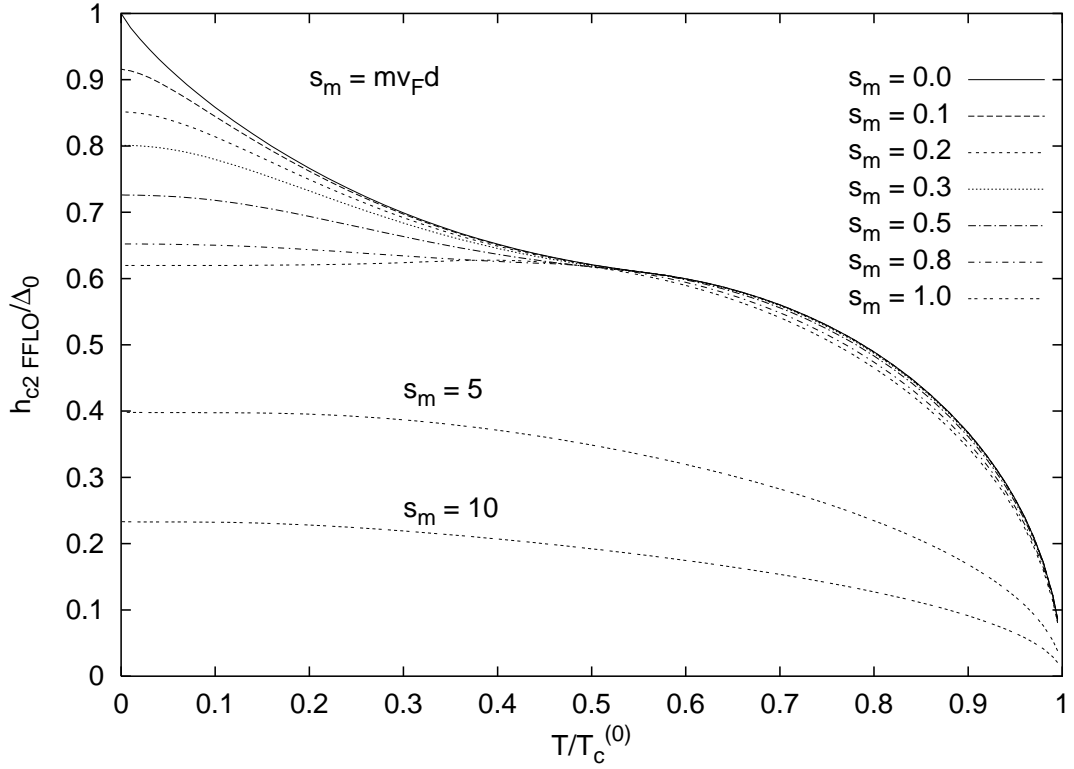
$$\int_0^{2\pi} \frac{d\varphi'}{2\pi} \left[1 - \frac{1}{\frac{1}{4\pi k_B T_c^{(0)}} s' v_F \kappa_{\parallel} d \hat{k}'_x} \sin \left(\frac{1}{4\pi k_B T_c^{(0)}} s' v_F \kappa_{\parallel} d \hat{k}'_x \right) \right], \quad (2.66)$$

because of

$$\lim_{\mu \rightarrow 0} \cos \left(s' \mu \frac{H_{\parallel}}{\pi k_B T_c^{(0)}} \right) = 1, \quad (2.67)$$

where h was set to $h = \mu |\mathbf{H}| = \mu H_{\parallel}$, and for fixed H_{\parallel} , s' , and $T_c^{(0)}$. The s' -dependent function in the integrand decreases quite fast with increasing s' , because of the $\sinh \left(s' \frac{T}{T_c^{(0)}} \right)$ in the denominator. If $\mu H_{\parallel} / \pi k_B T_c^{(0)} \sim 1$, the significant contribution of the function $(1 - \cos(s' \frac{T}{T_c^{(0)}})) / \sinh(s' \frac{T}{T_c^{(0)}})$ lies in the range $0 \leq s' \frac{T}{T_c^{(0)}} \leq 10$, if we consider temperatures $0 < T \leq T_c^{(0)}$. Now, the sine is expanded into its series

$$\frac{1}{\frac{1}{4\pi k_B T_c^{(0)}} s' v_F \kappa_{\parallel} d \hat{k}'_x} \sin \left(\frac{1}{4\pi k_B T_c^{(0)}} s' v_F \kappa_{\parallel} d \hat{k}'_x \right) =$$

FIGURE 2.10: FFLO critical field as a function of reduced temperature for various s_m .

$$\sum_{m=0}^{\infty} \frac{(-1)^m}{(2m+1)!} \left(\frac{1}{4\pi k_B T_c^{(0)}} s' v_F \kappa_{\parallel} d \cos \varphi' \right)^{2m}, \quad (2.68)$$

with $\hat{k}'_x = \cos \varphi'$, giving

$$\begin{aligned} -\ln \left(\frac{T}{T_c^{(0)}} \right) &= \frac{T}{T_c^{(0)}} \int_0^{\infty} ds' \frac{1}{\sinh \left(s' \frac{T}{T_c^{(0)}} \right)} \int_0^{2\pi} \frac{d\varphi'}{2\pi} \\ &\quad \sum_{m=1}^{\infty} \frac{(-1)^{m+1}}{(2m+1)!} \left(\frac{1}{4\pi k_B T_c^{(0)}} s' v_F \kappa_{\parallel} d \cos \varphi' \right)^{2m}. \end{aligned} \quad (2.69)$$

The $s = s' \frac{T}{T_c^{(0)}}$ -integration results in

$$\int_0^{\infty} ds \frac{s^{2m}}{\sinh(s)} = \left(2 - \frac{1}{2^{2m}} \right) (2m)! \zeta(2m+1), \quad (2.70)$$

where $\zeta(x)$ is Riemann's zeta-function. With the result of the ϕ' -integration

$$\int_0^{2\pi} \frac{d\varphi'}{2\pi} \cos^2 \varphi'^{2m} = \frac{\Gamma(m + \frac{1}{2})}{\sqrt{\pi} \Gamma(m+1)} = \frac{(2m)!}{2^{2m} m!^2}, \quad (2.71)$$

the gap-equation (2.66) becomes

$$-\ln\left(\frac{T}{T_c^{(0)}}\right) = \sum_{m=1}^{\infty} \frac{(-1)^{m+1}}{(2m+1)} \left(2 - \frac{1}{2^{2m}}\right) \frac{(2m)!\zeta(2m+1)}{2^{2m}m!^2} \left(\frac{1}{4\pi k_B T} v_F \kappa_{\parallel} d\right)^{2m}. \quad (2.72)$$

This equation for $H_{\parallel} = \kappa_{\parallel} c/2|e|$ is valid in the temperature range $0 < T \leq T_c^{(0)}$.

In the case of $(1 - T/T_c^{(0)}) \ll 1$, the logarithm on the left side of eq. (2.66) can be replaced by $-(1 - T/T_c^{(0)})$ and the temperature on the right side can be set to $T_c^{(0)}$, which results in

$$1 - \frac{T}{T_c^{(0)}} = \frac{7\zeta(3)}{24} \left(\frac{|e|}{c} \frac{v_F}{2\pi k_B T_c^{(0)}} H_{\parallel} d \right)^2, \quad (2.73)$$

if the term with d^4 ($m = 2$) is neglected, giving the H_{\parallel} -equation near $T_c^{(0)}$

$$H_{\parallel} = \sqrt{\left(1 - \frac{T}{T_c^{(0)}}\right)} \sqrt{\frac{24}{7\zeta(3)}} \frac{c}{|e|} \frac{2\pi T_c^{(0)}}{v_F} \frac{1}{d}. \quad (2.74)$$

With the BCS coherence length $\xi_0 = 0.18 \hbar v_F / k_B T_c^{(0)} = 0.18 v_F / T_c^{(0)}$, $\xi_{0,T} = \xi_0 (1 - T/T_c^{(0)})^{-1/2}$, the flux quantum $\phi_0 = hc/2e = \pi c/e$, and $\zeta(3) \simeq 1.2$, eq. (2.74) can be expressed as

$$H_{\parallel} = 0.61 \frac{\Phi_0}{\xi_{0,T} d}, \quad (2.75)$$

in agreement with the Ginzburg-Landau (GL) result for very thin films ($d \ll \lambda$). However, the experiments show $H_{\parallel} \propto d^{-3/2}$ for thin films such that $d \lesssim \xi_0$. Assuming specular reflexion, Toxen [39] (phenomenological approach), Casella and Miller [40] (Gor'kov equations), and Shapoval [41] (quasiclassical trajectory method), found a $d^{-3/2}$ -dependence of the critical field parallel to the conducting plane. The same applies for calculations of Shapoval [42], and De Gennes and Tinkham [43] in the case of diffuse scattering on the boundary of the superconducting film. In our calculations the same Kernel as in the three-dimensional case was used (2.6) and specular boundary conditions were not imposed on the eigenfunctions, which was not necessary as we have considered a circular Fermi surface. That may explain why the dependence of H_{\parallel} on d is the same as in the GL result or the calculations (Gor'kov equations) of [40] in the regime $d > \xi_T$, where $\xi_T = 1.75 \xi_0 T_c / T$.

For d -wave symmetry the right side of eq. (2.66) is multiplied with the symmetry function $1 + \cos(4\varphi')$. For temperatures near T_c the same results as in the s -wave case apply.

The limit $\kappa_{\perp} \rightarrow 0$ and Ginzburg-Landau approximation

The upper critical field without paramagnetic limiting and in the limit $\kappa_{\perp} \rightarrow 0$ is shown in reduced units $\mu_0 H_{\parallel} / \Delta_0 = h_{c2\parallel} / \Delta_0$ in figures 2.11 and 2.12 as a function of reduced

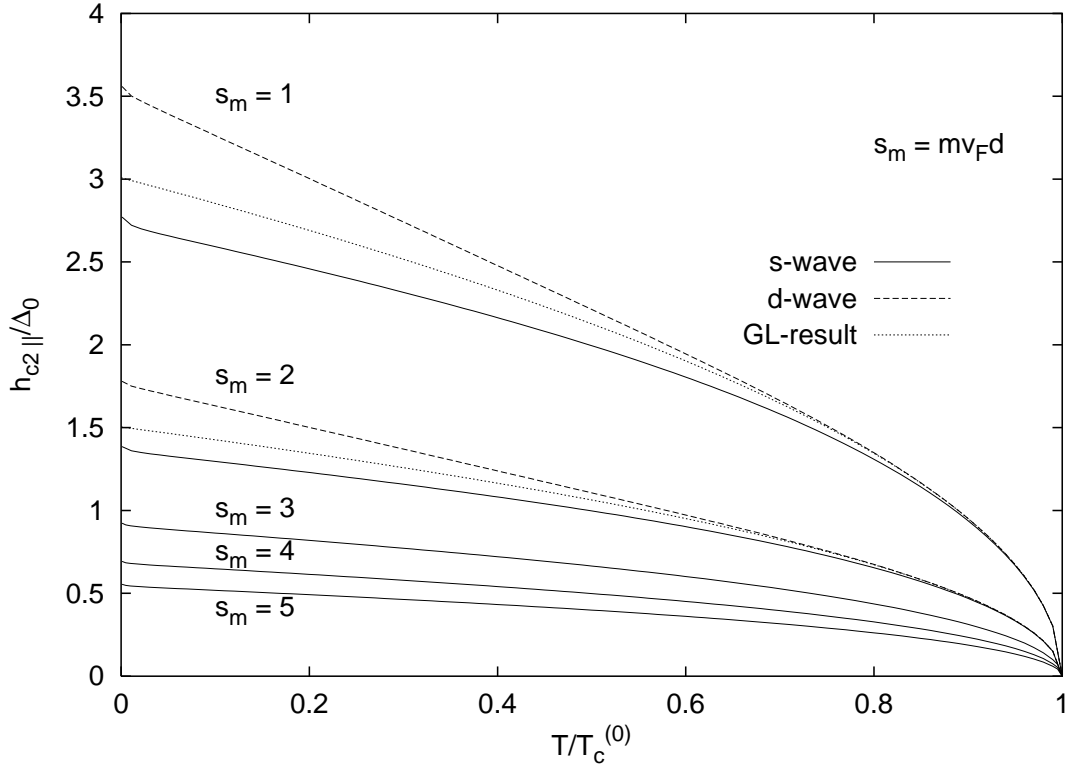


FIGURE 2.11: The upper critical field $h_{c2||}/\Delta_0$ as a function of reduced temperature $T/T_c^{(0)}$ without paramagnetic limiting and $\kappa_{\perp} \rightarrow 0$ for various values of $s_m = d/k_F^{-1}$ for s - and d -wave symmetry. The results of eq. (2.75) are shown for comparison in two cases.

temperature $t = T/T_c^{(0)}$ and $1/s_m$ with $s_m = mv_F d/\hbar$. In Fig. 2.11 the d -wave case is shown for comparison. For the approximation of T near $T_c^{(0)}$ eq. (2.75) yields

$$\frac{h_{c2||}}{\Delta_0} = \sqrt{1-t} \sqrt{\frac{24}{7\zeta(3)}} e^{\gamma} \frac{1}{s_m} \simeq \sqrt{1-t} \frac{3}{s_m}. \quad (2.76)$$

If v_F is $\sim 10^5$ m/s, and the thickness of the film $d \sim 10^{-10}$ m or ~ 1 Å, s_m would be ~ 1 as $m/\hbar \simeq 0.86 \cdot 10^5$ kg/Js.

The GL-approximation agrees well with the numerical results of eq. (2.66) for s - and d -wave symmetry up to $t \sim 0.9$ as can be seen in Figure 2.12.

2.2.2 h_{c2} in the limit $\vartheta \rightarrow 0$: FFLO critical field

The FFLO critical field for various values of s_m (Fig. 2.10) was calculated by optimizing the wavevector q to obtain the largest critical field of eq. (2.64). With increasing thickness of the film, one can clearly see that the steep rise and positive curvature of the two-dimensional case at very low temperatures is replaced by a decreasing slope and negative curvature. As layered

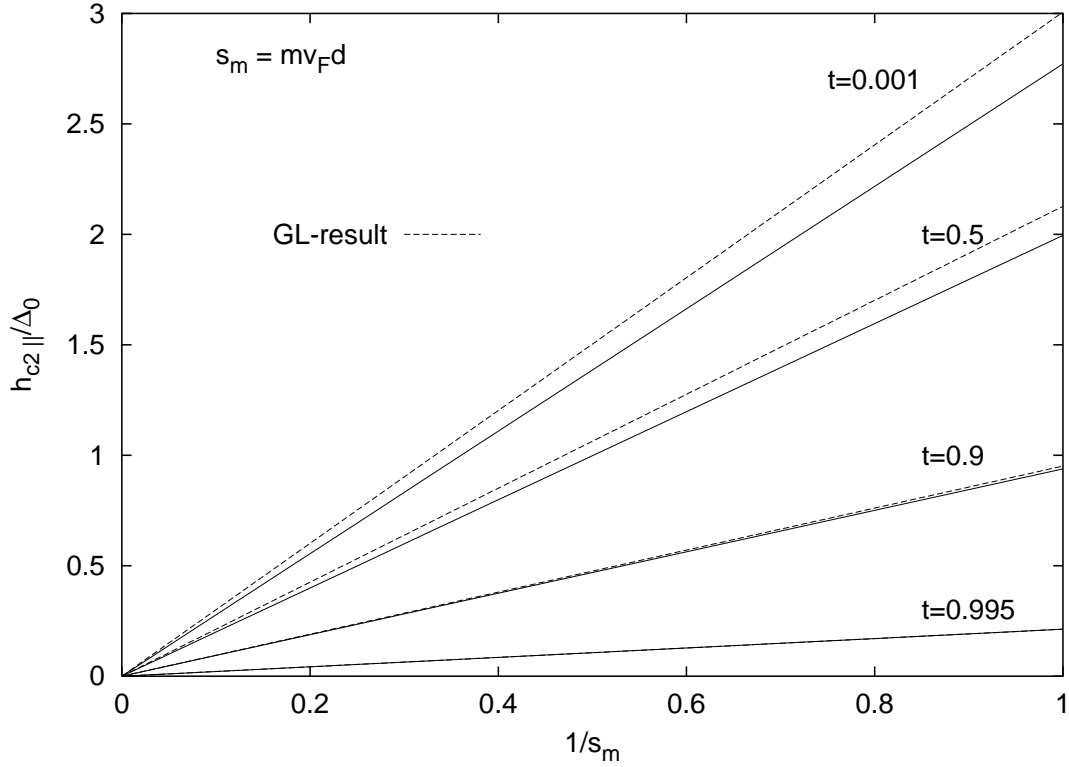


FIGURE 2.12: The upper critical field $h_{c2||}/\Delta_0$ as a function of $1/s_m$ for various reduced temperatures $T/T_c^{(0)}$. The results of eq. (2.75) are shown for comparison.

superconductors or films have a finite thickness, it may be an indication to why the steep rise at low temperatures is not so easily found by experiment. It should be pointed out that we continue to use here the term FFLO state, even if this term denotes, strictly speaking, a state without any orbital pair breaking contribution.

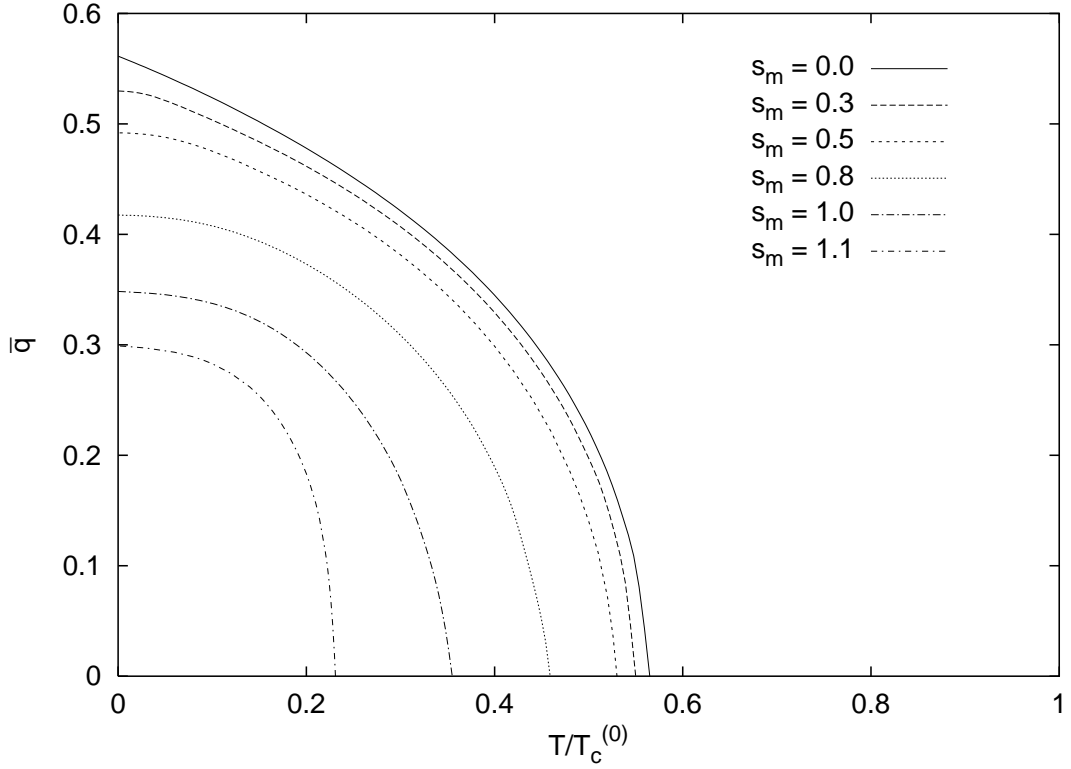
We want to examine the behavior of the upper critical field and the parameter \bar{q} with increasing thickness of the superconducting film. As $\gamma_\alpha(\hat{p}')^2 = 1$ for s -wave superconductors, eq. (2.64) reads

$$-\ln\left(\frac{T}{T_c^{(0)}}\right) = \pi k_B T \int_0^\infty ds \frac{1}{\sinh(\pi k_B T s)} \int_0^{2\pi} \frac{d\varphi'}{2\pi} \left[1 - \frac{1}{\frac{1}{4} s v_F \kappa_{||} d \hat{k}'_x} \times \right. \\ \left. \sin\left(\frac{1}{4} s v_F \kappa_{||} d \hat{k}'_x\right) \cos\left(s\left(h - \frac{\hbar}{2} \mathbf{v}_F \mathbf{q}\right)\right) \right], \quad (2.77)$$

with

$$\mathbf{q} = q \begin{pmatrix} \cos \varphi_q \\ \sin \varphi_q \end{pmatrix}. \quad (2.78)$$

It is sufficient to choose a fixed angle $\varphi_q = 0$, as there is no dependence on φ_q in the s -wave

FIGURE 2.13: Parameter \bar{q} as a function of temperature for various s_m .

case. Therefore, the product $\mathbf{v_F q}$ yields $v_F q \cos \varphi'$ and eq. (2.77) results in

$$-\ln \left(\frac{T}{T_c^{(0)}} \right) = \pi k_B T \int_0^\infty ds \frac{1}{\sinh(\pi k_B T s)} \int_0^{2\pi} \frac{d\varphi'}{2\pi} \left[1 - \frac{1}{\frac{1}{4} s v_F \kappa_{\parallel} d \hat{k}'_x} \times \right. \\ \left. \sin \left(\frac{1}{4} s v_F \kappa_{\parallel} d \hat{k}'_x \right) \left(\cos(hs) \cos(s\pi k_B T_c \bar{q} \cos \varphi') + \sin(hs) \sin(s\pi k_B T_c \bar{q} \cos \varphi') \right) \right], \quad (2.79)$$

with the dimensionless parameter $\bar{q} = \hbar v_F q / 2\pi k_B T_c$ to be optimized in order to obtain the largest critical field. Figure 2.13 depicts the numerical results on the temperature dependence of \bar{q} for various thickness parameters s_m . For $s_m = 0$ the pair momentum \bar{q} agrees with the numerical result obtained in Ref. [44]. At high temperatures \bar{q} is null, giving a critical field identical to that of the homogeneous case

$$-\ln \left(\frac{T}{T_c^{(0)}} \right) = \pi k_B T \int_0^\infty ds \frac{1}{\sinh(\pi k_B T s)} \int_0^{2\pi} \frac{d\varphi'}{2\pi} \left[1 - \frac{1}{\frac{1}{4} s v_F \kappa_{\parallel} d \hat{k}'_x} \times \right. \\ \left. \sin \left(\frac{1}{4} s v_F \kappa_{\parallel} d \hat{k}'_x \right) \cos(hs) \right], \quad (2.80)$$

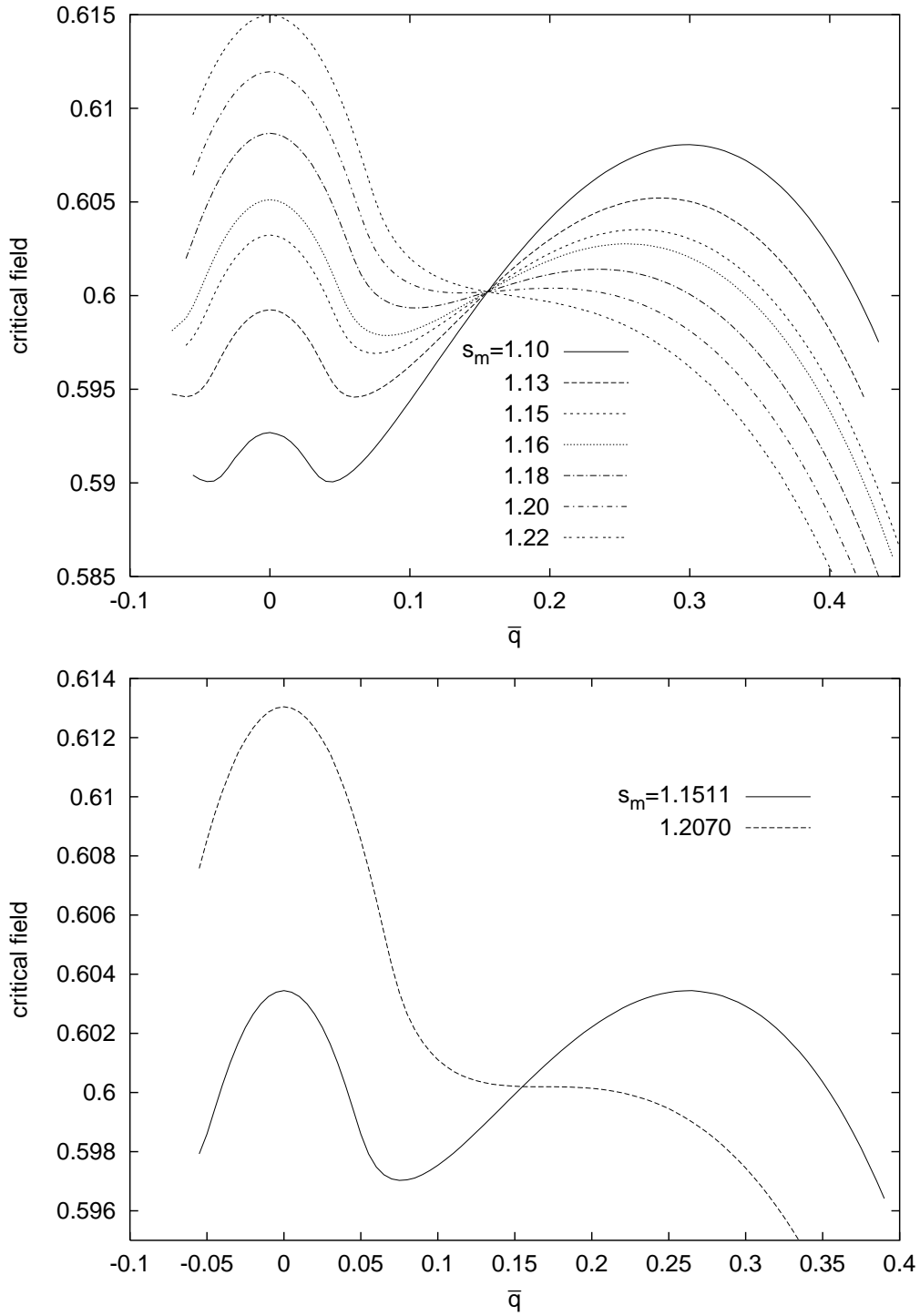


FIGURE 2.14: Solution of eq. (2.79) for the dimensionless field h/Δ_0 at $t = 0.01$ as a function of \bar{q} for various thickness parameters s_m . The absolute maximum of each plot corresponds to the FFLO critical field, while the maximum at $\bar{q} = 0$ is the critical field of the homogeneous case (2.80).

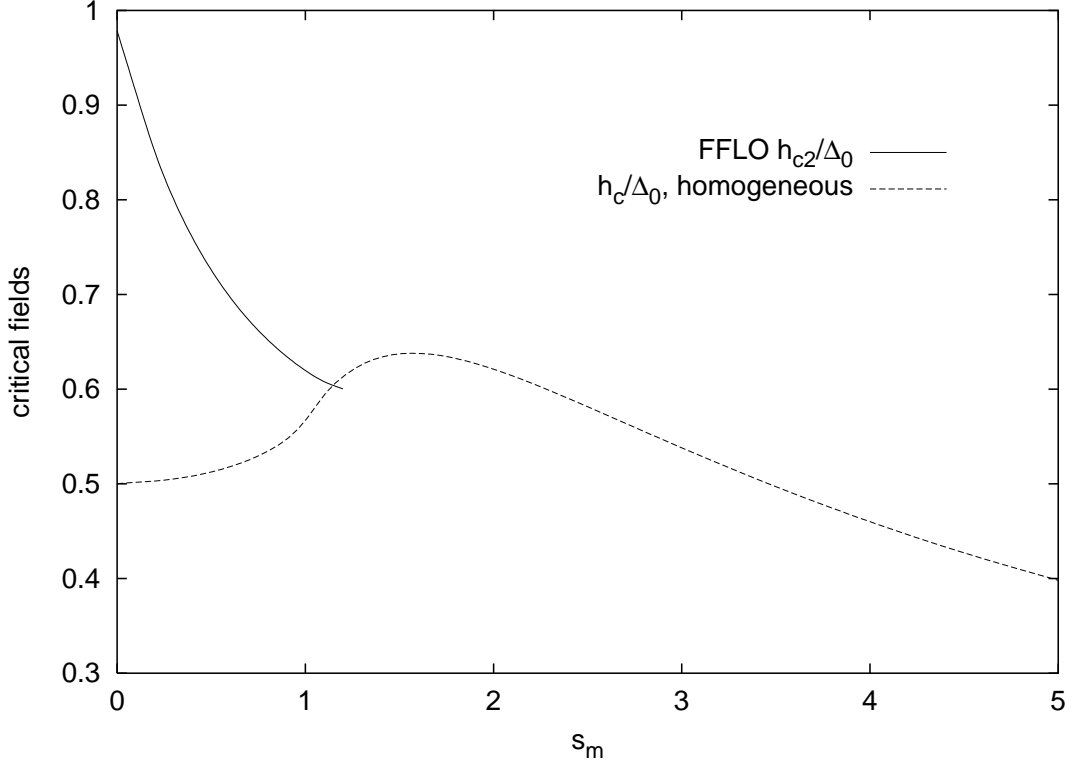


FIGURE 2.15: Critical fields as functions of the thickness parameter s_m at $t = 0.01$.

where the gap-function Δ is spatially constant over the whole superconducting plane. In case of $d = 0$, this critical field is identical to the unstable solution of the BCS equations given by Sarma [29]. The critical fields are identical for $t \geq 0.56$.

The solution of eq. (2.79) at $t = 0.01$ as a function of \bar{q} for various thickness parameters s_m has two maxima, one of which is the critical field of the homogeneous case 2.80 at $\bar{q} = 0$. At low values of s_m , the maximum at finite \bar{q} is greater than that of the homogeneous case, but at thickness parameters greater than $s_m \sim 1.15$, the maximum at $\bar{q} = 0$ exceeds the other at finite \bar{q} (Fig. 2.14). As the FFLO critical field is given by the maximal field which is a solution of eq. (2.79), it coincides with the homogeneous solution for these s_m . Note the disappearance of the maximum at finite \bar{q} for higher values of the thickness parameter. The bottom frame of Fig. 2.14 shows the critical field as a function of \bar{q} at $s_m = 1.1511$, where the critical field of the homogeneous case and the FFLO critical field match. At $s_m = 1.207$, the maximum at finite \bar{q} has disappeared. Fig. 2.15 shows the critical fields of the FFLO and of the homogeneous case as functions of the thickness parameter s_m . At the point of intersection ($s_m = 1.1511$), the curve of the FFLO critical field continues on that of the homogeneous case.

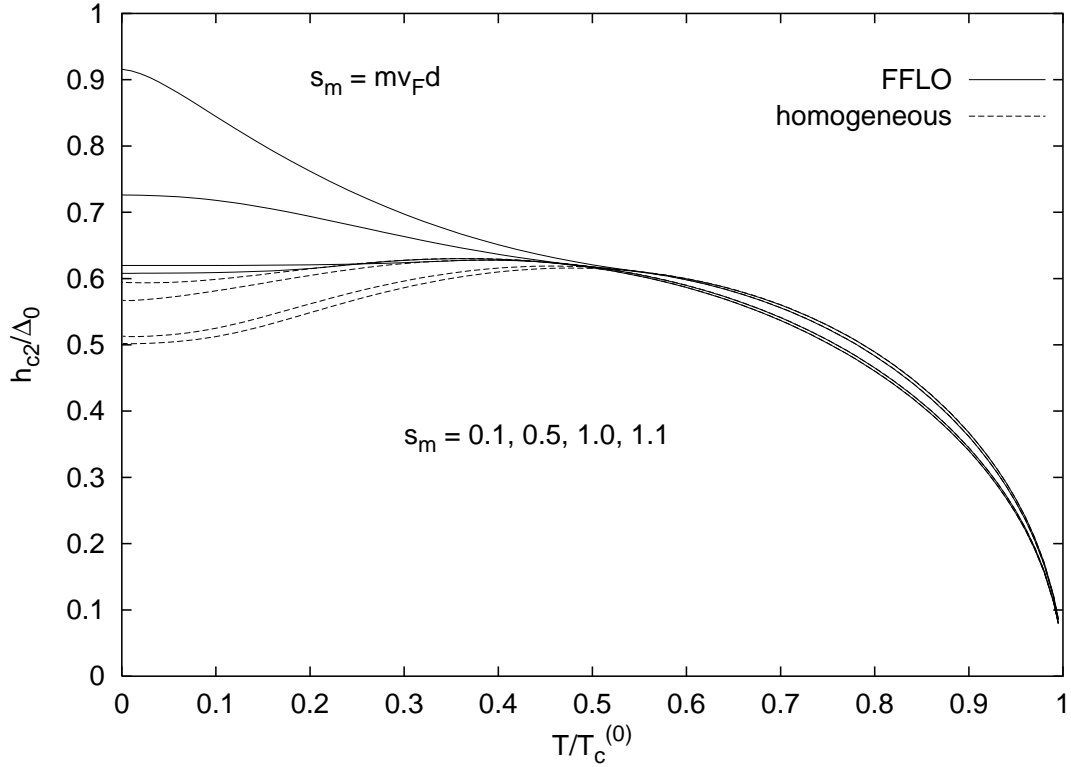


FIGURE 2.16: Upper critical fields of the FFLO- and the homogeneous case as a function of reduced temperature and for various s_m . The FFLO critical fields are labeled by solid lines and decrease as s_m increases. At low temperatures, h_{c2} of the homogeneous case (dashed lines) increases with the film thickness for these s_m -values.

Finally, the temperature dependence of both fields are compared in Fig. 2.16. The critical field of the homogeneous case increases for these s_m -values, while the FFLO critical field decreases (compare Fig. 2.15) and the characteristic temperature t_0 ($t_0|_{d=0} = 0.56$), at which both fields match for $t \geq t_0$, shifts towards lower temperatures.

2.3 Thermodynamic properties

In the previous sections of this chapter, the upper critical field was analyzed with respect to the thickness of the superconducting film. It was shown that especially the FFLO critical field is sensitive to changes in d and converges towards the critical field of the homogeneous case or the d -dependent unstable solution of the BCS equations. Another property of interest is the thermodynamic critical field, at which the free energy of the normal state equals that of the superconducting state. It was also calculated by Sarma [29] as the stable solution of the BCS equations. In case of $d = 0$, the FFLO critical field lies above the thermodynamic critical field for $t \leq 0.56$, but it was shown that $h_{c2,\text{FFLO}}$ is sensitive to changes in the film

thickness. It would be possible for the thermodynamic critical field to exceed $h_{c2,\text{FFLO}}$ for certain values of d . As a consequence, the system will undergo a transition analogous to the one from type II to type I superconductivity.

In this section, the quasiclassical equations are solved for a spatially constant gap function. At first, the numerical solutions for the gap function and the free energy in the case of $d = 0$ previously shown by Sarma [29] in the framework of BCS theory are reviewed. Afterwards, the quasiclassical equations are solved with respect to a finite thickness of the superconducting film. The gap function and free energy are analyzed as functions of the thickness parameter and the thermodynamic critical field is calculated and compared to the FFLO critical field.

2.3.1 Quasiclassical equations in the limit $d \rightarrow 0$ or the BCS state

For an infinitely thin film, the free energy of the FFLO state is only slightly lower than the free energy of the homogeneous (paramagnetically limited) superconducting state. The presence of an orbital pair breaking component, realized by a vector potential, in our film of thickness d may change the free energy balance in a decisive way. To clarify this point, we calculate the free energies of the homogeneous superconducting and normal-conducting states and compare the resulting phase boundaries and stability limits with the FFLO transition line.

We start with Eilenberger's transport equations given in Chapter 1 and substitute f for $f_{(+)}$, f^+ for $f_{(-)}^+$ and g for $g_{(+)}$:

$$\begin{aligned} \left[2\omega_s + \hbar\mathbf{v}_{\mathbf{F}}\partial_{\mathbf{r}}\right]f(\hat{k},\omega_s) &= 2\Delta g(\hat{k},\omega_s) \\ \left[2\omega_s - \hbar\mathbf{v}_{\mathbf{F}}\partial_{\mathbf{r}}^*\right]f^+(\hat{k},\omega_s) &= 2\Delta^*g(\hat{k},\omega_s) \\ g &= \sqrt{1 - ff^+}, \end{aligned} \quad (2.81)$$

with $\omega_s = \omega_l - i\mu H$. The self consistency equation for the gap is given by

$$\left(2\pi k_B T \sum_{l=0}^{\infty} \frac{1}{\omega_l} + \ln \frac{T}{T_c}\right) \Delta = \pi k_B T \sum_{l=0}^{\infty} \int \frac{d^2\hat{k}}{4\pi} \left(f(\hat{k},\omega_s) + f(\hat{k},\omega_s^*)\right), \quad (2.82)$$

and the free energy difference $F_s - F_n$ [33] per unit area A between the superconducting and normal state without considering demagnetization effects and for a spatially constant order parameter Δ

$$\begin{aligned} \frac{F_s - F_n}{A} &= N(E_F) \left[\left(\ln \frac{T}{T_c} + 2\pi k_B T \sum_{l=0}^{\infty} \frac{1}{\omega_l} \right) |\Delta|^2 - \right. \\ &\quad \left. \pi k_B T \sum_{l=0}^{\infty} \int \frac{d^2\hat{k}}{4\pi} \left(I(\hat{k},\omega_s) + I^*(\hat{k},\omega_s) \right) \right] \\ I &= \Delta f^+ + \Delta^* f + (g - 1) \times \end{aligned}$$

$$\left[\frac{1}{f} \left(\omega_s + \frac{\hbar v_F}{2} \hat{k} \partial_{\mathbf{r}} \right) f + \frac{1}{f^+} \left(\omega_s - \frac{\hbar v_F}{2} \hat{k} \partial_{\mathbf{r}} \right) f^+ \right], \quad (2.83)$$

Now the equations are transformed using Eilenberger units denoted by the symbol \diamond and given by equations (A.16-A.23). The corresponding equations for the critical fields of the previous chapter are given in Appendix A, section 3. The transport equations are transformed into

$$\begin{aligned} \left[\omega_s^\diamond + \hat{k} \partial_{\mathbf{r}}^\diamond \right] f &= \Delta^\diamond g \\ \left[\omega_s^\diamond - \hat{k} \partial_{\mathbf{r}}^{\diamond*} \right] f^+ &= \Delta^{\diamond*} g \\ g &= \sqrt{1 - f f^+}. \end{aligned} \quad (2.84)$$

With these units the self-consistency equation for the gap function and the free energy difference are given by

$$\left(2t \sum_{l=0}^{\infty} \frac{1}{\omega_l^\diamond} + \ln t \right) \Delta^\diamond = t \sum_{l=0}^{\infty} \int \frac{d^2 \hat{k}}{4\pi} \left(f(\hat{k}, \omega_s^\diamond) + f(\hat{k}, \omega_s^{\diamond*}) \right) \quad (2.85)$$

and

$$\begin{aligned} \left(\frac{F_s - F_n}{A} \right)^\diamond &= \left(\ln t + 2t \sum_{l=0}^{\infty} \frac{1}{\omega_l^\diamond} \right) |\Delta^\diamond|^2 - \\ &\quad t \sum_{l=0}^{\infty} \int \frac{d^2 \hat{k}}{4\pi} \left(I^\diamond(\hat{k}, \omega_s^\diamond) + I^{\diamond*}(\hat{k}, \omega_s^\diamond) \right) \\ I^\diamond &= \Delta^\diamond f^+ + \Delta^{\diamond*} f + (g - 1) \times \\ &\quad \left[\frac{1}{f} \left(\omega_s^\diamond + \hat{k} \partial_{\mathbf{r}}^\diamond \right) f + \frac{1}{f^+} \left(\omega_s^\diamond - \hat{k} \partial_{\mathbf{r}}^\diamond \right) f^+ \right]. \end{aligned} \quad (2.86)$$

The transport (2.84) and self-consistency (2.85) equations can be used to transform the free energy difference into

$$\begin{aligned} \left(\frac{F_s - F_n}{A} \right)^\diamond &= t \sum_{l=0}^{\infty} \int \frac{d^2 \hat{k}}{4\pi} \left\{ \left(f(\omega_s^\diamond) + f(\omega_s^{\diamond*}) \right) \Delta^{\diamond*} - \left[\Delta^\diamond f^+ + \Delta^{\diamond*} f + \right. \right. \\ &\quad \left. \left. (g - 1) \left(\frac{1}{f} \Delta^\diamond g + \frac{1}{f^+} \Delta^{\diamond*} g \right) + cc. \right] \right\} \end{aligned} \quad (2.87)$$

In the further calculations we keep in mind that the equations are expressed in Eilenberger units and omit the symbol \diamond .

Derivation of the gap-equation

In case of a constant gap function $\partial_{\mathbf{r}} \Delta = 0$ and the transport equations (2.84) yield for the Green's functions

$$\begin{aligned} f &= \frac{\Delta}{\sqrt{|\Delta|^2 + \omega_s^2}} \\ f^+ &= \frac{\Delta^*}{\sqrt{|\Delta|^2 + \omega_s^2}} \end{aligned}$$

$$g = \frac{\omega_s}{\sqrt{|\Delta|^2 + \omega_s^2}}. \quad (2.88)$$

Therefore, the self consistency equation for the gap function (2.85) results in

$$2t \sum_{l=0}^{\infty} \frac{1}{\omega_l} + \ln t = t \sum_{l=0}^{\infty} \left(\frac{1}{\sqrt{|\Delta|^2 + \omega_s^2}} + cc. \right), \quad (2.89)$$

which gives the gap as a function of temperature and external magnetic field.

The free-energy equation

We make use of the self-consistency (2.85) and transport equations (2.84) to transform the free energy equation (2.86) into

$$\begin{aligned} \frac{F_s - F_n}{A} &= t \sum_{l=0}^{\infty} |\Delta|^2 \left(\frac{1}{\sqrt{|\Delta|^2 + \omega_s^2}} + cc. \right) - \\ &\quad t \sum_{l=0}^{\infty} (I + I^*) \\ I &= \left(|\Delta|^2 + \omega_s^2 - \omega_s \sqrt{|\Delta|^2 + \omega_s^2} \right) \frac{2}{\sqrt{|\Delta|^2 + \omega_s^2}}, \end{aligned} \quad (2.90)$$

which results in

$$\frac{F_s - F_n}{A} = -t \sum_{l=0}^{\infty} \left(\frac{\left(\omega_s - \sqrt{|\Delta|^2 + \omega_s^2} \right)^2}{\sqrt{|\Delta|^2 + \omega_s^2}} + cc. \right). \quad (2.91)$$

2.3.2 Equations in the d-wave case

As in chapter one, the gap-function $\Delta(\mathbf{r}, \hat{\mathbf{k}})$ is assumed to be separable

$$\Delta(\mathbf{r}, \hat{\mathbf{k}}) = \Delta(\mathbf{r})\gamma(\hat{\mathbf{k}}) \quad (2.92)$$

and on the right side of the gap-equation (2.85) we insert the function $V(\hat{\mathbf{k}}, \hat{\mathbf{k}}') = \gamma(\hat{\mathbf{k}})\gamma(\hat{\mathbf{k}}')$.

Gap-equation

Therefore, the gap-equation (2.85) can be expressed as

$$\left(2t \sum_{l=0}^{\infty} \frac{1}{\omega_l} + \ln t \right) \Delta\gamma(\hat{\mathbf{k}}) = t \sum_{l=0}^{\infty} \int \frac{d^2 \hat{\mathbf{k}}'}{4\pi} V(\hat{\mathbf{k}}, \hat{\mathbf{k}}') \left(\frac{\Delta\gamma(\hat{\mathbf{k}}')}{\sqrt{|\Delta|^2 \gamma(\hat{\mathbf{k}}')^2 + \omega_s^2}} + cc. \right) \quad (2.93)$$

and get

$$\left(2t \sum_{l=0}^{\infty} \frac{1}{\omega_l} + \ln t \right) = t \sum_{l=0}^{\infty} \int \frac{d^2 \hat{\mathbf{k}}'}{4\pi} \left(\frac{\gamma(\hat{\mathbf{k}}')^2}{\sqrt{|\Delta|^2 \gamma(\hat{\mathbf{k}}')^2 + \omega_s^2}} + cc. \right). \quad (2.94)$$

Inserting the symmetry function $\gamma(\hat{\mathbf{k}})^2 = 1 + \cos(4\varphi)$ leads to

$$\left(2t \sum_{l=0}^{\infty} \frac{1}{\omega_l} + \ln t\right) = t \sum_{l=0}^{\infty} \int_0^{2\pi} \frac{d\varphi}{2\pi} \left(\frac{(1 + \cos(4\varphi))}{\sqrt{|\Delta|^2(1 + \cos(4\varphi)) + \omega_s^2}} + cc. \right). \quad (2.95)$$

Free-energy difference

Assuming separability of the gap-function and inserting $V(\hat{\mathbf{k}}, \hat{\mathbf{k}}')$ will lead to the free-energy difference of

$$\begin{aligned} \frac{F_s - F_n}{A} &= \int \frac{d^2 \hat{k}}{4\pi} \left(\ln t + 2t \sum_{l=0}^{\infty} \frac{1}{\omega_l} \right) |\Delta(\hat{\mathbf{k}})|^2 - \\ &\quad t \sum_{l=0}^{\infty} \int \frac{d^2 \hat{k}}{4\pi} \int \frac{d^2 \hat{k}'}{4\pi} V(\hat{\mathbf{k}}, \hat{\mathbf{k}}') \left(I(\hat{\mathbf{k}}, \hat{\mathbf{k}}', \omega_s) + I^*(\hat{\mathbf{k}}, \hat{\mathbf{k}}', \omega_s) \right) \\ I &= \Delta(\hat{\mathbf{k}}) f^+(\hat{\mathbf{k}}', \omega_s) + \Delta^*(\hat{\mathbf{k}}) f(\hat{\mathbf{k}}', \omega_s) + (g(\hat{\mathbf{k}}', \omega_s) - 1) \frac{\gamma(\hat{\mathbf{k}})}{\gamma(\hat{\mathbf{k}}')} \times \\ &\quad \left[\frac{1}{f(\hat{\mathbf{k}}', \omega_s)} (\omega_s + \hat{\mathbf{k}}' \partial_{\mathbf{r}}) f(\hat{\mathbf{k}}', \omega_s) + \frac{1}{f^+(\hat{\mathbf{k}}', \omega_s)} (\omega_s - \hat{\mathbf{k}}' \partial_{\mathbf{r}}) f^+(\hat{\mathbf{k}}', \omega_s) \right] \end{aligned} \quad (2.96)$$

The disappearance of the derivative of the free-energy difference with respect to Δ^* gives the gap-equation. Inserting the value of the symmetry function and further simplification of the equation analogous to eq. (2.91) gives

$$\begin{aligned} \frac{F_s - F_n}{A} &= - \int_0^{2\pi} \frac{d\varphi}{2\pi} (1 + \cos(4\phi)) \\ &\quad t \sum_{l=0}^{\infty} \int_0^{2\pi} \frac{d\varphi'}{2\pi} \left(\frac{(\omega_s - \sqrt{|\Delta|^2(1 + \cos(4\varphi')) + \omega_s^2})^2}{\sqrt{|\Delta|^2(1 + \cos(4\varphi')) + \omega_s^2}} + cc. \right) \\ &= -t \sum_{l=0}^{\infty} \int_0^{2\pi} \frac{d\varphi'}{2\pi} \left(\frac{(\omega_s - \sqrt{|\Delta|^2(1 + \cos(4\varphi')) + \omega_s^2})^2}{\sqrt{|\Delta|^2(1 + \cos(4\varphi')) + \omega_s^2}} + cc. \right). \end{aligned} \quad (2.97)$$

2.3.3 Phase boundary diagrams

The numerical solution of eq. (2.89) for a certain temperature and external field gives the gap function, which is used to calculate the free energy difference (2.91). A temperature dependent cutoff $N_D = \text{Max}(\mu H, \Delta_0)/t - 1$ was introduced to calculate the sum over the Matsubara index l . Both properties are depicted in figure 2.17 as functions of external field for various reduced temperatures. For $t = 0$ the solution for the gap function consists of two branches

$$\Delta = \begin{cases} \Delta_0, & 0 \leq \mu H \leq \Delta_0 \\ \sqrt{(2\mu H - \Delta_0)\Delta_0}, & \frac{\Delta_0}{2} \leq \mu H \leq \Delta_0 \end{cases}, \quad (2.98)$$

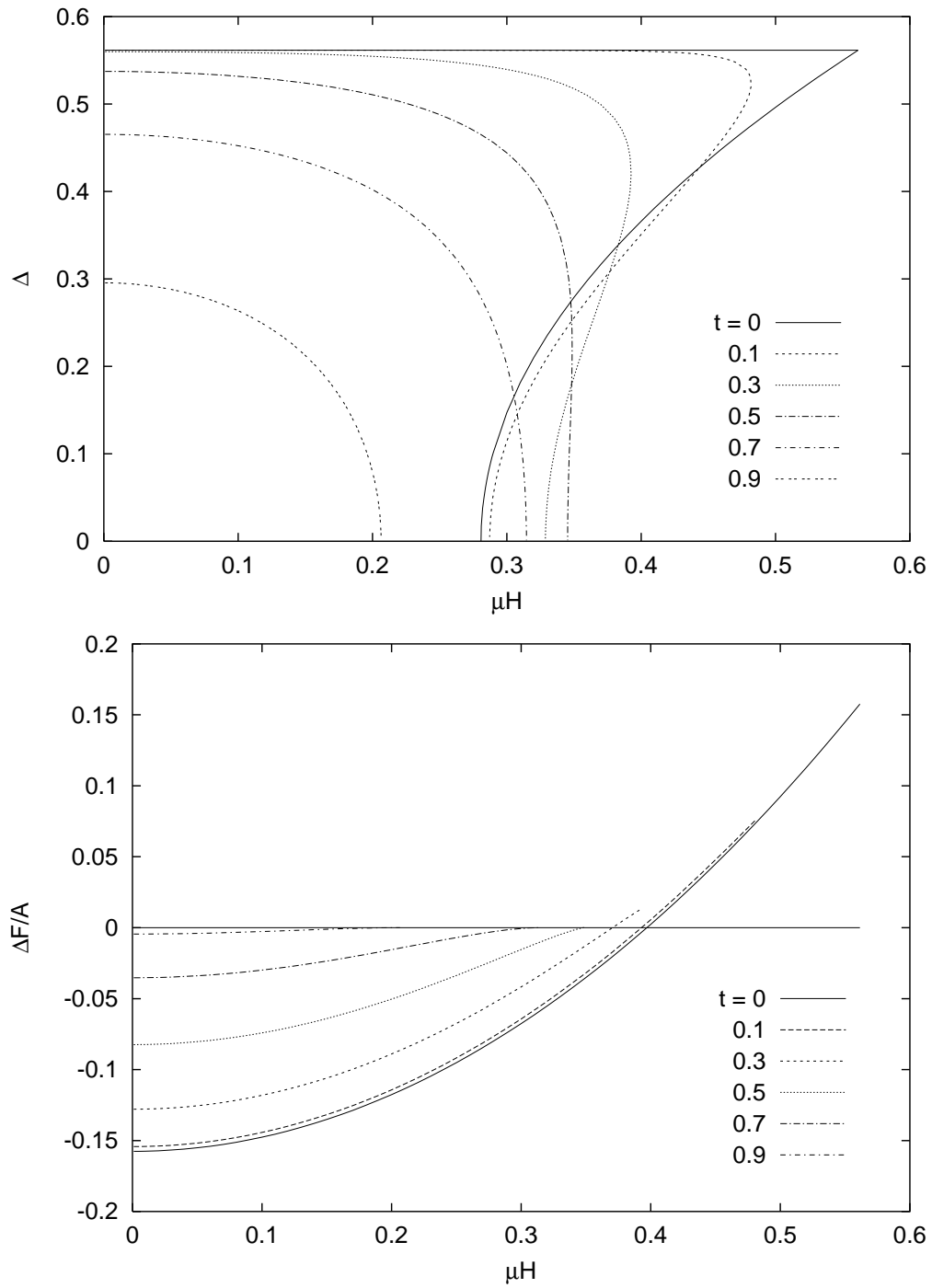


FIGURE 2.17: Gap function Δ (top) and free energy difference $\Delta F/A$ (bottom) as functions of external field for various temperatures. Only the stable branch of the gap function was used in the calculation of the free energy.

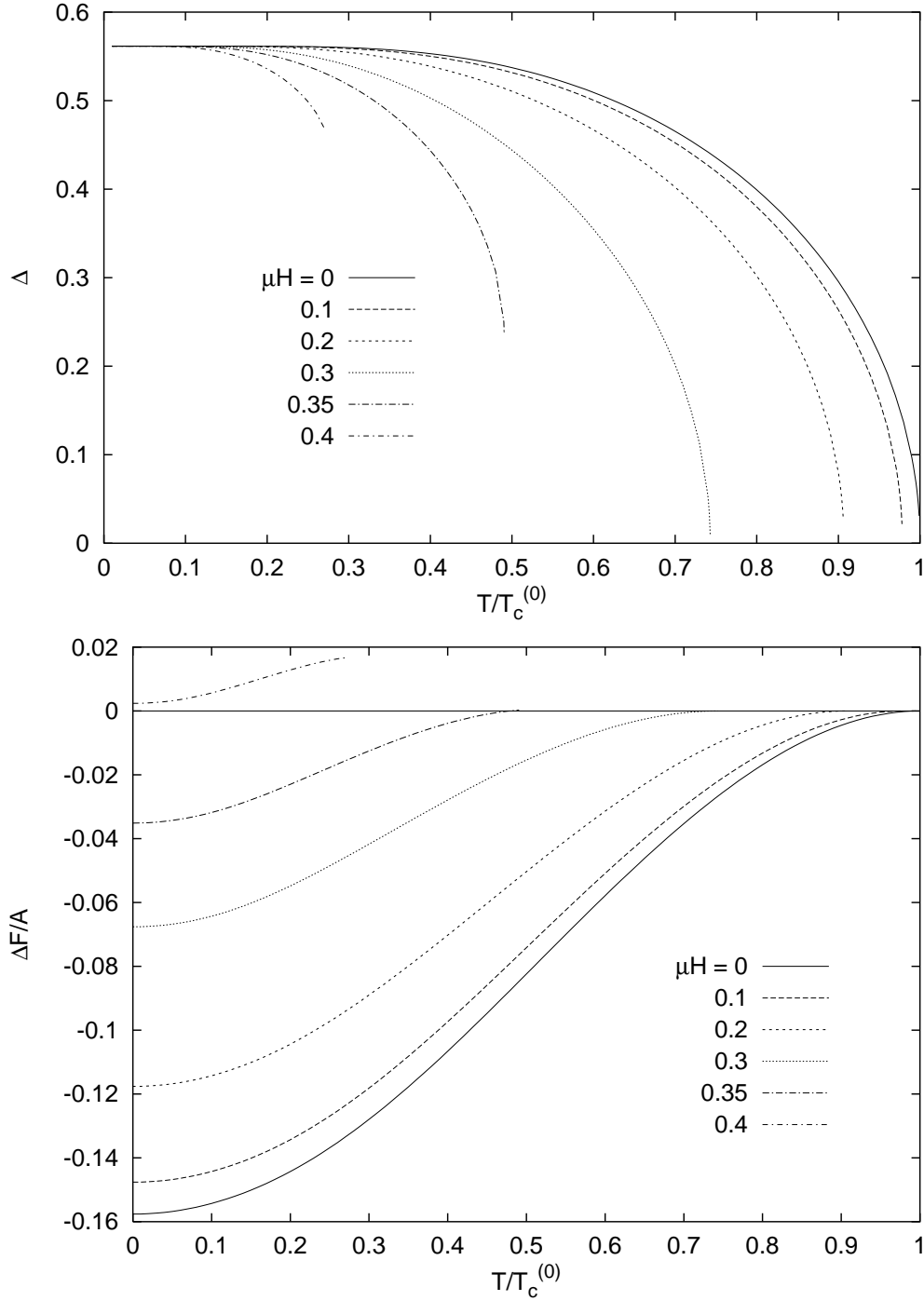


FIGURE 2.18: Gap function Δ (top) and free energy difference $\Delta F/A$ (bottom) as functions of reduced temperature for various external fields. Only the stable solution is shown in both cases.

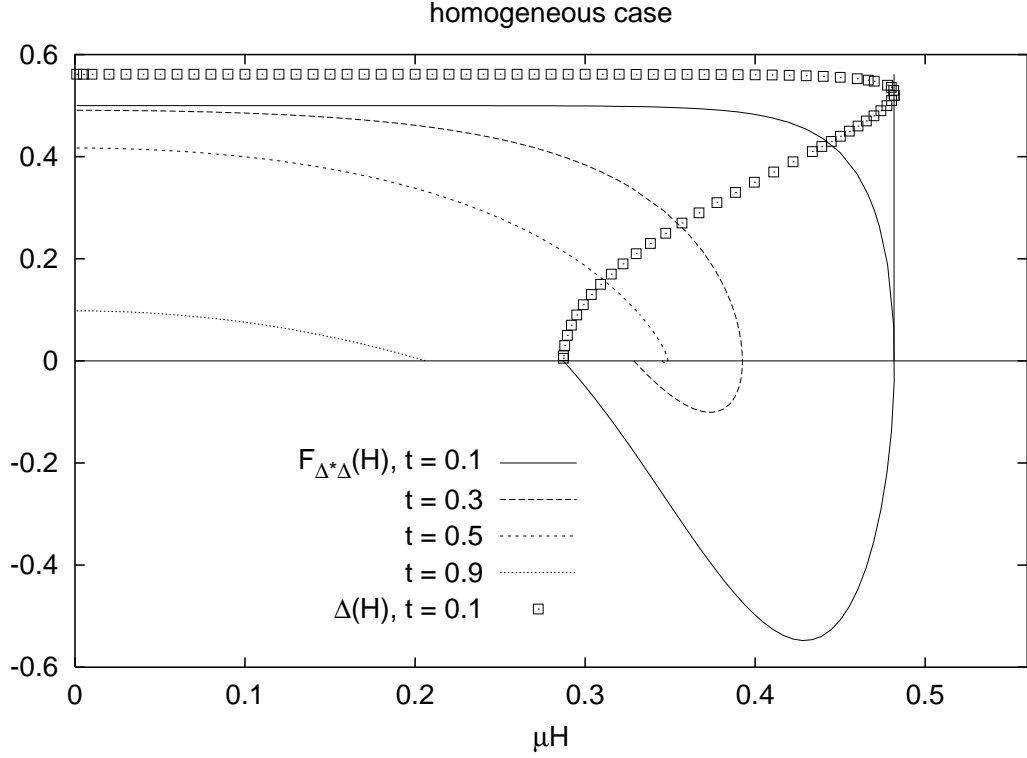


FIGURE 2.19: Second derivative of the free energy difference with respect to Δ^* and Δ as a function of external field for various reduced temperatures. The gap as a function of field for $t = 0.1$ is depicted to show that the upper stability point corresponds to the highest possible field which gives the gap as a solution of (2.85).

where $\Delta_0 = e^{-\gamma}$, and γ is Euler's constant $\gamma \simeq 0.57721$. The gap function is smoothened as the temperature increases and its ambiguity disappears for $t \geq 0.56$, corresponding to the disappearance of the FFLO state. The stable branch of the free energy difference $(F_s - F_n)/A = \Delta F/A$ at $t = 0$ is given by

$$\frac{\Delta F}{A} = \mu^2 H^2 - \frac{\Delta_0}{2}, \quad (2.99)$$

with the first branch of eq. (2.98) $\Delta = \Delta_0$. Only the stable branch of the free energy is depicted in the bottom frame of Fig. 2.17. At temperatures $t \leq 0.56$, the transition from the superconducting to the normal state already has taken place for a given μH , even though the gap function still has finite values. The temperature dependent gap function and the corresponding free energy diagram are shown in Fig. 2.18 for various external fields μH .

If one treats f , f^+ and Δ^* (or Δ) as arbitrary functions and calculates the variation of the

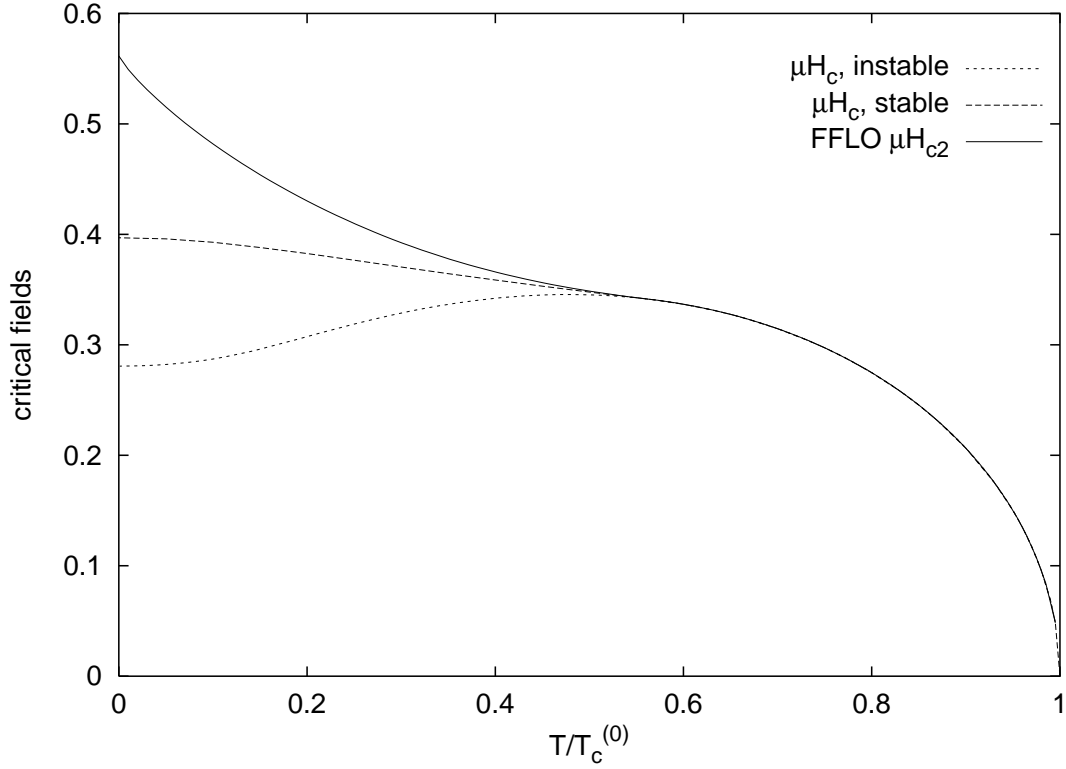


FIGURE 2.20: Critical fields in dimensionless Eilenberger units (A.26) as functions of reduced temperature. The solid line shows the FFLO critical field (2.79) for $d = 0$. The long dashed line shows the thermodynamic critical field, calculated from the free energy difference $\Delta F(\mu H_c)/A = 0$. The short dashed line is the solution of eq. (2.102).

free energy difference under these functions, which is in our case the first derivative

$$\nabla_f \frac{F_s - F_n}{A} = \left(\frac{\partial/\partial \Delta^*}{\partial/\partial f} \right) \frac{F_s - F_n}{A}, \quad (2.100)$$

it gives the self-consistency (2.85) and the transport equations (2.84) as Euler-Lagrange equations if one requires stationarity of the free energy difference under variation of these functions. However, it has no extremum for the correct solutions of (2.85) and (2.84). But a weaker statement holds: If one inserts the solutions of (2.84) into $(F_s - F_n)/A$, so that it is solely a function of Δ (or Δ^*), it consequently has its minimum (stable solution) or maximum (instable solution) for certain values of Δ which satisfy (2.85). Fig. 2.19 depicts the second derivative of the free energy difference

$$\frac{\partial^2}{\partial \Delta \partial \Delta^*} \frac{F_s - F_n}{A} = \frac{t}{2} \sum_{l=0}^{N_D} \left(\frac{|\Delta|^2}{(|\Delta|^2 + \omega_s^2)^{3/2}} + cc. \right) \quad (2.101)$$

with respect to Δ and Δ^* at the stationary point. For the upper branch of the gap-function, the second derivative is positive, meaning that $(F_s - F_n)/A$ is minimized and giving the stable

solution, while for the other branch it is maximized (instable solution). The stability point of the normal state (lower stability point), which is the lower value of the external field at which the second derivative (2.101) disappears, corresponds to the critical field given by eq. (2.102), while the upper stability point coincides with the FFLO critical field. This calculation shows (see the curves for $T/T_c = 0.1$ in Fig. 2.19) that the homogeneous superconducting state may be superheated up to the highest field, where the two branches cross. The lowest field where the lower branch exists defines, on the other hand, the supercooling limit of the normal-conducting state. Thus, the region of the lower branch corresponds, as expected, exactly to the metastable region of the first order transition. In this way, three transition lines, the phase transition line where the free energies coincide, the superheating line, and the supercooling line, are determined by solving equations (2.89) and (2.101). For finite d the same method is used to determine the metastable region.

Note that the equations (2.89) and (2.91) for the gap function and free energy do not depend on the out of plane angle ϑ of the external field as a consequence of the spatially constant gap function. Another property which does not depend on ϑ for the same reason is the equation for critical field (2.80), which results in

$$-\ln t = t \int_0^\infty ds \frac{1}{\sinh(ts)} \left(1 - \cos(\mu H s)\right), \quad (2.102)$$

in case of $d = 0$ and in Eilenberger units, and which is the instable solution of the free energy equation for the critical field as was shown by Sarma [29]. The superheating and supercooling critical fields, the thermodynamic critical field obtained from the free energy difference $\Delta F(\mu H_c)/A = 0$, and the FFLO critical field are depicted in Fig. 2.20. Eilenberger units were used in this plot, which can be reverted to the previous unit system by multiplying the critical field data with e^γ (A.26). These four transition lines were calculated in the purely paramagnetic limit. For $T > T_{tri} = 0.56 T_c$ all four lines merge into a single second order transition line. Below the tricritical point T_{tri} only three different lines are visible in Fig. 2.20 since, interestingly, the FFLO critical field and the superheating field exactly coincide. This coincidence occurs, however, only for a circular Fermi surface. Only the FFLO critical field is physically significant for $d = 0$, the other lines are meaningless. At the FFLO critical field, a second order phase transition to the FFLO state takes place.

If not stated explicitly, the stable branch of the thermodynamic critical field will from now on be referred to as the thermodynamic critical field. While the transition from the FFLO to the normal state is of second order, the transition at μH_c of the thermodynamic critical field to the normal state is of first order. Maki and Tsuneto [45] obtained the same result as Sarma [29] with the Gor'kov equations including the Pauli limiting term and discussed the order of transition of the critical field for the thermodynamic critical field and for the instable branch, which is of second order.

2.3.4 Finite thickness equations

In the previous chapter the finite thickness of the superconducting film was expressed by averaging the Green's functions $f_{(+)} = f$ and $f_{(-)}^+ = f^+$ over z (2.40), assuming that the gap function is constant in z for $d \ll \xi_0$. We consider the finite thickness of the film in a similar way by first starting with the z -dependent Green's functions derived in Chapter 2

$$\begin{aligned} f(z) &= \int_0^\infty ds e^{-s\omega_s} e^{-i\alpha s z} \Delta \operatorname{sgn}\omega_l \\ f^+(z) &= \int_0^\infty ds e^{-s\omega_s} e^{i\alpha s z} \Delta^* \operatorname{sgn}\omega_l, \end{aligned} \quad (2.103)$$

where $\alpha = \frac{1}{2\pi T_c} v_F \kappa_{\parallel} d \hat{k}_x$, and consider the full Green's function

$$g(z) = \sqrt{1 - f(z)f^+(z)} \quad (2.104)$$

in the theory, instead of simply taking the linearization $g = \operatorname{sgn}\omega_l$ as in the previous chapter:

$$\begin{aligned} f(z) &= \int_0^\infty ds e^{-s\omega_s} e^{-i\alpha s z} \Delta g(z) \\ f^+(z) &= \int_0^\infty ds e^{-s\omega_s} e^{i\alpha s z} \Delta^* g(z). \end{aligned} \quad (2.105)$$

The Green's functions f and f^+ are expanded in a z -independent and to the first order in a z -dependent part

$$\begin{aligned} f(z) &= \bar{f} + \delta f(z) \\ f^+(z) &= \bar{f}^+ + \delta f^+(z), \end{aligned} \quad (2.106)$$

where \bar{f} is the mean value of f in the z -direction

$$\bar{f} = \frac{1}{d} \int_{-d/2}^{d/2} dz f(z) = \bar{f} + \frac{1}{d} \int_{-d/2}^{d/2} dz \delta f(z), \quad (2.107)$$

which means that the integration over δf vanishes

$$\frac{1}{d} \int_{-d/2}^{d/2} dz \delta f(z) = 0. \quad (2.108)$$

The same applies for f^+ . We further assume that the Green's function only has a small variation in z , so that terms of quadratic and higher order in δf

$$\left(\delta f(z) \right)^n \sim 0 \quad \forall n \geq 2 \quad (2.109)$$

can be neglected. As for the Green's function g , it is also assumed that

$$g(z) = \bar{g} + \delta g(z), \quad (2.110)$$

and f in eq. (2.105) can be expressed as

$$f(z) = \int_0^\infty ds e^{-s\omega_s} e^{-i\alpha s z} \Delta \bar{g} + \int_0^\infty ds e^{-s\omega_s} e^{-i\alpha s z} \Delta \delta g(z). \quad (2.111)$$

Now, the mean value of g in z -direction is calculated

$$\bar{g} = \frac{1}{d} \int_{-d/2}^{d/2} dz \sqrt{1 - f(z)f^+(z)} \quad (2.112)$$

by first transforming the square root into its sum equivalent

$$\sqrt{1 - f(z)f^+(z)} = 1 - \frac{1}{2}f(z)f^+(z) - \frac{1}{8}\left(f(z)f^+(z)\right)^2 - \frac{1}{16}\left(f(z)f^+(z)\right)^3 \dots, \quad (2.113)$$

and by making use of eqs. (2.106), (2.108) and (2.109), terms of higher order in δf and integrations over single order terms in δf disappear, so that the equation for \bar{g} (2.112) finally yields

$$\bar{g} = 1 - \frac{1}{2}\bar{f}\bar{f}^+ - \frac{1}{8}\left(\bar{f}\bar{f}^+\right)^2 - \frac{1}{16}\left(\bar{f}\bar{f}^+\right)^3 \dots = \sqrt{1 - \bar{f}\bar{f}^+}. \quad (2.114)$$

In Chapter 2, it was assumed that the thickness of the film d is much smaller than the coherence length ξ_0 ($d \ll \xi_0$), so that the gap function on the left side of eq. (2.111) could be expressed as

$$\Delta(z) = \Delta + \delta\Delta(z), \quad (2.115)$$

where $\delta\Delta(z) \sim 0$. If one makes the same approximation for g , namely $\delta g(z) \sim 0$, which applies if $\delta f(z) \ll \bar{f}$ and $\delta f^+(z) \ll \bar{f}^+$ because of

$$g = \sqrt{1 - \bar{f}\bar{f}^+ \left(1 + \frac{\delta f(z)}{\bar{f}} + \frac{\delta f^+(z)}{\bar{f}^+}\right)} \simeq \sqrt{1 - \bar{f}\bar{f}^+} = \bar{g} \quad (2.116)$$

the Green's function f (eq. 2.111) yields

$$f(z) = \int_0^\infty ds e^{-s\omega_s} e^{-i\alpha s z} \Delta \bar{g}, \quad (2.117)$$

and its mean value is given by

$$\bar{f} = \int_0^\infty ds e^{-s\omega_s} \Delta \bar{g} \frac{1}{d} \int_{-d/2}^{d/2} dz e^{-i\alpha s z} = \int_0^\infty ds e^{-s\omega_s} \Delta \bar{g} \frac{1}{\frac{1}{2}d\alpha s} \sin\left(\frac{1}{2}d\alpha s\right). \quad (2.118)$$

We now have the set of equations

$$\begin{aligned}\bar{f} &= \int_0^\infty ds e^{-s\omega_s} \Delta \bar{g} \frac{1}{\frac{1}{2}d\alpha s} \sin\left(\frac{1}{2}d\alpha s\right) \\ \bar{f}^+ &= \int_0^\infty ds e^{-s\omega_s} \Delta^* \bar{g} \frac{1}{\frac{1}{2}d\alpha s} \sin\left(\frac{1}{2}d\alpha s\right) \\ \bar{g} &= \sqrt{1 - \bar{f}\bar{f}^+},\end{aligned}\tag{2.119}$$

to solve and use in the derivation of the gap and free energy functions. Starting with the Green's function \bar{f}

$$\bar{f} = \int_0^\infty ds e^{-s\omega_s} \frac{1}{\frac{1}{2}Hds \cos \vartheta \cos \varphi} \sin\left(\frac{1}{2}Hds \cos \vartheta \cos \varphi\right) \Delta \bar{g},\tag{2.120}$$

with the expression

$$\frac{1}{4\pi k_B T_c} s v_F \kappa_{\parallel} d \hat{k}_x = \frac{1}{2} H^\circ d^\circ s \cos \vartheta \cos \varphi = B_d(\varphi) s\tag{2.121}$$

transformed into Eilenberger units, the integration over s can be carried out, as \bar{f} , \bar{f}^+ , \bar{g} and Δ are independent of s

$$\int_0^\infty ds e^{-s\omega_s} \frac{1}{B_d(\varphi) s} \sin\left(B_d(\varphi) s\right) = \frac{1}{B_d(\varphi)} \text{atan}\left(\frac{B_d(\varphi)}{\omega_s}\right),\tag{2.122}$$

which results in the mean Green's function

$$\bar{f} = \frac{1}{B_d(\varphi)} \text{atan}\left(\frac{B_d(\varphi)}{\omega_s}\right) \Delta \bar{g}.\tag{2.123}$$

In the limit $d \rightarrow 0$ eq. (2.122) yields

$$\lim_{d \rightarrow 0} \frac{1}{B_d(\varphi)} \text{atan}\left(\frac{B_d(\varphi)}{\omega_s}\right) = \frac{1}{\omega_s}\tag{2.124}$$

and the Green's function \bar{f} takes its original form $f = \Delta g / \omega_s$. With

$$\bar{f}^+ = \frac{1}{B_d(\varphi)} \text{atan}\left(\frac{B_d(\varphi)}{\omega_s}\right) \Delta^* \bar{g}\tag{2.125}$$

and the normalization condition $\bar{g} = \sqrt{1 - \bar{f}\bar{f}^+}$ we obtain

$$\begin{aligned}\bar{f} &= \frac{\Delta}{\sqrt{|\Delta|^2 + A_{d,l}(\varphi)^2}} \\ \bar{f}^+ &= \frac{\Delta^*}{\sqrt{|\Delta|^2 + A_{d,l}(\varphi)^2}}\end{aligned}$$

$$\bar{g} = \frac{A_{d,l}(\varphi)}{\sqrt{|\Delta|^2 + A_{d,l}(\varphi)^2}}, \quad (2.126)$$

with the substitution

$$\frac{1}{A_{d,l}(\varphi)} = \frac{1}{B_d(\varphi)} \operatorname{atan} \left(\frac{B_d(\varphi)}{\omega_s} \right) \quad (2.127)$$

which gives

$$\lim_{d \rightarrow 0} A_{d,l}(\varphi) = \omega_s \quad (2.128)$$

in the limit $d \rightarrow 0$. The Green's functions (2.126) take the same form as eq. (2.88), if $A_{d,l}(\varphi)$ is replaced by ω_s .

Gap equation

With eqs. (2.126), the self consistency equation for the gap function (2.85) results in

$$2t \sum_{l=0}^{\infty} \frac{1}{\omega_l} + \ln t = t \sum_{l=0}^{\infty} \int_0^{2\pi} \frac{d\varphi}{2\pi} \left(\frac{1}{\sqrt{|\Delta|^2 + A_{d,l}(\varphi)^2}} + cc. \right), \quad (2.129)$$

which gives the gap as a function of temperature and external magnetic field.

Free energy difference

The free energy difference is derived the same way as its two dimensional counterpart (2.91), and the thickness dependent expression for $\Delta F/A$ is given by

$$\frac{F_s - F_n}{A} = -t \sum_{l=0}^{\infty} \int_0^{2\pi} \frac{d\varphi}{2\pi} \left(\frac{(A_{d,l}(\varphi) - \sqrt{|\Delta|^2 + A_{d,l}(\varphi)^2})^2}{\sqrt{|\Delta|^2 + A_{d,l}(\varphi)^2}} + cc. \right). \quad (2.130)$$

Note that the equations for the gap function and the free energy difference can be obtained by simply replacing ω_s by $A_{d,l}(\varphi)$ before integrating over the Fermi surface.

2.3.5 Phase boundary analysis and numerical results for $d > 0$

The numerical results shown in this section will be restricted to s -wave superconductors, with an isotropic gap. A few calculations have also been performed for d -wave superconductors, with results which generally confirm the behavior found for s -wave superconductors. An interesting peculiarity of d -wave superconductors without any orbital pair-breaking is a steep rise of $H_{c2,\text{FFLO}}$ with decreasing T below $T/T_c = 0.1$ (See Fig. 4 of Ref. [10]). This peak belongs to the $\varphi = 0$ portion of the critical field [12] and is much steeper than the corresponding part of the critical field curve for s -wave superconductors. Our calculations show that this peak can be effectively suppressed by a very small ($d/k_F^{-1} \simeq 0.2$) amount of orbital pair breaking. The absence of this peak in measurements [9] on κ -(BEDT-TTF)₂Cu(NCS)₂ may be an indication of a very small residual orbital pair-breaking contribution in this material.

As in the previous Chapter the summation over l was cut off at the temperature dependent index N_D . The phase diagrams now depend on the parameter

$$s_d = \frac{d}{2\mu} \cos \vartheta, \quad (2.131)$$

expressing the thickness of the film relative to the BCS coherence length ξ_0 , the parameter $\mu = \pi k_B T_c / 2E_F$ and the angle ϑ of the external magnetic field relative to the superconducting film. The dimensionality of the system does not show up in the framework of BCS theory as the quasiclassical propagator is isotropic. Therefore, there is no dependence on the angle of the external field with respect to the two dimensional superconducting plane in the corresponding equations. If the film is assumed to have a finite thickness, the Green's functions become dependent on \hat{k} (or on φ), and as in the case of the FFLO equations, one can expect the dimensionality of the system to affect its properties.

Fig. 2.21 shows the gap function and the free energy difference as functions of external field at $t = 0.5$ for various thickness parameters. One can clearly see that the ambiguity of the gap function disappears at a certain value of s_d . For $H = 0$ there is no dependence on s_d , as the limit $\sin(x)/x$ converges to 1 for $x \rightarrow 0$ in eq. 2.120. The gap function and free energy difference as functions of reduced temperature at $\mu H = 0.1$ for various s_d are depicted in Fig. 2.22.

The dependence of the critical field resulting from the equality of the free energies in the superconducting and normal state on s_d are shown in Fig. 2.23 for various reduced temperatures t . For $t = 0.9$, which is greater than the characteristic temperature $t = 0.56$, a continuous decrease in μH_c for increasing s_d is observed.

The paramagnetic pair-breaking effect dominates for very small d while the orbital effect dominates for large d . Thus, it should be possible to define a critical thickness d which roughly separates the two regimes. This crossover behavior is shown in Fig. 2.23 (above) for the thermodynamic critical field H_c . The value of d is of the order of k_F^{-1} in the region of low temperatures, in agreement with the estimate of section 2.1. Fig. 2.23 shows also the decreasing importance of paramagnetic pair breaking with increasing T . Generally, the additional orbital pair-breaking effect brought about by the finite thickness of the conducting layer, leads to a depression of all four fields.

By comparing the thickness parameter of the previous chapter s_m with s_d (eq. (A.28)) it can be easily shown that they have the following relation

$$s_d = s_m \cos \vartheta = \frac{d}{k_F^{-1}} \cos \vartheta. \quad (2.132)$$

A detailed plot of the T -dependence of the FFLO, thermodynamic, and supercooling ($H_{c,\text{instable}}$) critical fields for $s_d = 0.5, 1.0, 2.5$ as shown in Fig. 2.24 reveals, however, significant differences. The superheating field lies above the FFLO critical field for $d > 0$ and

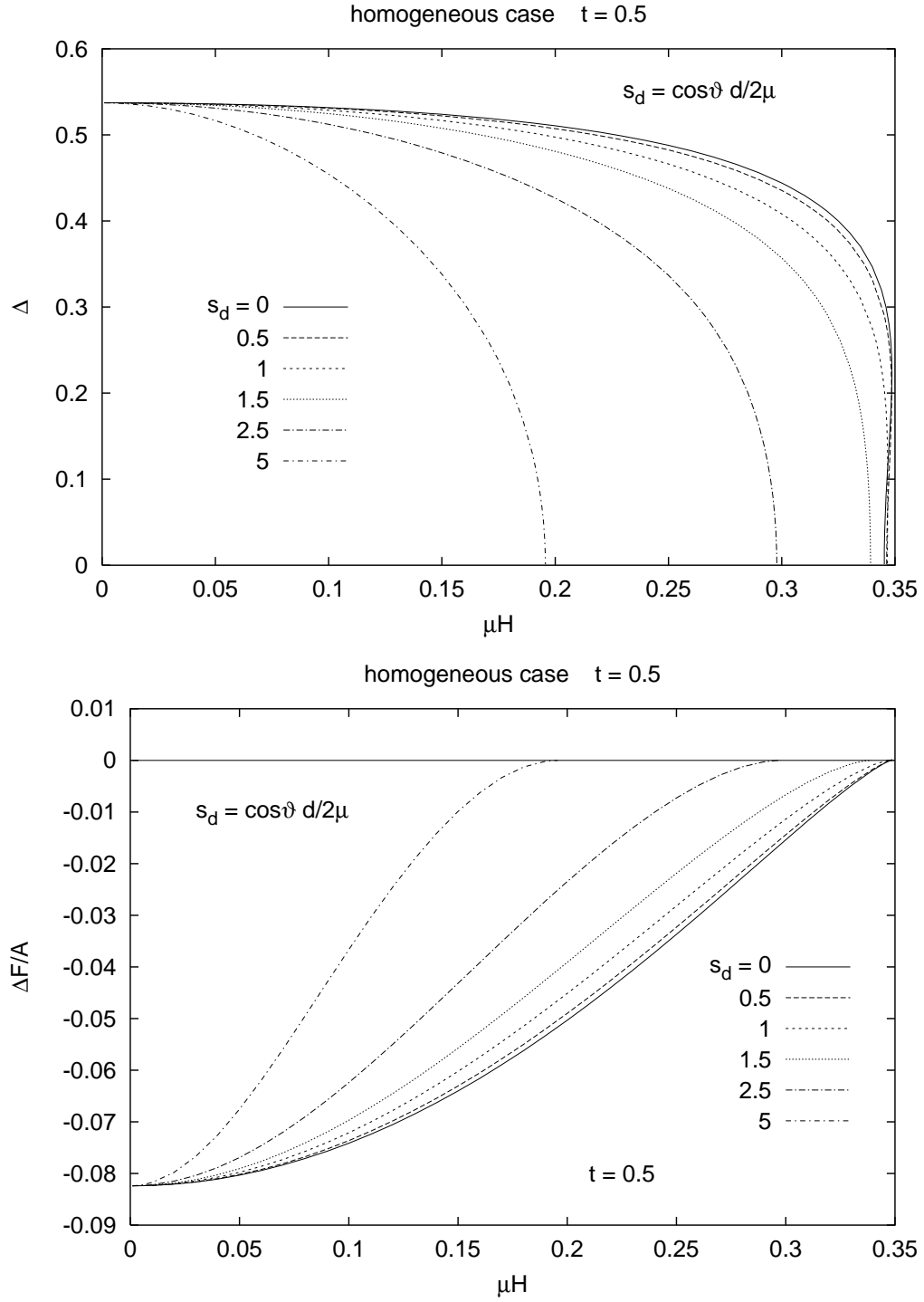


FIGURE 2.21: Gap function Δ (top) and free energy difference $\Delta F/A$ (bottom) as functions of external field at $t = 0.5$ for various thickness parameters s_d .

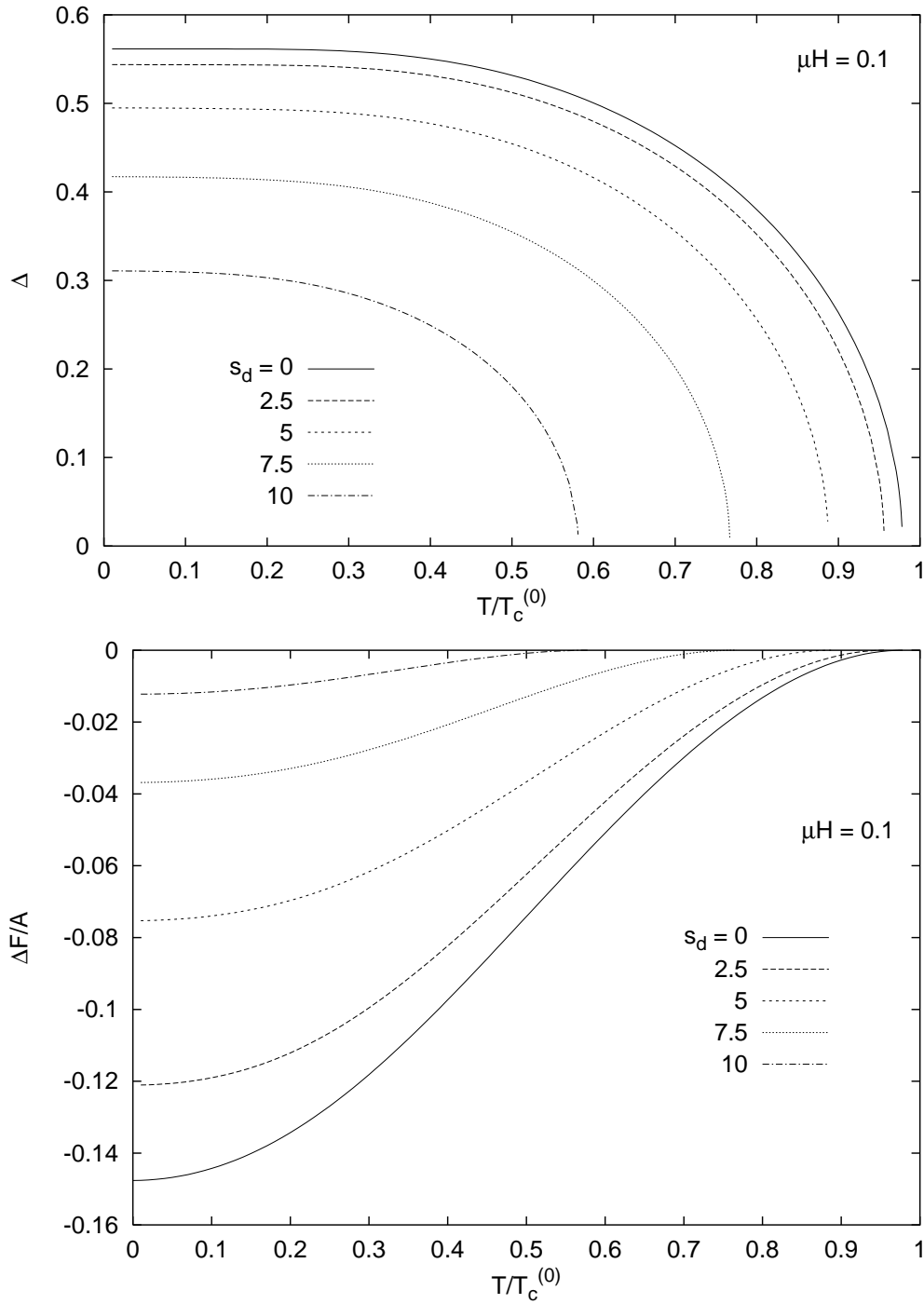


FIGURE 2.22: Gap function Δ (top) and free energy difference $\Delta F/A$ (bottom) as functions of reduced temperature at $\mu H = 0.1$ for various thickness parameters s_d .

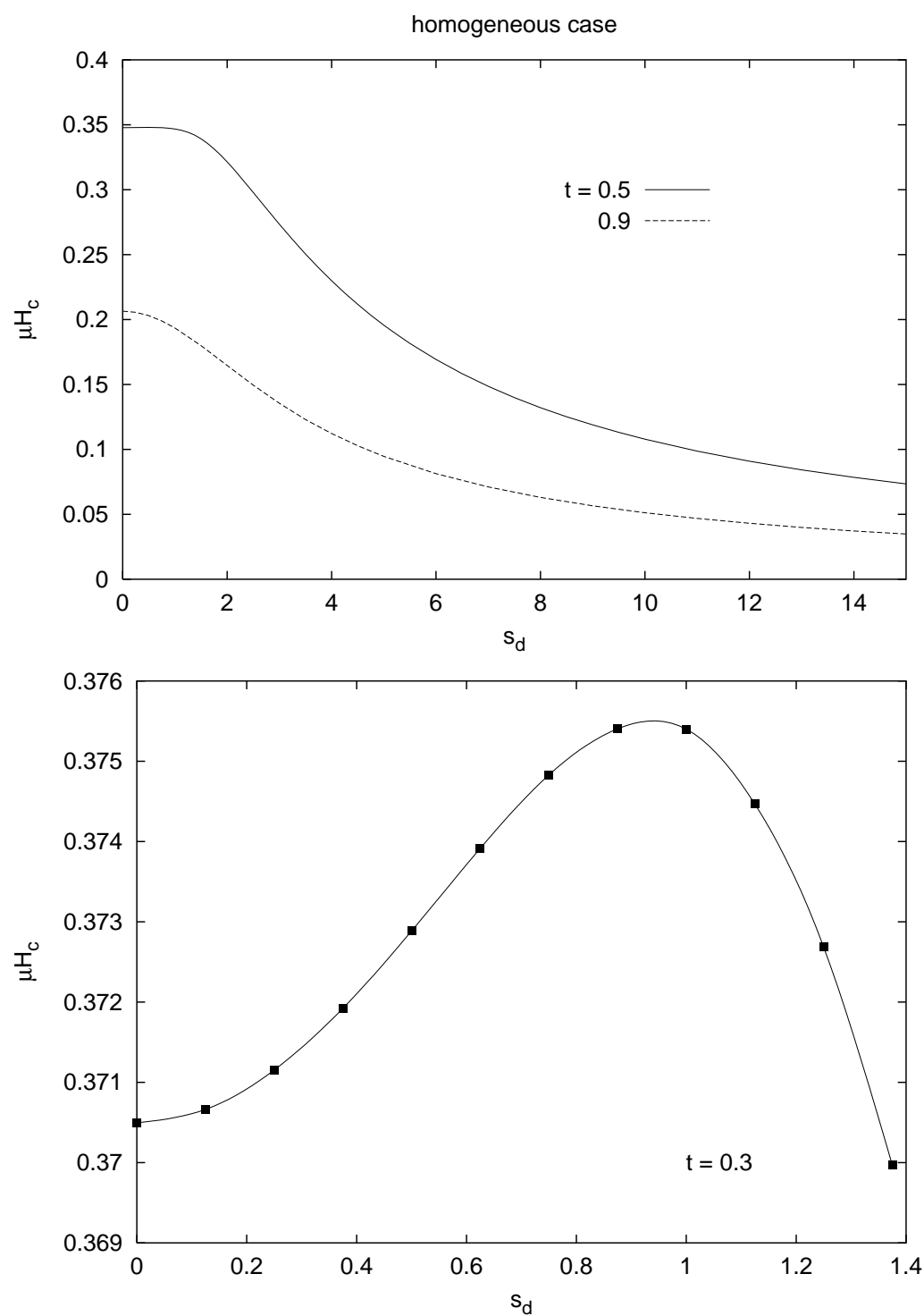


FIGURE 2.23: Thermodynamic critical field (stable branch) as a function of thickness parameter s_d for reduced temperatures $t = 0.5, 0.9$ (top) and $t = 0.3$ (bottom).

has been omitted for clarity. We have already shown in the previous section, that the superheating field coincides with the FFLO critical field in the 2-dimensional case. The FFLO transition field is much stronger suppressed than the line H_c where the free energies of the homogeneous states coincide. As a consequence, for $s_d = 0.5$ and consequently $d \gtrsim 0.5k_F^{-1}$ (see top of Fig. 2.24) the FFLO transition vanishes ($H_{c2,\text{FFLO}}$ becomes the supercooling field of the normal state) and is replaced by a first order transition at H_c to the homogeneous superconducting state. For these values of s_d and for low temperatures, the Ginzburg-Landau parameter defined by

$$\kappa = \frac{1}{\sqrt{2}} \frac{H_{c2}}{H_c} \quad (2.133)$$

is smaller than $1/\sqrt{2}$ and the system would theoretically become a type I superconductor. But this transition is not induced by surface boundary conditions as in bulk superconductors. We can only state the analogy of this transition to the original one, which results from the preference of the superconductor to build surface boundaries between normal and superconducting regions to minimize its energy. One can observe an analogous transition of the system from seemingly type II to I for $s_d = 0.5$ at the temperature $t \simeq 0.31$ (Fig. 2.24 top).

Note that a conducting layer of atomic thickness, the dimension of one unit cell in the plane, yields enough orbital pair breaking to produce this suppression of $H_{c2,\text{FFLO}}$ in favor of H_c . This behavior is not unreasonable, as spatially varying states are known to be much more sensitive to perturbations than homogeneous states (recall in this context Andersons theorem [46]). With further increasing orbital pair breaking (see middle and bottom of Fig. 2.24) the lines $H_{c2,\text{FFLO}}$ and $H_{c,\text{instable}}$ tend to merge and the metastable region shrinks; for $d > 3k_F^{-1}$ orbital pair-breaking dominates.

The critical fields as functions of the thickness parameter at $t = 0.01$ are shown in Fig. 2.25, where paramagnetic effects are most pronounced. This figure gives an overview of the cross-over from the paramagnetically dominated regime at very small d to the orbitally dominated regime at large d . If the thickness where $H_{c2,\text{FFLO}}$ and H_c cross is denoted by d_1 , then the FFLO state is only realized in the small range $d < d_1 \sim 0.5k_F^{-1}$, for $d > d_1$ a first order transition to the homogeneous (mainly) paramagnetically limited state occurs. The FFLO line plays the role of a supercooling limit of the normal state until it falls (at $d \sim 1.2k_F^{-1}$) below the line $H_{c,\text{instable}}$, where the normal-conducting state is limited by spatially constant superconducting fluctuations. The wavenumber q of the FFLO state decreases with increasing d until it jumps to $q = 0$ at the line $H_{c,\text{instable}}$ (at the crossing point two degenerate solutions exist for q). We continue to use the term FFLO state here, even if this term denotes, strictly speaking, a state without any orbital pair breaking contribution. With increasing d the lines all depicted fields approach each other and the transition becomes identical to the well-known second order transition of a thin film in a parallel field, which is entirely due to orbital pair breaking. The region of really large d where the difference between type I and type II

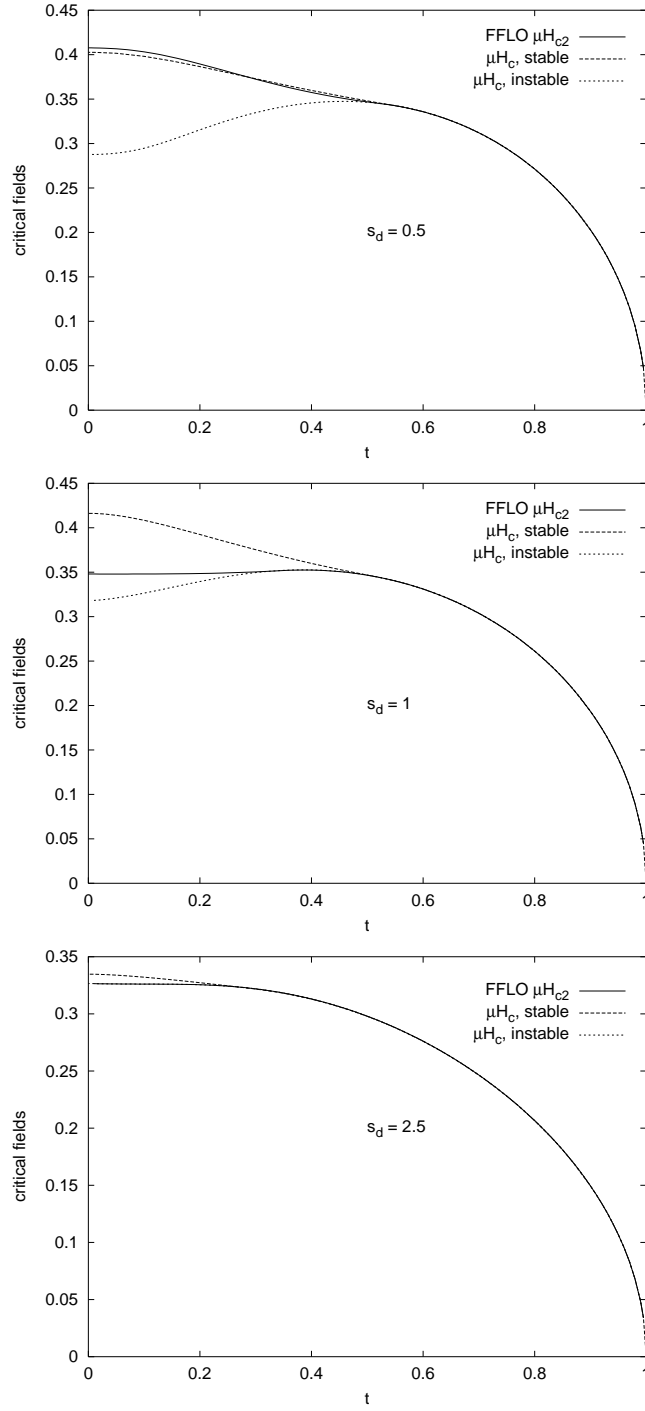


FIGURE 2.24: Critical fields in dimensionless Eilenberger units (A.26) as functions of reduced temperature for $s_d = 0.5$ (top), $s_d = 1$ (middle) and $s_d = 2.5$ (bottom).

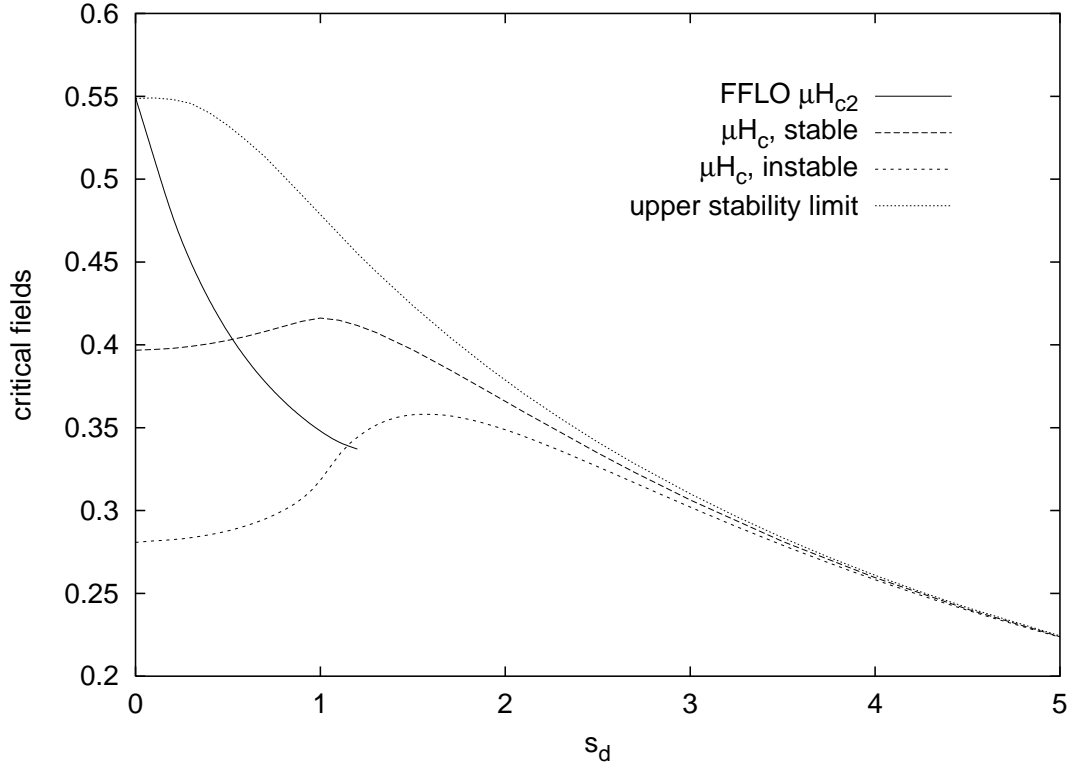


FIGURE 2.25: Critical fields in dimensionless Eilenberger units (A.26) as functions of s_d for $t = 0.01$.

superconductivity becomes important is clearly outside the range of validity of the present model.

We already mentioned in previous discussions that the upper stability limit of the superconducting state (dotted line), which is obtained from the second derivative of the free energy difference

$$\frac{\partial^2}{\partial \Delta^* \partial \Delta} \frac{(F_s - F_n)}{A} = \frac{t}{2} \sum_{l=0}^{N_D} \int_0^{2\pi} \frac{d\varphi}{2\pi} \left(\frac{|\Delta|^2}{(|\Delta|^2 + A_{d,l}(\varphi)^2)^{3/2}} + cc. \right), \quad (2.134)$$

equals the FFLO critical field at $d = 0$. This does not hold for finite thickness parameters as can be seen in figure 2.25. As in the two dimensional case, the upper stability limit corresponds to the highest possible field, where there is a solution for the gap (2.85) for a given temperature and thickness parameter, and at which the transition to the normal state is of first order. The lower stability limit of the normal phase corresponds to the unstable solution and is the field with vanishing gap Δ and second derivative of the free energy difference. Again, one of the two branches of the gap as a function of external field $\Delta(\mu H)$ gives a positive second derivative, meaning that the free energy is minimized for these solutions, while for the other branch it is negative (see Fig. 2.19).

2.3.6 Discussion on pair-breaking effects in $\text{YBa}_2\text{Cu}_3\text{O}_7$

Let us investigate the consequences of the fact that the FFLO state can be suppressed in favor of the homogeneous superconducting state by a very small admixture of orbital pair-breaking (see Figure 2.25). We have not mapped out a complete phase diagram like figure 2.25 for d -wave superconductors (where $H_{c2,\text{FFLO}}$ becomes anisotropic as a consequence of the finite d) but instead performed a few calculations in order to get an overview of what happens. The results confirm qualitatively the main feature visible in figure 2.25, namely a much stronger suppression of $H_{c2,\text{FFLO}}$, as compared to the upper stability limit of H_c , by orbital pair-breaking. For $\text{YBa}_2\text{Cu}_3\text{O}_7$ we have two conducting CuO_2 layers per unit cell with a distance of $\simeq 3.9\text{\AA}$ while the c -axis zero-temperature coherence length is estimated [47] to be $2\text{--}4\text{\AA}$. The coupling between bilayers in adjacent unit cells may obviously be neglected, as a consequence of the large length $c \simeq 11.7\text{\AA}$ of the unit cell in this direction. The coupling between the two layers in one unit cell, on the other hand, remains an open question, and the following two possibilities should be taken into consideration.

The first possibility is, that the two superconducting layers decouple at low T , below some crossover temperature T^* . As is well known, the orbital critical field of weakly coupled layers diverges [48] below some crossover temperature T^* , which means that paramagnetic pair-breaking is the only remaining mechanism to limit the superconducting state. This requires a two-dimensional, in-plane mechanism of superconductivity. The amount of orbital pair-breaking would be negligibly small in this case and the superconducting state below the critical field should be the FFLO state.

The second possibility is that the superconducting state keeps its finite extension for arbitrary T . This requires an inter-plane mechanism where the bilayer structure is essential for the superconducting pairing process. In this case, the bilayer may be approximately replaced by a single layer of finite thickness $d \simeq 2\text{--}4\text{\AA}$. Taking a value of $v_F \simeq 10^7\text{ cm/s}$ for the Fermi velocity in the $a - b$ plane, as measured by Andreev reflections [49], we estimate a value between 1 and 4 for our dimensionless thickness parameter d/k_F^{-1} , which measures the amount of orbital pair-breaking. Thus in this case, if the bilayer structure can be approximated by a finite slab, the amount of intrinsic orbital pair-breaking in YBCO, brought about by the finite thickness of this slab, will be by far large enough to suppress the FFLO state. The second order FFLO transition will be replaced by a first order transition to a homogeneous superconducting state; this transition is due to the combined action of both pair breaking mechanisms rather than a single one. For a typical value of $s_d = d/k_F^{-1} \simeq 2$, the critical field would be still of the same order of magnitude as the purely paramagnetically limited, (Pauli limiting) field at $d = 0$ but with a strongly reduced metastability region (see Fig. 2.25).

The transport measurement of Dzurak et al.[6] of the critical field of $\text{YBa}_2\text{Cu}_3\text{O}_7$ at 1.6 K

led to a result of the order of the Pauli limiting field $H_p = H_c(d = 0)$. The transition seems, however, too broad to distinguish between the FFLO and Pauli limiting fields. Further, more accurate experiments are required to settle this question, which concerns fundamental aspects of the superconducting state in High- T_c cuprates. Observation of the FFLO state in the plane-parallel field configuration of $\text{YBa}_2\text{Cu}_3\text{O}_7$ would be a strong argument in favor of an in-plane mechanism of superconductivity in this material.

The relevance of this question has also been discussed by Yang and Sondhi [50], using the framework of the Lawrence-Doniach model, which is in a sense complementary to the present approach. The orbital pair-breaking effect due to the finite thickness of the conducting layers has previously been taken into account in a theory by Schneider and Schmidt [51]. This theory may be used successfully to fit the experimental data [14] near T_c , but neglects all paramagnetic effects. The purely paramagnetic limit, on the other hand, has been studied by Maki and Won [12] and by Yang and Sondhi [52]. The present results show that both effects should be taken into account for a detailed description of the transition. The orbital effect cannot be neglected even if the orbital critical field is several times higher than the paramagnetic limiting field.

Finally, as our results point out in the previous chapter, that single atomic (molecular) layers are responsible for the superconducting state in the organic compound $\kappa\text{-(BEDT-TTF)}_2\text{Cu(NCS)}_2$ where phase boundaries compatible with a d -wave version of the FFLO state have recently been observed. Thus, a considerable influence of orbital pair-breaking, which would suppress the FFLO state in favor of the homogeneous superconducting state, does not exist in this material. Measurements of the detailed temperature-dependence of $H_{c2,\text{FFLO}}$ close to $T = 0$ could reveal even small admixtures of an orbital pair-breaking component.

2.4 System with impurities

In this section, the equations for the Green's functions and the gap equation are derived for a system with finite thickness including impurity scattering in first Born approximation. The Eilenberger equations (2.84) are modified such that impurity scattering is included in the system (see Ref. [33]),

$$\begin{aligned} \left[\omega_s + \hat{k} \partial_{\mathbf{r}} \right] f &= \Delta g + F g - G f \\ \left[\omega_s - \hat{k} \partial_{\mathbf{r}}^* \right] f^+ &= \Delta^* g + F^+ g - G f^+ \\ g &= \sqrt{1 - f f^+}, \end{aligned} \tag{2.135}$$

with the potentials

$$\begin{aligned} F(\omega_s) &= t_+ \int_0^{2\pi} \frac{d\varphi}{2\pi} f(\varphi, \omega_s) \\ F^+(\omega_s) &= t_+ \int_0^{2\pi} \frac{d\varphi}{2\pi} f^+(\varphi, \omega_s) \\ G(\omega_s) &= t_+ \int_0^{2\pi} \frac{d\varphi}{2\pi} g(\varphi, \omega_s). \end{aligned} \quad (2.136)$$

The dimensionless impurity parameter t_+ is

$$t_+ = \frac{1}{2\pi\tau_{tr}} \frac{1}{k_B T_c} \quad (2.137)$$

where τ_{tr} is the mean transport relaxation time given by

$$\frac{1}{\tau_{tr}} = 2\pi N(0) \int \frac{d\Omega}{4\pi} |u(\theta)|^2, \quad (2.138)$$

in first Born approximation, with the scattering potential u , the density of states at the Fermi level $N(0)$, and the angle θ between incoming and outgoing wavevectors \mathbf{k} and \mathbf{q} .

The modification of the finite thickness equations is analogous to the two dimensional case, if we again consider a system with thickness $d \ll \xi$. Eq. (2.106) is applied to the potential F

$$F = \bar{F} + \delta F(z) = t_+ \int_0^{2\pi} \frac{d\varphi}{2\pi} \bar{f} + t_+ \int_0^{2\pi} \frac{d\varphi}{2\pi} \delta f(z) \quad (2.139)$$

and the same is done for F^+ . For the potential G , one can simply write $G = \bar{G}$ because of Eq. (2.114). For thin ($d \ll \xi$) and not too dirty systems, such that $t_+ \rightarrow \infty$, one can approximate $\delta F(z) \sim 0$ and the potentials are represented by their mean values. The mean Green's function \bar{f} can be written as (2.120–2.122)

$$\begin{aligned} \bar{f} &= \int_0^\infty ds e^{-s(\omega_s + \bar{G})} (\Delta + \bar{F}) \bar{g} \frac{1}{B_d(\varphi)s} \sin(B_d(\varphi)s) \\ &= \frac{1}{B_d(\varphi)} \text{atan} \left(\frac{B_d(\varphi)}{\omega_s + \bar{G}} \right) (\Delta + \bar{F}) \bar{g}. \\ &= \frac{(\Delta + \bar{F}) \bar{g}}{A_{d,l}^{\bar{G}}(\varphi)}, \end{aligned} \quad (2.140)$$

where the limit

$$\lim_{d \rightarrow 0} A_{d,l}^{\bar{G}}(\varphi) = \omega_s + \bar{G} \quad (2.141)$$

holds. In this limit, Anderson's theorem [46] holds as there is no dependence of the Green's functions on φ . The terms with the potentials on the right side of the transport equations 2.135 disappear, because of

$$\begin{aligned} Fg &= t_+ fg = Gf \\ F^+g &= t_+ gf^+ = Gf^+. \end{aligned} \quad (2.142)$$

We now continue with the derivation of the mean Green's functions. Equations (2.123) and (2.125) and the normalization condition are then given by

$$\begin{aligned} \bar{f} A_{d,l}^{\bar{G}}(\varphi) &= (\Delta + \bar{F}) \bar{g} \\ \bar{f}^+ A_{d,l}^{\bar{G}}(\varphi) &= (\Delta^* + \bar{F}^+) \bar{g} \\ \bar{g} &= \sqrt{1 - \bar{f} \bar{f}^+}, \end{aligned} \quad (2.143)$$

with the mean impurity potentials

$$\begin{aligned} \bar{F}(\omega_s) &= t_+ \int_0^{2\pi} \frac{d\varphi}{2\pi} \bar{f}(\varphi, \omega_s) \\ \bar{F}^+(\omega_s) &= t_+ \int_0^{2\pi} \frac{d\varphi}{2\pi} \bar{f}^+(\varphi, \omega_s) \\ \bar{G}(\omega_s) &= t_+ \int_0^{2\pi} \frac{d\varphi}{2\pi} \bar{g}(\varphi, \omega_s). \end{aligned} \quad (2.144)$$

Again, the transport equations (2.143) are solved to obtain the expressions for the mean Green's functions

$$\begin{aligned} \bar{f} &= \frac{\Delta + \bar{F}}{\sqrt{(\Delta + \bar{F})(\Delta^* + \bar{F}^+) + A_{d,l}^{\bar{G}}(\varphi)^2}} \\ \bar{f}^+ &= \frac{\Delta^* + \bar{F}^+}{\sqrt{(\Delta + \bar{F})(\Delta^* + \bar{F}^+) + A_{d,l}^{\bar{G}}(\varphi)^2}} \\ \bar{g} &= \frac{A_{d,l}^{\bar{G}}(\varphi)}{\sqrt{(\Delta + \bar{F})(\Delta^* + \bar{F}^+) + A_{d,l}^{\bar{G}}(\varphi)^2}}. \end{aligned} \quad (2.145)$$

2.4.1 Gap equation

The Green's functions are inserted in the self-consistency equation (2.85) giving the gap function, which together with the equations for the potentials (2.144) have to be solved consistently. One can take advantage of the property of the Green's functions f and f^+

$$\frac{f}{\Delta} = \frac{f^+}{\Delta^*}, \quad (2.146)$$

which also holds for the mean functions

$$\bar{f}' = \frac{\bar{f}}{\Delta} = \frac{\bar{f}^+}{\Delta^*} = \frac{1 + \bar{F}'}{\sqrt{(1 + \bar{F}')^2 |\Delta|^2 + A_{d,l}^{\bar{G}}(\varphi)^2}}, \quad (2.147)$$

where

$$\bar{F}' = \frac{\bar{F}}{\Delta} = \frac{\bar{F}^+}{\Delta^*}, \quad (2.148)$$

to lessen the number of potentials to be solved. Now there are only two potentials to be considered

$$\begin{aligned} \bar{F}' &= t_+ \int_0^{2\pi} \frac{d\varphi}{2\pi} \frac{1 + \bar{F}'}{\sqrt{(1 + \bar{F}')^2 |\Delta|^2 + A_{d,l}^{\bar{G}}(\varphi)^2}} \\ \bar{G} &= t_+ \int_0^{2\pi} \frac{d\varphi}{2\pi} \frac{A_{d,l}^{\bar{G}}(\varphi)}{\sqrt{(1 + \bar{F}')^2 |\Delta|^2 + A_{d,l}^{\bar{G}}(\varphi)^2}}, \end{aligned} \quad (2.149)$$

and the gap-function (2.85) can be written as

$$2t \sum_{l=0}^{\infty} \frac{1}{\omega_l} + \ln t = t \sum_{l=0}^{\infty} \int \frac{d\varphi}{2\pi} \left(\frac{1 + \bar{F}'}{\sqrt{(1 + \bar{F}')^2 |\Delta|^2 + A_{d,l}^{\bar{G}}(\varphi)^2}} + cc. \right). \quad (2.150)$$

Equations (2.149-2.150) are then solved consistently for given thickness parameter s_d , impurity parameter t_+ , temperature t and external field μH to obtain the gap Δ .

2.4.2 Stability limits

The upper stability limit of the superconducting phase and the lower stability limit of the normal phase are obtained from the second derivative of the free energy difference $(F_s - F_n)/A$. The stationarity of the first derivative with respect to Δ^* results in the self-consistency equation for the gap (2.85)

$$\frac{\partial}{\partial \Delta^*} \frac{F_s - F_n}{A} = \Delta \left\{ 2t \sum_{l=0}^{\infty} \frac{1}{\omega_l} + \ln t - t \sum_{l=0}^{\infty} \int_0^{2\pi} \frac{d\varphi}{2\pi} (\bar{f}' + cc.) \right\} = 0, \quad (2.151)$$

which gives

$$\frac{\partial^2}{\partial \Delta^* \partial \Delta} \frac{F_s - F_n}{A} = -t \sum_{l=0}^{\infty} \int_0^{2\pi} \frac{d\varphi}{2\pi} \left(\Delta \frac{\partial \bar{f}'}{\partial \Delta} + cc. \right) \quad (2.152)$$

for the second derivative of the free energy difference. For simplicity we set

$$a_l(\varphi) = (1 + \bar{F}')^2 |\Delta|^2 + A_{d,l}^{\bar{G}}(\varphi)^2 \quad (2.153)$$

and calculate the derivative of \bar{f}'

$$\Delta \frac{\partial \bar{f}'}{\partial \Delta} = \Delta \frac{\partial}{\partial \Delta} \frac{1 + \bar{F}'}{\sqrt{a_l(\varphi)}} = \frac{1}{\sqrt{a_l(\varphi)}} \Delta \frac{\partial \bar{F}'}{\partial \Delta} - \frac{1}{2a_l(\varphi)^{3/2}} (1 + \bar{F}') \Delta \frac{\partial a_l(\varphi)}{\partial \Delta}, \quad (2.154)$$

which also gives the derivative of \bar{F}'

$$\Delta \frac{\partial \bar{F}'}{\partial \Delta} = t_+ \int_0^{2\pi} \frac{d\varphi}{2\pi} \left(\frac{1}{\sqrt{a_l(\varphi)}} \Delta \frac{\partial \bar{F}'}{\partial \Delta} - \frac{1}{2a_l(\varphi)^{3/2}} (1 + \bar{F}') \Delta \frac{\partial a_l(\varphi)}{\partial \Delta} \right). \quad (2.155)$$

With the equations

$$\Delta \frac{\partial a_l(\varphi)}{\partial \Delta} = |\Delta|^2 \left((1 + \bar{F}')^2 + 2(1 + \bar{F}') \Delta \frac{\partial \bar{F}'}{\partial \Delta} \right) + 2A_{d,l}^{\bar{G}}(\varphi) \Delta \frac{\partial A_{d,l}^{\bar{G}}(\varphi)}{\partial \Delta} \quad (2.156)$$

and

$$\Delta \frac{\partial A_{d,l}^{\bar{G}}(\varphi)}{\partial \Delta} = \frac{A_{d,l}^{\bar{G}}(\varphi)^2}{B_d(\varphi)^2 + (\omega_s + \bar{G})^2} \Delta \frac{\partial \bar{G}}{\partial \Delta}, \quad (2.157)$$

where the derivative of \bar{G} is given by

$$\Delta \frac{\partial \bar{G}}{\partial \Delta} = t_+ \int_0^{2\pi} \frac{d\varphi}{2\pi} \left(\frac{1}{\sqrt{a_l(\varphi)}} \Delta \frac{\partial A_{d,l}^{\bar{G}}(\varphi)}{\partial \Delta} - \frac{1}{2a_l(\varphi)^{3/2}} A_{d,l}^{\bar{G}}(\varphi) \Delta \frac{\partial a_l(\varphi)}{\partial \Delta} \right), \quad (2.158)$$

the basis is set for the calculation of the second derivative of the free energy difference and the stability limits, where the second derivative disappears. First, the gap function (2.150) and the potentials (2.149) are obtained self consistently. The values obtained for $|\Delta|^2$ and the potentials are subsequently used in the iteration of the derivatives (2.155) and (2.158) with the help of eqs. (2.156) and (2.157). With the self consistently obtained derivatives, the second derivative of the free energy (2.152) is obtained.

2.4.3 Comparison of numerical results with Al experimental data

As the thickness of a thin superconducting film in an external magnetic field parallel to the plane increases, the critical fields decrease because of the effect of orbital pair-breaking. Furthermore, the tricritical temperature $t_{tri} = T_{tri}/T_{c0}$, which is the temperature at which the critical fields match ($t_{tri} \simeq 0.56$ in the two-dimensional case) is shifted to lower values. At temperatures below the tricritical temperature we have shown that there are two boundary solutions for the critical field: the upper stability limit, which is of first order and at which the gap is still finite, and the lower stability limit, which is a second order phase transition. Above the tricritical temperature there is only one solution given by a second order phase transition. The order of the phase transitions was discussed in Ref. [45] in the framework of the generalized GL-equations and the possibility of determining the second order phase transition because of reentrant behavior in resistivity measurements as a function of temperature or field was discussed by Fulde [4]. Tunneling conductance measurements on a thin Al film in a parallel external field of Butko *et al.* [5] and later by Wu *et al.* [53] showed such reentrance behavior and a strongly hysteretic density of states. They have ruled out possibilities of the hysteretic behavior to be dependent on the film morphology and confirmed, that it is indeed

an intrinsic effect. In this section, the tunneling measurements of Ref. [5] on a thin Al film is compared with the numerical results on the upper and lower stability limit of a system with finite thickness. Note that Wu *et al.* [53] also show experimental results for a $d \sim 6$ nm thin film, which is two to three times thicker than that examined in Ref. [5]. The behaviour of the critical fields with increasing film thickness corresponds to our findings, that the low-temperature branch decreases to be even lower than a corresponding critical field at higher temperature. Such behaviour is already reflected in our clean-limit calculations (Fig. 2.16), and the curvature at low temperatures become even more pronounced as we add impurities to our calculations.

| | | |
|-----------------|------------|---------------------|
| d [nm] | 2–2.5 | $s_d \sim 35 - 43$ |
| $T_c^{(0)}$ [K] | ~ 2.7 | |
| T_{tri} [mK] | ~ 650 | $t_{tri} \sim 0.25$ |
| l [nm] | ~ 16 | $t_+ \sim 350$ |
| v_F^b [m/s] | $2 * 10^6$ | |
| E_F^b [eV] | 11.6 | |

Table 2.1: Data on the Al sample, where d is the film thickness, $T_c^{(0)}$ is the critical temperature at zero external field, T_{tri} is the tricritical temperature, l is the mean free path, v_F^b is the bulk value of the Fermi velocity and E_F^b is the corresponding Fermi energy. The parameters s_d and t_+ obtained using v_F^b is shown on the right side.

In a first test we begin with varying the film thickness of a clean system ($t_+ = 0$) to obtain a tricritical temperature similar to that of the experiment $t_{tri} \sim 0.25$ and a good agreement on the opening of the branches at low temperatures. The data on the Al sample are given in Tab. 2.1. However, it was necessary to introduce a rescaling factor c_r in order to enable comparison with the experimental data. This discrepancy may be explained by the difference in the value of the Fermi velocity in the a - b plane of a thin Al film compared to its bulk value. At this time, we cannot confirm the Fermi velocity value needed to describe the experimental data, but it cannot be completely ruled out (see also [49]).

The relation of the rescaling factor c_r to the bulk Fermi energy in eq. 2.161 is given by

$$E'_F = c_r E_F^b, \quad (2.159)$$

which gives a Fermi velocity of $v'_F = \sqrt{c_r} v_F^b$. One would obtain the same absolute values as the rescaled results, because $H^\diamond(E'_F) = c_r H^\diamond$ holds. For the parameters of the theory such as $s_d = mv_F d / \hbar = d / k_F^{-1}$ and $t_+ = \hbar v_F / (k_B T_c^{(0)} l)$ to remain unchanged, this means that one also has to modify d and l according to the change in the Fermi velocity

$$d' = \frac{d}{\sqrt{c_r}}$$

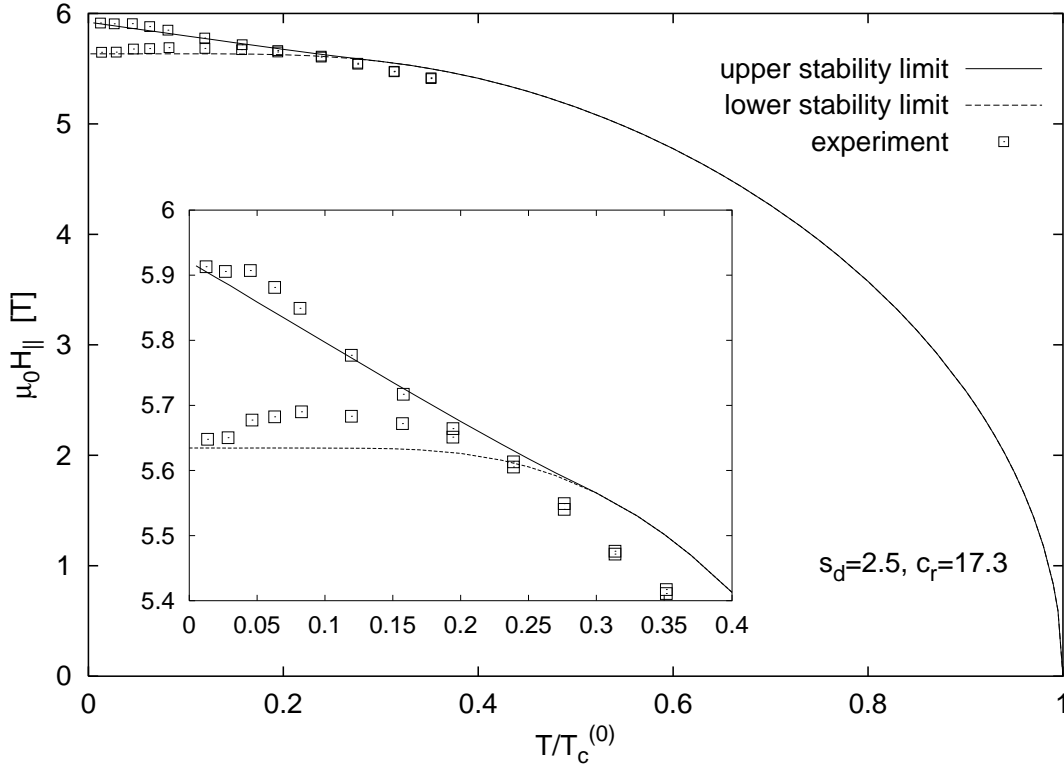


FIGURE 2.26: Upper and lower stability limit for $s_d = 2.5$ and a rescaling factor of $c_r = 17.3$ compared with the superheating and supercooling field obtained from tunneling measurements on a thin Al film in a parallel magnetic field [5].

$$l' = l\sqrt{c_r}. \quad (2.160)$$

Agreeable results for the general behaviour was found for a thickness parameter $s_d = 2.5$ (Fig. 2.26), corresponding to $d \sim 0.145$ nm, which is clearly too small compared to the given thickness of the film $d \sim 2\text{--}2.5$ nm. The tricritical temperature of the numerical results is $t_{tri} \simeq 0.3$, which is slightly above the experimental one. Furthermore, the curvature of the lower branch showing a maximum at $t \sim 0.1$ is not reproduced as the theory predicts a nearly horizontal behavior at low temperatures. For the upper stability limit it predicts a nearly linear behavior, which as in the case of the lower branch does not meet the experimental features.

If we include impurity scattering into our calculations, the general behaviour of the critical fields improves to meet the experimental results. Including impurity scattering in the system enlarges the critical fields and the effect of the thickness on the the tricritical temperature is reversed, i.e., it is shifted to higher temperatures as the impurity parameter t_+ increases for a constant thickness parameter s_d . As the effect of increasing thickness is to raise orbital pair breaking, it is diminished with impurity scattering as the mean free path of the electrons is

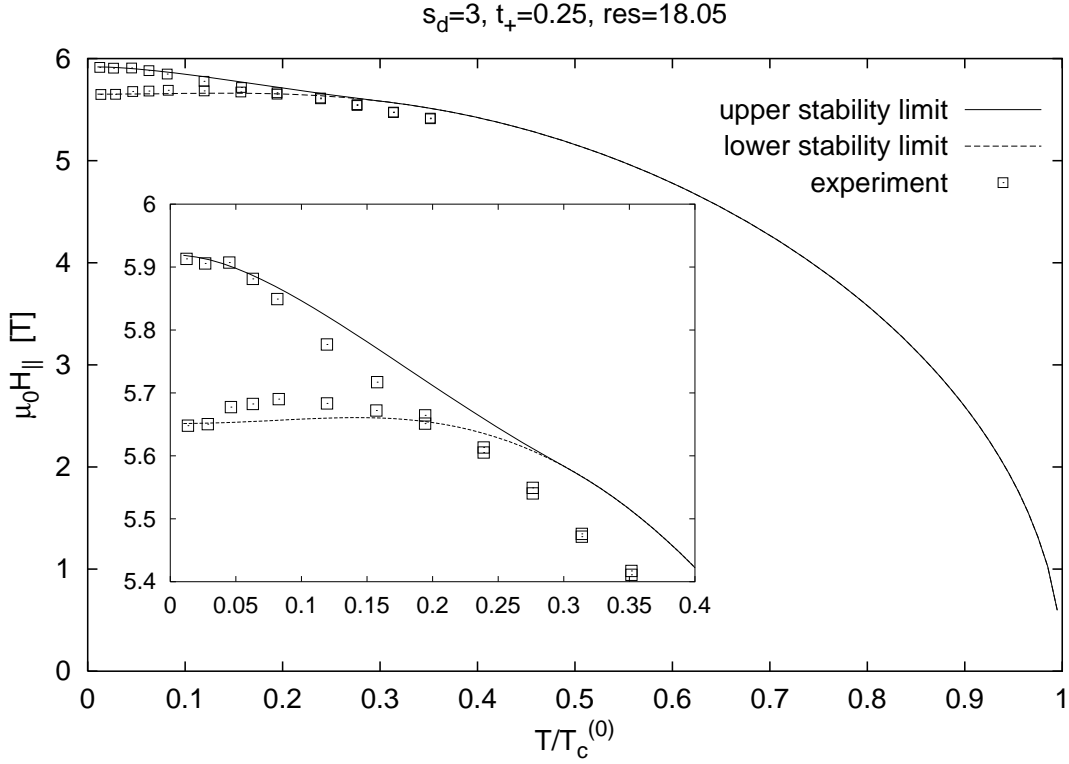


FIGURE 2.27: Upper and lower stability limit for $s_d = 3$, $t_+ = 0.25$ and a rescaling factor of $c_r = 18.05$ compared with the experimental data [5].

lessened. In a system with impurity scattering, the thickness parameter is shifted to higher values while the tricritical temperature remains constant. The critical fields for an arbitrary impurity parameter $t_+ = 0.25$ are shown in Fig. 2.27. In a clean system, the critical fields with $s_d = 3$ did not agree with the experiment, as the opening of the branches at low temperatures was too small. The agreement with the experimental data is improved with an appearing curvature of the upper and lower stability limits at low temperatures, compared to the previously linear behavior in the clean system. Furthermore, the lower stability limit decreases and a broad maximum emerges at low temperatures. Nevertheless, the thickness $d \sim 0.174$ nm obtained with $s_d = 3$ is still too small. We still need to describe the experimental data with the given dimensions.

We put the theory to test by setting the thickness parameter to the value of the real film $s_d = 43$, which corresponds to $d \sim 2.5$ nm (Tab. 2.1). The impurity parameter was varied to obtain the experimental tricritical temperature of $t_{tri} \sim 0.25$, which concluded in an impurity parameter of $t_+ = 110$. The experimental data were converted into Eilenberger units (denoted

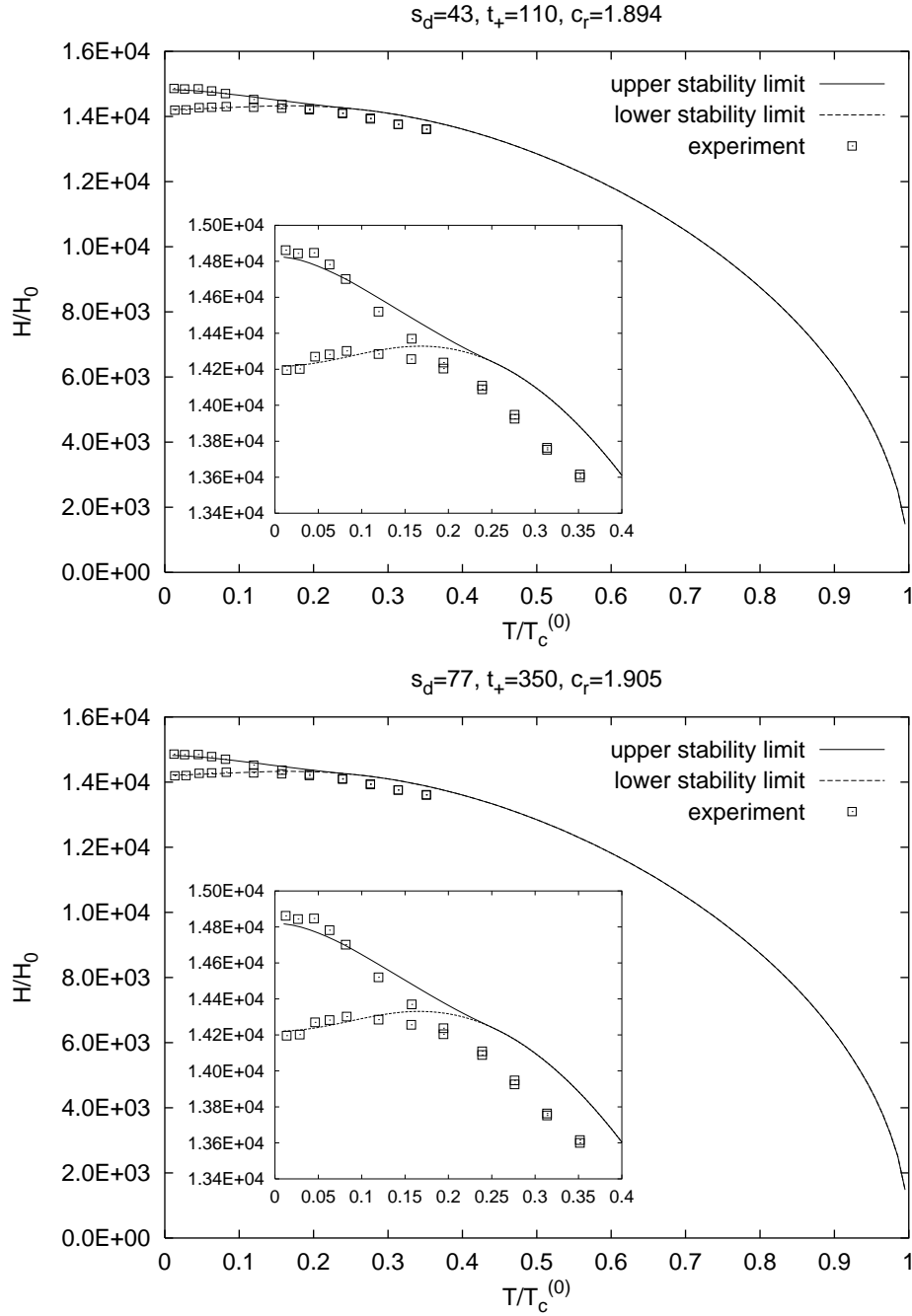


FIGURE 2.28: Upper and lower stability limit for $s_d = 43$, $t_+ = 110$ and a rescaling factor of $c_r = 1.894$ (top) and $s_d = 77$, $t_+ = 350$ and a rescaling factor of $c_r = 1.905$ (bottom) compared with the experimental data [5] in Eilenberger units.

with a symbol \diamond , see eqs. (A.16–A.23)) with the relation

$$H^\diamond = \frac{H^{real}}{H_0} = \frac{2E_F^b \mu_B}{(\pi k_B T_c^{(0)})^2} H^{real}[T], \quad (2.161)$$

where $H^{real}[T]$ corresponds to the experimental data in Tesla. As before, the numerical results lie below the experimental data, and it is necessary to introduce a rescaling factor $c_r = 1.894$ to enable comparison between experiment and theory (Fig. 2.28, top). This rescaling factor could be attributed to a higher Fermi velocity needed to describe the critical fields, but this assumption still has to be confirmed by either band-structure calculations on Al with a quasi two-dimensional fermi surface or by experiment. Nevertheless, it cannot be completely ruled out that the Fermi velocity in the a - b plane is higher than the given bulk value in the thin Al slab. The curvature of the lower and upper stability limit agrees well with the experimental results, but at higher temperatures the critical field is slightly overestimated by our analysis. As the resulting mean free path $l \sim 51.4$ is still higher than the mean free path of the experiment $l \sim 16$ and the theory predicts a $1/d$ -dependence without taking paramagnetic limiting into account (see Sec. 2.2.1 for details) instead of $1/d^{3/2}$ if specular reflection on the boundary of the film is considered, it would be more accurate to take the real impurity parameter resulting from the mean free path of the experiment ($t_+ = 350$) and fit the thickness parameter to obtain the tricritical temperature of $t_{tri} \sim 0.25$. One can see from Fig. 2.28 (bottom) that the behaviour of the critical fields is as good as the previous one, with $d \sim 4.5$ nm and a rescaling factor of $c_r = 1.905$. The results for the two data sets with $s_d = 43$ and $s_d = 77$ are shown in Tab. 2.2.

To summarize this section, we compared the tunneling measurements of Ref. [5] on a thin Al film with the numerical results on the upper and lower stability limit of a system with finite thickness. At temperatures below the tricritical temperature, the behaviour of the two boundary solutions for the critical field improves to meet the characteristics of the experimental data when impurity scattering is considered. However, there are still some discrepancies in the parameters needed to fit the experiment. One of the discrepancies lies in the mean free path and the film thickness, which slightly differ from the experimental specifications in

| | | | |
|--------|--------------------|---------------------|---------------------------|
| set 1: | $s_d = 43$ | $t_+ = 110$ | $c_r = 1.894$ |
| | $d \simeq 2.5$ nm | $l \simeq 51.4$ nm | $v_F = v_F^b$ |
| | $d' \simeq 1.8$ nm | $l' \simeq 70.7$ nm | $v'_F \simeq 1.376 v_F^b$ |
| set 2: | $s_d = 77$ | $t_+ = 350$ | $c_r = 1.905$ |
| | $d \simeq 4.5$ nm | $l \simeq 16$ nm | $v_F = v_F^b$ |
| | $d' \simeq 3.2$ nm | $l' \simeq 22.2$ nm | $v'_F \simeq 1.380 v_F^b$ |

Table 2.2: Data sets of the fit to the experimental data and the modified values according to the change in the Fermi velocity $E'_F = c_r * E_F$.

either cases described above. The other is the higher Fermi velocity needed to describe the critical fields. It cannot be completely ruled out that the Fermi velocity in the a - b plane is higher than the given bulk value in the thin Al slab. But this assumption still has to be confirmed by experiment.

Chapter 3

Bulk superconductivity

Conventional superconductors are well described by Eliashberg theory [16] which treats superconductivity as a boson-exchange phenomenon. The dominant feature of this theory is the electron-phonon interaction spectral function $\alpha^2 F(\omega)$ which can be determined from tunneling experiments [17] or theoretically from band structure calculations. Using such an $\alpha^2 F(\omega)$ within Eliashberg theory allows to reproduce the superconducting properties of a conventional superconductor within experimental accuracy and this established the phonons as the exchange boson between the two charge carriers building the Cooper pair in conventional superconductors.

3.1 Eliashberg Theory

The theoretical approach towards a theory of anisotropic polycrystalline superconductors within the framework of Eliashberg theory is based on the separable model for the anisotropic electron-phonon interaction introduced by Markovitz and Kadanoff [54] which was extended by Daams and Carbotte [55] to describe an anisotropic electron-phonon interaction spectral function:

$$\alpha^2 F(\omega)_{\mathbf{k},\mathbf{k}'} = (1 + a_{\mathbf{k}})\alpha^2 F(\omega)(1 + a_{\mathbf{k}'}), \quad (3.1)$$

where \mathbf{k} and \mathbf{k}' are the incoming and outgoing quasi-particle momentum vectors in the electron-phonon scattering process and $a_{\mathbf{k}}$ is an anisotropy function with the important feature $\langle a_{\mathbf{k}} \rangle = 0$, where $\langle \dots \rangle$ denotes the Fermi surface average. As anisotropy effects are generally assumed to be rather small, it is sufficient to keep the mean square anisotropy $\langle a^2 \rangle$ as the important anisotropy parameter. Finally, $\alpha^2 F(\omega)$ is the electron-phonon interaction spectral density of the equivalent isotropic system.

3.1.1 Thermodynamic properties

Thermodynamic properties of a superconductor are calculated from the free energy difference ΔF between the normal and superconducting state [56]:

$$\Delta F = \pi T N(0) \sum_n^{\omega_c} \left\langle \left(\sqrt{\tilde{\omega}_{\mathbf{k}}^2(\omega_n) + \tilde{\Delta}_{\mathbf{k}}^2(\omega_n)} - |\tilde{\omega}_{\mathbf{k}}(\omega_n)| \right) \left(1 - \frac{|\tilde{\omega}_{\mathbf{k}}^0(\omega_n)|}{\sqrt{\tilde{\omega}_{\mathbf{k}}^2(\omega_n) + \tilde{\Delta}_{\mathbf{k}}^2(\omega_n)}} \right) \right\rangle, \quad (3.2)$$

with the quasiparticle density of states $N(0)$ at the Fermi level, the renormalized quasiparticle frequencies $\tilde{\omega}_{\mathbf{k}}(\omega_n)$ and the Matsubara gaps $\tilde{\Delta}_{\mathbf{k}}(\omega_n)$ which are the solutions of the nonlinear s -wave Eliashberg equations:

$$\tilde{\omega}_{\mathbf{k}}(\omega_n) = \omega_n + \pi T \sum_m^{\omega_c} \left\langle \left(\lambda_{\mathbf{k},\mathbf{k}'}(m-n) + \delta_{m,n} \frac{t_{\mathbf{k},\mathbf{k}'}^+}{T} \right) \frac{\tilde{\omega}_{\mathbf{k}'}(\omega_m)}{\sqrt{\tilde{\omega}_{\mathbf{k}'}^2(\omega_m) + \tilde{\Delta}_{\mathbf{k}'}^2(\omega_m)}} \right\rangle' \quad (3.3)$$

$$\tilde{\Delta}_{\mathbf{k}}(\omega_n) = \pi T \sum_m^{\omega_c} \left\langle \left(\lambda_{\mathbf{k},\mathbf{k}'}(m-n) - \mu_{\mathbf{k},\mathbf{k}'}^* + \delta_{m,n} \frac{t_{\mathbf{k},\mathbf{k}'}^+}{T} \right) \frac{\tilde{\Delta}_{\mathbf{k}'}(\omega_m)}{\sqrt{\tilde{\omega}_{\mathbf{k}'}^2(\omega_m) + \tilde{\Delta}_{\mathbf{k}'}^2(\omega_m)}} \right\rangle' \quad (3.4)$$

The $\omega_{\mathbf{k}}^0(\omega_n)$ are the normal state quasiparticle frequencies determined by

$$\tilde{\omega}_{\mathbf{k}}^0(\omega_n) = \omega_n + \pi T \sum_m^{\omega_c} \left\langle \lambda_{\mathbf{k},\mathbf{k}'}(m-n) + \delta_{m,n} \frac{t_{\mathbf{k},\mathbf{k}'}^+}{T} \right\rangle' \text{sgn } \omega_m. \quad (3.5)$$

In these equations ω_c , the cutoff frequency, is usually an integer multiple of the Debye frequency of the system, $\omega_n = \pi T(2n+1)$, $n = 0, \pm 1, \pm 2, \dots$, $t_{\mathbf{k},\mathbf{k}'}^+ = 1/(2\pi(\tau_{tr})_{\mathbf{k},\mathbf{k}'})$ is the anisotropic scattering rate due to inelastic impurity scattering with $(\tau_{tr})_{\mathbf{k},\mathbf{k}'}$ as the anisotropic transport relaxation time, $\mu_{\mathbf{k},\mathbf{k}'}^*$ is the anisotropic Coulomb pseudopotential, and

$$\lambda_{\mathbf{k},\mathbf{k}'}(m-n) = 2 \int_0^\infty d\Omega \frac{\Omega \alpha^2 F(\Omega)_{\mathbf{k},\mathbf{k}'}}{\Omega^2 + (\omega_m - \omega_n)^2}. \quad (3.6)$$

In case of weak anisotropy effects the \mathbf{k}, \mathbf{k}' dependence of the Coulomb pseudopotential and of the impurity scattering is neglected and the anisotropy of the Matsubara gaps is described by the ansatz

$$\tilde{\Delta}_{\mathbf{k}}(\omega_n) = \tilde{\Delta}_0(\omega_n) + a_{\mathbf{k}} \tilde{\Delta}_1(\omega_n), \quad (3.7)$$

with $\tilde{\Delta}_{0,1}(\omega_n)$ being isotropic functions. In applying equation (3.7) to Eqs. (3.4) only terms of the order of $\langle a^2 \rangle$ are kept.

3.1.2 Upper critical field

The upper critical field $H_{c2}(T)$ of an anisotropic polycrystalline superconductor employs, in addition, a separable ansatz to describe the anisotropy of the Fermi velocity $v_{F,\mathbf{k}}$ [57]

$$v_{F,\mathbf{k}} = (1 + b_{\mathbf{k}}) \langle v_F \rangle, \quad (3.8)$$

with $\langle v_F \rangle$ the isotropic Fermi velocity. $b_{\mathbf{k}}$ is an anisotropy function defined in the same way as $a_{\mathbf{k}}$. Again, only terms of the order $\langle b^2 \rangle$ are kept in case of small anisotropy effects. The upper critical field in its temperature dependence is then described by the following set of equations [57]:

$$\begin{aligned} \tilde{\Delta}_{\mathbf{k}}(\omega_n) = & \pi T \sum_m (1 + a_{\mathbf{k}}) \lambda(m - n) \left\langle (1 + a_{\mathbf{k}'}) \tilde{\Delta}_{\mathbf{k}'}(\omega_m) \chi_{\mathbf{k}'}(m) \right\rangle' \\ & - \pi T \sum_m \left(\mu^* - \delta_{n,m} \frac{t^+}{T} \right) \left\langle \tilde{\Delta}_{\mathbf{k}'}(\omega_m) \chi_{\mathbf{k}'}(m) \right\rangle', \end{aligned} \quad (3.9)$$

$$\chi_{\mathbf{k}}(n) = \frac{2}{\sqrt{\alpha_{\mathbf{k}}}} \int_0^\infty dx e^{-x^2} \tan^{-1} \left(\frac{\sqrt{\alpha_{\mathbf{k}}} x}{|\tilde{\omega}_{\mathbf{k}}(\omega_n)|} \right), \quad (3.10)$$

and

$$\alpha_{\mathbf{k}} = \frac{e}{2} H_{c2}(T) (1 + b_{\mathbf{k}})^2 \langle v_F \rangle^2. \quad (3.11)$$

N -band models have been extensively studied as a tool to describe anisotropic features of superconductors. The separable model employed in this work can be described in its simplest form by a Fermi surface split into two half-spheres of equal weight

$$P(a) = \delta(-a)/2 + \delta(a)/2, \quad (3.12)$$

with radii $r \pm a$, if r is the radius of the equivalent isotropic Fermi sphere [58]. Using the Fermi surface harmonics (FSH) notation introduced by Allen [59], Daams [60] observed that this separable model was equivalently described by a restriction to zeroth-order FSH in each of the two subregions of the Fermi surface. According to her work, the separable model applied in further calculations of this work corresponds to a two-band model in which the two Fermi surface regions have equal weight. It is of course also possible to define different weights for the two regions, thus changing the distribution function (3.12), but Daams [60] demonstrated that in the case of weak anisotropy the influence of different weights in a separable model is of negligible significance for the thermodynamics of anisotropic superconductors.

In the case of the upper critical field any deviation from the equal weight configuration causes $H_{c2}(T)$ to approach the isotropic case (Fig. 3.1). The deviation function in the insert of Fig. 3.1

$$D_{H_{c2}}(T/T_c) = D_{H_{c2}}(t) = \frac{H_{c2,a}(t)}{H_{c2,i}(t)} - 1 \quad (3.13)$$

demonstrates the deviation of the upper critical field of an anisotropic system $H_{c2,a}(T)$ from the upper critical field of an isotropic, equivalent system $H_{c2,i}(T)$. The numerical result for equal weights (1:1) was fitted to the upper critical field of $\text{LuNi}_2\text{B}_2\text{C}$ to fix the parameters $\langle a_{\mathbf{k}}^2 \rangle$, $\langle b_{\mathbf{k}}^2 \rangle$, and $\langle v_F \rangle$. The mean Fermi velocity $\langle v_F \rangle$ and its anisotropy parameter $\langle b_{\mathbf{k}}^2 \rangle$ were used to fit the experimental data near T_c , and $\langle a_{\mathbf{k}}^2 \rangle$ was changed to describe $H_{c2}(T)$ at lower temperatures. With these parameters, we calculated the upper critical field for different

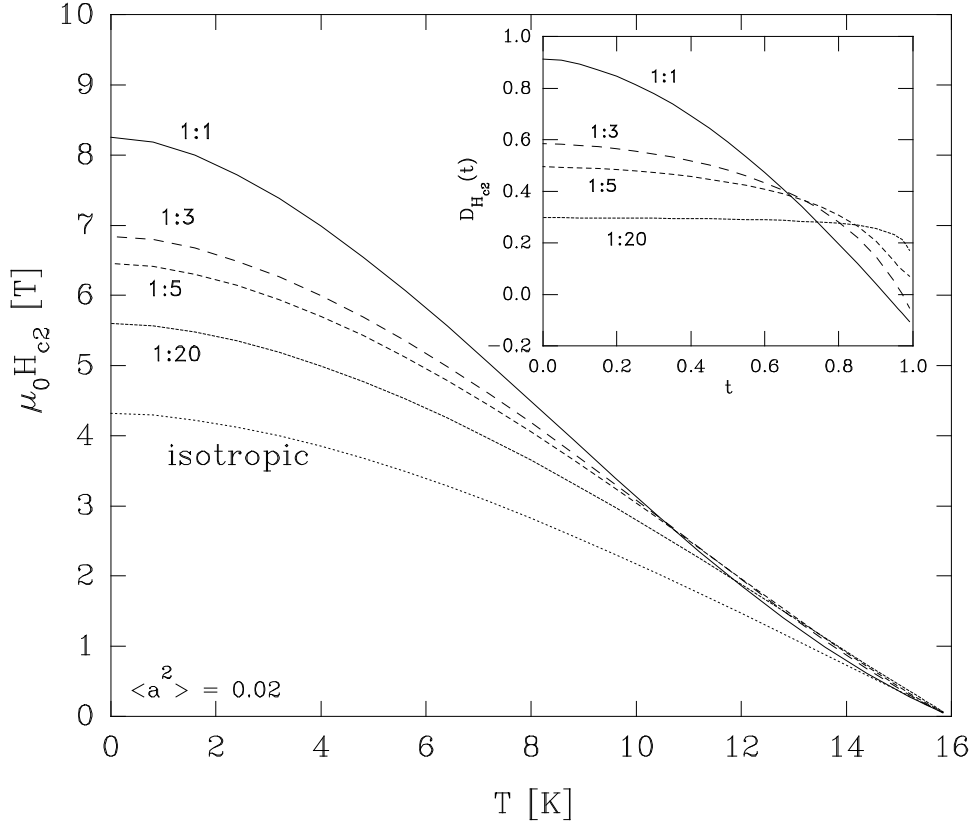


FIGURE 3.1: Influence of different weights for the two Fermi-surface sheets on the upper critical field $H_{c2}(T)$ [21]. The numerical result in the case of equal weights (1:1) is a fit to the upper critical field of $\text{LuNi}_2\text{B}_2\text{C}$ with $\langle a^2 \rangle = 0.02$, $\langle b^2 \rangle = 0.25$, and $\langle v_F \rangle = 0.280 \times 10^6$ m/s. $D_{H_{c2}}(t)$ is depicted in the small insert.

weights of the Fermi sheets (1: n) to investigate the change in the behavior of H_{c2} . Obviously, $H_{c2,a}$ approaches $H_{c2,i}$ as one of the two sheets becomes dominant in weight and this is indicated by a flattening of $D_{H_{c2}}(t)$.

The relative signs of $a_{\mathbf{k}}$ and $b_{\mathbf{k}}$ in the same Fermi-surface sheet is also of importance to the analysis of H_{c2} . With same signs of $a_{\mathbf{k}}$ and $b_{\mathbf{k}}$ in same sheets, $H_{c2,a}(T)$ is reduced compared to $H_{c2,i}(T)$ (Fig. 3.2). Opposite signs within same sheets give rise to an enhancement of $H_{c2,a}$ over $H_{c2,i}$. In this case, the reduction of $H_{c2,a}(T)$ due to the influence of $\langle b_{\mathbf{k}}^2 \rangle$ is compensated by the electron-phonon interaction anisotropy. Bandstructure calculations can give a good estimate for the weight and the relative signs of $a_{\mathbf{k}}$ and $b_{\mathbf{k}}$ in the corresponding regions of the Fermi surface.

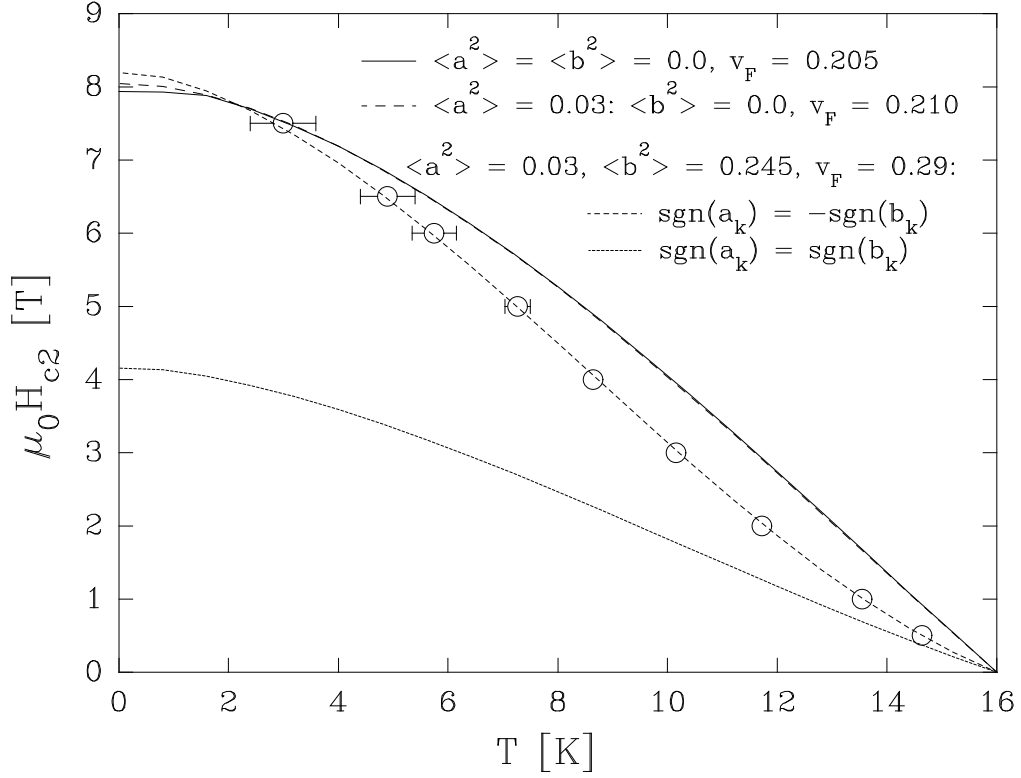


FIGURE 3.2: Influence of different signs of $a_{\mathbf{k}}$ and $b_{\mathbf{k}}$ on the upper critical field $H_{c2}(T)$. Both Fermi-surface sheets were weighed with the same factor (1:1).

3.1.3 Impurity scattering

Impurities are treated in Born's limit [61] which assumes the impurities to be randomly distributed and to be of dilute concentration. In such a limit impurities are characterized by a scattering rate t_+ which is proportional to the impurities' concentration. Their main effect is the smearing out of the electron-phonon interaction anisotropy resulting in a slight reduction of T_c [54], an enhancement of H_{c2} at low temperatures, and a reduction of the high temperature upward curvature of H_{c2} as was demonstrated by Weber *et al.* [62] for Nb.

3.1.4 Optimal spectrum

Concentrating on isotropic systems Carbotte [63] developed the concept of an optimum spectrum based on earlier work of Leavens [64] and Mitrović and Carbotte [65]. Such a spectrum can be developed from a theorem which states that for a given strength $A = \int_0^\infty d\omega \alpha^2 F(\omega)$ of the spectral density $\alpha^2 F(\omega)$ the best shape that will maximize the critical temperature T_c is a delta function spectrum

$$\alpha^2 F(\omega)_{\text{opt}} = A \delta[\omega - \omega^*(\mu^*)], \quad (3.14)$$

with the delta function placed at the frequency $\omega^*(\mu^*)$ at which the functional derivative $\delta T_c / \delta \alpha^2 F(\omega)$ displays its maximum for a fixed value of the Coulomb pseudopotential μ^* . Carbotte[63] extended this concept to encompass other physical properties such as $2\Delta(0)/k_B T_c$, the zero temperature gap $\Delta(0)$ to T_c ratio, and a number of others. This concept establishes that a relation

$$X = A x(\mu^*) \quad (3.15)$$

always exists, where X stands for T_c , $2\Delta(0)/k_B T_c$, etc. and $x(\mu^*)$ is a universal number determined from Eliashberg theory for each property X and which varies only slightly with μ^* .

In essence the optimum spectrum gives information about the phonon frequency important to maximize a certain physical property (such as T_c) of a conventional superconductor. Such a concept is very appealing and it suggests an expansion to the concept of an *optimal* spectrum which is again a delta peak spectrum with a delta peak of strength A at some position $\omega^*(\mu^*)$ both chosen to reproduce all known properties of a superconductor optimally. Such a spectrum will then provide information on the phonon mode most important for a specific superconductor if an $\alpha^2 F(\omega)$ cannot be derived from experiment. It can also help to develop an $\alpha^2 F(\omega)$ in all cases where the phonon density of states $G(\omega)$ is known.

We put this concept to test [66] by using the borocarbides $\text{LuNi}_2\text{B}_2\text{C}$ and $\text{YNi}_2\text{B}_2\text{C}$ for which extensive experimental data exist [20] and for which $G(\omega)$ is known from theoretical work [67, 68]. From experimental data of the upper critical field H_{c2} which displays a pronounced upward curvature close to T_c in single crystal [69] and polycrystalline [20] samples we also assume these systems to be anisotropic [21] as in the sense of [57]. Shulga *et al.* [70] explained this upward curvature of $H_{c2}(T)$ close to T_c by considering two bands, one of which being more deeply involved in the transport properties of the compound. The authors utilized an *s*-wave electron-phonon Eliashberg formalism and there is strong evidence that the order parameter in $\text{YNi}_2\text{B}_2\text{C}$ is indeed of *s*-wave symmetry [71, 72]. It is interesting to note in passing that this concept introduced by Prohammer and Schachinger [57] is effectively a two-band model described by an anisotropic electron-phonon interaction spectral density [73, 74].

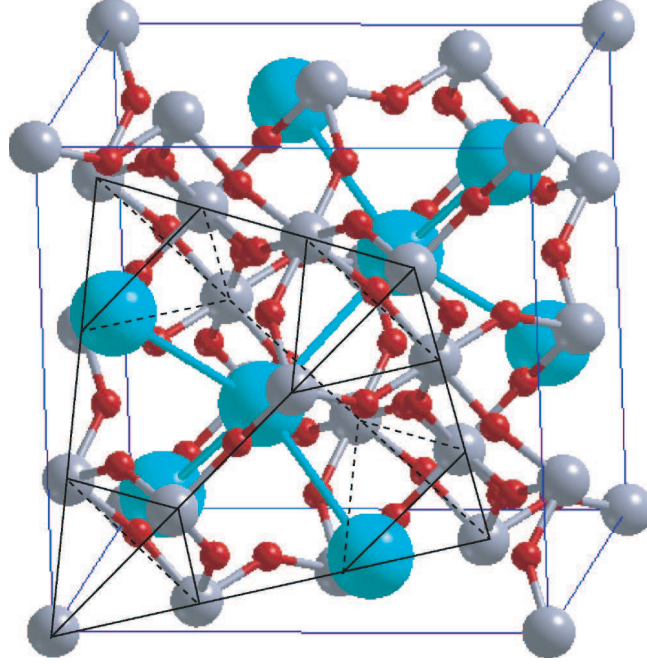


FIGURE 3.3: The pyrochlore sublattice formed by Os tetrahedra and truncated-tetrahedral cavities containing Rb ions is highlighted. Blue atoms: Rb, Red spheres: O, Gray atoms: Os (Structure Figure taken from [93])

3.2 Thermodynamic properties of RbOs_2O_6 analyzed within Eliashberg theory

Thermodynamic properties such as the specific-heat difference between superconducting and normal states $C_s - C_n$, the thermodynamic critical field $H_c(T)$, and the upper critical field $H_{c2}(T)$ of the beta-pyrochlore superconductor RbOs_2O_6 were analyzed within Eliashberg theory including anisotropy effects, yielding $\lambda_{ep} \simeq 1$, a small electron-phonon coupling anisotropy parameter of about $\langle a_{\mathbf{k}}^2 \rangle \simeq 0.005$, and a Fermi velocity anisotropy parameter $\langle b_{\mathbf{k}}^2 \rangle \simeq 0.23$. Excellent agreement between theory and experiment was achieved for these parameters, the Sommerfeld constant γ , and model phonon spectra consisting of a debye spectrum and two Einstein peaks. The results indicate that RbOs_2O_6 is a conventional electron-phonon superconductor with s-wave symmetry.

3.2.1 Introduction

Pyrochlore oxides constitute a large family of transition-metal (TM) oxides like perovskites and have the general chemical formula $\text{A}_2\text{B}_2\text{O}_7$ or $\text{A}_2\text{B}_2\text{O}_6\text{O}$ where A is a larger cation and B is a smaller TM cation. The first superconductor in the family of pyrochlore oxides was discovered in $\text{Cd}_2\text{Re}_2\text{O}_7$ at $T_c = 1.0$ K [75, 76, 77]. Yonezawa et al. found another

type of pyrochlore oxides with the general formula AB_2O_6 called the β -pyrochlore oxide [78], where A is a large monovalent alkaline metal cation. Soon, superconductivity was reported in KOs_2O_6 [79, 80], with a T_c of 9.6 K, and more reports of superconductivity in the same family of compounds have followed at a rapid pace, with superconductivity being observed in $RbOs_2O_6$ with $T_c = 6.3$ K [78, 81] and in $CsOs_2O_6$ with $T_c = 3.3$ K [82].

The discovery of superconductivity in the β -pyrochlores raises the question of the underlying mechanism. While the mechanism in the α -pyrochlore $Cd_2Re_2O_7$ can be understood within the weak-coupling Bardeen, Cooper, and Schrieffer (BCS) theory of superconductivity [83], Hiroi and co-workers have suggested [80] that KOs_2O_6 is an unconventional superconductor, with the pairing mediated by spin fluctuations [84]. On the other hand, Brühwiler et al. suggested that $RbOs_2O_6$ could be a conventional BCS-type superconductor [81, 91], and recent pressure effects [85] and NMR [86] measurements appear to substantiate their conclusions [85]. Our analysis of the thermodynamic and superconducting properties of $RbOs_2O_6$ within Eliashberg theory [18] and recent work on the investigation of rattling and anharmonic phonons in KOs_2O_6 [87, 88] give further support to this suggestion, indicating that $RbOs_2O_6$ is a conventional electron-phonon superconductor with s-wave symmetry. It seems rather unlikely that the underlying mechanism of superconductivity has a different origin between these two similar compounds.

3.2.2 Spectral function

As there are no data available which would allow to determine the electron-phonon interaction spectral density $\alpha^2F(\omega)$ directly by inversion, we have to start our analysis with a model spectrum. The concept of an optimal electron-phonon interaction spectral density as an Einstein spectrum which allows to describe all physical properties of a superconductor in an optimal way was developed from Carbotte's original definition of an optimum spectrum [63]. We have shown, using the borocarbides YNi_2B_2C and $LuNi_2B_2C$ as examples, that such a concept is meaningful even for anisotropic systems [66]. An Einstein spectrum is sufficient for clean-limit systems, a 2δ -peak spectrum is better suited for anisotropic systems with impurities.

We follow this approach and model a phonon spectrum consisting of two Einstein peaks given by Hiroi et al. [89] at 5.3 meV and 11.9 meV with an amplitude ratio of 1:2 (for the Rb and Cs atoms) and a Debye spectrum for the O atoms. As an arbitrary choice, the contributions to the phonon spectrum area were weighed with the number of atoms per formula unit 1:9, 2:9 for the 5.3, 11.9 meV peaks and 6:9 for the debye spectrum (Fig. 3.4).

As a first test, this model phonon spectrum was used to calculate the thermodynamic properties. In the isotropic case with $\langle a^2 \rangle = 0$ it showed good agreement with the experimental data, and a Coulomb pseudopotential μ^* slightly greater than 0.2 if $\lambda \sim 1.0$. For most common

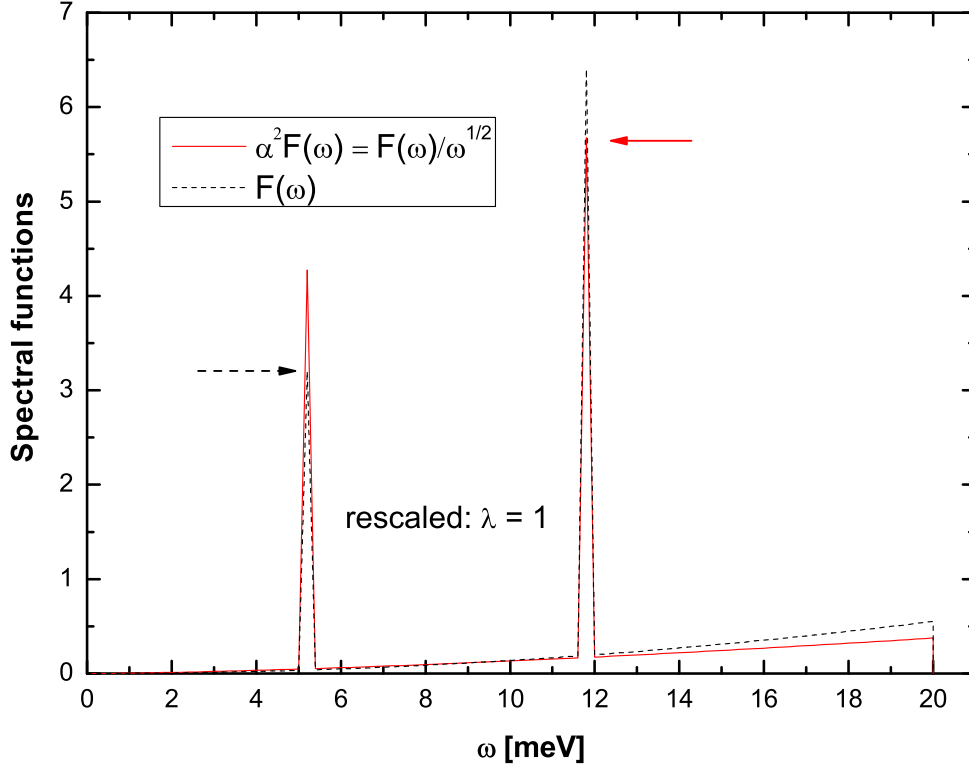


FIGURE 3.4: Model phonon spectrum $G(\omega)$ and electron phonon spectral function $\alpha^2 F(\omega)$, with $\alpha^2(\omega) = 1/\sqrt{\omega}$, used in the analysis of RbOs_2O_6 . The functions were rescaled to obtain a coupling parameter of $\lambda = 1.0$.

superconductors, μ^* usually lies in the range $0.1 - 0.2$. Comparison of the numerical results with the experimental data showed that it is possible to consider the phonon spectrum to describe the thermodynamic properties in the isotropic case. However, adding small anisotropy values of $\langle a^2 \rangle$ resulted in worse agreement between experiment and numerical results.

A usual method in obtaining $\alpha^2 F(\omega)$ is to rescale the phonon spectrum with $1/\sqrt{\omega}$ as was done in the description of the A15 [90] and borocarbide superconductors [21, 66]. We apply this method and find the resulting spectral function $\alpha^2 F(\omega)$ to be suitable in describing the thermodynamic properties of RbOs_2O_6 in the superconducting regime. It enhances the results of the calculations to the stronger coupling regime, which can be compensated by $\langle a^2 \rangle$ to reproduce the experimental data within experimental accuracy. With this spectral function (Fig. 3.4) and in the isotropic case, the Coulomb pseudopotential is $\mu^* = 0.1647$, a

| | |
|---|----------------------|
| γ [mJ/mol K ²] | 44 |
| a [Å] | 10.114 |
| N (Number of atoms) [10 ²² / cm ³] | 6.96 |
| T_c [K] | 6.37 |
| Θ_D [K] | 240 |
| v_F [cm/s] | 1.48 10 ⁷ |

Table 3.1: Input parameters for the theoretical analysis of RbOs₂O₆

value which lies well within the usual range.

3.2.3 Results

The input parameters used to obtain the numerical results are given in Table 3.1. The γ -value of 44 mJ/mol K², $v_F = 1.47 \cdot 10^7$ cm/s (which is only needed for H_{c2}) for KOs₂O₆, and the lattice parameter were taken from [91, 92, 93]. This Fermi velocity was multiplied by the ratio $N(E_F)/a^3$ of the K and Rb-samples to give an estimated value of about $v_F = 1.48 \cdot 10^7$ cm/s for RbOs₂O₆.

Comparison of the numerical results for $C_s - C_n$, $H_c(T)$ (Fig. 3.5) and the deviation function $D(T/T_c)$ (Fig. 3.6) with experimental data provided by Markus Brühwiler (ETH Zürich) already show fairly good results for the isotropic case, which improves with increasing anisotropy values $\langle a^2 \rangle$, especially in the case of the deviation function where one can see an observable change. The experimental data was rescaled with a factor ~ 1.3 , as a result of considering that the superconducting volume fraction is not 100 % and a second metallic component is present. The data for the thermodynamic critical field $H_c(T)/H_c(0)$ was multiplied with $H_c(0) = 124.9$ mT given in [91].

In reality, the sample develops some residual resistivity at low temperatures which is an indication of some impurity content. Thus, a clean limit analysis of experimental data can only be a first step which allows to put some margins on the various anisotropy parameters. It would then be standard procedure [62] to load the sample under investigation in a controlled way with some impurities and to measure the change in T_c and in the residual resistivity ρ_n as a function of impurity concentration. This gives another, rather reliable estimate for the anisotropy parameter $\langle a^2 \rangle$ [54] and allows to calculate the impurity parameter t^+ which enters Eqs. (3.4) and (3.10) from the Drude relation

$$t^+ = \frac{\rho_n \hbar \omega_p}{8\pi^2}, \quad (3.16)$$

with the plasma frequency of a free electron gas $\omega_p = 4\pi n e^2 / m$, where n , m and e are the

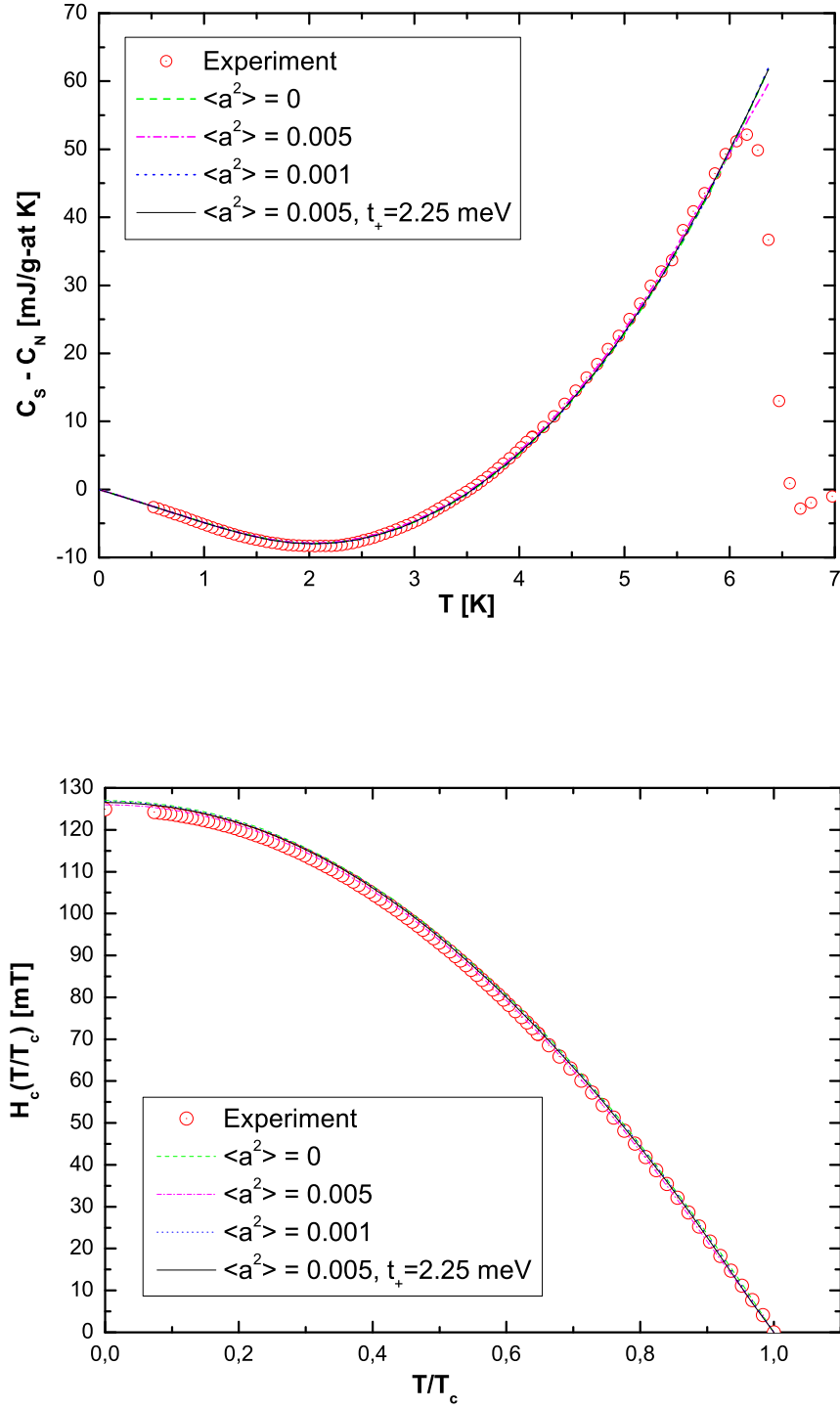


FIGURE 3.5: Specific heat difference between superconducting and normal states and thermodynamic critical field of RbOs_2O_6 for the isotropic case and with anisotropy values of $\langle a^2 \rangle = 0.001, 0.005$ in the clean limit, and with an impurity parameter $t_+ = 2.25$ meV for $\langle a^2 \rangle = 0.005$ [19].

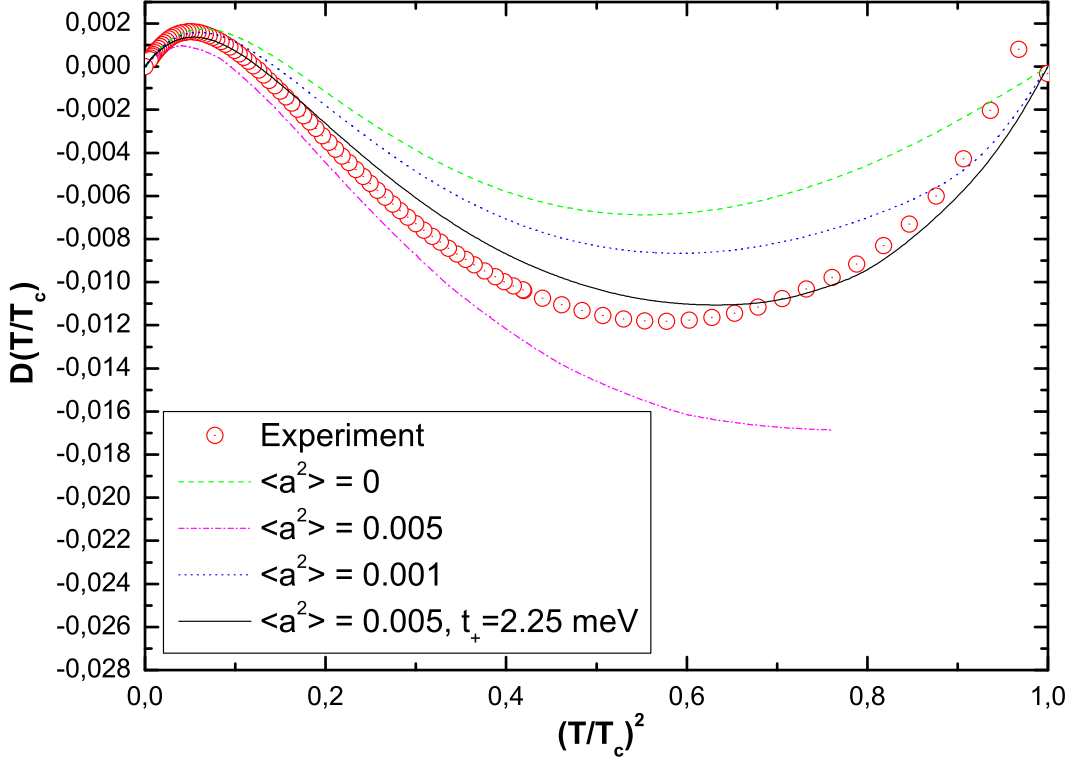


FIGURE 3.6: Deviation function of RbOs_2O_6 for the isotropic case and with anisotropy values of $\langle a^2 \rangle = 0.001, 0.005$ in the clean limit, and with an impurity parameter $t_+ = 2.25$ meV for $\langle a^2 \rangle = 0.005$ [19].

density, mass and charge of an electron. Such data is not available for RbOs_2O_6 and we have to rely on another strategy to obtain the anisotropy parameters including t_+ .

The upper critical field H_{c2} (Fig. 3.7,top) of this sample can not be described in the clean limit with $t_+ = 0$. We have to keep in mind that adding impurities increases $H_{c2}(T)$ even in isotropic systems [57, 95]. Moreover, adding impurities ‘smears out’ the anisotropy[54] which results in increasing values of $H_c(T)$ and an additional increase of $H_{c2}(T)$, and, furthermore, in a less pronounced upward curvature of $H_{c2}(T)$ close to T_c [62] if $\langle a^2 \rangle$ and $\langle b^2 \rangle$ are kept constant in the calculations. In order to cause an increase of $H_{c2}(T)$ obtained in the clean-limit calculations, it is therefore necessary to take impurity scattering into account, resulting in a $t_+ = 2.25$ meV and a Fermi velocity anisotropy parameter of $\langle b^2 \rangle = 0.23$ for the best fit.

| | |
|-----------------------|-----------------------|
| λ_{ep} | 1 |
| μ^* | 0.16606 |
| $\langle a^2 \rangle$ | 0.005 |
| $\langle b^2 \rangle$ | 0.23 |
| t_+ [meV] | 2.25 ($l = 43.3$ nm) |
| $H_c(0)$ [mT] | 126.5 |

Table 3.2: Results of the analysis of RbOs₂O₆

With this value for t_+ and an anisotropy parameter $\langle a^2 \rangle = 0.005$, the deviation function is even closer to the experimental data (Fig. 3.6). The results of the analysis are given in Table 3.2.

The scattering rate is related to the transport relaxation time via

$$t_+ = \frac{\hbar}{\tau_{tr}}. \quad (3.17)$$

With $v_F = l/\tau_{tr}$, we can calculate the mean free path of cooper pairs

$$l = \frac{\hbar v_F}{t_+}, \quad (3.18)$$

resulting in a mean free path of $l \simeq 43.3$ nm, which could be explained by defects at the oxygen sites. For comparison, the mean free path for a KOs₂O₆-sample estimated by Saniz et al. [92] is about $l = 3.5$ nm, meaning that the sample measured by Hiroi et al. [89] is in the dirty limit. Note, that in the description with Eliashberg theory the γ -value obtained from the specific heat of RbOs₂O₆, and not γ_{bs} from band structure calculations, was used. The Sommerfeld coefficient and density of states at the Fermi energy are related by

$$\gamma = \frac{\pi^2}{3} k_B^2 N(E_F)(1 + \lambda). \quad (3.19)$$

The density of states obtained from band structure calculations is $N(E_F)_{bs} = 4.9$ states/eV f.u. [93, 92], which results in $\gamma_{bs} = 11.56$ mJ/mole K², whereas the value from specific heat measurements $\gamma = 44$ mJ/mole K² gives $N(E_F) = 18.7$ states/eV f.u. It is about three to four times larger than the value obtained from band structure calculations, which would result in a renormalisation constant $1 + \lambda$ ranging from 3 to 4. The analysis of experimental data with Eliashberg theory confirms $\lambda_{ep} \simeq 1$ obtained from the specific heat jump at T_c [91], and the value obtained using the McMillan-Hopfield equation and a $\Theta_D = 240$ K (20 meV) to estimate λ_{ep} [93], but it does not give an explanation for the additional factor λ_{add} with unknown source. Of course, there is always the possibility of some discrepancies between structure models and real structures as it has been e.g. revealed for RNi₂B₂C with intrinsic defects (7-11% of B-C interchanged) [94].

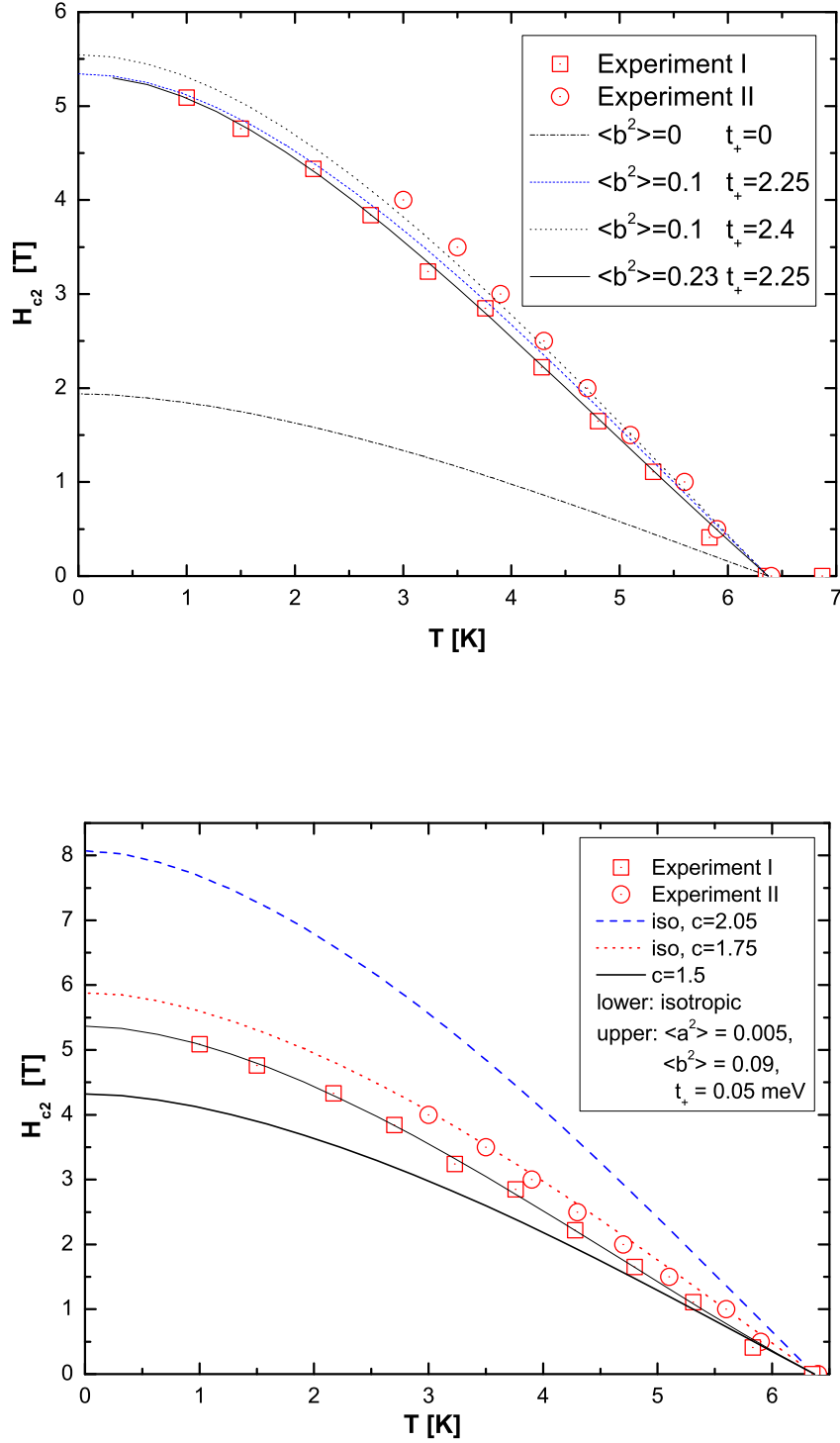


FIGURE 3.7: Upper critical field $H_{c2}(T)$ of RbOs₂O₆ with an electron phonon anisotropy parameter of $\langle a^2 \rangle = 0.005$ and various Fermi velocity anisotropy $\langle b^2 \rangle$ and impurity scattering parameters t_+ [19]. (top: fixed $v_F = 1.48 \times 10^7$ cm/s, bottom: various input Fermi velocities $v_{F,i}$)

An enhancement of the Fermi velocity due to the above-mentioned unknown effects could be obtained from an analysis of H_{c2} if we assume that impurity scattering in the sample is smaller. The effective Fermi velocity is given by

$$v_F^\dagger = \frac{v_F}{1 + \lambda}, \quad (3.20)$$

where v_F is the bare Fermi velocity obtained from band structure calculations and $\lambda = \lambda_{ep} + \lambda_{add}$. We have to keep in mind that electron-phonon coupling is already included in Eliashberg theory via the spectral function. Therefore, renormalizing the bare Fermi velocity

$$v_F^* = \frac{v_F}{1 + \lambda_{ep}} \quad (3.21)$$

as an input parameter to account for additional electron-phonon coupling does not apply. However, it is possible to analyze the behavior of $H_{c2}(T)$ with various Fermi velocity input values and calculate an additional enhancement factor λ_{add} from

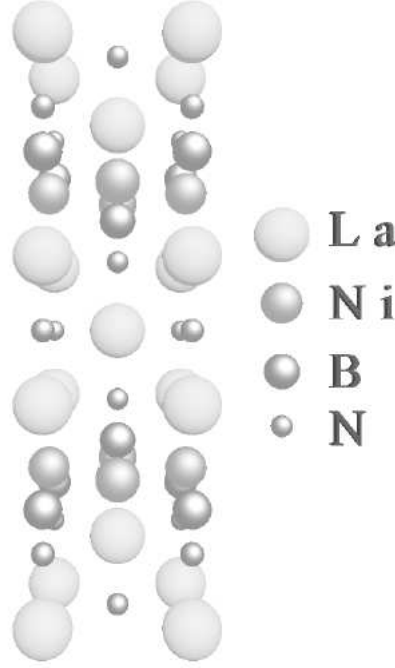
$$c = \frac{1 + \lambda_{ep} + \lambda_{add}}{1 + \lambda_{ep}}, \quad (3.22)$$

where one obtains the relation

$$v_F^\dagger = \frac{v_F^*}{c} \quad \text{or} \quad v_{F,i} = \frac{v_F}{c}, \quad (3.23)$$

and $v_{F,i}$ is the Fermi velocity input parameter of the theory. As an approximation, we substitute the electron-phonon renormalized value of the Fermi velocity for the bare Fermi velocity leading to properties including electron-phonon coupling in the following $H_{c2}(T)$ -fits. At first, the upper critical field in the clean limit $t_+ = 0$ is calculated with various input Fermi velocities $v_{F,i}$ until the theoretical curve is below the experimental data. In the second step, anisotropy and impurity scattering are added to obtain a good H_{c2} -fit (Fig 3.7). If the RbOs_2O_6 -sample is assumed to be near the clean limit, with a scattering parameter of $t_+ = 0.05$ meV corresponding to a mean free-path of about $l \sim 2 \mu\text{m}$, the Fermi velocity anisotropy parameter is $\langle b^2 \rangle = 0.09$, with $\langle a^2 \rangle = 0.005$ and $c = 1.5$. This c -value corresponds to an additional enhancement factor of $\lambda_{add} = 1$. This value is near the minimal value for λ_{add} , which ranges from 0.8 to 2.1. Adding impurity scattering in the calculations leads to a further reduction of λ_{add} . We emphasize that oxygen defects are common in these systems and the analysis of $H_{c2}(T)$ to obtain an additional enhancement factor would be more reliable if the residual resistivity of the sample is known. It is more likely that $H_{c2}(T)$ is described by the bare Fermi velocity including anisotropy and scattering effects, as was done in the case of the borocarbide superconductors [21].

To summarize, the spectral function used in order to describe the thermodynamic properties of RbOs_2O_6 with Eliashberg theory is suitable to obtain good agreement with the experimental data. With a Coulomb pseudopotential of 0.166, which lies well in the range of usual

FIGURE 3.8: The crystal structure of $\text{La}_3\text{Ni}_2\text{B}_2\text{N}_{3-\delta}$

values, the coupling parameter λ_{ep} of previous publications are confirmed. Adding a small anisotropy parameter of the electron phonon interaction of $\langle a^2 \rangle = 0.005$ and non-magnetic scattering impurity of $t_+ = 2.25$ meV, and a mean squared anisotropy of the Fermi velocity $\langle b^2 \rangle = 0.23$, which is quite large compared to other systems, very well describes all the provided experimental data [18, 19].

3.3 Analysis of the T_c reduction in $\text{La}_3\text{Ni}_2\text{B}_2\text{N}_{3-\delta}$

The transition-metal borocarbide superconductors $R\text{Ni}_2\text{B}_2\text{C}$ with transition temperatures comparable to those of the A-15 compounds (e.g. $R = \text{Lu}$ with $T_c \simeq 16.5$ K, Nb_3Ge with $T_c \simeq 23$ K) are a subject of broad interest for research on intermetallic superconductors. Siegrist and others [96] reported the crystal structure of the $R\text{Ni}_2\text{B}_2\text{C}$ superconductors to be a filled version of the ThCr_2Si_2 -type structure stabilized by the incorporation of carbon, where Ni_2B_2 layers are separated by RC layers. In the related $\text{La}_3\text{Ni}_2\text{B}_2\text{N}_{3-\delta}$, three LaN-planes separate the Ni_2B_2 layers. Despite of the layered structure reminiscent of the cuprate superconductors, the electronic structure of the triple LaN-layer boronitride is three-dimensional [97]. Nickel-site substitutions revealed similar electronic properties of the bands related to the 3d-electrons [98]. At a first glance, the thermodynamic properties of $\text{La}_3\text{Ni}_2\text{B}_2\text{N}_{3-\delta}$ seem to be close to

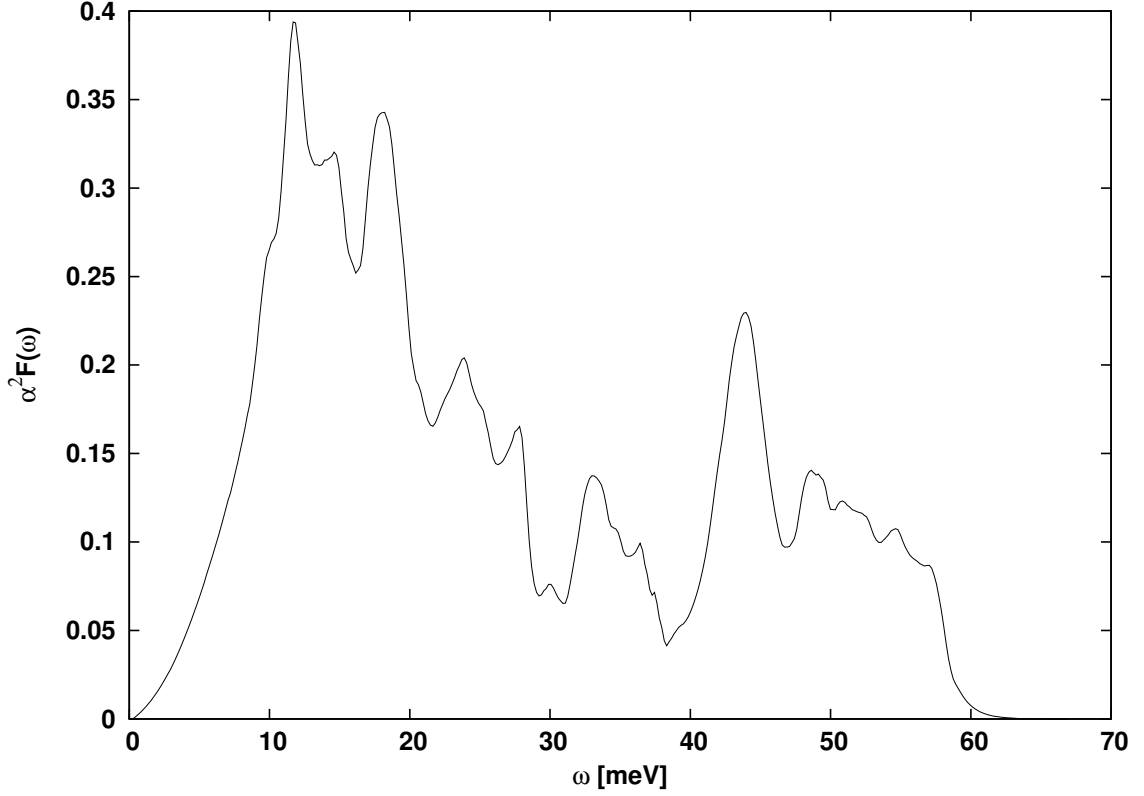


FIGURE 3.9: Model spectral function $\alpha^2 F(\omega)$ derived by weighing the calculated phonon spectrum of $\text{La}_3\text{Ni}_2\text{B}_2\text{N}_{2.875}$ [100] with $1/\sqrt{\omega}$.

the weak coupling BCS-predictions [99] but standard single-band BCS-theory cannot explain the pronounced upward curvature of the upper critical field $H_{c2}(T)$ close to T_c . An isotropic single band model cannot reproduce the positive curvature near T_c apparently, because of the dominant role of anisotropy effects in this system.

In a previous analysis [21], we achieved excellent agreement between Eliashberg theory and experimental data on $\text{La}_3\text{Ni}_2\text{B}_2\text{N}_{3-\delta}$ by using a model phonon spectrum, which yielded $\lambda = 1.02$. It was of importance to include anisotropy in order to describe its upper critical field and its thermodynamic properties. Both properties were well described with an electron-phonon anisotropy parameter $\langle a^2 \rangle \simeq 0.08$ and a Fermi velocity anisotropy parameter $\langle b^2 \rangle \simeq 0.245$. In order to stay within the constraints of the known experimental data, t^+ had to be rather small and therefore we then regarded the clean limit to be an acceptable approximation.

3.3.1 Do N site vacancies act as scattering centers?

In the thesis of Tahir Ali [22], he prepared various compositions of $\text{La}_3\text{Ni}_2\text{B}_2\text{N}_{3-\delta}$ with the aim to achieve a systematic variation of the N site occupancy. One of the results of this

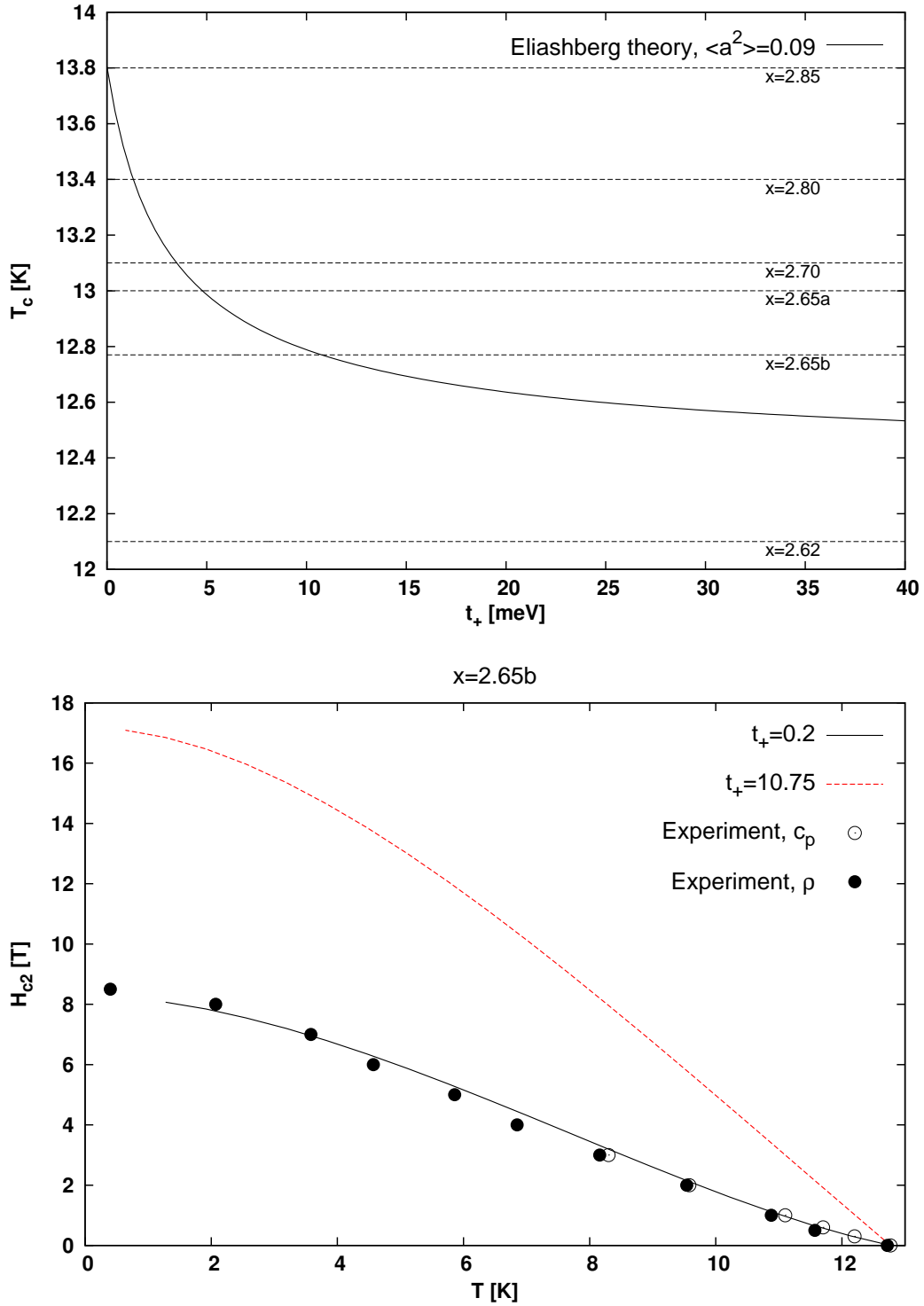


FIGURE 3.10: Top: Critical temperature T_c vs. impurity scattering parameter t_+ calculated with an electron-phonon anisotropy of $\langle a^2 \rangle = 0.09$ and the model phonon spectrum. The horizontal lines are the experimental critical temperatures of $\text{La}_3\text{Ni}_2\text{B}_2\text{N}_x$ obtained from specific heat measurements. Bottom: Upper critical field of $\text{La}_3\text{Ni}_2\text{B}_2\text{N}_x$, $x = 2.65$, (dots, experiment) and calculated H_{c2} with the corresponding t_+ of 10.75 meV. The results for $t_+ = 0.2$ meV is shown for comparison.

work was the decrease of critical temperature of the $\text{La}_3\text{Ni}_2\text{B}_2\text{N}_x$ samples with a nominal nitrogen content x , which ranges from 2.9 to 2.6. At a first glance, this could be an indication that the vacancies at the nitrogen site may act as scattering centers. In such a case, the critical temperature of $\text{La}_3\text{Ni}_2\text{B}_2\text{N}_x$ would be correlated to increasing N vacancies and, if this speculation is valid, to an increase of the scattering parameter t_+ with decreasing x . We put this theory to test by calculating T_c as a function of t_+ with constant $\lambda = 1$ and $\mu^* = 0.1$, consistent to the previous results. We used a model spectral function $\alpha^2 F(\omega)$ derived by weighing the calculated phonon spectrum of $\text{La}_3\text{Ni}_2\text{B}_2\text{N}_{2.875}$ [100] with $1/\sqrt{\omega}$. Furthermore, the sample with the highest $x = 2.9$ and $T_c = 13.8$ K was assumed to be in the clean limit $t_+ = 0$ and $\langle a^2 \rangle = 0.09$ to be slightly higher than the previous calculations. The results are shown in Figures 3.10 and suggest higher impurity concentrations as the T_c vs. t_+ slope becomes flat (Fig. 3.10, top). With such t_+ -values, the upper critical field curvature near T_c disappears and is clearly higher than in the clean limit calculations (Fig. 3.10, bottom) at lower temperatures. However, experimental results show similar $H_{c2}(T)$ -behaviour with varying nitrogen content. Therefore, we conclude that the decrease in T_c cannot be fully attributed to increased impurity scattering in the samples but rather to a shift in phonon modes as discussed below.

3.3.2 Shift in phonon modes: Analysis with an Einstein spectrum

A possible reason for the behaviour of T_c in $\text{La}_3\text{Ni}_2\text{B}_2\text{N}_x$ could be a shift in electron-phonon coupling modes with increasing nitrogen vacancies. This would result in a different electron-phonon spectral function $\alpha^2 F(\omega)$, which may lead to a change in T_c . To test this assumption, we simplify the analysis by using a δ -function as electron-phonon spectral function. We have shown in a previous analysis [66], that the concept of an optimal electron phonon interaction spectral density as an Einstein spectrum allows to describe all physical properties of a superconductor in an optimal way. Such a concept is meaningful even for anisotropic systems. An Einstein spectrum is sufficient for clean-limit systems, a 2δ -peak spectrum is better suited for anisotropic systems with impurities. We could conclude from the results of describing the experimental $H_{c2}(T)$ -data with Eliashberg theory, that the effect of impurity scattering is rather small in the samples. Therefore, to minimize the number of unknown parameters, we assume the samples to be in the clean limit.

In the analysis presented here, the actual energy dependence of the $\alpha^2 F(\omega)$ spectrum is of no importance as we are going to replace the $\alpha^2 F(\omega)$ by an Einstein spectrum with its δ -peak of strength A at some fixed frequency ω^* and fixed μ^*

$$\alpha^2 F(\omega) = A\delta(\omega - \omega^*), \quad (3.24)$$

with A , μ^* and ω^* initially chosen to give the measured T_c , the appropriate value for λ , and the best possible fit to experiment. Nevertheless, these $\alpha^2 F(\omega)$ spectra already give a pretty

| x | T_c [K] | ω^* [meV] | A [1/meV] |
|-------|-----------|------------------|-------------|
| 2.62 | 12.1 | 11.80 | 5.90 |
| 2.65a | 12.8 | 12.47 | 6.24 |
| 2.65b | 13.0 | 12.70 | 6.35 |
| 2.70 | 13.1 | 12.80 | 6.40 |
| 2.80 | 13.4 | 13.10 | 6.55 |
| 2.85 | 13.8 | 13.50 | 6.75 |

Table 3.3: $\text{La}_3\text{Ni}_2\text{B}_2\text{N}_x$ and corresponding critical temperatures T_c obtained from the specific heat jump. The centers ω^* and strength A of the model spectrum δ -function peaks are obtained with constant $\lambda = 1.0$, $\mu^* = 0.109$, $\langle a^2 \rangle = 0.09$, and $t_+ = 0$

good idea where to place the δ -peak because a quite natural choice is to place the δ -peak near the center of the area under the respective $\alpha^2 F(\omega)$ spectrum at low frequencies. In a first step we used $\mu^* = 0.109$, the anisotropy parameter $\langle a^2 \rangle = 0.09$, and a fixed $\lambda = 1.0$ to calculate the critical temperature for different centers ω^* of the model spectrum δ -function peaks. The results are listed in table 3.3.

In the next step we wanted to test if the upper critical field can be described with the δ -spectrum and the anisotropy parameters $\langle a^2 \rangle = 0.09$, $\langle b^2 \rangle = 0.205$, and mean Fermi velocity $v_F = 0.222 \cdot 10^6$ m/s obtained by describing the experimental data by using the model phonon spectrum (Fig. 3.9). The results of the calculations fit the experimental data surprisingly well for every sample, and we have taken the data for $x = 2.65$ and $x = 2.85$ as examples in Fig. 3.11. Experimental data from resistivity measurements are shown as open circles and the results of the calculations by using Eliashberg theory as a solid line. This concept to use an Einstein spectrum with its peak placed near the center of the area under a model phonon spectrum proved sufficient to obtain a reasonable agreement between theoretical predictions and experiment over the whole temperature range for $H_{c2}(T)$, which is particularly sensitive to anisotropy effects and details in $\alpha^2 F(\omega)$.

In our simplified analysis, we used a δ -function as electron-phonon coupling spectrum with constant parameters $\mu^* = 0.109$, $\lambda = 1.0$ and $\langle a^2 \rangle = 0.09$ to model the T_c -depression and experimental data. However, it would be more realistic to introduce a change in the electron-phonon coupling strength λ , which in turn will have an influence in our choice for ω^* . Ali *et al.* [22, 101] measured the resistivity of $\text{La}_3\text{Ni}_2\text{B}_2\text{N}_{2.9}$ with increasing pressure and obtained a decrease of T_c , an increase of Debye frequencies ω_D and a decrease of the coupling factor $\lambda(\omega_D)$ by applying a Bloch Grüneisen fit to the normal state resistivity. The analysis of thermal factors measured via powder neutron diffractometry on the samples $\text{La}_3\text{Ni}_2\text{B}_2\text{N}_{2.65}$ and $\text{La}_3\text{Ni}_2\text{B}_2\text{N}_{2.9}$ suggests a similar trend for T_c vs ω_D . Note that within the framework of

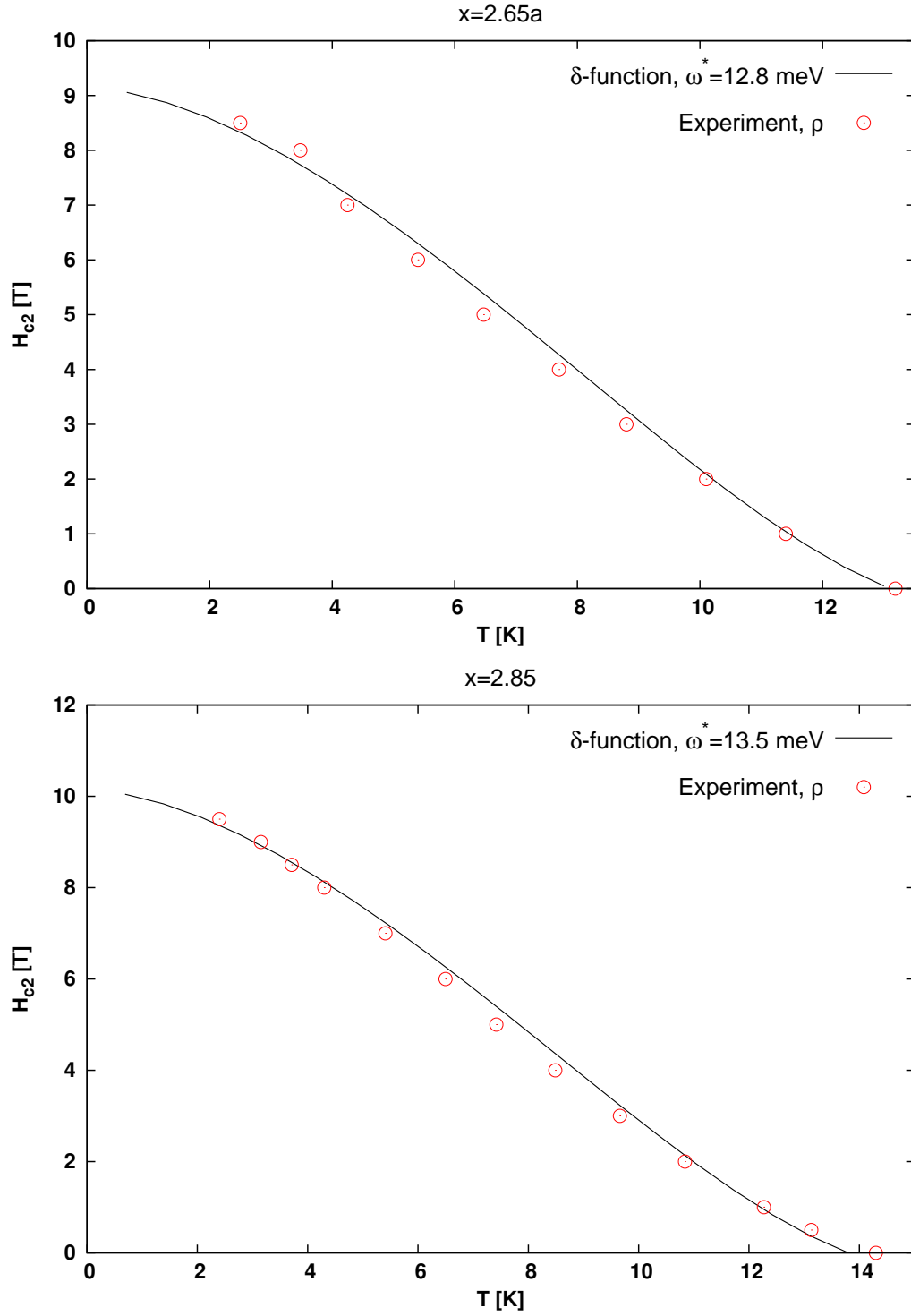


FIGURE 3.11: Results for the upper critical field H_{c2} with $\omega^* = 12.8$ and 13.5 meV compared to experimental resistivity data of $\text{La}_3\text{Ni}_2\text{B}_2\text{N}_x$ with $x = 2.65$, $T_c = 13.0$ K and $x = 2.85$, $T_c = 13.8$ K.

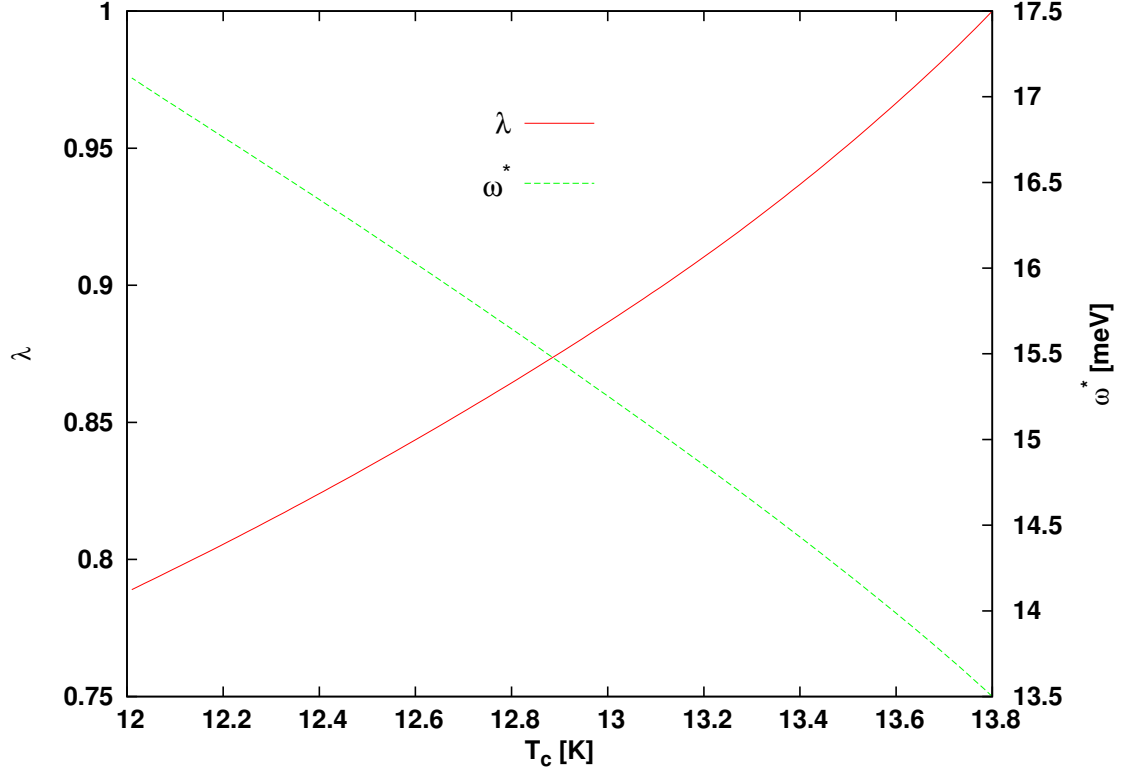


FIGURE 3.12: Relation of the critical temperature to ω^* , the center of the δ -peak, and λ at a fixed μ^* , $\langle a^2 \rangle$ and coupling strength A .

Eliashberg theory, the relation of the coupling frequency ω^* to the coupling factor λ is

$$\lambda = 2 \int_0^\infty d\omega \frac{\alpha^2 F(\omega)}{\omega} = 2 \int_0^\infty d\omega \frac{A \delta(\omega - \omega^*)}{\omega} = \frac{2A}{\omega^*}. \quad (3.25)$$

If we allow λ to decrease and hold the coupling strength A constant, it would clearly lead to a higher electron-phonon coupling frequency ω^* . The effect of λ on the critical temperature should be stronger than that of ω^* for it to show the experimentally observed behaviour (see high pressure studies in [22, 99, 101]): T_c decreases with an increase of ω^* and decrease of λ . To substantiate this trend within Eliashberg theory, we performed calculations with constant $\mu^* = 0.109$ and $\langle a^2 \rangle = 0.09$, and by tuning ω^* and λ to obtain the same strength A of the reference sample with $T_c = 13.8$. The results are shown in table 3.4. A decrease of λ . *i.e.* from 1.0 to 0.965 would need a higher coupling frequency ω^* of 14 meV compared to 13.5 meV, in order to obtain the same coupling strength $A = 6.75 \text{ meV}^{-1}$ of the reference sample. This decrease of λ (increase of ω^*) corresponds to a decrease of T_c from 13.8 K to 13.6 K. Therefore, we can model the effect of pressure on $\text{La}_3\text{Ni}_2\text{B}_2\text{N}_{3-\delta}$, which stiffens the lattice and results in higher Debye frequencies (equivalent to higher coupling frequencies),

| λ | T_c [K] | ω^* [meV] |
|-----------|-----------|------------------|
| 1.0 | 13.8 | 13.50 |
| 0.965 | 13.61 | 14.00 |
| 0.913 | 13.24 | 14.79 |
| 0.871 | 12.88 | 15.50 |
| 0.818 | 12.35 | 16.50 |
| 0.789 | 12.01 | 17.11 |

Table 3.4: Calculation of T_c with $\mu^* = 0.109$, $\langle a^2 \rangle = 0.09$, and $t_+ = 0$. λ was decreased and ω^* increased to obtain the strength $A = 6.75 \text{ meV}^{-1}$ of a reference sample with $T_c = 13.8 \text{ K}$.

provided that λ decreases and the coupling strength A is held constant (Fig. 3.12). This reverses the trend indicated in table 3.3 for the center ω^* of the electron-phonon coupling δ -function to decrease with increasing T_c .

3.3.3 Conclusion

Measurements on $\text{La}_3\text{Ni}_2\text{B}_2\text{N}_{3-\delta}$ reveal a decrease in the critical temperature with increasing vacancy on the nitrogen site [22]. We investigated the vacancy related T_c -depression with respect to impurity scattering at a given electron-phonon coupling anisotropy $\langle a^2 \rangle$ and obtained high t_+ -values, which would result in rather big and unrealistic values for the anisotropy and Fermi velocity parameters to reproduce $H_{c2}(T)$ on an absolute scale. However, experimental results show similar $H_{c2}(T)$ -behaviour with varying nominal nitrogen content. Therefore, we conclude that the decrease in T_c cannot be only attributed to increased impurity scattering in the samples. However, a shift of the electron-phonon coupling pairing frequency yields an important contribution to this phenomenon. We used an Einstein spectrum and shifted the center of the δ -peak to reproduce the experimental critical temperatures. The consistency of our calculations was then checked with the ability of the theory to describe the experimental data on the upper critical field $H_{c2}(T)$, which is very sensitive to changes in anisotropy and impurity scattering. We achieved reasonable agreement between theoretical predictions and experiment over the whole temperature range for $H_{c2}(T)$ and for all investigated samples of $\text{La}_3\text{Ni}_2\text{B}_2\text{N}_x$ with varying x . In our simplified analysis, we used a δ -function as electron-phonon coupling spectrum with variable ω^* , while keeping other parameters constant, to model the T_c -depression and experimental data. The analysis of thermal factors measured via powder neutron diffractometry done by Tahir Ali [22] resulted in an increase of Debye frequencies ω_D from 22.06 meV to 22.83 meV ($\Delta\omega_D = 0.77 \text{ meV}$) for the samples $\text{La}_3\text{Ni}_2\text{B}_2\text{N}_{2.9}$ and $\text{La}_3\text{Ni}_2\text{B}_2\text{N}_{2.65}$ with critical temperatures of $T_c = 14 \text{ K}$ and 13 K ($\Delta T_c = -1.0 \text{ K}$), respectively. We were able to model this effect on $\text{La}_3\text{Ni}_2\text{B}_2\text{N}_{3-\delta}$ with a stiffening of the lattice, which results in higher Debye frequencies (and therefore higher coupling frequencies), provided that λ decreases and the coupling strength A is held constant. In our calculations of

λ and ω^* vs. T_c in Fig. 3.12, an increase of $\Delta\omega^* = 0.77$ meV can account for a decrease of the critical temperature $\Delta T_c = -0.4$. Another major contribution to the T_c -decrease may also be attributed to increased impurity scattering caused by nitrogen vacancies. As we have discussed before, it cannot be solely responsible for the T_c -behaviour, but in combination with phonon effects the samples do not have to be in the dirty limit to achieve the experimental critical temperatures. In the clean limit range (near $t_+ = 0$), an impurity concentration of about $t_+ \sim 1.3$ meV can cause T_c to drop from 13.8 K to 13.4 K (see also Fig. 3.10), which can result in an additional $|\Delta T_c| \leq 0.4$ K. As we cannot rule out initial impurities in the sample with the highest T_c , the contribution of impurity scattering is assumed to be less or equal 0.4 K. With these combined effects of a change of the coupling frequency and an increase of impurity scattering, a difference in T_c of approximately 0.8 K is consistent with our Eliashberg model calculations. The remaining 20% may be attributed to electronic effects such as minor modifications of the complex Fermi surface topology of this quaternary borocarbide, which could also give an additional contribution to the T_c -reduction in $\text{La}_3\text{Ni}_2\text{B}_2\text{N}_x$ with increasing nitrogen vacancies.

Summary

The focus of Chapter 1 was the Fulde-Ferrell-Larkin-Ovchinnikov (FFLO) state [7, 8], which is a spatially inhomogeneous superconducting state predicted to occur in clean superconductors with purely paramagnetic limiting. Critical field measurements in the quasi-two-dimensional organic superconductor κ -(BEDT-TTF)₂Cu(NCS)₂ strongly suggest that a state of the FFLO type exists in this material. Agreement between experiment [9] and existing theories has been successfully checked [10] both in view of the angle-dependence [11] and the temperature dependence [12] of the upper critical field [13]. This was the first time since the original predictions [7, 8] that quantitative agreement between theory and experiment with regard to the FFLO phase boundary has been established.

For an applied magnetic field parallel to the films [5] or conducting planes [6], Pauli paramagnetism can be the dominating pair breaking effect, provided the conducting layers are sufficiently separated from each other or the thickness of the films is sufficiently small. In many of these compounds, including High- T_c cuprates and organic superconductors, impurity scattering and spin-orbit coupling is small and orbital pair breaking is the most important second order effect next to the spin effect to be taken into account. In Chapter 2, we investigated a superconducting film of finite thickness in a magnetic field with an arbitrary angle to the conducting plane. The usual model of purely paramagnetic pair breaking was generalized in a different way, taking into account the influence of a finite orbital pair breaking component on the FFLO state. The model was formulated in the first part of this Chapter, using the framework of the quasiclassical Eilenberger equations, and thermodynamic properties were derived. This new theory of competing spin and orbital pair breaking in clean superconducting films or layers was discussed with the help of experimental results on YBa₂Cu₃O₇ and possible orbital pair breaking contributions in the plane-parallel field configuration [15]. To conclude this Chapter, we included impurity scattering in our equations and compared the tunneling measurements of Ref. [5] on a thin Al film with the numerical results on the upper and lower stability limit of a system with finite thickness. At temperatures below a tricritical temperature, the behaviour of the two boundary solutions for the critical field improved to meet the characteristics of the experimental data.

Orbital pair breaking will always be the dominating mechanism in bulk superconductors, which holds in the framework of conventional BCS and related theories. Conventional superconductors are well described by Eliashberg theory [16] which treats superconductivity as a boson-exchange phenomenon. In Chapter 3, the upper critical field $H_{c2}(T)$ of the β -pyrochlore superconductor RbOs_2O_6 was analyzed within the framework of s -wave Eliashberg theory including anisotropy and scattering effects. Comparison between experiment and theory of thermodynamic properties such as the specific-heat difference between superconducting and normal states $C_s - C_n$, and the thermodynamic critical field $H_c(T)$ are well aligned with the results from the upper critical field analysis [18, 19].

Measurements on $\text{La}_3\text{Ni}_2\text{B}_2\text{N}_{3-\delta}$ show a decrease in the critical temperature with increasing vacancy on the nitrogen site [22] and the nitrogen vacancies may act as scattering centers, which smear out the effect of the electron-phonon coupling anisotropy. We investigated the vacancy related T_c -depression both with respect to impurity scattering and with a model Einstein spectrum, by shifting the center of the δ -peak. The consistency of our calculations was then checked with the ability of the theory to describe the experimental data on the upper critical field $H_{c2}(T)$, which is very sensitive to changes in anisotropy and impurity scattering. Our results show, that the effect of the additional scattering centers on anisotropy is too weak to explain the decrease in T_c . However, the shift of the electron-phonon pairing frequency yields an important contribution to this phenomenon. We achieved an excellent agreement between theoretical predictions and experiment over the whole temperature range for $H_{c2}(T)$ and for all investigated samples of $\text{La}_3\text{Ni}_2\text{B}_2\text{N}_x$ with varying x .

Bibliography

- [1] A. M. Clogston, *Phys. Rev. Lett.* **9**, 266 (1962)
- [2] B. S. Chandrasekhar, *Appl. Phys. Lett.* **1**, 7 (1962)
- [3] K. Maki, *in Superconductivity*, **vol.2** p.1035, edited by R. D. Parks (M.Dekker, New York, 1969)
- [4] P. Fulde, *Adv. Phys.* **22**, 667 (1973)
- [5] V. Yu. Butko, P. W. Adams, and E. I. Meletis, *Phys. Rev Lett.* **83**, 3725 (1999)
- [6] A. S. Dzurak, B. E. Kane, R. G. Clark, N. E. Lumpkin, J. O. Brien, G. R. Facer, R. P. Starrett, A. Skougarevsky, H. Nakagawa, N. Miura, Y. Enomoto, D. G. Rickel, J. D. Goettee, L. J. Campbell, C. M. Fowler, C. Mielke, J. C. King, W. D. Zerwekh, A. I. Bykov, O. M. Tatsenko, V. V. Platonov, E. E. Michell, J. Herrmann, and K. H. Müller, *Phys.Rev. B*, **57** R14084 (1998)
- [7] P. Fulde and R. A. Ferrell, *Phys. Rev.* **135**, A550 (1964)
- [8] A. I. Larkin and Y. N. Ovchinnikov, *Sov. Phys. JETP* **20**, 762 (1965)
- [9] M. S. Nam, J. A. Symington, J. Singleton, S.J. Blundell, A. Ardavan, J. A. A. J. Perenboom, M. Kurmoo, and P. Day *J.Phys.: Condens. Matter* **11**, L477 (1999)
- [10] S. Manalo and U. Klein, *J.Phys.: Condens. Matter* **12**, L471 (2000)
- [11] H. Shimahara and D. Rainer, *J. Phys. Soc. Jpn.* **66**, 3591 (1997)
- [12] K. Maki and H. Won, *Czech. J. Phys.* **46**, 1035 (1996)
- [13] J. Singleton, J. A. Symington, M. S. Nam, A. Ardavan, M. Kurmoo and P. Day, *J.Phys.:Condens.Matter* **12**, L641 (2000)
- [14] J. L. Brien, H. Nakagawa, A. S. Dzurak, R. G. Clark, B. E. Kane, N. E. Lumpkin, R. P. Starrett, N. Muira, E. E. Mitchell, J. D. Goettee, D. G. Rickel, and J. S. Brooks, *Phys.Rev. B* **61**, 1584 (2000)

- [15] S. Manalo and U. Klein, *Phys. Rev. B* **65**, 144510 (2002)
- [16] G.M. Eliashberg, *Sov. Phys. JETP* **11**, 696 (1960)
- [17] W.L. McMillan and J.M. Rowell, *Phys. Rev. Lett* **14**, 108 (1965)
- [18] S. Manalo, H. Michor, G. Hilscher, M. Brühwiler and B. Batlogg, *Phys. Rev. B* **73**, 224520 (2006)
- [19] S. Manalo, H. Michor, G. Hilscher, M. Brühwiler and B. Batlogg, *Physica C* **460-462**, 530-531 (2007)
- [20] S. Manalo, Diploma thesis, Technische Universität Wien, Karlsplatz 13, 1040 Wien, Austria (1999) unpulished;
- [21] S. Manalo, H. Michor, M. El-Hagary, G. Hilscher, and E. Schachinger, *Phys. Rev. B* **63**, 104508 (2001)
- [22] Tahir Ali, Dissertation, Superconductivity and Magnetism in Rare-Earth Nickel Boronitrides, Technische Universität Wien, Austria (2011)
- [23] G. Zwicknagl and J. Wosnitza, *BCS: 50 Years*, World Scientific Publishing, 337 (2011)
- [24] Y. Matsuda and H. Shimahara, *J. Phys. Soc. Jpn.* **76**, 051005 (2007)
- [25] A. I. Buzdin, *Rev. Mod. Phys.* **77**(3), 935 (2005)
- [26] D. E. Sheehy and L. Radzihovsky, *Ann. Phys.* **322**, 1790 (2007)
- [27] M. Alford, J. Bowers, K. Rajagopal *Phys. Rev. D* **63**, 074016 (2001)
- [28] R. Casalbuoni and G. Nardulli, *Rev. Mod. Phys.* **76**, 263 (2004)
- [29] G. Sarma, *J.Phys.Chem.Solids* **24**, 1029 (1963)
- [30] E. Gubankova, W. V. Liu and F. Wilczek *Phys. Rev. Lett.* **91**, 032001 (2003)
- [31] A. A. Abrikosov, *Zh. Eksp. Teor. Fiz.* **32**, 1442 (1957)
- [32] K. Maki, *Phys. Rev. B* **148**, 362 (1966)
- [33] G. Eilenberger, *Zeitschrift für Physik* **214**, 195 (1968)
- [34] L. N. Bulaevskii, *Sov. Phys. JETP* **38**, 634 (1974)
- [35] U. Klein, D. Rainer and H. Shimahara, *J. Low Temp. Phys.* **118**, 91 (2000)
- [36] H. Won and K. Maki, *Physica B* **199&200**, 354 (1994)

- [37] R. H. McKenzie, *Comments Cond. Matt. Phys.* **18**, 309 (1998)
- [38] R. C. Morris and R. V. Coleman, *Phys. Rev. B* **7**, 991 (1973)
- [39] A. M. Toxen, *Phys. Rev.* **127**, 382 (1962)
- [40] R. C. Casella and P. B. Miller, *Phys. Rev.* **136**, 928 (1964)
- [41] E. A. Shapoval, *JETP* **24**, 443 (1967)
- [42] E. A. Shapoval, *JETP* **22**, 647 (1966)
- [43] P. G. de Gennes and M. Tinkham, *Physics* **1**, 107 (1964)
- [44] H. Shimahara, *Phys. Rev. B.* **50**, 12760 (1994)
- [45] K. Maki and T. Tsuneto, *Progr.Theoret.Phys.* (Kyoto) **31**, 945 (1964)
- [46] P. W. Anderson, *J. Phys. Chem. Solids* **11** 26 (1959)
- [47] U. Welp, W. K. Kwok, G. W. Crabtree, K. G. Vandervoort, and J. Z. Liu, *Phys.Rev.Lett* **62**, 1908 (1989)
- [48] R. A. Klemm, A. Luther, and M. R. Beasley, *Phys.Rev. B* **12**, 877 (1975)
- [49] N. Mass, D. Ilzyer, G. Deutscher, G. Desgardin, I. Monot, and M. Weger, *J. Supercond.* **5**, 191 (1992)
- [50] K. Yang and S. L. Sondhi, *J. Appl. Phys.* **87**, 5549 (2000)
- [51] T. Schneider and A. Schmidt, *Phys.Rev. B* **47**, 5915 (1992)
- [52] K. Yang and S. L. Sondhi, *Phys. Rev. B* **57**, 8566 (1998)
- [53] X.S. Wu, P.W. Adams, G. Catelani, *Phys. Rev. B* **74**, 144519 (2006)
- [54] D. Markovitz, L.P. Kadanoff, *Phys. Rev.* **131**, 563 (1963)
- [55] J.M. Daams, J.P. Carbotte, *J. Low Temp. Phys.* **43**, 263 (1981)
- [56] J. Bardeen and M. Stephen, *Phys. Rev.* **136**, 1485 (1964)
- [57] M. Prohammer and E. Schachinger, *Phys. Rev. B* **36**, 8353 (1987)
- [58] L. Niel, N. Giesinger, H.W. Weber and E. Schachinger, *Phys. Rev. B* **32**, 2976 (1985)
- [59] P.B. Allen, *Phys. Rev. B* **13**, 1416 (1976)
- [60] J.M. Daams, Ph.D. thesis, McMaster University, Ontario, 1977 (unpublished)

- [61] V. Ambegaokar, in *Superconductivity*, ed.: R.D. Parks, Marcel Dekker, New York (1969), pp. 259
- [62] H.W. Weber, E. Seidl, C. Laa, E. Schachinger, M. Prohammer, A. Junod, D. Eckert, *Phys. Rev. B* **44**, 7585 (1991)
- [63] J.P. Carbotte, *Rev. Mod. Phys.* **62**, 1027 (1990)
- [64] C.R. Leavens, *Solid State Commun.* **17**, 1499 (1975)
- [65] B. Mitrović and J.P. Carbotte, *Solid State Commun.* **40**, 249 (1981)
- [66] S. Manalo and E. Schachinger, *Journal of Low Temp. Phys.* **123**, 149 (2001)
- [67] F. Gompf, W. Reichardt, H. Schober, B. Renker, and M. Buchgeister, *Phys. Rev. B* **55**, 9058 (1997)
- [68] W. Weber, private communication, Universität Dortmund, Institut für Theoretische Physik II, Otto-Hahn-Str. 4, D-44221 Dortmund (unpublished)
- [69] Shi Li, *et al.*, *Int. J. Mod. Phys.* **13**, 3725 (1999)
- [70] V. Shulga, S.-L. Drechsler, G. Fuchs, k.-H. Müller, K. Winzer, M. Heinecke, and K. Krug, *Phys. Rev. Lett* **80**, 1730 (1998)
- [71] R.S. Gonnelli, A. Morello, G.A. Ummarino, V.A. Stepanov, G. Behr, G. Graw, V. Shulga, and S.-L. Drechsler, *Int. Journal of Mod. Phys. B* **14**, 2840-2845 (2000)
- [72] G. Hilscher and H. Michor, *Studies of High Temperature Superconductors* **28**, 241 (1999)
- [73] E. Langmann, *Phys. Rev. B* **46**, 9104 (1992).
- [74] W. Pitscheneder and E. Schachinger, *Phys. Rev. B* **47**, 3300 (1993)
- [75] M. Hanawa, Y. Muraoka, T. Tayama, T. Sakakibara, J. Yamaura and Z. Hiroi, *Phys. Rev. Lett.* **87** 187001 (2001)
- [76] H. Sakai, K. Yoshimura, H. Ohno, H. Kato, S. Kambe, R. E. Walstedt, T. D. Matsuda, Y. Haga and Y. Onuki, *J. Phys.: Condens. Matter* **13**, L785 (2001)
- [77] R. Jin, J. He, S. McCall, C. S. Alexander, F. Drymiotis and D. Mandrus, *Phys. Rev. B* **64**, 180503 (2001)
- [78] S. Yonezawa, Y. Muraoka, Y. Matsushita and Z. Hiroi, *J. Phys. Soc. Jpn.* **73**, 819 (2004)
- [79] S. Yonezawa, Y. Muraoka, Y. Matsushita, and Z. Hiroi, *J. Phys. Condens. Matter* **16**, L9 (2004)

- [80] Z. Hiroi, S. Yonezawa, and Y. Muraoka, *J. Phys. Soc. Jpn* **73**, 1651-1654 (2004)
- [81] M. Brühwiler, S. M. Kazakov, N. D. Zhigadlo, J. Karpinski, and B. Batlogg, *Phys. Rev. B* **70**, 020503(R) (2004).
- [82] S. Yonezawa, Y. Muraoka, and Z. Hiroi, *J. Phys. Soc. Jpn.* **73**, 1655 (2004)
- [83] Z. Hiroi and M. Hanawa, *J. Phys. Chem. Solids* **63**, 1021 (2002)
- [84] A. Koda, W. Higemoto, K. Ohishi, S. R. Saha, R. Kadono, S. Yonezawa, Y. Muraoka, and Z. Hiroi, *J. Phys. Soc. Jpn.* **74**, 1678-1681 (2005)
- [85] R. Khasanov, D. G. Eshchenko, J. Karpinski, S. M. Kazakov, N. D. Zhigadlo, R. Brütsch, D. Gavillet, D. Di Castro, A. Shengelaya, F. La Mattina, A. Maisuradze, C. Baines, and H. Keller, *Phys. Rev. Lett.* **93**, 157004 (2004)
- [86] K. Magishi, J. L. Gavilano, B. Pedrini, J. Hinderer, M. Weller, H. R. Ott, S. M. Kazakov, and J. Karpinski, *Phys. Rev. B* **71**, 024524 (2005)
- [87] J. Chang, I. Eremin, and P. Thalmeier, *New Jour. Phys* **11**, 055068 (2009)
- [88] K. Hattori and H. Tsunetsugu, *Phys. Rev. B* **81**, 134503 (2010)
- [89] Z. Hiroi, S. Yonezawa, T. Muramatsu, J. Yamaura, Y. Muraoka, *J. Phys. Soc. Jpn.* **74**, 1255 (2005)
- [90] A. Junod, T. Jarlborg, and J. Muller, *Phys. Rev. B* **27**, 1568 (1983)
- [91] M. Brühwiler, S. M. Kazakov, J. Karpinski, and B. Batlogg, *Phys. Rev. B* **71**, 214517 (2005)
- [92] R. Saniz, J. E. Medvedeva, Lin-Hui Ye, T. Shishidou, and A. J. Freeman, *Phys. Rev. B* **70**, 100505(R) (2004)
- [93] J. Kunes, T. Jeong, and W. E. Pickett, *Phys. Rev. B* **70**, 174510 (2004)
- [94] A.D. Hillier, R.I. Smith, and R. Cywinski, *Applied Physics A* **74**, 823 (2002)
- [95] N.R. Werthammer, E. Helfand, and P.C. Hohenberg, *Phys. Rev.* **147**, 295 (1966).
- [96] T. Siegrist, H.W. Zandbergen, R.J. Cava, J.J. Krajewski, W.F. Peck Jr., *Nature (London)* **367**, 254 (1994); T. Siegrist, R.J. Cava, J.J. Krajewski, W.F. Peck Jr., *J. Alloys and Compounds* **216**, 135 (1994)
- [97] D. Singh and W. Pickett, *Phys. Rev. B* **51**, 8668 (1995)

- [98] H. Michor, G. Hilscher, R. Krendelsberger, P. Rogl, and F. Bouré, *Phys. Rev. B* **58**, 15045 (1998)
- [99] H. Michor, R. Krendelsberger, G. Hilscher, E. Bauer, C. Dusek, R. Hauser, L. Naber, D. Werner, P. Rogl, and H.W. Zandbergen, *Phys. Rev. B* **54**, 9408 (1996)
- [100] R. Podloucky and D. Reith, Private communication with Tahir Ali, 2010, see also [22]
- [101] T. Ali, C. Rupprecht, R.T. Khan, E. Bauer, G. Hilscher, H. Michor, *J. Phys.: Conf. Series* **200**, 012004 (2010)

Appendix A

Units and summary of equations

A.1 Equations in units used in the numerical calculations

The magnetic field energy h is positive and has the dimension [J] in SI-units:

$$h = \mu |\mathbf{H}| \quad \mu = \frac{g_L}{2} \frac{\hbar |e|}{2mc}. \quad (\text{A.1})$$

For $d = 0$ the dimensionless upper critical field h/Δ_0 , using the zero-field gap

$$\Delta_0 = \pi k_B T_c^{(0)} e^{-\gamma} \quad \gamma \simeq 0.57721, \quad (\text{A.2})$$

as a function of the reduced temperature

$$t = \frac{T}{T_c^{(0)}} \quad (\text{A.3})$$

depends on the dimensionless parameter r_m alone, which is a function of z_m and the tilt angle ϑ

$$r_m = \frac{H_\perp}{z_m H} = \frac{\sin \vartheta}{z_m} \quad z_m = \frac{g_L}{4} \frac{\pi k_B T_c^{(0)}}{m v_F^2}. \quad (\text{A.4})$$

After the substitution $s' = s \pi k_B T$, with the condition $T > 0$ and subsequently setting $s' = s$, the κ_\perp -dependent argument of the exponential function and in the sum of the previous equations (1.34), (1.49-1.52) reads

$$\frac{\hbar v_F^2 \kappa_\perp}{(\pi k_B T)^2} = \frac{2}{t^2} r_m \frac{h}{\Delta_0} e^{-\gamma}. \quad (\text{A.5})$$

In the case of $d > 0$ the additional κ_\parallel -dependent argument appears,

$$\frac{v_F^2 \kappa_\parallel^2 d^2}{(\pi k_B T)^2} = \frac{16}{t^2} s_m^2 \cos^2 \vartheta \left(e^{-\gamma} \frac{h}{\Delta_0} \right)^2, \quad (\text{A.6})$$

with the dimensionless parameter s_m

$$s_m = \frac{m v_F d}{\hbar}. \quad (\text{A.7})$$

A.1.1 Upper critical field at $d = 0$

s -wave symmetry

$$\begin{aligned}
 -\ln(t) &= \int_0^\infty ds \frac{1}{\sinh(s)} \left(1 - \cos\left(\frac{h}{\Delta_0} e^{-\gamma} \frac{s}{t}\right) \right. \\
 &\quad \times \left. e^{-\frac{s^2}{8t^2} r_m \frac{h}{\Delta_0} e^{-\gamma}} \sum_{l=0}^n \frac{(-1)^l n!}{l!^2 (n-l)!} \left(\frac{s^2}{4t^2} r_m \frac{h}{\Delta_0} e^{-\gamma} \right)^l \right)
 \end{aligned} \tag{A.8}$$

d -wave symmetry

Gap-equation:

$$-\ln(t) \Delta_n = \sum_{n'=0}^{\infty} D_{n,n'} \Delta_{n'} \tag{A.9}$$

$$D_{n,n'} = \delta_{n,n'} D_{n,n} + (\delta_{n,n'+4} + \delta_{n+4,n'}) D_{n,n'}^{(4)} \tag{A.10}$$

Diagonal matrix $D_{n,n}$:

$$\begin{aligned}
 D_{n,n} &= \int_0^\infty ds \frac{1}{\sinh(s)} \left(1 - \cos\left(\frac{h}{\Delta_0} e^{-\gamma} \frac{s}{t}\right) \right. \\
 &\quad \times \left. e^{-\frac{s^2}{8t^2} r_m \frac{h}{\Delta_0} e^{-\gamma}} \sum_{l=0}^n \frac{(-1)^l n!}{l!^2 (n-l)!} \left(\frac{s^2}{4t^2} r_m \frac{h}{\Delta_0} e^{-\gamma} \right)^l \right)
 \end{aligned} \tag{A.11}$$

Matrix $D_{n,n'}^{(4)}$:

$$\begin{aligned}
 D_{n,n'}^{(4)} &= -\frac{1}{2} \int_0^\infty ds \frac{1}{\sinh(s)} \cos\left(\frac{h}{\Delta_0} e^{-\gamma} \frac{s}{t}\right) e^{-\frac{s^2}{8t^2} r_m \frac{h}{\Delta_0} e^{-\gamma}} \\
 &\quad \times \sum_{l=0}^{\min(n,n')} \frac{(-1)^l \sqrt{n!n'}}{l!(l+4)!(\min(n,n')-l)!} \left(\frac{s^2}{4t^2} r_m \frac{h}{\Delta_0} e^{-\gamma} \right)^l
 \end{aligned} \tag{A.12}$$

A.1.2 Upper critical field at $d > 0$

s -wave symmetry

$$\begin{aligned}
 -\ln(t) &= \int_0^\infty ds \frac{1}{\sinh(s)} \left(1 - \cos\left(\frac{h}{\Delta_0} e^{-\gamma} \frac{s}{t}\right) e^{-\frac{s^2}{8t^2} \frac{\sin \vartheta}{z_m} \frac{h}{\Delta_0} e^{-\gamma}} \right. \\
 &\quad \times \sum_{l=0}^n \sum_{j=0}^{\infty} \sum_{k=0}^{2j} \left(\frac{s^2}{4t^2} \frac{\sin \vartheta}{z_m} \frac{h}{\Delta_0} e^{-\gamma} \right)^{l+j-k} \frac{(-1)^{l+k}}{k!(2j-k)!(2j+1)}
 \end{aligned}$$

$$\times \left[\frac{s^2}{4t^2} s_m^2 \cos^2 \vartheta \left(\frac{h}{\Delta_0} e^{-\gamma} \right)^2 \right]^j \frac{\sqrt{n!(n+2(j-k))!}}{(n-l)!l!(l+2(j-k))!} \frac{\Delta_{n+2(j-k)}}{\Delta_n} \quad (\text{A.13})$$

Condition: $l + 2(j - k) \geq 0$

d-wave symmetry

Gap-equation: See (2.57-2.59).

Matrix $D_{n,n+2(j-k),j,k}$:

$$\begin{aligned} D_{n,n+2(j-k),j,k} &= - \sum_{l=0}^n \int_0^\infty ds \frac{\cos\left(\frac{h}{\Delta_0} e^{-\gamma} \frac{s}{t}\right)}{\sinh(s)} e^{-\frac{s^2}{8t^2} \frac{\sin \vartheta}{z_m} \frac{h}{\Delta_0} e^{-\gamma}} \left(\frac{s^2}{4t^2} \frac{\sin \vartheta}{z_m} \frac{h}{\Delta_0} e^{-\gamma} \right)^{l+j-k} \\ &\times \frac{(-1)^{l+k}}{k!(2j-k)!(2j+1)} \left[\frac{s^2}{4t^2} s_m^2 \cos^2 \vartheta \left(\frac{h}{\Delta_0} e^{-\gamma} \right)^2 \right]^j \\ &\times \frac{\sqrt{n!(n+2(j-k))!}}{(n-l)!l!(l+2(j-k))!} \end{aligned} \quad (\text{A.14})$$

Matrices $D_{n,n',j,k}^{(4,i)}$:

$$\begin{aligned} D_{n,n+2(j-k)+4,j,k}^{(4,1)} &= -\frac{1}{2} \sum_{l=0}^n \int_0^\infty ds \frac{\cos\left(\frac{h}{\Delta_0} e^{-\gamma} \frac{s}{t}\right)}{\sinh(s)} e^{-\frac{s^2}{8t^2} \frac{\sin \vartheta}{z_m} \frac{h}{\Delta_0} e^{-\gamma}} \frac{(-1)^{l+k}}{k!(2j-k)!(2j+1)} \\ &\times \left[\frac{s^2}{4t^2} s_m^2 \cos^2 \vartheta \left(\frac{h}{\Delta_0} e^{-\gamma} \right)^2 \right]^j \frac{1}{l!(l+2(j-k)+4)!} \\ &\times \left(\frac{s^2}{4t^2} \frac{\sin \vartheta}{z_m} \frac{h}{\Delta_0} e^{-\gamma} \right)^{l+j-k+2} \frac{\sqrt{n!(n+2(j-k)+4)!}}{(n-l)!} \\ D_{n,n+2(j-k)-4,j,k}^{(4,2)} &= -\frac{1}{2} \sum_{l=0}^n \int_0^\infty ds \frac{\cos\left(\frac{h}{\Delta_0} e^{-\gamma} \frac{s}{t}\right)}{\sinh(s)} e^{-\frac{s^2}{8t^2} \frac{\sin \vartheta}{z_m} \frac{h}{\Delta_0} e^{-\gamma}} \\ &\times \frac{(-1)^{l+k}}{k!(2j-k)!(2j+1)} \left[\frac{s^2}{4t^2} s_m^2 \cos^2 \vartheta \left(\frac{h}{\Delta_0} e^{-\gamma} \right)^2 \right]^j \\ &\times \frac{1}{l!(l+2(j-k)-4)!} \left(\frac{s^2}{4t^2} \frac{\sin \vartheta}{z_m} \frac{h}{\Delta_0} e^{-\gamma} \right)^{l+j-k-2} \\ &\times \frac{\sqrt{n!(n+2(j-k)-4)!}}{(n-l)!} \end{aligned} \quad (\text{A.15})$$

Conditions: $l + 2(j - k) \pm 4 \geq 0$ (A.15) and $l + 2(j - k) \geq 0$ (A.14)

A.2 Equations in Eilenberger units

The equations are now transformed using Eilenberger units, with the relations for the space coordinates

$$\mathbf{r} = R_0 \mathbf{r}^\diamond \quad R_0 = \frac{\hbar v_F}{2\pi k_B T_c^{(0)}}, \quad (\text{A.16})$$

the magnetic field strength

$$\mathbf{H} = H_0 \mathbf{H}^\diamond \quad H_0 = \frac{\hbar c}{2|e|R_0^2}, \quad (\text{A.17})$$

the vector potential

$$\mathbf{A} = A_0 \mathbf{A}^\diamond \quad A_0 = H_0 R_0, \quad (\text{A.18})$$

the gapfunction

$$\Delta = \pi k_B T_c^{(0)} \Delta^\diamond, \quad (\text{A.19})$$

the Matsubara frequencies

$$\omega_l = \pi k_B T_c \omega_l^\diamond \quad \omega_l^\diamond = t(2l + 1), \quad (\text{A.20})$$

the magnetic moment

$$\mu = \mu_0 \mu^\diamond \quad \mu_0 = \frac{\pi k_B T_c}{H_0}, \quad (\text{A.21})$$

with the dimensionless magnetic moment of the electron

$$\mu^\diamond = \frac{\pi k_B T_c^{(0)}}{m v_F^2}. \quad (\text{A.22})$$

and the free energy

$$F = F^\diamond (\pi k_B T_c)^2 N(E_F) R_0^3. \quad (\text{A.23})$$

After the substitution $s' = s\pi k_B T$, with the condition $T > 0$ and subsequently setting $s' = s$, the κ_\perp -dependent argument of the exponential function and in the sum of the previous equations (1.34), (1.49-1.52) is given by

$$\frac{\hbar v_F^2 \kappa_\perp}{(\pi k_B T)^2} = \frac{4}{t^2} H_\perp^\diamond = \frac{4}{t^2} \mu^\diamond H^\diamond \frac{\sin \vartheta}{\mu^\diamond} = \frac{2}{t^2} \mu^\diamond H^\diamond r_m, \quad (\text{A.24})$$

with

$$2 \frac{\sin \vartheta}{\mu^\diamond} = r_m \quad \frac{\mu^\diamond}{2} = z_m. \quad (\text{A.25})$$

In general the relation between the Eilenberger dimensionless magnetic field $\mu^\diamond H^\diamond$ and the dimensionless field obtained in the numerical calculations h/Δ_0 is

$$\mu^\diamond H^\diamond = \frac{h}{\Delta_0} e^{-\gamma}. \quad (\text{A.26})$$

In the case of $d > 0$ we have

$$\frac{v_F^2 \kappa_{\parallel}^2 d^2}{(\pi k_B T)^2} = \frac{4}{t^2} d^{\diamond 2} \cos^2 \vartheta H^{\diamond 2} = \frac{16}{t^2} s_m^2 \cos^2 \vartheta (\mu^{\diamond} H^{\diamond})^2, \quad (\text{A.27})$$

with

$$\frac{1}{2} \frac{d^{\diamond}}{\mu^{\diamond}} = s_m. \quad (\text{A.28})$$

A.2.1 Upper critical field at $d = 0$

s-wave symmetry

$$\begin{aligned} -\ln(t) &= \int_0^{\infty} ds \frac{1}{\sinh(s)} \left(1 - \cos\left(\mu^{\diamond} H^{\diamond} \frac{s}{t}\right) \right. \\ &\quad \times \left. e^{-\frac{s^2}{4t^2} H^{\diamond} \sin \vartheta} \sum_{l=0}^n \frac{(-1)^l n!}{l!^2 (n-l)!} \left(\frac{s^2}{2t^2} H^{\diamond} \sin \vartheta \right)^l \right) \\ &= \int_0^{\infty} ds \frac{1}{\sinh(s)} \left(1 - \cos\left(\mu^{\diamond} H^{\diamond} \frac{s}{t}\right) \right. \\ &\quad \times \left. e^{-\frac{s^2}{8t^2} \mu^{\diamond} H^{\diamond} r_m} \sum_{l=0}^n \frac{(-1)^l n!}{l!^2 (n-l)!} \left(\frac{s^2}{4t^2} \mu^{\diamond} H^{\diamond} r_m \right)^l \right) \end{aligned} \quad (\text{A.29})$$

d-wave symmetry

Gap-equation:

$$-\ln(t) \Delta_n^{\diamond} = \sum_{n'=0}^{\infty} D_{n,n'}^{\diamond} \Delta_{n'}^{\diamond} \quad (\text{A.30})$$

$$D_{n,n'}^{\diamond} = \delta_{n,n'} D_{n,n}^{\diamond} + (\delta_{n,n'+4} + \delta_{n+4,n'}) D_{n,n'}^{\diamond(4)} \quad (\text{A.31})$$

Diagonal matrix $D_{n,n}^{\diamond}$:

$$\begin{aligned} D_{n,n}^{\diamond} &= \int_0^{\infty} ds \frac{1}{\sinh(s)} \left(1 - \cos\left(\mu^{\diamond} H^{\diamond} \frac{s}{t}\right) \right. \\ &\quad \times \left. e^{-\frac{s^2}{4t^2} H^{\diamond} \sin \vartheta} \sum_{l=0}^n \frac{(-1)^l n!}{l!^2 (n-l)!} \left(\frac{s^2}{2t^2} H^{\diamond} \sin \vartheta \right)^l \right) \\ &= \int_0^{\infty} ds \frac{1}{\sinh(s)} \left(1 - \cos\left(\mu^{\diamond} H^{\diamond} \frac{s}{t}\right) \right. \\ &\quad \times \left. e^{-\frac{s^2}{8t^2} \mu^{\diamond} H^{\diamond} r_m} \sum_{l=0}^n \frac{(-1)^l n!}{l!^2 (n-l)!} \left(\frac{s^2}{4t^2} \mu^{\diamond} H^{\diamond} r_m \right)^l \right) \end{aligned} \quad (\text{A.32})$$

Matrix $D_{n,n'}^{\diamond(4)}$:

$$\begin{aligned}
D_{n,n'}^{\diamond(4)} &= -\frac{1}{2} \int_0^\infty ds \frac{1}{\sinh(s)} \cos\left(\mu^\diamond H^\diamond \frac{s}{t}\right) e^{-\frac{s^2}{4t^2} H^\diamond \sin \vartheta} \\
&\times \sum_{l=0}^{\min(n,n')} \frac{(-1)^l \sqrt{n!n'}}{l!(l+4)!(\min(n,n')-l)!} \left(\frac{s^2}{2t^2} H^\diamond \sin \vartheta\right)^l \\
&= -\frac{1}{2} \int_0^\infty ds \frac{1}{\sinh(s)} \cos\left(\mu^\diamond H^\diamond \frac{s}{t}\right) e^{-\frac{s^2}{8t^2} \mu^\diamond H^\diamond r_m} \\
&\times \sum_{l=0}^{\min(n,n')} \frac{(-1)^l \sqrt{n!n'}}{l!(l+4)!(\min(n,n')-l)!} \left(\frac{s^2}{4t^2} \mu^\diamond H^\diamond r_m\right)^l \quad (\text{A.33})
\end{aligned}$$

A.2.2 Upper critical field at $d > 0$

s-wave symmetry

$$\begin{aligned}
-\ln(t) &= \int_0^\infty ds \frac{1}{\sinh(s)} \left(1 - \cos\left(\mu^\diamond H^\diamond \frac{s}{t}\right) e^{-\frac{s^2}{4t^2} H^\diamond \sin \vartheta}\right) \\
&\times \sum_{l=0}^n \sum_{j=0}^\infty \sum_{k=0}^{2j} \left(\frac{s^2}{2t^2} H^\diamond \sin \vartheta\right)^{l+j-k} \frac{(-1)^{l+j}}{k!(2j-k)!(2j+1)} \\
&\times \left[\frac{s^2}{16t^2} d^{\diamond 2} \cos^2 \vartheta H^{\diamond 2}\right]^j \frac{\sqrt{n!(n+2(j-k))!}}{(n-l)!l!(l+2(j-k))!} \frac{\Delta_{n+2(j-k)}}{\Delta_n} \\
&= \int_0^\infty ds \frac{1}{\sinh(s)} \left(1 - \cos\left(\mu^\diamond H^\diamond \frac{s}{t}\right) e^{-\frac{s^2}{8t^2} \frac{\sin \vartheta}{z_m} \mu^\diamond H^\diamond}\right) \\
&\times \sum_{l=0}^n \sum_{j=0}^\infty \sum_{k=0}^{2j} \left(\frac{s^2}{4t^2} \frac{\sin \vartheta}{z_m} \mu^\diamond H^\diamond\right)^{l+j-k} \frac{(-1)^{l+j}}{k!(2j-k)!(2j+1)} \\
&\times \left[\frac{s^2}{4t^2} s_m^2 \cos^2 \vartheta (\mu^\diamond H^\diamond)^2\right]^j \frac{\sqrt{n!(n+2(j-k))!}}{(n-l)!l!(l+2(j-k))!} \frac{\Delta_{n+2(j-k)}}{\Delta_n} \quad (\text{A.34})
\end{aligned}$$

Condition: $l + 2(j - k) \geq 0$

d-wave symmetry

Gap-equation: See (2.57-2.59).

Matrix $D_{n,n+2(j-k),j,k}$:

$$D_{n,n+2(j-k),j,k} = -\sum_{l=0}^n \int_0^\infty ds \frac{\cos\left(\mu^\diamond H^\diamond \frac{s}{t}\right)}{\sinh(s)} e^{-\frac{s^2}{4t^2} H^\diamond \sin \vartheta} \left(\frac{s^2}{2t^2} H^\diamond \sin \vartheta\right)^{l+j-k}$$

$$\begin{aligned}
& \times \frac{(-1)^{l+k}}{k!(2j-k)!(2j+1)} \left[\frac{s^2}{16t^2} d^{\circ 2} \cos^2 \vartheta H^{\circ 2} \right]^j \frac{\sqrt{n!(n+2(j-k))!}}{(n-l)!l!(l+2(j-k))!} \\
& = - \sum_{l=0}^n \int_0^\infty ds \frac{\cos\left(\mu^\diamond H^\diamond \frac{s}{t}\right)}{\sinh(s)} e^{-\frac{s^2}{8t^2} \frac{\sin \vartheta}{z_m} \mu^\diamond H^\diamond} \left(\frac{s^2}{4t^2} \frac{\sin \vartheta}{z_m} \mu^\diamond H^\diamond \right)^{l+j-k} \\
& \times \frac{(-1)^{l+k}}{k!(2j-k)!(2j+1)} \left[\frac{s^2}{4t^2} s_m^2 \cos^2 \vartheta (\mu^\diamond H^\diamond)^2 \right]^j \frac{\sqrt{n!(n+2(j-k))!}}{(n-l)!l!(l+2(j-k))!}
\end{aligned} \tag{A.35}$$

Matrices $D_{n,n',j,k}^{(4,i)}$:

$$\begin{aligned}
D_{n,n+2(j-k)+4,j,k}^{(4,1)} & = -\frac{1}{2} \sum_{l=0}^n \int_0^\infty ds \frac{\cos\left(\mu^\diamond H^\diamond \frac{s}{t}\right)}{\sinh(s)} e^{-\frac{s^2}{4t^2} H^\diamond \sin \vartheta} \frac{(-1)^{l+k}}{k!(2j-k)!(2j+1)} \\
& \times \left[\frac{s^2}{16t^2} d^{\circ 2} \cos^2 \vartheta H^{\circ 2} \right]^j \frac{1}{l!(l+2(j-k)+4)!} \left(\frac{s^2}{2t^2} H^\diamond \sin \vartheta \right)^{l+j-k+2} \\
& \times \frac{\sqrt{n!(n+2(j-k)+4)!}}{(n-l)!} \\
& = -\frac{1}{2} \sum_{l=0}^n \int_0^\infty ds \frac{\cos\left(\mu^\diamond H^\diamond \frac{s}{t}\right)}{\sinh(s)} e^{-\frac{s^2}{8t^2} \frac{\sin \vartheta}{z_m} \mu^\diamond H^\diamond} \frac{(-1)^{l+k}}{k!(2j-k)!(2j+1)} \\
& \times \left[\frac{s^2}{4t^2} s_m^2 \cos^2 \vartheta (\mu^\diamond H^\diamond)^2 \right]^j \frac{1}{l!(l+2(j-k)+4)!} \\
& \times \left(\frac{s^2}{4t^2} \frac{\sin \vartheta}{z_m} \mu^\diamond H^\diamond \right)^{l+j-k+2} \frac{\sqrt{n!(n+2(j-k)+4)!}}{(n-l)!} \\
D_{n,n+2(j-k)-4,j,k}^{(4,2)} & = -\frac{1}{2} \sum_{l=0}^n \int_0^\infty ds \frac{\cos\left(\mu^\diamond H^\diamond \frac{s}{t}\right)}{\sinh(s)} e^{-\frac{s^2}{4t^2} H^\diamond \sin \vartheta} \\
& \times \frac{(-1)^{l+k}}{k!(2j-k)!(2j+1)} \left[\frac{s^2}{16t^2} d^{\circ 2} \cos^2 \vartheta H^{\circ 2} \right]^j \frac{1}{l!(l+2(j-k)-4)!} \\
& \times \left(\frac{s^2}{2t^2} H^\diamond \sin \vartheta \right)^{l+j-k-2} \frac{\sqrt{n!(n+2(j-k)-4)!}}{(n-l)!} \\
& = -\frac{1}{2} \sum_{l=0}^n \int_0^\infty ds \frac{\cos\left(\mu^\diamond H^\diamond \frac{s}{t}\right)}{\sinh(s)} e^{-\frac{s^2}{8t^2} \frac{\sin \vartheta}{z_m} \mu^\diamond H^\diamond} \\
& \times \frac{(-1)^{l+k}}{k!(2j-k)!(2j+1)} \left[\frac{s^2}{4t^2} s_m^2 \cos^2 \vartheta (\mu^\diamond H^\diamond)^2 \right]^j \frac{1}{l!(l+2(j-k)-4)!} \\
& \times \left(\frac{s^2}{4t^2} \frac{\sin \vartheta}{z_m} \mu^\diamond H^\diamond \right)^{l+j-k-2} \frac{\sqrt{n!(n+2(j-k)-4)!}}{(n-l)!}
\end{aligned} \tag{A.36}$$

Conditions: $l+2(j-k) \pm 4 \geq 0$ (A.36) and $l+2(j-k) \geq 0$ (A.35)

Appendix B

Detailed calculations to chapter 2

B.1 A different way to calculate $f_{(+)}(\mathbf{r})$

In this section it is shown that the solution for the Green's function $f_{(+)}(\mathbf{r})$ (2.25) for $\hat{k}_z = 0$ is also obtained by first carrying out the z_1 -integration in the limits between $\pm d/2$, instead of the p -integration in eq. (2.19) leading to the condition (2.20). For simplicity, and as it is not important in these calculations, \hbar was set to 1.

In order to calculate the integral

$$\begin{aligned}
 f_{(+)}(\mathbf{r}) &= \int_0^\infty ds e^{-s\omega_a} \int_{-\infty}^\infty d^2 r_1 \int_{-d/2}^{d/2} dz_1 e^{-\frac{i}{2} \frac{2|e|}{c} [(\hat{\mathbf{k}}\mathbf{r})((\mathbf{H} \times \mathbf{r})\hat{\mathbf{k}}) - (\hat{\mathbf{k}}\mathbf{r}_1)((\mathbf{H} \times \mathbf{r}_1)\hat{\mathbf{k}})]} \\
 &\times e^{-\frac{i}{2} [(\kappa_{\parallel} z - \kappa_{\perp} y)x] - (\kappa_{\parallel} z_1 - \kappa_{\perp} y_1)x_1} \int \frac{d^3 p}{(2\pi)^3} e^{i\mathbf{p}(\mathbf{r} - \mathbf{r}_1 - \mathbf{v}_{\mathbf{F}} \text{sgn}\omega_l \frac{s}{2})} \Delta(\mathbf{r}_1),
 \end{aligned} \tag{B.1}$$

the terms containing z_1 are separated from the rest:

$$\begin{aligned}
 \frac{2|e|}{c}(\hat{\mathbf{k}}\mathbf{r}_1)(\mathbf{H} \times \mathbf{r}_1)\hat{\mathbf{k}} &= z_1[\kappa_{\parallel}(x_1\hat{k}_x^2 + y_1\hat{k}_x\hat{k}_y)] \\
 &+ \kappa_{\perp}[(x_1^2 - y_1^2)\hat{k}_x\hat{k}_y + x_1y_1(\hat{k}_x^2 - \hat{k}_y^2)]
 \end{aligned} \tag{B.2}$$

and

$$\begin{aligned}
 &\frac{2|e|}{c}(\hat{\mathbf{k}}\mathbf{r}_1)(\mathbf{H} \times \mathbf{r}_1)\hat{\mathbf{k}} + (\kappa_{\parallel} z_1 - \kappa_{\perp} y_1)x_1 \\
 &= z_1[\kappa_{\parallel}(x_1(\hat{k}_x^2 + 1) + y_1\hat{k}_x\hat{k}_y)] + \kappa_{\perp}[(x_1^2 - y_1^2)\hat{k}_x\hat{k}_y - 2x_1y_1\hat{k}_y^2]
 \end{aligned} \tag{B.3}$$

give the integral over z_1

$$\int_{-d/2}^{d/2} dz_1 e^{\frac{i}{2} z_1 [\kappa_{\parallel}(x_1(\hat{k}_x^2 + 1) + y_1\hat{k}_x\hat{k}_y) - p_z]}$$

$$= \frac{1}{i(B(x_1, y_1) - p_z)} \left(e^{i\frac{d}{2}(B(x_1, y_1) - p_z)} - e^{-i\frac{d}{2}(B(x_1, y_1) - p_z)} \right), \quad (\text{B.4})$$

with

$$B(x_1, y_1) = \frac{1}{2}\kappa_{\parallel} [x_1(\hat{k}_x^2 + 1) + y_1\hat{k}_x\hat{k}_y]. \quad (\text{B.5})$$

Now the p -integration is carried out, yielding δ -functions

$$\begin{aligned} & \int \frac{d^2p}{(2\pi)^2} e^{ip_x(x-x_1-v_F\frac{s}{2}\text{sgn}\omega_l\hat{k}_x)+ip_y(y-y_1-v_F\frac{s}{2}\text{sgn}\omega_l\hat{k}_y)} \\ &= \delta\left(x-x_1-v_F\frac{s}{2}\text{sgn}\omega_l\hat{k}_x\right) \delta\left(y-y_1-v_F\frac{s}{2}\text{sgn}\omega_l\hat{k}_y\right), \end{aligned} \quad (\text{B.6})$$

leading to

$$\begin{aligned} & \kappa_{\perp} \left(\left[\left(x - v_F\frac{s}{2}\text{sgn}\omega_l\hat{k}_x \right)^2 - \left(y - v_F\frac{s}{2}\text{sgn}\omega_l\hat{k}_y \right)^2 \right] \hat{k}_x\hat{k}_y + \right. \\ & \quad \left. \left(x - v_F\frac{s}{2}\text{sgn}\omega_l\hat{k}_x \right) \left(y - v_F\frac{s}{2}\text{sgn}\omega_l\hat{k}_y \right) (\hat{k}_x^2 - \hat{k}_y^2) \right) - \\ & \quad \kappa_{\perp} \left((x^2 - y^2)\hat{k}_x\hat{k}_y + xy(\hat{k}_x^2 - \hat{k}_y^2) \right) \\ &= \kappa_{\perp} \left(v_F s \text{sgn}\omega_l y \hat{k}_x - v_F^2 \frac{s^2}{4} \hat{k}_x\hat{k}_y \right) \end{aligned} \quad (\text{B.7})$$

for the contributions with κ_{\perp} . With the function

$$A(x, y) = B\left(x - v_F\frac{s}{2}\text{sgn}\omega_l\hat{k}_x, y - v_F\frac{s}{2}\text{sgn}\omega_l\hat{k}_y\right), \quad (\text{B.8})$$

the p_z integration is given by

$$\begin{aligned} & \int_{-\infty}^{\infty} \frac{dp_z}{2\pi} e^{ip_z z} \frac{1}{i(A(x, y) - p_z)} \left(e^{i\frac{d}{2}(A(x, y) - p_z)} - e^{-i\frac{d}{2}(A(x, y) - p_z)} \right) = \\ & e^{iA(x, y)z} \int_{-\infty}^{\infty} \frac{dp_z}{2\pi} \frac{1}{i(A(x, y) - p_z)} \left(e^{i(A(x, y) - p_z)(\frac{d}{2} - z)} - e^{-(A(x, y) - p_z)(\frac{d}{2} + z)} \right) = \\ & e^{iA(x, y)z} \int_{-\infty}^{\infty} \frac{d\bar{p}_z}{2\pi} \frac{1}{i\bar{p}_z} \left(e^{i\bar{p}_z(\frac{d}{2} - z)} - e^{-\bar{p}_z(\frac{d}{2} + z)} \right). \end{aligned} \quad (\text{B.9})$$

If $A(x, y) - p_z$ is substituted by \bar{p}_z , one can see with the definition of the Theta-function

$$\Theta(x) = \lim_{\epsilon \rightarrow 0} \int_{-\infty}^{\infty} \frac{d\tau}{2\pi i} \frac{1}{\tau + i\epsilon} e^{i\tau x}, \quad (\text{B.10})$$

that eq. (B.9) gives the solution

$$e^{iA(x, y)z} \int_{-\infty}^{\infty} \frac{d\bar{p}_z}{2\pi} \frac{1}{i\bar{p}_z} \left(e^{i\bar{p}_z(\frac{d}{2} - z)} - e^{-\bar{p}_z(\frac{d}{2} + z)} \right) = e^{iA(x, y)z} \left(\Theta\left(\frac{d}{2} - z\right) + \Theta\left(\frac{d}{2} + z\right) \right). \quad (\text{B.11})$$

Summing up the other terms with κ_{\parallel}

$$\begin{aligned} A(x, y)z - z\kappa_{\parallel} \left[x(\hat{k}_x^2 + 1) + y\hat{k}_x\hat{k}_y \right] = \\ z\kappa_{\parallel} \left[\left(x - v_F \frac{s}{2} \text{sgn}\omega_l \hat{k}_x \right) (\hat{k}_x^2 + 1) + \left(y - v_F \frac{s}{2} \text{sgn}\omega_l \hat{k}_y \right) \hat{k}_x\hat{k}_y \right] - \\ z\kappa_{\parallel} \left[x(\hat{k}_x^2 + 1) + y\hat{k}_x\hat{k}_y \right] = \\ -v_F s \text{sgn}\omega_l z\kappa_{\parallel} \hat{k}_x, \end{aligned} \quad (\text{B.12})$$

we obtain

$$f_{(+)}(\mathbf{r}) = \int_0^{\infty} ds e^{-s\omega_a} e^{-\frac{i}{2} [\text{sgn}\omega_l s v_F (\kappa_{\parallel} z - \kappa_{\perp} y) \hat{k}_x + \frac{s^2}{4} v_F^2 \kappa_{\perp} \hat{k}_y \hat{k}_x]} \Delta \left(\mathbf{r} - \text{sgn}\omega_l \frac{s}{2} \mathbf{v}_F \right), \quad (\text{B.13})$$

which corresponds to eq. (2.25) with $\hat{k}_z = 0$.

B.2 Periodicity in the p_z -direction

If the p_z -component is periodic with a period $2\pi/d$

$$\mathbf{p} = \begin{pmatrix} p_x \\ p_y \\ \frac{2\pi}{d}m \end{pmatrix} = \begin{pmatrix} p_x \\ p_y \\ 0 \end{pmatrix} + \begin{pmatrix} 0 \\ 0 \\ \frac{2\pi}{d}m \end{pmatrix} = \mathbf{p}^{(2)} + \frac{2\pi}{d}m \hat{e}_z, \quad (\text{B.14})$$

with the whole number $m = 0, \pm 1, \pm 2 \dots$, the integration transforms into

$$\int \frac{d^3p}{(2\pi)^3} \rightarrow \int \frac{d^2p}{(2\pi)^2} \sum_{m=-\infty}^{\infty}. \quad (\text{B.15})$$

First, it must be shown that eq. (2.5) still applies:

$$\begin{aligned} F(\mathbf{r}) &= \int d^3r_1 \delta(\mathbf{r} - \mathbf{r}_1) F(\mathbf{r}_1) \\ &= \sum_m \int \frac{d^2p}{(2\pi)^2} \int d^3r_1 f_{\mathbf{k}, \mathbf{p}^{(2)}, m}^*(\mathbf{r}_1) f_{\mathbf{k}, \mathbf{p}^{(2)}, m}(\mathbf{r}) F(\mathbf{r}_1). \end{aligned} \quad (\text{B.16})$$

The p -integration is evaluated first, which gives

$$\int \frac{d^2p}{(2\pi)^2} e^{i\mathbf{p}^{(2)}(\mathbf{r}^{(2)} - \mathbf{r}_1^{(2)})} \sum_m e^{i\frac{2\pi}{d}m(z - z_1)} = \delta(x - x_1) \delta(y - y_1) \sum_m e^{i\frac{2\pi}{d}m(z - z_1)}. \quad (\text{B.17})$$

According to the Sturm-Liouville expansion theorem for finite intervals (a,b) the function $\delta(x - \xi)$ can be expanded into

$$\delta(x - \xi) = \frac{2}{b - a} \sum_m e^{i\frac{2\pi m}{b-a}(x - \xi)}, \quad (\text{B.18})$$

if the relations $x \geq a$ and $\xi \leq b$ are valid. Hence, if x is renamed to z , ξ to z_1 , $b = d/2$, and $a = -d/2$, z_1 is indeed smaller than or equals to $d/2$, as well as z is greater than or equals to $-d/2$. Eq. (B.17) gives

$$\frac{d}{2} \delta(x - x_1) \delta(y - y_1) \delta(z - z_1). \quad (\text{B.19})$$

Further on, the eigenfunctions $f_{\hat{\mathbf{k}}, \mathbf{p}}^{(2), m}(\mathbf{r})$ are normalized with $\sqrt{\frac{2}{d}}$ and it can be easily shown, that eq. (B.16) is fulfilled.

The p -integration/summation corresponding to eq. (2.19) is

$$\begin{aligned} & \int \frac{d^2 p}{(2\pi)^2} e^{i\mathbf{p}^{(2)}(\mathbf{r}^{(2)} - \mathbf{r}_1^{(2)} - \mathbf{v}_F^{(2)} \frac{s}{2})} \frac{2}{d} \sum_m e^{i\frac{2\pi}{d} m(z - z_1 - v_F \hat{k}_z \text{sgn}\omega_l \frac{s}{2})} \\ &= \delta\left(\mathbf{r}^{(2)} - \mathbf{r}_1^{(2)} - \mathbf{v}_F^{(2)} \text{sgn}\omega_l \frac{s}{2}\right) \delta\left(z - z_1 - v_F \hat{k}_z \text{sgn}\omega_l \frac{s}{2}\right) \\ &= \delta\left(\mathbf{r} - \mathbf{r}_1 - \mathbf{v}_F \text{sgn}\omega_l \frac{s}{2}\right), \end{aligned} \quad (\text{B.20})$$

giving the same result as with a continuous p_z -component as the restriction (2.20) applies. The same equations and conditions (2.20-2.25) for the Green's function $f_{(+)}(\mathbf{r})$ apply after the calculation of this integral.

B.3 Critical field for $\kappa_\perp \rightarrow 0$

To further simplify eq. (2.72), it is transformed by using the representation of the zeta function as the series

$$\zeta(x) = \sum_{n=1}^{\infty} \frac{1}{n^x}, \quad (\text{B.21})$$

and with the relations

$$\frac{1}{2m+1} = \frac{\left(\frac{1}{2}\right)_m}{\left(\frac{3}{2}\right)_m}, \quad (\text{B.22})$$

where $(a)_m$ is defined as

$$\begin{array}{ccccccccc} m & = & 0 & 1 & 2 & 3 & 4 & \dots \\ (a)_m & = & 1 & a & a(a+1) & a(a+1)(a+2) & a(a+1)(a+2)(a+3) & \dots \end{array},$$

and

$$\frac{(2m)!}{2^m m!} = \frac{1}{\sqrt{\pi}} \Gamma\left(m + \frac{1}{2}\right) = \left(\frac{1}{2}\right)_m, \quad (\text{B.23})$$

we obtain for eq. (2.72) with $x = \frac{1}{4\pi T} v_F \kappa_\parallel d$

$$-\ln\left(\frac{T}{T_c^{(0)}}\right) = \sum_{n=1}^{\infty} \frac{1}{n} \sum_{m=1}^{\infty} (-1)^{m+1} \frac{\left(\frac{1}{2}\right)_m \left(\frac{1}{2}\right)_m}{\left(\frac{3}{2}\right)_m} \left(2 - \frac{1}{2^{2m}}\right) \frac{1}{m!} \left(\frac{x}{n}\right)^{2m}. \quad (\text{B.24})$$

This equation can be transformed with the help of the hypergeometric function ${}_2F_1(a, b; c; z)$, which is defined as

$${}_2F_1(a, b; c; z) = \sum_{m=0}^{\infty} \frac{(a)_m (b)_m}{(c)_m} \frac{z^m}{m!}. \quad (\text{B.25})$$

The sums over m yield

$$2 \sum_{m=1}^{\infty} (-1)^{m+1} \frac{(\frac{1}{2})_m (\frac{1}{2})_m}{(\frac{3}{2})_m} \frac{1}{m!} \left(\frac{x}{n}\right)^{2m} = 2 \left[1 - {}_2F_1 \left(\frac{1}{2}, \frac{1}{2}; \frac{3}{2}; -\frac{x^2}{n^2} \right) \right] \quad (\text{B.26})$$

and

$$\sum_{m=1}^{\infty} (-1)^{m+1} \frac{(\frac{1}{2})_m (\frac{1}{2})_m}{(\frac{3}{2})_m} \frac{1}{m!} \left(\frac{x}{2n}\right)^{2m} = 1 - {}_2F_1 \left(\frac{1}{2}, \frac{1}{2}; \frac{3}{2}; -\frac{x^2}{4n^2} \right), \quad (\text{B.27})$$

giving

$$\begin{aligned} -\ln \left(\frac{T}{T_c^{(0)}} \right) &= \sum_{n=1}^{\infty} \frac{1}{n} \left\{ 1 - \left[{}_2F_1 \left(\frac{1}{2}, \frac{1}{2}; \frac{3}{2}; -\frac{\left(\frac{1}{4\pi T} v_F \kappa_{\parallel} d \right)^2}{n^2} \right) - \right. \right. \\ &\quad \left. \left. {}_2F_1 \left(\frac{1}{2}, \frac{1}{2}; \frac{3}{2}; -\frac{\left(\frac{1}{4\pi T} v_F \kappa_{\parallel} d \right)^2}{4n^2} \right) \right] \right\}. \end{aligned} \quad (\text{B.28})$$

Appendix C

Notes on the equations in Chapter 3

C.1 Ad 2.3.1, Derivation of the gap-equation for $d = 0$

The gap as a function of temperature and external magnetic field (2.89) is obtained from

$$2t \sum_{l=0}^{\infty} \frac{1}{\omega_l} + \ln t = t \sum_{l=0}^{\infty} \left(\frac{1}{\sqrt{|\Delta|^2 + \omega_s^2}} + cc. \right), \quad (C.1)$$

with

$$\omega_s = \omega_l - i\mu H. \quad (C.2)$$

Concentrating on the right side of the equation, the real term

$$\frac{1}{\sqrt{|\Delta|^2 + \omega_s^2}} + cc. = \frac{1}{\sqrt{|\Delta|^2 + \omega_s^2}} + \frac{1}{\sqrt{|\Delta|^2 + \omega_s^{*2}}} \quad (C.3)$$

is simplified by introducing

$$a_l = |\Delta|^2 + \omega_s^2 = \omega_l^2 + |\Delta|^2 - \mu^2 H^2 - i2\omega_l \mu H, \quad (C.4)$$

with the properties

$$a_l^* = |\Delta|^2 + \omega_s^{*2}, \quad (C.5)$$

$$\sqrt{a_l} = |a_l|^{\frac{1}{2}} \left(\cos \frac{\varphi_0}{2} + i \sin \frac{\varphi_0}{2} \right), \quad (C.6)$$

and

$$\sqrt{a_l^*} = |a_l|^{\frac{1}{2}} \left(\cos \frac{\varphi_0}{2} - i \sin \frac{\varphi_0}{2} \right) = (\sqrt{a_l})^*, \quad (C.7)$$

with the angle of a_l in the complex plane

$$\varphi_0 = (\mathbf{p}, i\omega_n)(a_l), \quad (C.8)$$

which gives

$$\varphi_0 = \text{atan} \left(\frac{\text{Im}(a_l)}{\text{Re}(a_l)} \right) \begin{cases} +\pi & \text{Re}(a_l) < 0, \text{Im}(a_l) > 0 \\ -\pi & \text{Re}(a_l) < 0, \text{Im}(a_l) < 0 \end{cases} . \quad (\text{C.9})$$

Eq. (C.1) is then transformed into

$$\ln t = 2t \sum_{l=0}^{\infty} \left(\frac{\text{Re}(\sqrt{a_l})}{|a_l|} - \frac{1}{\omega_l} \right) . \quad (\text{C.10})$$

C.2 Ad 2.3.1, The free-energy equation for $d = 0$

The free energy equation (2.91)

$$\frac{F_s - F_n}{A} = -t \sum_{l=0}^{\infty} \left(\frac{(\omega_s - \sqrt{|\Delta|^2 + \omega_s^2})^2}{\sqrt{|\Delta|^2 + \omega_s^2}} + cc. \right) , \quad (\text{C.11})$$

is transformed by applying eq. (C.4) into

$$\frac{F_s - F_n}{A} = -t \sum_{l=0}^{\infty} \left(\frac{(\omega_s - \sqrt{a_l})^2}{\sqrt{a_l}} + cc. \right) , \quad (\text{C.12})$$

which further gives

$$\begin{aligned} \frac{F_s - F_n}{A} &= -2t \sum_{l=0}^{\infty} \left[\left(\text{Re}(\omega_s)^2 - \text{Im}(\omega_s)^2 \right) \text{Re}(\sqrt{a_l}) + \text{Re}(a_l) \text{Re}(\sqrt{a_l}) \right. \\ &\quad \left. + 2\text{Im}(a_l) \text{Im}(\sqrt{a_l}) - 2\text{Re}(\omega_s) |a_l| \right] \frac{1}{|a_l|} . \end{aligned} \quad (\text{C.13})$$

C.3 Ad 2.3.4, gap equation for $d \geq 0$

We start with the gap equation for $d \geq 0$ given in eq (2.129)

$$2t \sum_{l=0}^{\infty} \frac{1}{\omega_l} + \ln t = t \sum_{l=0}^{\infty} \int_0^{2\pi} \frac{d\varphi}{2\pi} \left(\frac{1}{\sqrt{|\Delta|^2 + A_d(\varphi)^2}} + cc. \right) , \quad (\text{C.14})$$

and investigate the properties of the term

$$A'_d(\varphi) = \frac{1}{A_d(\varphi)} = \frac{1}{B_d(\varphi)} \text{atan} \left(\frac{B_d(\varphi)}{\omega_s} \right) . \quad (\text{C.15})$$

The complex expansion of $\text{atan}(x + iy)$ yields

$$\text{atan}(x + iy) = \frac{1}{2} \left((\mathbf{p}, i\omega_n)(1 + ix - y) - (\mathbf{p}, i\omega_n)(1 - ix + y) \right) + \frac{1}{2} \ln \frac{|1 - ix + y|}{|1 - ix - y|} . \quad (\text{C.16})$$

Therefore, the real and imaginary parts of the complex term $A'_d(\varphi)$ are given by

$$\begin{aligned}\operatorname{Re}(A'_d(\varphi)) &= \frac{1}{2B_d(\varphi)} \left((\mathbf{p}, i\omega_n)(1 + ix - y) - (\mathbf{p}, i\omega_n)(1 - ix + y) \right) \\ \operatorname{Im}(A'_d(\varphi)) &= \frac{1}{2B_d(\varphi)} \ln \frac{\sqrt{(1-y)^2 + x^2}}{\sqrt{(1+y)^2 + x^2}},\end{aligned}\quad (\text{C.17})$$

where

$$\begin{aligned}x &= B_d(\varphi) \frac{\omega_l}{\omega_l^2 + \mu^2 H^2} \\ y &= B_d(\varphi) \frac{\mu H}{\omega_l^2 + \mu^2 H^2}.\end{aligned}\quad (\text{C.18})$$

This results in

$$A_d(\varphi) = \operatorname{Re}(A_d(\varphi)) + i\operatorname{Im}(A_d(\varphi)), \quad (\text{C.19})$$

with

$$\begin{aligned}\operatorname{Re}(A_d(\varphi)) &= \frac{\operatorname{Re}(A'_d(\varphi))}{|A'_d(\varphi)|^2} \\ \operatorname{Im}(A_d(\varphi)) &= -\frac{\operatorname{Im}(A'_d(\varphi))}{|A'_d(\varphi)|^2}.\end{aligned}\quad (\text{C.20})$$

As in section C.1, an expression similar to a_l of eq. (C.4) is introduced

$$\begin{aligned}a_l(\varphi) &= |\Delta|^2 + A_d(\varphi)^2 \\ &= |\Delta|^2 + \operatorname{Re}(A_d(\varphi))^2 - \operatorname{Im}(A_d(\varphi))^2 - i2\operatorname{Re}(A_d(\varphi))\operatorname{Im}(A_d(\varphi)),\end{aligned}\quad (\text{C.21})$$

and the gap function is finally given by

$$\ln t = 2t \sum_{l=0}^{\infty} \int_0^{2\pi} \frac{d\varphi}{2\pi} \left(\frac{\operatorname{Re}(\sqrt{a_l(\varphi)})}{|a_l(\varphi)|} - \frac{1}{\omega_l} \right). \quad (\text{C.22})$$

C.4 Ad 2.3.4, free energy difference for $d \geq 0$

The free energy difference (2.130)

$$\frac{F_s - F_n}{A} = -t \sum_{l=0}^{\infty} \int_0^{2\pi} \frac{d\varphi}{2\pi} \left(\frac{\left(A_d(\varphi) - \sqrt{|\Delta|^2 + A_d(\varphi)^2} \right)^2}{\sqrt{|\Delta|^2 + A_d(\varphi)^2}} + cc. \right), \quad (\text{C.23})$$

is transformed into

$$\begin{aligned}\frac{F_s - F_n}{A} &= -2t \sum_{l=0}^{\infty} \int_0^{2\pi} \frac{d\varphi}{2\pi} \left[\left(\operatorname{Re}(A_d(\varphi))^2 - \operatorname{Im}(A_d(\varphi))^2 \right) \operatorname{Re} \left(\sqrt{a_l(\varphi)} \right) \right. \\ &\quad + \operatorname{Re}(a_l(\varphi)) \operatorname{Re} \left(\sqrt{a_l(\varphi)} \right) + 2\operatorname{Im}(a_l(\varphi)) \operatorname{Im} \left(\sqrt{a_l(\varphi)} \right) \\ &\quad \left. - 2\operatorname{Re}(A_d(\varphi)) |a_l(\varphi)| \right] \frac{1}{|a_l(\varphi)|}\end{aligned}\quad (\text{C.24})$$

by simply replacing ω_s by $A_d(\varphi)$ in eq. (C.13) before integrating over φ .

Appendix D

Eigenfunctions of the Hamiltonian

D.1 Landau gauge

Eigenfunctions of the Hamiltonian with a Landau gauge for the vector potential \mathbf{A} are derived. The magnetic field H lies in the y - z plane and is given by

$$\mathbf{H} = H \begin{pmatrix} 0 \\ \cos \vartheta \\ \sin \vartheta \end{pmatrix} = \begin{pmatrix} 0 \\ H_{\parallel} \\ H_{\perp} \end{pmatrix}. \quad (\text{D.1})$$

The vector potential in the Landau gauge is

$$\mathbf{A} = \begin{pmatrix} H_{\parallel} z - H_{\perp} y \\ 0 \\ 0 \end{pmatrix}, \quad (\text{D.2})$$

which satisfies the equation $\nabla \times \mathbf{A} = \mathbf{H}$, and as we are investigating a z -independent problem, z is set to $z = 0$. The kinetic part of the Hamiltonian is then given by

$$\hat{H} = \frac{1}{2M} \left(\mathbf{p} - \frac{q}{c} \mathbf{A} \right)^2. \quad (\text{D.3})$$

Actually the z -component of the momentum can also be neglected, but for the sake of completeness, it will still be considered in the calculations. We now set

$$\omega_0 = \frac{|q|H_{\perp}}{Mc} = \frac{\kappa_{\perp}}{M} \quad (\text{D.4})$$

and obtain the Hamiltonian

$$\hat{H} = \frac{1}{2M} (\hat{p}_x - M\omega_0 y)^2 + \frac{\hat{p}_y^2}{2M} + \frac{\hat{p}_z^2}{2M}. \quad (\text{D.5})$$

As the operators \hat{p}_x and \hat{p}_y do not commute, we have to look for another set of operators commuting with each other and with \hat{H} . We introduce¹

$$U = \exp \left(\frac{i}{\hbar M \omega_0} \hat{p}_x \hat{p}_y \right) \quad (\text{D.6})$$

¹D. Grau, *Übungsaufgaben zur Quantentheorie*, Carl Hanser Verlag München Wien, 3. Auflage

and obtain

$$UyU^\dagger = y + \frac{1}{\hbar M \omega_0} \hat{p}_x. \quad (\text{D.7})$$

Because of $U\hat{p}_iU^\dagger = \hat{p}_i$, $i = x, y$ we get the transformed Hamiltonian

$$\hat{H}' = U\hat{H}U^\dagger = \frac{1}{2M} (\hat{p}_y^2 + M^2 \omega_0^2 y^2) + \frac{1}{2M} \hat{p}_z^2. \quad (\text{D.8})$$

The self-adjoint operators

$$H_{osc,y} = \frac{1}{2M} (\hat{p}_y^2 + M^2 \omega_0^2 y^2), \quad (\text{D.9})$$

\hat{p}_x , and \hat{p}_z now build a complete set of commuting operators, which also commute with the Hamiltonian \hat{H}' . Thus, the eigenfunction ψ of the Hamiltonian \hat{H}' can now be built from the eigenfunctions of these operators:

$$\psi' = \phi_{osc,y} \phi_{k_x} \phi_{k_z} \quad (\text{D.10})$$

$$\begin{aligned} H_{osc} \psi' &= \hbar \omega_0 \left(n + \frac{1}{2} \right) \psi' \quad n = 0, 1, 2, \dots \quad (\text{Landau levels}) \\ \hat{p}_x \psi' &= k_x \psi' \\ \hat{p}_z \psi' &= k_z \psi', \end{aligned} \quad (\text{D.11})$$

with the normalized and orthogonal eigenfunctions

$$\begin{aligned} \phi_{osc,y} &= \sqrt{\frac{l_0^{-1}}{2^n n! \sqrt{\pi}}} \exp\left(-\frac{y^2}{2l_0^2}\right) H_n\left(\frac{y}{l_0}\right) \quad l_0^{-1} \equiv \sqrt{\frac{M\omega_0}{\hbar}} = \sqrt{\frac{\kappa_\perp}{\hbar}} \\ \phi_{k_x} &= \frac{1}{\sqrt{2\pi\hbar}} \exp\left(\frac{i}{\hbar} k_x x\right) \\ \phi_{k_z} &= \frac{1}{\sqrt{2\pi\hbar}} \exp\left(\frac{i}{\hbar} k_z z\right), \end{aligned} \quad (\text{D.12})$$

where $H_n(x)$ are the common Hermite polynomials and l_0 is the Larmor radius. If the integration in x -direction is restricted to a length L_x , the orthogonality relation is given by

$$(\phi_{k'_x}, \phi_{k_x}) = \frac{1}{L_x} \int_{-L_x/2}^{L_x/2} dx \phi_{k'_x}^* \phi_{k_x} = \frac{1}{L_x} \int_{-L_x/2}^{L_x/2} dx \exp\left(\frac{i}{\hbar} (k_x - k'_x) x\right) = \tilde{\delta}(k'_x - k_x), \quad (\text{D.13})$$

where $\tilde{\delta}$ indicates that the δ -function is not given by an infinite integration over x . In this case the normalization constant for ϕ_{k_x} is $L_x^{-1/2}$ instead of $\frac{1}{\sqrt{2\pi\hbar}}$ as in eq. (D.12). The eigenfunction ψ of the former Hamiltonian, however, is given by

$$\psi = U^{-1} \psi' = \exp\left(-\frac{1}{\hbar M \omega_0} \hat{p}_x \hat{p}_y\right) \psi' = \exp\left(-\frac{i}{\hbar} y_0 \hat{p}_y\right) \psi', \quad (\text{D.14})$$

with

$$y_0 \equiv \frac{k_x}{M \omega_0} = \frac{k_x}{\kappa_\perp}. \quad (\text{D.15})$$

We can write down the eigenfunction (D.14) at once, considering that the operator

$$\exp\left(-\frac{i}{\hbar}y_0\hat{p}_y\right) = \tau_y(y_0) \quad (\text{D.16})$$

is a translational operator

$$\mathbf{r}' = \tau_y(y_0)\mathbf{r} = (x, y - y_0, z), \quad (\text{D.17})$$

finally giving

$$\psi_n = \sqrt{\frac{l_0^{-1}}{2^n n! \sqrt{\pi}}} \exp\left(-\frac{(y - y_0)^2}{2l_0^2}\right) H_n\left(\frac{y - y_0}{l_0}\right) \frac{1}{2\pi\hbar} \exp\left(\frac{i}{\hbar}k_x x\right) \exp\left(\frac{i}{\hbar}k_z z\right). \quad (\text{D.18})$$

As the eigenvalues which constitute Landau levels

$$E_n = \hbar\omega_0\left(n + \frac{1}{2}\right) + \frac{k_z^2}{2M} \quad (\text{D.19})$$

of \hat{H} do not depend on k_x , the eigenfunctions are infinitely degenerate with respect to the continuous eigenvalue k_x .

D.1.1 Quasi-periodic solutions

We now want to construct a quasi-periodic solution in two dimensions, which is periodic up to a phase factor. First, the unit cell in the x - y plane must be defined, with the lattice axes denoted by X and Y , where X coincides with the x -axis. The period in x or X -direction is denoted by a , the angle between the lattice axes X and Y by α , and the period in Y -direction by b . The corresponding coordinates $\mathbf{r} = (x, y)$ for a point $\mathbf{R} = (X, Y)$ in lattice coordinates are given by

$$\begin{aligned} x &= X + Y \cos \alpha \\ y &= Y \sin \alpha. \end{aligned} \quad (\text{D.20})$$

We now transform the continuous eigenvalue k_x in a discrete quantum number, which reflects the periodicity in X -direction,

$$\begin{aligned} k_x &\rightarrow k_l = \frac{2\pi\hbar}{a}l \quad l = 0, \pm 1, \pm 2, \dots \\ y_0 &\rightarrow y_l = \frac{2\pi\hbar}{a\kappa_\perp}l, \end{aligned} \quad (\text{D.21})$$

and the eigenfunctions (D.18) can be written as a linear combination of eigenfunctions belonging to the infinitely degenerate state, giving

$$\psi_n = \sum_{l=-\infty}^{\infty} C_{n,l} \exp\left(\frac{i}{\hbar}k_l x\right) h_n(y - y_l), \quad (\text{D.22})$$

if we consider $z = 0$, and with

$$h_n(x) = \sqrt{\frac{l_0^{-1}}{2^n n! \sqrt{\pi}}} \exp\left(-\frac{x^2}{2l_0^2}\right) H_n\left(\frac{x}{l_0}\right). \quad (\text{D.23})$$

The coefficients $C_{n,l}$ are determined such, that the eigenfunctions fulfill the requirement

$$|\psi_n(X, Y)| = |\psi_n(X, Y + b)|. \quad (\text{D.24})$$

Inserting eqs. (D.20) in (D.22) gives

$$\psi_n(X, Y) = \sum_{l=-\infty}^{\infty} C_{n,l} \exp\left(\frac{i}{\hbar} k_l [X + Y \cos \alpha]\right) h_n\left(\sin \alpha \left(Y - \frac{y_l}{\sin \alpha}\right)\right), \quad (\text{D.25})$$

and transforming Y to $Y + b$

$$\begin{aligned} \psi_n(X, Y + b) = \sum_{l=-\infty}^{\infty} C_{n,l} \exp\left(\frac{i}{\hbar} k_l [X + Y \cos \alpha]\right) \exp\left(\frac{i}{\hbar} k_l b \cos \alpha\right) \times \\ h_n\left(\sin \alpha \left(Y - \left[\frac{y_l}{\sin \alpha} - b\right]\right)\right). \end{aligned} \quad (\text{D.26})$$

As the total flux per unit cell, which is a positive (≥ 0) integer p times the flux quantum ϕ_0 , is given by the area F of the cell times the perpendicular field H_{\perp}

$$F H_{\perp} = ab \sin \alpha H_{\perp} = p \phi_0 = p \frac{hc}{2|e|}, \quad (\text{D.27})$$

we can write for b

$$b = \frac{y_p}{\sin \alpha} = \frac{2\pi \hbar}{a \kappa_{\perp}} p. \quad (\text{D.28})$$

We set $l' = l - p$ in eq. (D.26) and get

$$\begin{aligned} \psi_n(X, Y + b) = \exp\left(\frac{i}{\hbar} k_p [X + Y \cos \alpha]\right) \sum_{l'=-\infty}^{\infty} C_{n,l} \exp\left(\frac{i}{\hbar} k_l b \cos \alpha\right) \times \\ \exp\left(\frac{i}{\hbar} k_{l'} [X + Y \cos \alpha]\right) h_n\left(\sin \alpha \left(Y - \frac{y_{l'}}{\sin \alpha}\right)\right), \end{aligned} \quad (\text{D.29})$$

which fulfills the condition eq. (D.24) if

$$C_{n,l'} = C_{n,l-p} = C_{n,l} \exp\left(\frac{i}{\hbar} k_l b \cos \alpha\right). \quad (\text{D.30})$$

It can be easily shown that from $C_{n,i} | i = 0, \dots, p-1$ all other $C_{n,j}$ can be generated. The complete set of coefficients are given by $\{C_{n,j+mp} | j = 0, \dots, p-1; m = 0, \pm 1, \pm 2, \dots\}$, and $C_{n,j+mp}$ can be generated from $C_{n,j}$ by means of

$$C_{n,j+mp} = \exp\left(i \frac{2\pi b}{a} \cos \alpha \left[-mj - \frac{m(m+1)}{2} p\right]\right) C_{n,j} = g^{-mj - \frac{m(m+1)}{2} p} C_{n,j}, \quad (\text{D.31})$$

which can be constructed from eq. (D.30) by setting $l = j + p$ and by consequently adding p to l up to $l = j + mp$ and recursively setting the $C_{n,j+(m-1)p}$ on the right side to the former coefficients up to the first, $C_{n,j}$:

$$\begin{aligned}
C_{n,l} &= g^{-l} C_{n,l-p} \quad l = j + p \\
C_{n,j+p} &= g^{-j-p} C_{n,j} \\
C_{n,j+2p} &= g^{-j-2p} C_{n,j+p} \\
C_{n,j+3p} &= g^{-j-3p} C_{n,j+2p} \\
&\vdots \\
C_{n,j+mp} &= g^{-j-mp} C_{n,j+(m-1)p} = g^{-j-mp} g^{-j-(m-1)p} C_{n,j+(m-2)p} \\
&= g^{-j-mp} g^{-j-(m-1)p} \dots g^{-j-p} C_{n,j} = g^{-mj - \frac{m(m+1)}{2}p} C_{n,j}.
\end{aligned} \tag{D.32}$$

The same can be done for negative m leading to the same result. Setting $l = j + mp$ in eq. D.25 finally gives

$$\begin{aligned}
\psi_n(X, Y) &= \sum_{j=0}^{p-1} C_{n,j} \exp\left(\frac{i}{\hbar} k_j (X + Y \cos \alpha)\right) \sum_{m=-\infty}^{\infty} \exp\left(\frac{i}{\hbar} k_{mp} (X + Y \cos \alpha)\right) \times \\
&\quad \exp\left(i \frac{2\pi b}{a} \cos \alpha \left[-mj - \frac{m(m+1)}{2}p\right]\right) h_n\left(\sin \alpha \left[Y - b \frac{j}{p} - mb\right]\right).
\end{aligned} \tag{D.33}$$

For the case of one flux quantum per unit cell ($p = 1$) the eigenfunctions

$$\begin{aligned}
\psi_n(X, Y) &= C_{n,0} \sum_{m=-\infty}^{\infty} \exp\left(\frac{i}{\hbar} k_m (X + Y \cos \alpha)\right) \exp\left(i \frac{2\pi b}{a} \cos \alpha \left[-\frac{m(m+1)}{2}\right]\right) \times \\
&\quad h_n(\sin \alpha [Y - mb]).
\end{aligned} \tag{D.34}$$

are obtained.

D.2 Symmetric gauge

In this section two representations of the solution of the Hamilton operator for a symmetric gauge are presented. The *orbit center* representation results from a simple gauge transformation from the Landau gauge, for which the eigenfunctions were obtained in the last chapter. As the resulting eigenfunctions in the orbit center representation do not show the symmetry between the two coordinates x and y explicitly, the solution for the eigenfunctions in the *angular momentum* representation is also shown.

As in eq. (D.1), the magnetic field H lies in the y - z plane. From the magnetic field the vector potential in the symmetric gauge, which is symmetric in x and y , is obtained

$$\mathbf{A} = \begin{pmatrix} H_{\parallel} z - \frac{1}{2} H_{\perp} y \\ \frac{1}{2} H_{\perp} x \\ 0 \end{pmatrix}. \tag{D.35}$$

It satisfies the relation $\nabla \times \mathbf{A} = \mathbf{H}$.

D.2.1 Orbit center representation

It is widely known that a transformation of the kind

$$\mathbf{A}' = \mathbf{A} + \nabla_{\mathbf{r}} f(\mathbf{r}) \quad (\text{D.36})$$

is not of importance for the resulting one-particle eigenfunctions of the Hamiltonian, as it only changes the eigenfunctions ψ by means of a phase factor

$$\psi' = \psi \exp \left(i \frac{q}{\hbar c} f(\mathbf{r}) \right) \quad (\text{D.37})$$

which does not influence, *e.g.* $|\psi|^2$. We now transform the Landau gauge (D.2) into the symmetric one (D.35) with the function

$$f(\mathbf{r}) = \frac{1}{2} H_{\perp} xy \quad (\text{D.38})$$

and obtain

$$\psi' = \psi \exp \left(i \frac{q}{2\hbar c} H_{\perp} xy \right) = \psi \exp \left(-i \frac{\kappa_{\perp}}{2\hbar} xy \right) = \psi \exp \left(-i \frac{xy}{2l_0^2} \right). \quad (\text{D.39})$$

With ψ provided by eq. (D.18) and the change resulting from the gauge transformation (D.39) the eigenfunctions are given by

$$\psi_n = \sqrt{\frac{l_0^{-1}}{2^n n! \sqrt{\pi}}} \exp \left(-\frac{(y - y_0)^2}{2l_0^2} \right) H_n \left(\frac{y - y_0}{l_0} \right) \frac{1}{2\pi\hbar} \exp \left(i \frac{xy_0}{l_0^2} \right) \exp \left(-i \frac{xy}{2l_0^2} \right). \quad (\text{D.40})$$

in the orbit center representation and for $z = 0$.

D.2.2 Angular momentum representation

Eigenfunctions of the Hamiltonian with a symmetric gauge for \mathbf{A} , which explicitly express the symmetry between the coordinates x and y , are calculated by separating the Hamiltonian into three parts: a Hamiltonian for the two dimensional harmonic oscillator, one proportional to the angular Momentum, and the Hamiltonian for a free movement in z -direction.

As we are describing superconductors with two dimensional electronic properties, which means that the system is z -independent, we can simply write $z = 0$ and the Hamiltonian is given by

$$\hat{H} = \frac{1}{2M} \left(\mathbf{p} - \frac{q}{c} \mathbf{A} \right)^2 = \frac{1}{2M} \left[\left(\hat{p}_x + \frac{qH_{\perp}}{2c} y \right)^2 + \left(\hat{p}_y - \frac{qH_{\perp}}{2c} x \right)^2 + \hat{p}_z^2 \right] \quad (\text{D.41})$$

As in the previous section, the z -component of the momentum will still be considered in the calculations. We now introduce $\omega_1 = \omega_0/2$ (see eq. (D.4)) and obtain the Hamiltonian

$$\hat{H} = \frac{1}{2M} (\hat{p}_x^2 + M^2 \omega_1^2 x^2) + \frac{1}{2M} (\hat{p}_y^2 + M^2 \omega_1^2 y^2) + \omega_1 (x \hat{p}_y - y \hat{p}_x) + \frac{\hat{p}_z^2}{2M}, \quad (\text{D.42})$$

which with the angular Momentum in z -direction $\hat{L}_z = x\hat{p}_y - y\hat{p}_x$ can be written as

$$\hat{H} = \hat{H}_{osz}^{2d} + \hat{H}_{\hat{L}_z} + \hat{H}_{\hat{p}_z}. \quad (\text{D.43})$$

If \hat{H}_{osz}^{2d} , \hat{L}_z and \hat{p}_z are all commuting operators, the eigenfunction of the Hamiltonian can be written as

$$\psi = \phi_{osz}^{2d} \phi_{L_z} \phi_{k_z}, \quad (\text{D.44})$$

which satisfies the differential equation

$$\hat{H}\psi = E\psi, \quad (\text{D.45})$$

with

$$E = E_{osz}^{2d} + E_{L_z} + E_{k_z}. \quad (\text{D.46})$$

Calculation of the commutators

As $\hat{L}_z = x\hat{p}_y - y\hat{p}_x$ is z -independent, it is obvious that

$$[\hat{p}_z, \hat{L}_z] = 0, \quad (\text{D.47})$$

and for the same reason we can write

$$[\hat{p}_z, \hat{H}_{osz}^{2d}] = 0. \quad (\text{D.48})$$

The only non-vanishing commutators when calculating $[\hat{L}_z, \hat{H}_{osz}^{2d}]$ are given by

$$[\hat{p}_x, x^2] = \frac{2\hbar}{i}x \quad \text{and} \quad [\hat{p}_y, y^2] = \frac{2\hbar}{i}y, \quad (\text{D.49})$$

which results in

$$[\hat{L}_z, \hat{H}_{osz}^{2d}] = \frac{M\omega_1^2}{2} (-y [\hat{p}_x, x^2] + x [\hat{p}_y, y^2]) = 0, \quad (\text{D.50})$$

meaning that the eigenfunctions can be calculated as proposed above.

Calculation of the eigenfunctions

The eigenfunction of \hat{p}_z can be directly given as

$$\phi_{k_z}(z) = e^{\frac{i}{\hbar}k_z z}, \quad (\text{D.51})$$

with energy-eigenvalues

$$E_{k_z} = \frac{k_z^2}{2M}. \quad (\text{D.52})$$

We now transform the cartesian into polar coordinates

$$\begin{pmatrix} x \\ y \\ z \end{pmatrix} = \begin{pmatrix} r \cos \varphi \\ r \sin \varphi \\ z \end{pmatrix}, \quad (\text{D.53})$$

so that \hat{L}_z is given by

$$\hat{L}_z = \frac{\hbar}{i} \frac{\partial}{\partial \varphi}, \quad (\text{D.54})$$

with orthonormal eigenfunctions

$$\phi_{L_z} = \phi_m(\varphi) = \frac{1}{\sqrt{2\pi}} e^{-im\varphi} \quad m = 0 \pm 1 \pm 2 \dots \quad (\text{D.55})$$

and eigenvalue

$$\hat{L}_z \phi_m(\varphi) = -\hbar m \phi_m(\varphi), \quad (\text{D.56})$$

resulting in the eigenvalue of $\hat{H}_{\hat{L}_z}$

$$E_{L_z} = E_m = -\hbar \omega_1 m. \quad (\text{D.57})$$

Now the differential equation for the two dimensional harmonic oscillator

$$\hat{H}_{osz}^{2d} \psi = E_{osz}^{2d} \psi \quad (\text{D.58})$$

is solved. Unlike the one dimensional harmonic oscillator, the solution for the eigenfunctions of eq. (D.58) is very scarce in literature. Actually there are many publications giving the solution for ϕ_{osz}^{2d} , but not the way of solving eq. (D.58), and not even with the conditions for the quantum numbers n and m , except for Rajagopal and Ryan.² Nevertheless, the way of solving the differential equation (D.58) can be hardly found, but there were some sites on the internet, one of which was the work of a finnish physicist³, giving useful hints of how to solve it. And with the help of a very useful book⁴ it was only a matter of time to be able to calculate the eigenfunctions thoroughly.

The Laplace operator $\nabla^2 = \Delta$ in polar coordinates is

$$\Delta = \frac{1}{r} \frac{\partial}{\partial r} \left(r \frac{\partial}{\partial r} \right) + \frac{1}{r^2} \frac{\partial^2}{\partial \varphi^2} \quad (\text{D.59})$$

and eq. (D.58) can be written as

$$\left\{ \frac{-\hbar^2}{2M} \left(\frac{1}{r} \frac{\partial}{\partial r} \left(r \frac{\partial}{\partial r} \right) + \frac{1}{r^2} \frac{\partial^2}{\partial \varphi^2} \right) + \frac{M\omega_1^2}{2} r^2 \right\} \psi = E_{osz}^{2d} \psi. \quad (\text{D.60})$$

Because the two variables r and φ are not coupled, ψ can be assumed to be separable

$$\psi = \phi(r) \phi_m(\varphi), \quad (\text{D.61})$$

²A.K. Rajagopal and J.C. Ryan, *Phys. Rev. B* **44** 10280 (1991)

³S. Sahrakorpi, Physics Department Tampere, University of Technology Tampere, Finland, <http://alpha.cc.tut.fi/~sahrakor/research/teksti/teksti.html> (unpublished)

⁴H. Dirschmid, W. Kummer and M. Schweda, Einführung in die mathematischen Methoden der theoretischen Physik, Vieweg, Braunschweig ISBN 3-528-03319-3 (1976)

of which one solution we already know from the differential equation of the angular momentum (D.55). As

$$\frac{\partial^2}{\partial \varphi^2} \phi_m(\varphi) = -m^2 \phi_m(\varphi), \quad (\text{D.62})$$

only the differential equation in r is left to be solved

$$\left\{ \frac{-\hbar^2}{2M} \left(\frac{1}{r} \frac{\partial}{\partial r} \left(r \frac{\partial}{\partial r} \right) - \frac{m^2}{r^2} \right) + \frac{M\omega_1^2}{2} r^2 \right\} \phi(r) = E_{osc}^{2d} \phi(r). \quad (\text{D.63})$$

With the Ansatz for the eigenfunction

$$\phi(r) = r^{|m|} e^{-\frac{Cr^2}{2}} F(r). \quad (\text{D.64})$$

which could be found in a book on quantum mechanics⁵, eq. D.63 can be simplified further. But before doing that, the substitution

$$t = Cr^2 \quad dt = 2Cr dr, \quad (\text{D.65})$$

is applied to eqs. (D.63-D.64), with $C = M\omega_1/\hbar = \kappa_\perp/2\hbar = 1/2l_0^2$. Equation (D.64) becomes

$$\phi(t) = C^{-|m|/2} t^{|m|/2} e^{-\frac{t}{2}} F(t), \quad (\text{D.66})$$

and eq. (D.63) is transformed into

$$\left\{ \left(4C \frac{\partial}{\partial t} \left(t \frac{\partial}{\partial t} \right) - \frac{m^2 C}{t} \right) - Ct + \frac{2ME_{osc}^{2d}}{\hbar^2} \right\} \phi(t) = 0. \quad (\text{D.67})$$

The first derivative of $\phi(t)$ is

$$t \frac{\partial}{\partial t} \phi(t) = C^{-|m|/2} t^{|m|/2} e^{-\frac{t}{2}} \left(\frac{|m|}{2} F(t) - \frac{1}{2} t F(t) - t F'(t) \right), \quad (\text{D.68})$$

which further derivative

$$\begin{aligned} \frac{\partial}{\partial t} \left(t \frac{\partial}{\partial t} \phi(t) \right) &= C^{-|m|/2} t^{|m|/2} e^{-\frac{t}{2}} \left\{ t F''(t) + F'(t) (|m| + 1 - t) \right. \\ &\quad \left. + F(t) \left(-\frac{1}{2} (|m| + 1) + \frac{|m|^2}{4t} + \frac{t}{4} \right) \right\}, \end{aligned} \quad (\text{D.69})$$

is inserted into eq. (D.67), giving the differential equation for $F(t)$

$$t F''(t) + F'(t) (|m| + 1 - t) - F(t) \left(\frac{1}{2} (|m| + 1) - \frac{E_{osc}^{2d}}{2\hbar\omega_1} \right) = 0. \quad (\text{D.70})$$

This equation is identical to the confluent hypergeometric or Kummer's differential equation

$$zw''(z) + (c - z)w'(z) - aw(z) = 0, \quad (\text{D.71})$$

⁵S. Flügge, Practical Quantum Mechanics, Springer International, Berlin Heidelberg (1971)

which solution is the confluent hypergeometric function

$$\Phi(a, c; z) \equiv {}_1F_1(a, c; z). \quad (\text{D.72})$$

For arbitrary a and c it has a regular singularity at $z = 0$ and an irregular singularity at infinite z . For square integrability

$$\int_0^\infty |\Phi(a, c; z)|^2 dz < \infty \quad (\text{D.73})$$

a has to be negative or zero and c has to be positive because of the behavior of Kummer's function for large z

$$\lim_{x \rightarrow \infty} \Phi(a, c; z) = \frac{\Gamma(c)}{\Gamma(a)} e^z z^{a-c} \left[1 + O\left(\frac{1}{z}\right) \right]. \quad (\text{D.74})$$

By comparing eqs. D.70 and D.71 a and c can be set to

$$\begin{aligned} a &= \frac{1}{2}(|m| + 1) - \frac{E_{osc}^{2d}}{2\hbar\omega_1} = -n \quad n = 0, 1, 2, \dots \\ c &= |m| + 1 > 0 \end{aligned} \quad (\text{D.75})$$

with the radial quantum number n . The unnormalized eigenfunctions are therefore given by

$$\phi_{n,m}(r) = r^{|m|} e^{-\frac{Cr^2}{2}} \Phi(-n, |m| + 1; Cr^2). \quad (\text{D.76})$$

With the relation between Kummer's function and the associated Laguerre polynomials

$$\Phi(-n, \alpha + 1; z) = \frac{n! \alpha!}{(n + \alpha)!} L_n^\alpha(z) \quad (\text{D.77})$$

the unnormalized eigenfunctions become

$$\phi_{n,m}(r) = r^{|m|} e^{-\frac{Cr^2}{2}} \frac{n! |m|!}{(n + |m|)!} L_n^{|m|}(Cr^2). \quad (\text{D.78})$$

Conditions for the quantum numbers

Now the conditions for the quantum numbers n and m should be set. As the following relation for the energies holds

$$E_N = \hbar\omega_1(2N + 1) = E_m + E_{n,m}, \quad (\text{D.79})$$

with

$$E_{osc}^{2d} \equiv E_{n,m} = \hbar\omega_1(2n + |m| + 1), \quad (\text{D.80})$$

which is calculated from eq. (D.75) and $E_m = -\hbar\omega_1 m$ (eq. D.57), the radial quantum number is given by

$$n = N + \frac{1}{2}(m - |m|), \quad (\text{D.81})$$

and as $n \geq 0$, it means that the quantum number of the angular momentum has to follow the condition

$$m \geq -N \quad m = -N, -N + 1, \dots, 0, \dots, \infty. \quad (\text{D.82})$$

Normalization and orthogonality

With the use of the orthogonality relation

$$\int_0^\infty dt t^\alpha e^{-t} L_n^\alpha(t) L_{n'}^\alpha(t) = \frac{(\alpha+n)!}{n!} \delta_{n,n'} \quad (\text{D.83})$$

the radial eigenfunction (D.78) is normalized. Again, the substitution $t = Cr^2$ is made, which gives

$$\phi_{n,m}(t) = A_{n,m} C^{-|m|/2} t^{|m|/2} e^{-\frac{t}{2}} \frac{n!|m|!}{(n+|m|)!} L_n^{|m|}(t), \quad (\text{D.84})$$

so that the square integration is given by

$$\int_0^\infty dt |\phi_n(t)|^2 = 1 = |A_{n,m}|^2 \frac{n!|m|!^2}{(n+|m|)!} C^{-|m|} \frac{1}{2C}, \quad (\text{D.85})$$

resulting in

$$A_{n,m} = \sqrt{2C} C^{|m|/2} \left(\frac{n!}{(n+|m|)!} \right)^{-1/2} \frac{1}{|m|!}. \quad (\text{D.86})$$

The normalized radial eigenfunctions are therefore

$$\phi_{osc}^{2d} \equiv \phi_{n,m}(r) = \sqrt{2C} \left(\frac{n!}{(n+|m|)!} \right)^{1/2} (Cr^2)^{|m|/2} e^{-\frac{Cr^2}{2}} L_n^{|m|}(Cr^2), \quad (\text{D.87})$$

with $C = M\omega_1/\hbar = |q|H_\perp/(2\hbar c)$. Because of eq. (D.83) it is obvious that

$$\int_0^\infty r dr \phi_{n',m}^*(r) \phi_{n,m}(r) = \delta_{n,n'}, \quad (\text{D.88})$$

and with

$$\int_0^{2\pi} d\varphi \phi_{m'}^*(\varphi) \phi_m(\varphi) = \delta_{m,m'} \quad (\text{D.89})$$

the whole z -independent (we have set $z = 0$ before, so $e^{\frac{i}{\hbar}k_z z} = 1$) eigenfunction is normalized and orthogonal.

For the orthonormal eigenfunctions of the Hamiltonian $\hat{H} = \hat{H}_{osz}^{2d} + \hat{H}_{\hat{L}_z} + \hat{H}_{\hat{p}_z}$ with $z = 0$ we therefore get

$$\psi_{n,m} = \phi_m(\varphi) \phi_{n,m}(r) = e^{-im\varphi} \sqrt{\frac{C}{\pi}} \left(\frac{n!}{(n+|m|)!} \right)^{1/2} (Cr^2)^{|m|/2} e^{-\frac{Cr^2}{2}} L_n^{|m|}(Cr^2), \quad (\text{D.90})$$

with $C = (2l_0)^{-1}$.

List of Publications

1. H. Michor, S. Manalo, M. El-Hagary, G. Hilscher
Disorder and/or density of states effect in $Y_xLu_{1-x}Ni_2B_2C$
 Physica B **283-284**, 491 (2000)
2. S. Manalo, H. Michor, M. El-Hagary, G. Hilscher
Superconducting Properties of $Y_xLu_{1-x}Ni_2B_2C$ and $La_3Ni_2B_2N_3$: A comparison between Eliashberg theory and experiment
 Physical Review B **63**, 104508 (2001)
3. H. Michor, S. Manalo, G. Hilscher
Comparison of the borocarbide and boronitride superconductors
 in NATO Science Series II. Mathematics, Physics and Chemistry - Vol **14**: Rare Earth Transition Metal Borocarbides (Nitrides): Superconducting, Magnetic and Normal State Properties, Ed. K.-H. Mller and V. Narozhnyi, Kluwer Academic Publishers, 45-50 (Dortrecht, 2001)
4. S. Manalo, U. Klein
Has the FFLO state been observed in the organic superconductor kappa-(BEDT-TTF) $_2Cu(NCS)_2$?
 Journal of Physics: Condensed Matter **28**, L471-476 (2001)
5. S. Manalo, E. Schachinger
Optimal spectrum for the borocarbides YNi_2B_2C and $LuNi_2B_2C$
 Journal of Low Temperature Physics **123**, 149 (2001)
6. S. Manalo, U. Klein
Influence of orbital pair breaking on paramagnetically limited states in clean superconductors
 Physical Review B **65**, 144510 (2002)
7. S. Manalo, H. Michor, G. Hilscher, M. Brühwiler, B. Batlogg
Superconducting properties of $RbOs_2O_6$ analyzed within Eliashberg theory
 Physical Review B **73**, 224520-1 (2006)

8. H. Michor, D.T. Adroja, E. Bauer, R. Bewley, D. Dobozanov, A.D. Hillier, G. Hilscher, U. Killer, M. Koza, S. Manalo, P. Manuel, M. Reissner, P. Rogl, M. Rotter, E.-W. Scheidt
Unusual non-Fermi liquid behavior in $CeNi_9Ge_4$
Physica B **378-380**, 640 (2006)
9. M. Sieberer, H. Michor, S. Manalo, M. Della Mea, G. Hilscher, A. Grytsiv, P. Rogl
The effect of hydrogenation upon superconductivity in layered $La_3Ni_2B_2N_{3-\delta}$
Physica B **378-380** 904 (2006)
10. S. Manalo, H. Michor, M. Brühwiler, G. Hilscher, B. Batlogg
Upper critical field of $RbOs_2O_6$ analyzed within Eliashberg theory
Physica C **460-462**, 530 (2007)
11. H. Michor, E.-W. Scheidt, S. Manalo, M. Müller, E. Bauer, G. Hilscher
Superconductivity in layered YB_2C_2
Journal of Physics: Conference Series **150**, 052160 (2009)
12. H. Michor, D.T. Adroja, A.D. Hillier, M.M. Koza, S. Manalo, C. Gold, L. Peyker, E.-W. Scheidt
Evolution of quantum criticality in the system $CeNi_9Ge_4$
to be published

List of conference contributions

1. S. Manalo, H. Michor, G. Hilscher, I. Felner, U. Asaf
Magnetism and superconductivity in $Sr_2(Gd,Ce)_2RuCu_2O_{10-d}$
16th General Meeting of the EPS Condensed Matter Division, Leuven (B)
25.-28.8.1997
2. S. Manalo, H. Michor, G. Hilscher, I. Felner, U. Asaf
Magnetism and superconductivity in $Sr_2(Gd,Ce)_2RuCu_2O_{10-d}$
13th Workshop on correlated systems and superconductivity, Planneralm
22.-28.2.1998
3. S. Manalo, M. Willner, M. El-Hagary, H. Michor, G. Hilscher
Superconducting properties of the borocarbides analyzed in terms of the Eliashberg formalism
14th Workshop on strongly correlated systems and superconductivity, Planneralm
21.-27.2.1999
4. S. Manalo, H. Michor, M. El-Hagary, G. Hilscher
Superconducting properties of the borocarbides analyzed in terms of the Eliashberg formalism
First trilateral seminar Dresden-Vienna-Wroclaw
25.-28.5.1999
5. H. Michor, S. Manalo, M. El-Hagary, G. Hilscher
Disorder and/or density of states effect in $Y_xLu_{1-x}Ni_2B_2C$
International Conference on Low Temperature Physics, Helsinki
4.-11.8.1999
6. S. Manalo, H. Michor, M. Brühwiler
Thermodynamic properties of $RbOs_2O_6$ analyzed within Eliashberg theory
Int. Conference on Strongly Correlated Electron Systems SCES'05, Wien, Österreich
26.-30.07.2005

7. M. Sieberer, H. Michor, S. Manalo, M. Della Mea, G. Hilscher, A. Grytsiv, P. Rogl
The effect of hydrogenation upon superconductivity in layered $\text{La}_3\text{Ni}_2\text{B}_2\text{N}_3$
 Int. Conference on Strongly Correlated Electron Systems SCES'05, Wien, Österreich;
 26.-30.07.2005
8. H. Michor, D. Dobozanov, S. Manalo, M. Müller, E. Bauer, G. Hilscher, P. Rogl, E.-W. Scheidt
Quantum critical behavior in $\text{CeNi}_{9-x}\text{Cu}_x\text{Ge}_4$
 21. Workshop on Novel materials and superconductivity, Planneralp, Österreich;
 11.-18.02.2006
9. S. Manalo, H. Michor, G. Hilscher, M. Brühwiler, B. Batlogg
Eliashberg theory applied on the superconducting properties of RbOs_2O_6
 8. Int. Conference on Materials and Mechanisms of Superconductivity High Temperature Superconductors, Dresden, Deutschland;
 09.-14.07.2006
10. H. Michor, S. Manalo, M. Sieberer, M. Della Mea, G. Hilscher
The influence of N-deficiency upon T_c of $\text{La}_3\text{Ni}_2\text{B}_2\text{N}_{3-\delta}$
 8. Int. Conference on Materials and Mechanisms of Superconductivity High Temperature Superconductors, Dresden, Germany;
 09.-14.07.2006.
11. S. Manalo, D.T. Adroja, A.D. Hillier, M.M. Koza, M. Telling, T. Huber, L. Peyker, E.-W. Scheidt, G.Hilscher, H. Michor
 μSR and inelastic neutron studies on CeNi_9Ge_4
 Theoretical and Experimental Magnetism Meeting, Abingdon, tU.K.
 26.-27.07.2007

Session talks

12. *Superconducting properties of the borocarbides analyzed in terms of the Eliashberg formalism*
 III Pendulum Seminar Krakow-Vienna, Magnetism and Superconductivity, Lindabrunn
 14.-17.4.1998
13. *Superconducting properties of the borocarbides analyzed in terms of the Eliashberg formalism*
 Seminar Lecture, Institut für Experimentalphysik, TU-Wien, 1998
14. *Supraleitende Eigenschaften von $\text{Y}_x\text{Lu}_{1-x}\text{Ni}_2\text{B}_2\text{C}$ und $\text{La}_3\text{Ni}_2\text{B}_2\text{N}_3$: Ein Vergleich zwischen Experiment und Eliashberg-Theorie*

Talk at Frühjahrstagung des Arbeitskreises Festkörperphysik, TT 11.2, Regensburg, 27.-31.3.2000

15. *Paramagnetic effects in thin superconducting films*

Seminar Lecture, Institut für theoretische Physik, JK Universität Linz, 19.3.2001

16. *Superconducting properties of the borocarbides YNi_2B_2C and $LuNi_2B_2C$: A comparison between experiment and Eliashberg theory*

Seminar lecture, invitation of the research group Transportphänomene in Supraleitern und Superfluiden, Universität Bayreuth, 20.4.2001

17. *Competing pair-breaking effects in thin superconducting films and bulk superconductivity*

Seminar Lecture, Institut für Festkörperphysik, TU-Wien, 19.10.2011

CURRICULUM VITAE

SHERRYL MANALO

Personal information:

Date of birth: September 18, 1974
Place of birth: Manila, Philippines
Nationality: Austria
Country of residence: Austria
Marital status: married since 2005

University Education:

| | |
|-----------------------|--|
| Oct. 1993 - Jun. 1999 | Technical Physics at Technical University of Vienna (TU-Vienna), Austria |
| Main focus | Solid State Physics, Superconductivity |
| Topic of diploma | Superconducting and thermodynamic properties of rare-earth borocarbides |
| Jun. 1999 | University degree Dipl.-Ing. (corresponding to MSc.) with honors |
| Topic of thesis | Competing pair-braking effects in thin superconducting films and Bulk Superconductivity |
| Jan. 2000 - Aug. 2001 | Institute for Theoretical Physics at Johannes Kepler-Universität Linz |
| | Generalization of Eilenberger equations for thin films and numerical evaluations of phase diagrams |
| Jan. 2005-Feb. 2006 | Institute for Solid State Physics, TU-Vienna |
| | Experimental work on YB_2C_2 , CeNi_9Ge_4 and analysis of RbOs_2O_6 with Eliashberg theory |
| Oct. 2010 until now | Institute for Solid State Physics, TU-Vienna |
| | Continued dissertation with the analysis of $\text{La}_3\text{Ni}_2\text{B}_2\text{N}_x$ |

School Education:

| | |
|------------|--|
| 1981-1983 | Elementary School, Philippines |
| 1983-1984 | Kusaki Primary School, Nigeria |
| 1984-1985 | Elementary School, Topeka Drive, USA |
| 1985-1993 | Bundesgymnasium Mödling, Untere Bachgasse 8, 2340 Mödling, Austria |
| June, 1993 | Matura (general qualification for university entrance) with honors |

Job experience:

| | |
|-----------------------|---|
| Dec. 1999 | Research employee in the Institute for Experimental Physics at TU-Vienna |
| Jan. 2000 - Aug. 2001 | Research employee in the Institute for Theoretical Physics at Johannes Kepler-University Linz |
| Sept. 2001-Dec. 2007 | General Manager of antitachyon - Manalo & Willner OEG |
| Jan. 2005-Feb. 2006 | Research employee in the Institute for Solid State Physics at TU-Vienna (dissertation contd.) |
| 01.02.2008-30.06.2010 | Senior Consultant, Microsoft |
| since 01.07.2010 | Engagement Manager, Microsoft |

Certifications:

| | | |
|------------|-------------------|---------------------------------|
| Sept. 2007 | Certification CMC | Certified Management Consultant |
| Jul. 2010 | Certification PMP | Project Management Professional |